

Dissertation
submitted to the
Combined Faculty of Natural Sciences and Mathematics
of Heidelberg University, Germany
for the degree of
Doctor of Natural Sciences

Put forward by
Samantha B. Brown-Sevilla
born in: Mexico City, Mexico
Oral examination: 20.12.2022

High-contrast imaging study of exoplanets and circumstellar disks

Referees:

Prof. Dr. Thomas Henning

PD Dr. Sabine Reffert

Abstract

High-contrast imaging provides an excellent tool to detect and characterise exoplanets and circumstellar disks. Understanding the connection between them is key for the improvement of planet formation and evolution theories. In this thesis, I analyse near-infrared (NIR) observations obtained with the Spectro-Polarimetric High-contrast Exoplanet REsearch instrument (SPHERE) to look into various stages of the evolution of planetary systems. I combine the high-contrast imaging technique with observations in the millimetre continuum, hydrodynamical simulations, and radiative transfer models, as well as atmospheric retrievals and self-consistent models to analyse and interpret the different systems. Starting with protoplanetary disks as the birthplaces of planets, I study the morphology of the disk around WaOph 6 at different wavelengths (NIR and millimetre continuum) and find the presence of spiral arms in scattered light for the first time in such a young disk. Additionally, I test the hypothesis of a planet driving the architecture of the disk through hydrodynamical simulations and radiative transfer. Moving on to more evolved systems, I first demonstrate the use of the high-contrast imaging technique to characterise companion candidates and to determine their membership to the system. Furthermore, I analyse spectro-photometric data of the exoplanet 51 Eridani b and apply an atmospheric retrieval to estimate the physical parameters of the planet, revisiting previously reported values and finding a cloud-free atmosphere. Finally, I analyse a sample of debris disks with a double belt architecture inferred via SED modelling. I present mass and location estimates of planets that may be orbiting in the gaps between the belts, as well as detection limits from the observations and plans for future research. This thesis illustrates the current challenges in our understanding of planet formation and evolution and provides possible paths to overcome them.

Zusammenfassung

Die Hochkontrast-Bildgebung ist ein hervorragendes Mittel, um Exoplaneten und zirkumstellare Scheiben nachzuweisen und zu charakterisieren. Ein klares Verständnis von deren Zusammenhang ist essentiell, um Theorien zur Entstehung und Entwicklung von Planeten weiter zu verbessern. In dieser Doktorarbeit analysiere ich Beobachtungen im nahen Infrarotbereich (NIR), die mit dem SPHERE-Instrument (Spectro-Polarimetric High-contrast Exoplanet REsearch instrument) gewonnen wurden, um Planetensysteme in verschiedenen Phasen ihrer Entwicklung zu untersuchen. Dazu kombiniere ich die Hochkontrast-Bildgebung mit Beobachtungen im Millimeter-Kontinuum, hydrodynamischen Simulationen und Strahlungstransportmodellen, sowie Retrievalcodes und selbstkonsistenten Modellen von Atmosphären, um verschiedene Systeme zu analysieren und zu interpretieren. Ich beginne mit protoplanetaren Scheiben, den Geburtsstätten von Planeten, und untersuche die Morphologie der Scheibe um WaOph 6 in verschiedenen Wellenlängen (NIR und Millimeter-Kontinuum), die – als erste, so junge Scheibe ihrer Art – Spiralarme im Streulicht aufweist. Darüber hinaus zeige ich durch hydrodynamische Simulationen und Strahlungstransfer, dass ein Planet für die Architektur der Scheibe verantwortlich sein könnte. Im Anschluss konzentriere ich mich auf weiterentwickelte Systeme und setze Hochkontrast-Bildgebung ein, um Begleiterkandidaten eines Sterns zu charakterisieren und ihre Zugehörigkeit zum System zu bestimmen. Darüber hinaus analysiere ich spektrophotometrische Daten des Exoplaneten 51 Eridani b und wende einen Retrievalcode an, um physikalische Parameter seiner Atmosphäre abzuschätzen. Diese vergleiche ich mit zuvor berichteten Werten und finde eine wolkenfreie Atmosphäre. Schließlich analysiere ich ein Sample von Trümmerscheiben mit Doppelgürtelstrukturen, welche aus SED-Modellen abgeleitet wurden. Ich gebe Abschätzungen für Massen und Positionen von Planeten, die sich möglicherweise in den Lücken zwischen den Gürteln befinden, leite Detektionsgrenzen aus den Beobachtungen ab und spezifiziere Pläne für weitere Untersuchungen. Diese Doktorarbeit veranschaulicht die aktuellen Grenzen in unserem Verständnis der Planetenentstehung und -entwicklung und zeigt Möglichkeiten auf, um diese in Zukunft zu überwinden.

Contents

Abstract	v
List of Figures	xi
List of Tables	xiii
1 Introduction	1
1.1 From disks to planets	1
1.1.1 Protoplanetary disks	1
Properties of protoplanetary disks	2
1.1.2 Disk lifetime and evolution	5
1.1.3 Planet formation	7
1.2 Debris disks	8
1.2.1 Debris disk observations	8
1.2.2 Properties of debris disks	9
1.3 Planet detection	11
1.3.1 Detection methods	12
Transit	12
Radial velocity	12
Astrometry	12
Microlensing	13
Direct imaging	13
1.4 High-contrast imaging	13
1.4.1 Coronagraphy and adaptive optics	14
1.4.2 Observing strategies	15
Angular differential imaging	15
Reference star differential imaging	16
Spectral and polarimetric differential imaging	16
1.4.3 SPHERE	16
1.4.4 Connection between planets and disks	17
1.4.5 Exoplanet atmospheres	17
1.5 Rationale and outline of the thesis	18
1.5.1 Thesis outline	18

2	Analysis of the spiral arms in the disk around WaOph 6	21
2.1	Motivation	21
2.2	WaOph 6	22
2.3	Observations and data reduction	23
2.3.1	IRDIS polarimetric observations and data reduction	23
2.4	Disk analysis	26
2.4.1	The disk in polarized scattered light	26
2.4.2	Companion candidate analysis	27
2.4.3	Comparison to millimetre observations	27
	Radial profiles	27
	Spiral arms	29
2.4.4	Origin of the spirals	32
2.5	Modelling	32
2.5.1	Hydrodynamical models	33
2.5.2	Radiative transfer	36
2.5.3	Results and comparison to observations	37
2.6	Discussion	38
2.6.1	Observations in NIR and mm	38
2.6.2	Upper limits on the brightness of point sources	39
2.7	Summary	40
3	Candidate companions around AH Lep	43
3.1	Motivation	43
3.2	AH Lep	43
3.3	Observations and data reduction	44
3.4	Analysis of the companion candidates	45
3.5	Astrometric analysis	45
3.6	Summary	47
4	Revisiting the atmosphere of 51 Eridani b with VLT/SPHERE	49
4.1	Motivation	49
4.2	51 Eri b	50
4.3	Observations	51
4.4	Data reduction and spectrum extraction	52
4.4.1	Spectrum extraction	53
4.4.2	Detection limits	54
4.5	Retrieval analysis	55
4.5.1	Modelling setup	57
	petitRADTRANS setup	57
	MultiNest setup	58
4.5.2	Input data	58
4.5.3	Results and comparison with previous data	59
	Retrieval results	59

Atmospheric retrieval on old data	62
4.6 Discussion	62
4.6.1 Parameters of 51 Eri b	62
C/O ratio	62
[Fe/H]	63
Clouds and $\log \tau_{\text{clouds}}$	63
Radius and surface gravity	64
Mass	64
4.6.2 Atmospheric retrievals vs self-consistent models	65
4.7 Summary	67
5 Debris disks with SPHERE	69
5.1 Motivation	69
5.2 Sample selection	69
5.2.1 SED Modelling	70
5.3 Characterization of gaps in the disks	74
5.3.1 Population of planets within the belts	74
5.4 SHPERE observations	76
5.4.1 Data reduction	76
5.4.2 Detection limits	77
5.5 Discussion	77
5.5.1 Future work	81
5.6 Summary	81
6 Conclusions and Outlook	83
6.1 Summary	83
6.2 Outlook	85
A Complementary material to Chapter 2	87
A.1 Dust mass estimate	87
A.2 Unprocessed reduced Q_ϕ and U_ϕ SPHERE images	87
A.3 Extracting the non-axisymmetric information from the ALMA data	87
A.4 Toomre parameter calculation	88
A.5 Gallery of density distributions from the hydrodynamical simulations and radiative transfer images	89
B Complementary material to Chapter 4	91
B.1 Wavelength calibration and spectral differential imaging	91
B.2 Telluric monitoring and correction	92
B.3 Spectral correlation matrix	94
B.4 Enforced clouds retrieval and attempt to reproduce previous results	95
List of Publications	103

Bibliography	105
Acknowledgements	129

List of Figures

1.1	Cross-section diagram of a protoplanetary disk structure	2
1.2	Gallery of protoplanetary disks observed with ALMA	3
1.3	Evolution of a typical circumstellar disk	6
1.4	Typical temperatures and peak emission λ s for a debris disk	10
1.5	Planet mass vs orbital period of confirmed exoplanets	11
2.1	ALMA continuum image of WaOph 6	23
2.2	Reduced SPHERE/IRDIS-DPI images of WaOph 6	26
2.3	Azimuthal profile of the deprojected Q_ϕ image	27
2.4	Total intensity SPHERE/IRDIS-DPI image of WaOph 6	28
2.5	Comparison of the radial intensity profiles of the SPHERE and ALMA images	28
2.6	Comparison of the spiral structure of WaOph 6 between the SPHERE and ALMA images	30
2.7	Polar plot showing the spiral arms of both the SPHERE and ALMA images of WaOph 6	31
2.8	Radiative transfer images showing the spirals formed by a $10 M_{\text{Jup}}$ planet at 140 au	33
2.9	Planet detection limits as a function of the separation from the star for the SPHERE H -band	39
3.1	AH Lep and the two companion candidates	44
3.2	Contrast limits	45
3.3	Colour-magnitude diagram of the companion candidates	46
3.4	Contrast of the companion candidates	46
3.5	Astrometric analysis of AH Lep	47
4.1	S/N detection map from ANDROMEDA for the SPHERE/IFS data	51
4.2	51 Eri b spectra and photometry from different epochs	54
4.3	Flux uncertainty over wavelength for the YH spectra of 51 Eri b	55
4.4	Contrast and mass limits	56
4.5	<i>petitRADTRANS</i> best-fit spectrum of 51 Eri b	60
4.6	Corner plot of the posterior PDFs	61
4.7	Retrieved pressure-temperature profiles for the four different cases	64
5.1	SEDs for the selected targets	72
5.1	(continued) SEDs for the selected targets	73

5.2	Population of potential planets within the gaps of the two belts	76
5.3	5σ contrast limits from the SPHERE data	78
5.4	Mass detection limits	79
5.4	(continued) Mass detection limits	80
A.1	Reduced Q_ϕ and U_ϕ SPHERE/IRDIS-DPI images	88
A.2	Density maps from the 3D and 2D hydrodynamical simulations	89
A.3	Radiative transfer images from the 3D and 2D hydrodynamical simulations	90
B.1	SPHERE/IFS dispersion solutions	92
B.2	Telluric absorption as traced by SPHERE/IFS, sky infrared temperature and PWV	93
B.3	Spectral correlation matrix	95
B.4	<code>petitRADTRANS</code> best-fit spectrum of 51 Eri b for the “enforced clouds” retrieval with the new data	96
B.5	Corner plot of the posterior PDFs of the “enforced clouds” retrieval with the new data	97
B.6	<code>petitRADTRANS</code> best-fit spectrum of the “nominal” retrieval run on the data set from Samland et al. (2017)	98
B.7	Corner plot of the posterior PDFs of the “nominal” retrieval with the data set from Samland et al. (2017)	99
B.8	<code>petitRADTRANS</code> best-fit spectrum for the “enforced clouds” retrieval run on the data set from Samland et al. (2017)	100
B.9	Corner plot of the posterior PDFs of the “enforced clouds” retrieval with the data set from Samland et al. (2017)	101

List of Tables

2.1	WaOph 6 stellar and disk parameters	24
2.2	Observing log	24
2.3	Spiral fit parameters	29
2.4	Simulation parameters	35
4.1	Observing log	52
4.2	IRDIS photometry	54
4.3	Retrieval priors	56
4.4	Retrieval results	60
5.1	Target parameters	71
5.2	Debris disks parameters	74
5.3	Parameters of the possible planets in the disks	75
5.4	Observing log	77
B.1	Best fit parameters for the reproduction attempts	95

**"We make our world significant by the courage of our questions
and the depth of our answers"**

Carl Sagan

*Dedicada a la memoria de Teresa Ibarra Jiménez y Luis Brown
González*

Chapter 1

Introduction

Throughout history, humans have wondered about the existence of other worlds like ours. Thanks to the development of dedicated techniques to search for planets outside of the Solar System (i.e. exoplanets), in the last thirty years not only have we confirmed the existence of other worlds, but we have learnt that there is a vast diversity of them. Indeed, to this date there are 5,178¹ confirmed exoplanets. However, the success of this quest has also brought with it many questions, of which some are still unanswered. In the following, I describe the open questions that this thesis addresses in the context of the current state of the field, with a focus on the high-contrast imaging technique

1.1 From disks to planets

1.1.1 Protoplanetary disks

Planets are a by-product of the star formation process since they are thought to be born in the disk of gas and dust that surrounds a newly formed star. In order to study the conditions from which planets emerge, it is necessary to understand the materials from which they form (i.e. the gas and dust in protoplanetary disks). In a nutshell, stars form in large molecular clouds, which are giant reservoirs of cold, molecular gas (Dobbs et al. 2014; Chevance et al. 2022). Dense cores are present in these clouds and when they collapse due to their own gravity, star formation begins. This can occur either spontaneously or it can be triggered by external factors such as shocks (e.g. Kinoshita et al. 2021). Following the collapse, a circumstellar disk rapidly forms due to the conservation of angular momentum. Initially, the protostar is embedded in a dusty envelope where the disk transports material to be accreted into it. After a fraction of a Myr (Evans et al. 2009; Offner and McKee 2011), the envelope has completely dispersed and the star has drawn most of its mass from the disk. At this particular stage of evolution, the disk is considered a protoplanetary disk (hereafter PPD). In this moment, the evolution of the disk is dominated by several processes, namely, accretion onto the star, photo-evaporation from either local or external radiation sources, agglomeration into larger bodies, and dynamical interactions with companions. The disk is now observable through excess emission relative to the stellar photosphere from the visible to the near-infrared (NIR) wavelengths.

¹10.10.2022; <https://exoplanetarchive.ipac.caltech.edu/>

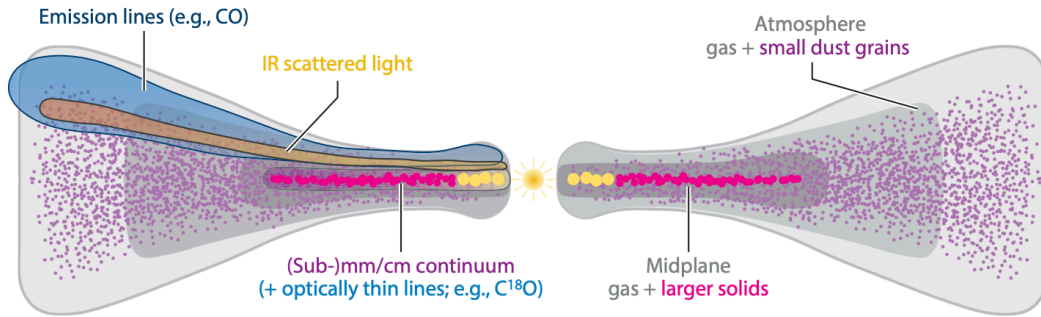


Figure 1.1: Cross-section diagram of a protoplanetary disk structure. The gas is denoted in gray scale, while dust is shown as circles of different sizes. On the left, the locations of emission tracers are indicated. Credit: Andrews (2020).

Initially, PPDs are composed of gas (99%) and dust particles (1%) inherited from the interstellar medium (ISM). Most of the gas in the disks is cool ($T \lesssim 100$ K), diatomic, molecular hydrogen H_2 , while the dust is made up of silicates of size $\leq 0.1 \mu\text{m}$ that are coated with an ice mantle from gas molecules that have frozen out (e.g., Alarcón et al. 2020). Even if the dust contribution to the disk mass is small, it is easier to detect due to its opacity. The gas emits only at specific wavelengths, resulting in a more complicated detection. Nowadays, three observational tracers are mainly used to study PPDs: scattered light, thermal continuum emission, and spectral line emission. The first two are sensitive to the dust particles, while the third one is used to study the gas (e.g., Baruteau et al. 2021).

Figure 1.1 shows a cross-section of the PPD with its components and respective tracers. Scattered light is sensitive to the micrometre-sized dust grains at the surface of the disk, which – given their location – reflect the radiation emitted by the host star. Polarised light by scattering can also be detected at micrometre wavelengths. Observations in scattered light with high-contrast imaging have the advantage of being able to achieve a higher sensitivity in the inner regions compared to other tracers such as the mm continuum. This is achieved through sophisticated adaptive optics (AO) systems (more on AO in Section 1.4.1). Observations in continuum emission trace the solids in the disk that emit a long thermal continuum ($\lambda \approx 1 \mu\text{m} - 1\text{cm}$). As illustrated, these solids are mainly located in the mid-planes of PPDs. Most of the emission at these wavelengths is optically thick, which allows to obtain temperature estimates of the disks. Because the most abundant species of gas in PPDs (H_2) does not have a permanent dipole moment, it does not emit efficiently over the disk volume. Therefore, in order to study the gas, measurements of spectral lines from other tracers such as CO or rarer species are used.

Properties of protoplanetary disks

Mass

A key property of PPDs is their mass, since this property constrains the future contents of planetary systems. As a common practice, (sub-)millimetre observations are used to determine the mass of the disks, as the dust emission at these wavelengths is optically thin and therefore the flux (F_ν) can be directly related to the mass:

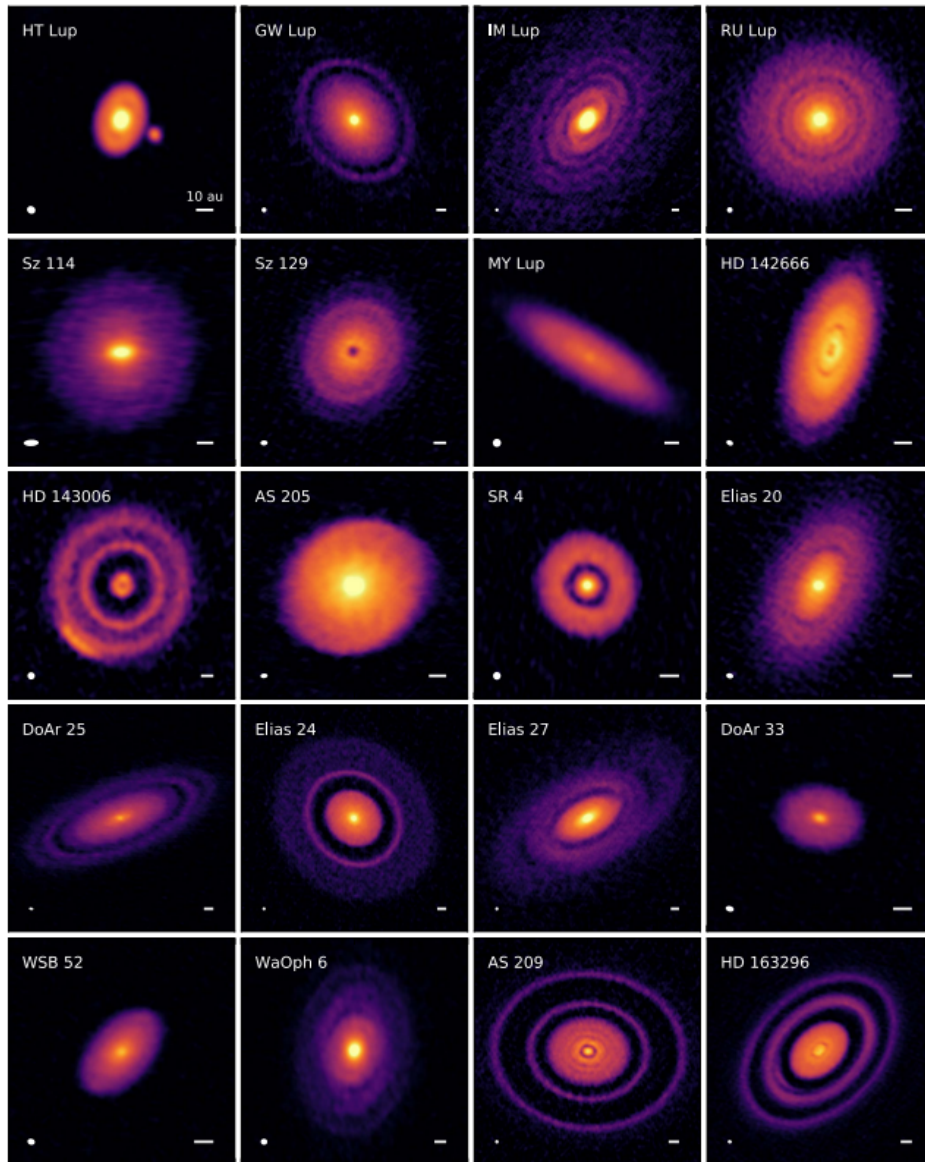


Figure 1.2: Gallery of protoplanetary disks observed with ALMA within the Disk Substructures at High Angular Resolution Project (DSHARP). The scale bars represent a projected distance of 10 au. Credit: Andrews et al. (2018).

$$M = \frac{F_\nu d^2}{\kappa_\nu B_\nu(T)}, \quad (1.1)$$

with d the distance to the source and the Planck function (in the Rayleigh-Jeans regime) $B_\nu \approx 2\nu^2 \kappa T / c^2$.

However, mass estimates remain mostly uncertain because they rely on a large amount of assumptions about the emitting particles, such as the dust-to-gas ratio, which may evolve to a substantially higher fraction (e.g., Chachan et al. 2021), the CO/H₂ abundance, or the dust opacities. Another very important source of uncertainty is the hidden mass in large grains, which have little to no effect on the spectral energy distribution (SED) of the disks. Thus, current mass estimates are considered to be lower bounds.

Size

An actual definition of the size of the disks remains ambiguous throughout the literature. A practical approach is to determine an effective size R_j , which is the radius that encircles a fraction of the luminosity from a given tracer j . As an example, typical PPDs sizes at millimetre wavelengths are of the order of tens to a few hundreds of au. It is noteworthy to mention that the outer radii of the gaseous components is typically much larger than that of the dust components (e.g., Sanchis et al. 2021; Long et al. 2022).

Surface density

Measuring the surface density is of great interest since it gives insight into the evolution of PPDs. For example, helping to understand how angular momentum is transported in the disks through different processes such as winds or turbulent viscosity (e.g., Bai and Stone 2013; Isella et al. 2009), as well as the impact that the surface density has on potential architectures of the planetary systems (Miguel et al. 2011) and their possible evolution (e.g., Drazkowska et al. 2022). However, accurate surface density measurements remain to be a challenge for the same reason as mass determination.

Scale height

The scale height, which measures how flared the disk is, depends on the balance between the temperature and surface density profile of the disk. The vertical structure of PPDs increases with radius as $H \propto R^h$, with $h \approx 1.3 - 1.5$ (Chiang and Goldreich 1997). Characterising the scale height is key to model the thermal and chemical structure, and hence to understand the spectroscopic observations.

Substructure

The advances in instrumentation and data processing techniques represented a revolution in imaging PPDs. Enhanced sensitivity and angular resolution have revealed a wide variety of substructures in PPDs, such as rings, gaps, spirals, and shadows (e.g.,

Long et al. 2018; Andrews 2020; Kepler et al. 2020). The physical origin of these substructures is diverse; for example, rings can arise from substantial mass loss through photo-evaporation or winds, as well as from the presence of one or more giant planets clearing the central cavity and creating a gap. Furthermore, if a disk is sufficiently cold, self-gravity can cause gravitational instability throughout the disk and drive the formation of spiral arms. Gravitational instability can occur if the Toomre parameter Q (Toomre 1964), given by

$$Q \equiv \frac{\Omega_k c_s}{\pi G \Sigma}, \quad (1.2)$$

is greater than the critical value $Q_{\text{crit}} \simeq 1$. In the equation, Ω_k is the angular velocity, c_s is the sound speed, and Σ is the surface density of the disk. Another potential reason for the presence of spirals are tidal forces by a giant planet perturbing the disk via gravitational interactions. In these cases, the planet can cause spiral arms both in the interior and exterior of its orbit. An additional possible cause for the presence of spiral structure is a flyby event of a close companion to the system (e.g., Cuello et al. 2019; Ménard et al. 2020) that perturbs the disk material and causes over-densities that form the spiral pattern. By studying the structures in PPDs, we can gain insight into what might be shaping their current architecture (see Section 1.4.4 for more details).

1.1.2 Disk lifetime and evolution

Disk lifetimes are essential in order to understand the timescales over which physical processes dissipate the disks and to estimate the time available for planet formation. Most of the constraints on disk lifetimes have been obtained from the thermal emission of dust, which absorbs stellar light and re-emits in the $1 \mu\text{m}$ to 1mm range. NIR observations find disk lifetimes between $\lesssim 1 \text{Myr}$ to up to 10Myr (Li and Xiao 2016). The processes through which the material in the disks dissipate include accretion onto the star or companions, other processes, especially at early stages, include viscous accretion. The gas in the disks rotates in a Keplerian orbit, where the specific angular momentum increases with radius. Therefore, in order for accretion to occur, the material in the disk must lose angular momentum. This can happen either via the redistribution of angular momentum (possible due to viscosity in the gas) or by photo-evaporation of the dust by stellar radiation. These processes drive the evolution of the gas and consequently lead to the depletion of the disk. The outward transport of angular momentum allows the material in the disk to move inward. Pure molecular viscosity has proven to be insufficient at transporting angular momentum (Pringle 1981), thus turbulence was introduced. Turbulence can be caused by different mechanisms, such as hydrodynamical instabilities (e.g., Lyra and Umurhan 2019) or the magneto-rotational instability (Balbus and Hawley 1991). Another mechanism driving accretion might be disk winds, which remove angular momentum by blowing away the surface layers of the disk (see Turner et al. 2014 for details on all these processes). The dust, on the other hand, evolves through different processes besides viscous accretion. These processes are essential for the

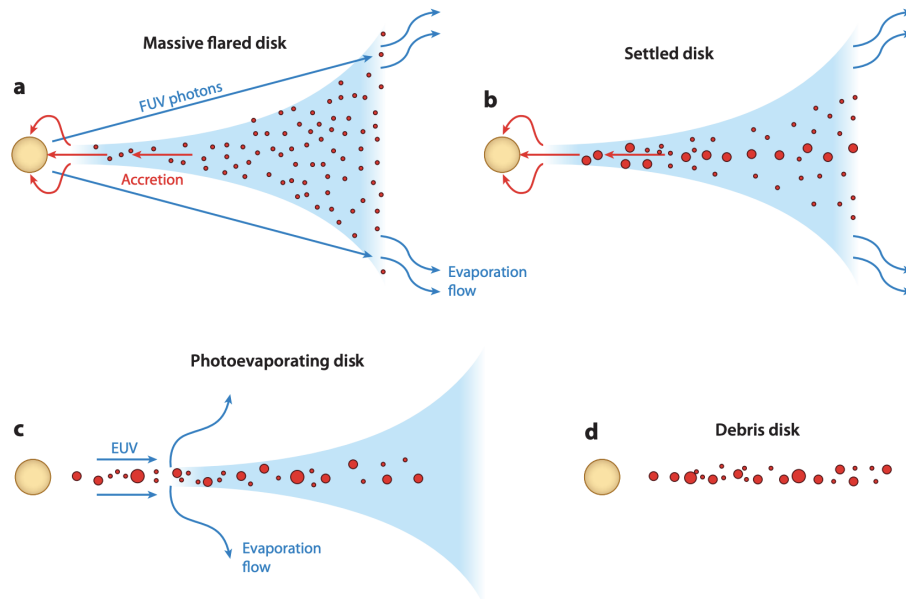


Figure 1.3: Evolution of a circumstellar disk. Dust is shown in red and gas in blue. a) In the early stages, the mass loss is driven by viscous accretion onto the star and far-UV photo-evaporation of the outer disk. b) Meanwhile, the dust grains agglomerate into larger bodies and settle into the midplane. c) As the accretion rate decreases due to the reduced disk mass, extreme-UV photo-evaporation becomes dominant, opening a gap in the disk. This prevents the outer disk to resupply the inner disk, causing it to drain in less than a Myr. Accretion onto the star stops and the remaining disk quickly dissipates from the inside out. Credit: Williams and Cieza (2011).

first steps of planet formation, in which the submicron particles need to grow ~ 13 orders of magnitude in size in order to build planets. They are described below in Section 1.1.3.

PPDs that have substantially cleared their inner regions, resulting in holes or large gaps, are called transitional disks. Their name refers to the transition phase between a PPD and a debris disk (see Section 1.2). Transition disks still maintain high gas-to-dust ratios and gaseous accretion onto the central star is often found to be occurring (Espaillat et al. 2014). They are identified from the lack of NIR or mid-IR (MIR) excess emission in their SED, which is caused by the absence of dust in their inner regions. Transitional disks represent a small fraction ($\sim 15\%$) of the disk population, however, it has been argued that this is not necessarily an indication of these disks being very short lived ($\lesssim 0.1$ Myr; e.g., Currie and Sicilia-Aguilar 2011). A proposed explanation for their morphology, besides the mechanisms that remove the primordial gas, has been ongoing planet formation. Since giant planet formation must occur before the gas in the disk is dissipated, these disks are excellent systems to study planet formation theories and disk evolution (Mawet et al. 2017). Transition disks eventually dissipate through a combination of physical mechanisms involving the central star and planetary companions (see Wyatt et al. 2015, and references therein). Figure 1.3 shows the different evolutionary stages previously described up to the point at which the disk reaches the debris disk phase (see Section 1.2).

1.1.3 Planet formation

Two models have been proposed to explain planet formation: *core accretion* (Bodenheimer and Pollack 1986; Pollack et al. 1996) and *gravitational instability* (Cameron 1978; Boss 1997). The former consists of the formation of a solid core (forming a terrestrial planet) that can reach a critical mass after which it undergoes rapid gas accretion (forming a gas giant planet); this is also called a bottom-up model. The latter builds planets by the direct gravitational collapse from the gas (forming gas giant planets, typically in the outer part of the disk); this model is also known as top-down formation.

In the core accretion model, planet formation can be classified into three stages: from dust to pebbles, from pebbles to planetesimals, and from planetesimals to protoplanets/planets. At the beginning, small, μm -sized dust grains collide with each other and stick together to form larger particles; this process is known as *dust coagulation*. These dust grains are initially coupled to the gas but as they grow, they settle into the disk midplane and detach from the gas. Because the amount of gas decreases with the distance to the star, the gas experiences a radial pressure force outwards that forces it to move at sub-Keplerian speeds. The dust in turn, moves at Keplerian velocity unaware of this pressure gradient. Thus, it feels a headwind from the gas opposing its movement, causing it to spiral inwards towards the star (Whipple 1972). This process is known as *radial drift* and represents a major obstacle for the growth of planetesimals. One of the proposed mechanisms to overcome this problem is the *streaming instability*, which clusters pebbles and collapses them into planetesimals by self-gravity (Youdin and Goodman 2005). Subsequently, planetesimals can grow by accreting other surrounding planetesimals or pebbles that drift inward from outer parts of the disk. At the point when the core mass reaches $\sim 10 M_{\oplus}$ (Pollack et al. 1996), there are two possibilities: if a sufficient amount of gas is left in the disk, the protoplanets are able to rapidly accrete surrounding gas to form giant planets within a timescale much shorter than the disk lifetime; on the contrary, if the disk has been mostly depleted of gas, the protoplanets form into low-mass terrestrial or super-Earth planets (see review by Liu and Ji 2020).

In the gravitational instability model, a massive and cold disk can become gravitationally unstable and fragment to form gas clumps of the order of a few Jupiter masses (Kley 2019). Quantitatively, the condition for a disk to become gravitationally unstable can be determined from the Toomre parameter Q (see Section 1.1.1 and Equation (1.2)). If the disk is able to cool efficiently (i.e. on a timescale comparable to the dynamical time), the clumps collapse and eventually form a gaseous giant planet by rapid gas accretion over a period of 1 kyr to 1 Myr (e.g., Durisen et al. 2007; Mandell 2011). Furthermore, the conditions for instability and fragmentation appear to not be present in the inner regions of the disk (i.e. the closer tens of au). Thus, gravitational instability can only occur in the outermost parts of the disk (Rafikov 2007).

One way to constrain the mechanism of planet formation is through the statistical properties of the detected exoplanets. Most of the detection techniques are more sensitive to close-in separations (see Section 1.3.1) where the core accretion model is more efficient. On the other hand, direct imaging can probe the parameter space at larger orbital radii where

giant planets formed via gravitational instability can be located (see Section 1.4). However, direct imaging surveys have found that giant planets at wide separations are rare (e.g., Vigan et al. 2021), which suggests that gravitational instability is not the dominant planet formation mechanism. Nevertheless, both formation mechanisms are needed to explain the observations.

1.2 Debris disks

Once the mechanisms of accretion, photo-evaporation, winds, and agglomeration of large solid bodies dissipate most of the material in the PPD, what is left is called a debris disk. They are generally optically thin, almost gas-free, and they are typically identified by infrared or mm emission excesses in the stellar SED, coming from dust that is heated by stellar radiation and re-emits at longer wavelengths. This dust must continuously be replenished by collisional processes given that the first generation dust from the PPD phase has been lost. Due to their older age, debris disks are not limited to be found in star forming regions, which favours their detection around nearby stars. From observations, it is estimated that a significant fraction of main sequence stars older than ~ 10 Myr are hosts to debris disks (e.g., Eiroa et al. 2013). Their typical architecture resembles that of the asteroid (~ 3 au) and Kuiper (~ 30 au) belts in our Solar System. The components of debris disks are thus commonly referred to as *inner disk*, characterised by warm or hot dust emission (typically $T > 150$ K) and faster evolutionary timescales, and *outer disk*, characterised by cold dust (typically $T < 100$ K) with longer evolutionary timescales. Another component, which may be present as a result of the physical processes taking place in debris disks, is a radially extended halo of small grains in eccentric orbits. The solids in debris disks span a huge size range, from fractions of micrometres (fine dust) up to hundreds or thousands of kilometres (large planetesimals).

Due to their low optical depths, debris disks provide a unique opportunity to study planet-disk interactions by imaging planets within them. Furthermore, the material from which they are composed (mainly dust and potentially gas) can give us insight into the material exoplanets might have formed from.

1.2.1 Debris disk observations

Debris disks are commonly observed through the thermal emission that their dust emits in the infrared. In general, the grains causing the excess are located at a distance to the star that scales with the wavelength of the observation (as can be seen in Fig. 1.4), i.e. the shorter the wavelength, the closer to the star are the grains that we are observing, and vice versa. In addition, the wavelength at which emission is observed is related to the size of the particles that emit most efficiently. Thus, we can trace different parts of the disk with multiwavelength observations. In this way, (sub-)mm observations will detect mm-size grains that are not affected by radiation pressure, which make them excellent to trace the distribution of parent planetesimals; mid-IR wavelengths will probe the small dust still coupled to

the gas, and scattered light NIR or optical observations will allow to probe the very small (not coupled) dust. Debris disks were discovered with the Infrared Astronomical Satellite (IRAS) since then several other missions (e.g., Spitzer Space Telescope, Wide-field Infrared Survey Explorer (WISE), and Herschel Space Observatory) have observed thousands of stars to measure their excesses.

Some debris disks present a gas component in addition to the dust, which can be detected through emission or absorption spectroscopy (e.g., Rebollido et al. 2022). The gas in these disks is thought to either be a remnant of the primordial PPD or, like the dust, to have a secondary origin. However, this has only recently become possible, thanks to the development of high sensitivity instruments such as the Atacama Large Millimeter-submillimeter Array (ALMA).

A common way to characterise debris disks is to look at the SED of their stars. In the presence of a debris disk, an excess in the IR may exceed the stellar photospheric emission at the same wavelengths. This can be characterised by the *fractional luminosity* $f = L_{\text{disk}}/L_*$, by which a disk is considered optically thin if $f \ll 1$. Typical fractional luminosities are of the order of $10^{-3} - 10^{-6}$, decreasing with the age of the system (Matthews et al. 2014). The stellar + dust emission can be fitted by blackbody spectra (although some corrections should be applied due to the fact that dust grains are not perfect blackbodies) to estimate the equilibrium temperature (T_{belt}) of the dust grains. In the case of multiple dust components (as in Fig. 1.4), different blackbody functions can be fitted for each of them. The fractional luminosity and temperature are essential parameters to constrain debris disks, especially if they are unresolved. As can be seen in Fig. 1.4, from the wavelength of the peak emission we can infer the temperature, as well as the location from which the emission is coming.

It is also possible to resolve debris disks through their thermal emission and scattered light. This has been of great help in constraining the disks' parameters by complementing SED observations. As stated above, dust particles are not perfect blackbody emitters and due to this, the radii of the belts inferred from the SED fits can be underestimated. Another problem is that SED modelling is degenerate, in the sense that the same temperature can be fitted with belts of different grain sizes at different locations. These issues can be overcome with resolved images of the disks, from which the radial structure, and therefore the temperature and composition, can be constrained. Scattered light images have also revealed substructures in debris disks, such as warps, gaps, or spiral arms (e.g., Lagrange et al. 2010), which can provide evidence for the presence of unseen planets (see Section 1.4.4). Additionally, disk observations allow to study the smallest particles and give insight into the building blocks of exoplanets, as well as planet-disk interactions (e.g., Lu et al. 2022).

1.2.2 Properties of debris disks

Orbiting the central star, the planetesimals in debris disks are subjected to its gravitational force. For smaller particles ($\lesssim 1$ mm), the radiation pressure of the star, which scales as the inverse of the square distance but – contrary to the gravitational force – is directed outward, plays an additional role. The smaller the particles, the more the radiation pressure acts on them, which causes the orbits of small grains to differ from those of the larger bodies. This

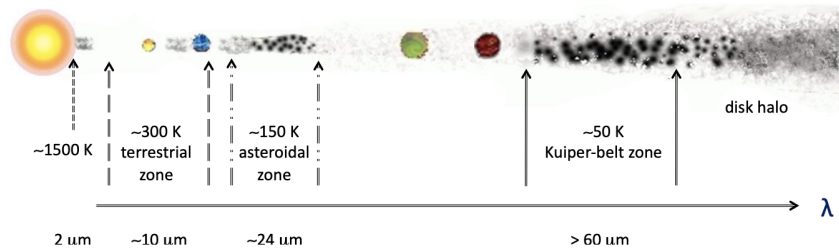


Figure 1.4: Typical temperatures and peak emission wavelengths for the Solar System architecture as an example of the common structure of a debris disk. Credit: Matthews et al. (2014).

can result not only in larger semi-major axes but also in highly eccentric orbits. The latter are also known as *parent bodies* since the small grains come from the collisions and fragmentations between them. These collisions are able to occur in debris disks thanks to the absence of gas, which would otherwise damp the relative velocities of the particles, as it occurs in PPDs. However, in order for the relative velocities to increase from the PPD to the debris disk phase, and therefore, to trigger the production of dust via collisions, the disk needs to be *stirred* by some mechanism. There are two main sources of stirring: “self-stirring”, when it comes from large planetesimals (~ 1000 km) in the belt (Kenyon and Bromley 2004); and stirring from the planets orbiting within the disk cavity (e.g., Mustill and Wyatt 2009). Additional sources of stirring such as stellar encounters have also been proposed, although they are less likely to occur (Kenyon and Bromley 2002).

When the disk has been sufficiently stirred, a collisional cascade occurs. This generates small particles down to dust sizes, which can be blown away by the radiation pressure. The size limit for particles to be expelled by this stellar pressure is called the *blowout size*. It is defined as $\beta = \frac{F_{\text{rad}} + F_{\text{wind}}}{F_{\text{grav}}} \geq 0.5$, where F_{rad} , F_{wind} , and F_{grav} are the radiation pressure, the wind pressure, and the gravitational force, respectively. For dust up to $\beta = 0.5$, the grains will move in bound elliptical orbits with larger semi-major axes and eccentricities than their parent bodies, while dust within $0.5 < \beta < 1$ will orbit in hyperbolic unbound orbits and eventually be expelled. Assuming a steady-state cascade, the distribution of solids in the disk can be approximated by $n(D) \propto D^{-\alpha}$, where D is the grain size and $\alpha \approx 3.5$ (Dohnanyi 1969).

Besides the radiation pressure, there is another mechanism that removes slightly larger grains after the collisional cascade, the so-called *Poynting-Robertson effect*. It arises from the tangential component of the radiation pressure and causes a drag that leads the grains to spiral slowly towards the star. In the reference frame of the dust grain, the stellar radiation appears to be coming at a small angle in the forward direction, which results in a force with a component opposite to the direction of motion. This causes the dust grain to gradually lose its orbital energy and angular momentum and be pulled inwards on a timescale of thousands of years (Krivov 2010). If the belts in debris disks are dense, collisions between small dust grains are frequent enough for the dust to reach small sizes and be blown out by radiation pressure instead (Wyatt 2005). However, for disks where the belt is not dense enough, the dust will get closer to the star and be sublimated. This happens in the Solar

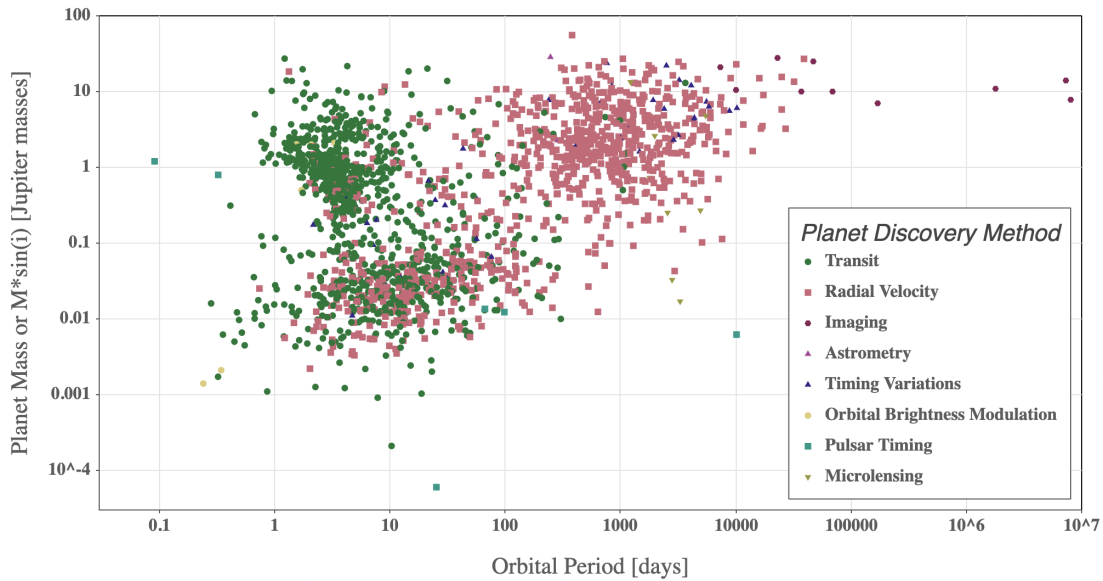


Figure 1.5: Companion mass versus orbital period of the current population of detected companions. The different colours indicate the primary method of discovery. Credit: NASA Exoplanet Archive.

System with the dust that is being dragged inwards from the asteroid belt and cometary activity, which is known as *zodiacal dust* (e.g., Szalay et al. 2021). Analogously, in extrasolar systems this is called *exozodiacal dust* and it has been detected in a few systems via NIR interferometry (e.g., Nuñez et al. 2017).

In order to interpret the observations and understand how the structures in debris disks formed, theoretical models have been developed to extract physical information from the dust. To model the collisional cascade, for example, three kinds of methods are available: *collisional models* that analyse the dust production from different scenarios and can be moved forwards or backwards in time to study how the grain size distributions evolve to explain IR excesses; *dynamical models* that consider the interaction between the dust and the planets (or other stars) to explain the structures that result from this interplay; and *hybrid models*, that combine collisions and dynamics to see how particles are produced and evolve under the gravitational influence of planetary mass bodies. In addition, *radiative transfer models* are used to understand how the dust interacts with the stellar light (see review by Kral 2016).

1.3 Planet detection

The discovery of the first planetary companions dates back to the late 1980s and early 1990s (e.g., Campbell et al. 1988; Latham et al. 1989; Wolszczan and Frail 1992), however, it was the discovery of the Jupiter-mass companion around a solar-type star (Mayor and Queloz 1995) that kicked off the field of exoplanets. Since then, an abundance of diverse planets has been discovered mainly using the following techniques: transits, radial velocities, imaging and microlensing. This can be seen in the distribution of properties in Fig. 1.5.

1.3.1 Detection methods

Two main groups of exoplanets have been discovered: (ice) giant planets over several orders of magnitude of orbital separation; and super-Earths and sub-Neptunes orbiting within 1 au of their host star. The main techniques that have been used to detect them as well as the principles behind each of them are briefly described below.

Transit

In recent years, this method has proven to be the most fruitful in the detection of exoplanets. It is based on observing the temporary dimming of the stellar light due to a planet passing in front of it with respect to our line of sight, such an event being called a transit. By measuring the change in brightness, the radius of the planet can be determined. The orbital period can be inferred from the periodic decrease in the stellar luminosity. Additionally, measuring the stellar spectrum in and out of transit gives insight into the atmosphere of the planet (e.g., Seidel et al. 2020). This method favours a specific geometric configuration, namely planets in edge-on orbits. The fact that multiple transits are required in order to confirm a detection makes this technique biased towards planets with shorter orbital periods (up to ~ 10 yr; e.g., Giles et al. 2018). Ground-based surveys such as SuperWASP (Smith and WASP Consortium 2014) and Kelt (Pepper et al. 2007), as well as space missions such as Kepler (Borucki 2016) and TESS (Ricker et al. 2015), among others, have contributed greatly to the discovery of many new worlds using this technique.

Radial velocity

This was the first successful and currently the second most fruitful method to detect exoplanets. It relies on the fact that in planetary systems, all the bodies orbit around the common centre of mass; the presence of a planet exerts a gravitational pull that causes the stellar spectrum to appear red-shifted (when moving away from the observer) or blue-shifted (when moving towards the observer). The radial velocity (RV) curve can be computed by measuring the Doppler shift in the spectral lines. The orbital period of the planet is directly measured from the periodic variations in the RV curve. The orbital period, eccentricity, and a lower limit on the mass of the planet $M_p \sin(i)$ can also be obtained with this method. RV favors the detection of massive planets, which have a greater gravitational influence on their host stars, as well as the detection of close-in planets that not only exert a larger gravitational tug but also have shorter periods, which allows for detections with short-term monitoring. Additionally, due to the distance projection, RV is more effective toward edge-on systems. One of the successful instruments that have detected planets with this technique is CARMENES (Quirrenbach et al. 2014).

Astrometry

This method consists of measuring the position of the star relative to the background sky. In the presence of a planet, the gravitational pull that it exerts on its host star will cause

the star to move on the sky over time periodically. The astrometry signal depends on the mass ratio between the planet and the star, therefore the mass of the planet can be obtained provided the mass of the star is known. Astrometry is more sensitive to planets orbiting nearby stars in wide orbits, as the center of mass displacement amplitude increases with the orbital period. For this reason, astrometry requires measurement stability and precision over a long time baseline, which represented a challenge for the available Earth-based instrumentation. However, with the launch of satellites like Gaia (Gaia Collaboration et al. 2016), this difficulty has been surmounted.

Microensing

Based on the larger scale idea of gravitational lensing, microlensing occurs when a foreground star acts as a lens for a star at a greater distance. If the foreground star hosts a planet, its gravitational field further distorts the light of the background star. This method allows to determine the mass and period of the planet. It is most sensitive to planets that orbit in moderate to large distances from their host star, complementing the parameter space that can be probed with other techniques. Due to its nature, microlensing events generally occur a single time, however, there have been promising recent developments to perform follow-up observations (e.g., Yang et al. 2022).

Direct imaging

All the techniques mentioned so far are *indirect*, since the presence of planets is inferred by the influence they exert on their host stars. The only *direct* way of detecting exoplanets is direct imaging, which, as its name suggests, consists of observing the exoplanet itself. This is done by using high-contrast imaging, which is the base technique used in this thesis and is detailed in the following section.

1.4 High-contrast imaging

High-contrast imaging helps to probe a different region of the parameter space, i.e. companions orbiting at wide separations in a variety of orbital configurations (including face-on orbits), as well as companions in very young systems (e.g., PDS 70 b; Keppler et al. 2018). Typically, high-contrast imaging observations are carried out in the infrared where the thermal emission from planetary companions is higher, while the stellar emission is lower than in the visual. In order to confirm a detection with direct imaging, it is necessary to carry out follow-up observations of the target and perform an astrometric analysis. From direct imaging we can obtain the semi-major axis of the companion and, by combining the brightness of the companion with its age and assuming a planet evolutionary model, we can estimate its mass. Furthermore, this technique allows to directly measure the spectrum of the companion, from which its effective temperature T_{eff} , radius, and other physical properties can be inferred (see Section 1.4.5). Since the determination of the mass with this method can

be highly uncertain, it is more common to classify companions according to their T_{eff} . Contrary to stars, brown dwarfs and planetary mass objects cool steadily with age, beginning their life as hot M-type objects, cooling to L-type (very red NIR colours and silicate clouds; Kirkpatrick 2005), then to T-type (blue NIR colours and strong methane absorption at 1.6 and 2.2 μm ; Kirkpatrick 2005), and eventually to the very cool Y-type (Cushing et al. 2011).

Attempting to directly image a planetary mass companion comes with some challenges, the main one being that the companions are several orders of magnitude (10^{-10} in the optical to 10^{-5} in the IR) fainter than their host stars. In order to make this possible, it is essential to successfully remove most of the light coming from the star. Another challenge is to be able to detect companions at very close separations from their stars (typically within a fraction of an arcsecond). These challenges impose limitations on the kind of planets that can currently be observed directly; namely, young, self-luminous planets orbiting nearby stars (~ 200 pc) at wide separations ($a \gtrsim 5$ au).

1.4.1 Coronagraphy and adaptive optics

There are a number of solutions to overcome the aforementioned challenges. On the instrumentation side, the use of a coronagraph attenuates the light from the star and allows the light from the companion to pass through. The use of this device has several advantages, such as preventing the central star from saturating the detector, allowing for longer exposures; diminishing the stellar photon noise; and allowing a better control of scattering and reflections in the optical system (Boffin et al. 2016). Modern coronagraphs are based on interference to reduce the light from the star and thus require a flat wavefront to work efficiently: the more distorted the wavefront, the more residual light from the star would get through.

A useful resource to increase the sensitivity at small projected separations and aid in flattening the wavefront is adaptive optics (AO). It works by correcting the stellar wavefront errors caused by turbulence in Earth's atmosphere and allows to obtain nearly diffraction-limited² images. These wavefront errors create speckles in the image plane that can mimic point sources, which affects the contrast. Moreover, these speckles vary as a function of the wind speed in timescales of the order of milliseconds, which imply a loss in resolution (Racine et al. 1999).

In order to overcome these wavefront aberrations and their consequences, AO systems are used along with high-contrast imaging instruments. The basic architecture of an AO system includes:

- A **wavefront sensor** (WFS), which measures the distortion at different locations of the wavefront and then sends the measurements to a computer that reads the distortion and reconstructs the wavefront.

²The diffraction limit describes the size of the smallest feature that the telescope can resolve. It is defined as λ_{obs}/D , where λ_{obs} is the wavelength at which the observations are carried out, and D is the diameter of the primary mirror of the telescope.

- The computer then sends commands to a **deformable mirror** (DM). The DM is composed by a series of actuators in the back that adjust the mirror accordingly to counteract the wavefront deformations and flatten it again (Milli et al. 2016).

The timescale over which the wavefront needs to be corrected is set by the coherence time (τ), which is a function of the wind speed. A typical value of τ is of the order of milliseconds. Therefore, the rate at which the DM has to update the actuators ($1/\tau$) would be several hundred times per second. τ is also proportional to the wavelength, which makes correcting in NIR easier than in the visible due to turbulence evolving faster at longer wavelengths (Roddier 1981).

1.4.2 Observing strategies

Angular differential imaging

From the different sources that can affect the contrast, the main contributor is generally the speckle noise, in particular the noise coming from the quasi-static speckles arising from imperfections in the telescope and optical system, mechanical movements, and temperature changes. The temporal evolution of these speckles ranges from the order of seconds to several minutes (e.g., Martinez et al. 2013), which means that within typical exposure times they will be fixed in the telescope pupil plane rather than in the sky frame. Therefore, by performing the observations in pupil-stabilised mode, the relative motion of an on-sky signal with respect to the telescope pupil can be used to distinguish between a fixed speckle and a rotating companion. This observing strategy is called Angular Differential Imaging (ADI; Marois et al. 2006). Afterwards, a reference PSF of the star built from a combination of selected images in the same observing sequence is subtracted from each individual frame to remove quasi-static PSF structure. Finally, the resulting images are de-rotated to align the field and collapsed into a single final frame. There are several algorithms that have been developed to further improve the efficiency of ADI by varying the process to construct the reference PSF, such as the Locally Optimised Combination of Images (LOCI; Lafrenière et al. 2007), and Principal Component Analysis (PCA) based algorithms (e.g. KLIP, Soummer et al. 2012; VIP, Gomez Gonzalez et al. 2017). In addition, there are other algorithms that use alternative methods to characterise a planetary signal, such as the ANgular DiffeRential Op-tiMal Exoplanet Detection Algorithm (ANDROMEDA; Cantalloube et al. 2015). It works by first selecting suitable pairs of frames to subtract from each other, carries out pairwise subtraction and, by median-combining the resulting images, generates the companion signal. Afterwards it uses a maximum likelihood estimation to distinguish between the speckles and an actual companion signal.

An important drawback of the ADI observing strategy is that flux loss can occur if some of the signal filtrates into the reference image, which can cause the companion to be self-subtracted in the process. For a given rotation angle, the displacement of a companion gets smaller at closer projected separations from the star, which is why high rotation angles are preferred in order to minimise self-subtraction. It is also important to note that extended sources, such as circumstellar disks, are more affected by self-subtraction, which can also

alter the observed disk morphology. Thus, this technique is preferred for point sources and low-inclined disks (Milli et al. 2012).

Reference star differential imaging

A solution to avoid self-subtraction and to improve sensitivity at small separations is to use Reference Star Differential Imaging (RDI; e.g., Lafrenière et al. 2009). This can be done either by using a similar, close star to the target and going back and forth during the observing sequence (this is known as “star hopping”, e.g., Wahhaj et al. 2021), or by building a PSF reference from a large library of stellar observations acquired as part of a survey (e.g., Xie et al. 2022).

Spectral and polarimetric differential imaging

Other observing strategies are Spectral Differential Imaging (SDI; Racine et al. 1999) and Polarimetric Differential Imaging (PDI; Kuhn et al. 2001). The former requires the target to have a peculiar spectral feature and relies on the fact that the speckle pattern, unlike the on-sky signal, scales with the wavelength. The latter makes use of the fact that scattered light (for example coming from dusty disks), unlike the stellar thermal emission, is polarised, which makes PDI efficient to observe circumstellar disks. In both cases, it is possible to model and subtract the stellar contribution while preserving the signal of interest. These techniques can also be used in combination with ADI.

1.4.3 SPHERE

The Spectro-Polarimetric High contrast imager for Exoplanet REsearch (SPHERE; Beuzit et al. 2019) is a second generation³ extreme AO instrument installed on the Very Large Telescope (VLT). It has three science instruments:

- The Infra-Red Differential Imaging camera and Spectrograph (**IRDIS**; Dohlen et al. 2008) produces imaging, spectroscopy, and polarimetry in two parallel channels, covering a wavelength range from 0.95 to 2.4 μm over a wide field of view (FoV; 11" \times 11" in imaging, 10" in spectroscopy) with a pixel scale of ~ 12.25 mas/pixel. The instrument is divided into four observing modes: classical imaging (CI) mode, dual-band imaging (DBI; Vigan et al. 2010), dual polarimetric mode (DPI; Langlois et al. 2010), and long-slit spectroscopy mode (LSS; Vigan et al. 2008). The main mode is DBI, which provides two neighbouring spectral channels. The main filter pair is *H23*, centred in the *H*-band (with $\lambda_c = 1.625 \mu\text{m}$; $\Delta\lambda = 0.291 \mu\text{m}$; where λ_c denotes the central wavelength and $\Delta\lambda$ denotes the full width at half maximum (FWHM) of the filter transmission curve) around the CH_4 absorption band, expected for planetary companions.

³First generation AO instruments such as the NAOS-CONICA (NaCo; Lenzen et al. 2003; Rousset et al. 2003), despite being successful in leading to major discoveries, such as the first direct planetary companion ever imaged (Chauvin et al. 2004), or the first spectrum of the spatially resolved exoplanet HR 8799 c (Janson et al. 2010), presented some limitations on performing high-contrast imaging.

- The Integral Field Spectrograph (**IFS**; Claudi et al. 2008) was designed to exploit both ADI and SDI on a four dimensional data-cube (x , y , wavelength λ , and time). It has a smaller FoV ($1.7'' \times 1.7''$), but can provide a higher contrast at closer separations. It has two possible configurations with $\lambda_{\min} = 0.95 \mu\text{m}$: YJ ($\lambda_{\max} \sim 1.35 \mu\text{m}$) and YH ($\lambda_{\max} \sim 1.65 \mu\text{m}$). IFS was designed to be used in combination with IRDIS; they have a similar spectral resolution (~ 30) but IFS provides 39 spectral channels.
- The Zurich IMaging POLarimeter (**ZIMPOL**; Schmid et al. 2018) is the visible focal plane instrument of SPHERE. It covers a wavelength range from 510 to 900 nm and provides observational modes for imaging, PDI, SDI, and ADI. ZIMPOL is mainly used to detect circumstellar disks.

Some of the most important milestones achieved with SPHERE, in particular through the SHINE (SpHere INfrared survey for Exoplanets) survey, are detailed in Desidera et al. (2021), Langlois et al. (2021), and Vigan et al. (2021).

1.4.4 Connection between planets and disks

As pointed out in the previous sections, the presence of a forming planet in a PPD leaves traces (substructure such as rings, gaps, or spirals) that can be further investigated, for example, via observations at different wavelengths, to probe different regions of the disk and determine whether its architecture can be caused by a planet within or outside the disk (e.g., Dong et al. 2015; Boccaletti et al. 2020). Another possibility is to measure the kinematic interactions between the planet and the gas of the disk by comparing observations of the gas at different velocity channels with models that include the presence of a planet (e.g., Norfolk et al. 2022) or, so far just in a couple of cases, by directly imaging a forming planet (e.g., Keppler et al. 2018).

In the case of debris disks, the fact that we observe them indicates that the process of planetesimal formation has been successful, as collisions between larger bodies (~ 1000 km) are needed to supply the disks with dust that can then be observed. Therefore, targeting these disks with high-contrast imaging can lead to the discovery of companions orbiting between the belts (e.g., Desgrange et al. 2022). The presence of companions orbiting within the belts can also be inferred by, for example, applying dynamical arguments to infer the masses of such planets along with the constraints imposed by stirring mechanisms (e.g., Pearce et al. 2022). Additionally, the existence of unseen planets in debris disks can be inferred from the presence of structure such as warps, clumps, spirals, or gaps, which can tell us about the interactions between such planets and the disk (e.g., Marino et al. 2018).

1.4.5 Exoplanet atmospheres

There are two methods to study the atmospheres of exoplanets and substellar objects: direct imaging and transit spectroscopy. While both techniques have been used in recent years with remarkable results to study the atmospheres of young giant planets (e.g., Macintosh et al. 2015; Bonnefoy et al. 2016; Chauvin et al. 2017a), as well as transiting super-Earths and

mini-Neptunes (e.g., Kreidberg et al. 2014; Zhang et al. 2022), the number of directly imaged exoplanets is quite small compared to the transiting ones, mainly due to the stringent requirements of direct observations. However, direct imaging has the potential to provide a more complete census of the atmospheres of planets, as it can probe deeper into the atmospheres enabling higher signal-to-noise (S/N) detection of interesting spectral features (Morley et al. 2015). High-contrast imaging spectra can provide constraints on the composition and temperature profile of the atmospheres. Moreover, bona fide detections of important molecules such as H₂O, CO, and CH₄ have recently been reported for directly imaged companions (e.g., Lavie et al. 2017; Lee and Gu 2015; Samland et al. 2017, respectively).

In order to better characterise the detected companions and explore their physical properties, observations are often compared with synthetic models. Two of the most commonly used are self-consistent models and atmospheric retrievals. In brief, the first one involves comparing the observed spectrum to an extensive grid of self-consistent model spectra of the planet, which are pre-computed assuming an elemental composition and equilibrium conditions. The second one makes use of a Bayesian framework (such as Markov-chain Monte Carlo, or nested sampling) to evaluate each model of the spectrum and infer posterior distributions on each free parameter. For further details on each of these approaches, see the review by Madhusudhan (2019).

1.5 Rationale and outline of the thesis

As previously discussed, the advent of new discoveries in the field of exoplanets has brought up several questions that remain unanswered. In particular, the formation and early evolution of planetary systems, as well as the complexity of the physical processes in circumstellar disks and planet atmospheres are not yet well understood. The current theoretical models can greatly benefit from observational constraints and vice versa.

With the aim of shedding some light on these open questions, this thesis explores different stages of the life of planetary systems using the high-contrast imaging technique: from the birthplace of planets and their interactions with their parent disk, through the study of the atmosphere of a planetary-mass object, to later-stage circumstellar disks whose architecture may display the imprints of planet formation.

1.5.1 Thesis outline

Chapter 2

shows the first scattered light observations of the protoplanetary disk WaOph 6 in the H -band. We present a comparison of the observed morphology of the disk with archival ALMA data. We test the planetary mass perturber hypothesis as the underlying cause for the spiral structure by performing hydrodynamical simulations and using radiative transfer. This chapter is based on the published work of Brown-Sevilla et al. (2021).

Chapter 3

presents a short study on the two companion candidates of the star AH Lep, which is a clear example of the process used to identify and characterise planetary companions. We perform an astrometric analysis to determine whether these candidates are bound to the system. Additionally, we show their SPHERE *YJ* spectra and draw some conclusions about their nature. This chapter is based on the research note Brown Sevilla et al. (2019).

Chapter 4

discusses the study of the atmosphere of the exoplanet 51 Eridani b. We use new SPHERE spectro-photometric observations along with the atmospheric retrieval code `petitRADTRANS` to estimate the parameters of the planet. Furthermore, we apply the retrieval approach to previously published data and compare the outcomes of retrievals to those of self-consistent models. This chapter is based on the work of Brown-Sevilla et al. [submitted](#).

Chapter 5

describes the first part of a larger study on debris disks observed with SPHERE. We focus on double belt debris disks, estimate the position of the belts and use this to calculate the masses of companions that could be orbiting within the belts. We compare our results with the detection limits from SPHERE. This chapter is based on ongoing work whose expansion will appear in a future publication (Brown-Sevilla et al. [in prep.](#)).

Chapter 6

presents and summarizes the final results of the thesis and the plans for future research.

Chapter 2

A multiwavelength analysis of the spiral arms in the protoplanetary disk around WaOph 6

The contents of this chapter are adapted from Brown-Sevilla et al. 2021, published in *Astronomy and Astrophysics (A&A)*, 654, 35, from which I am the first author from a team effort of 25 co-authors. I was under the supervision of Thomas Henning, Markus Feldt, and Wolfgang Brandner, and worked in close collaboration with David Melon-Fuksman, Marcelo Barraza-Alfaro and Hubert Klahr. The hydrodynamical and radiative transfer simulations for the polarimetric data of WaOph 6 were performed by David Melon-Fuksman and Marcelo Barraza-Alfaro. The data were provided by Christian Ginski and reduced using the tool from Rob van Holstein.

2.1 Motivation

As pointed out in Chapter 1, despite the great amount of discovered exoplanets little is known about their formation and early evolution processes. The study and characterisation of protoplanetary disks (PPDs), where planets are thought to be formed, provides insight into our understanding of these early stages of planet formation. Recent observations in both scattered light and millimetre continuum have shown the striking frequency with which these disks present structures, such as gaps, rings, or spirals (e.g., Avenhaus et al. 2018; Long et al. 2018; Andrews 2020; Cieza et al. 2020). In particular, the presence of spiral arms has frequently been linked with the presence of planets forming within the disk (e.g., Muto et al., 2012; Pohl et al., 2015; Dong et al., 2018b; Calcino et al., 2020; Ren et al., 2020). These planets perturb the disks via gravitational interactions, and these perturbations can cause the formation of spirals. From such planet-driven spirals, we can study the mass and location of the potential planets.

This Chapter presents NIR polarimetric observations of the protoplanetary disk around WaOph 6 obtained using the VLT/SPHERE instrument in the *H*-band. The disk has previously been imaged as part of large millimetre continuum surveys aiming to constrain and characterise the structure in PPDs. Its most characteristic feature is a set of symmetric spiral

arms. Multiwavelength observations of PPDs allow to better interpret their different components, as each wavelength traces different parts of the disks. For this work, the morphology of WaOph 6 in the NIR is compared to ALMA-DSHARP observations at a similar resolution. Additionally, one of the scenarios that can give rise to the spiral pattern observed in the disk is explored with the use of hydrodynamical simulations and radiative transfer.

Section 2.2 introduces WaOph 6 and previous studies on its disk. Section 2.3 describes the scattered light observations and data reduction procedure. The analysis of the disk structure is presented in Section 2.4. The modelling setup and the comparison between simulations and observations is described in Section 2.5. Section 2.6 presents a discussion of the results, and finally Section 2.7 summarizes the findings of this work.

2.2 WaOph 6

The target is a K6 star (Eisner et al. 2005), and member of the Ophiuchus moving group at a distance of $122.5^{+0.3}_{-0.2}$ pc (Gaia Collaboration et al. 2020) located near the L162 dark cloud. It was first identified as a suspected T Tauri star by Henize (1976), and then confirmed by Walter (1986). Here we constrain the stellar mass and age based on the updated photometry and Gaia parallax. We retrieved the full spectral energy distribution (SED) from Vizier¹ and employed a Phoenix model of the stellar photosphere (Hauschildt et al. 1999) with effective temperature $T_{\text{eff}} = 4200$ K (Eisner et al. 2005), surface gravity $\log(g)=-4.0$, and an optical extinction $A_V = 2.8 \pm 0.3$ mag calculated from the V, R, and I photometric fluxes. We integrated the stellar model scaled to the average V magnitude and Gaia distance of 122.5 pc obtaining a stellar luminosity of $L_* = 1.91^{+0.70}_{-0.51} L_{\odot}$. Then, we placed the source on the HR diagram and constrain a stellar mass $M_* = 0.7 \pm 0.1 M_{\odot}$ and an age $t = 0.6 \pm 0.3$ Myr through different sets of PMS tracks (Parsec, MIST, Baraffe; Bressan et al. 2012; Choi et al. 2016; Baraffe et al. 2015) with error bars propagated from L_* and T_{eff} (± 100 K).

The disk around WaOph 6 has been a common target for millimetre continuum surveys looking to constrain and characterise the structure in protoplanetary disks (e.g., Andrews and Williams 2007; Andrews et al. 2009; Ricci et al. 2010; Andrews et al. 2018). Submillimetre Array (SMA) observations were used along with a parametric model to constrain density structure parameters (Andrews et al. 2009). The disk model that best fitted the thermal continuum data and spectral energy distribution (SED) was that of a flat cold disk with a total disk mass (gas + dust-to-gas ratio of 1:100) of $0.077 M_{\odot}$. With observations from the Australia Telescope Compact Array (ATCA), Ricci et al. (2010) analysed and modelled the SED of WaOph 6, adopting a distance of ~ 130 pc and an outer radius (R_{out}) interval of 175 – 375 au, and they find dust mass estimates (M_{dust}) between $8 \times 10^{-5} M_{\odot}$ and $9.8 \times 10^{-5} M_{\odot}$, depending on the assumed dust size distribution power-law index ($q = 2.5$ or $q = 3$). More recently, WaOph 6 was observed by ALMA within the DSHARP program (Disk Substructures at High Angular Resolution Project, Andrews et al. 2018). These millimetre continuum observations showed that the disk has a set of symmetric spiral arms that extend to ~ 70 au, a gap at 79 au and a bright ring at 88 au (Huang et al. 2018b). The disk has an

¹<http://vizier.unistra.fr/vizier/sed/>

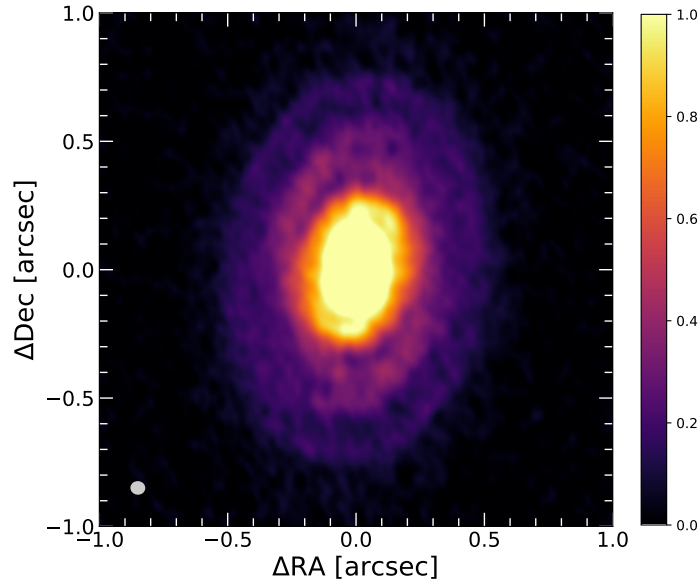


Figure 2.1: ALMA 1.25 mm continuum image of WaOph 6 from the ALMA-DSHARP survey (Huang et al. 2018b). The beam size is shown in the lower left corner.

inclination (i) of 47.3° and a position angle (PA) of 174.2° obtained from ellipse fitting on the dust continuum emission (see Huang et al. 2018a, for more details), and gas observations have shown that it suffers from mild molecular cloud contamination (Reboussin et al. 2015). We summarize the stellar and disk physical parameters in Table 2.1, where we include the different values for the disk mass found in the literature, as well as our own M_{dust} estimate obtained following the procedure described in Appendix A.1.

Up to now, only seven disks have been known to have spiral arms in millimetre continuum wavelengths: WaOph 6, Elias 27, IM Lup, HT Lup A, AS 205 N, MWC 758, and HD100453 (Huang et al. 2018b; Kurtovic et al. 2018; Dong et al. 2018b; Rosotti et al. 2020), and only the first three are single systems. Out of these three, only IM Lup has published polarized scattered light observations (Avenhaus et al. 2018), however, with no spiral arms visible at these wavelengths.

2.3 Observations and data reduction

2.3.1 IRDIS polarimetric observations and data reduction

WaOph 6 was observed with the VLT/SPHERE high-contrast instrument (Beuzit et al. 2019) within the DISK/SHINE (SpHERE INfrared survey for Exoplanets, Chauvin et al. 2017b) Guaranteed Time Observations (GTO) program on the night of June 21, 2018 (see Table 2.2). The observations were carried out with the IRDIS Dual-beam Polarimetric Imaging (DPI) mode (Langlois et al. 2014; de Boer et al. 2020; van Holstein et al. 2020) in H -band ($\lambda_c=1.625 \mu\text{m}$; $\Delta\lambda=0.291 \mu\text{m}$; where λ_c denotes the central wavelength and $\Delta\lambda$ denotes the full width at half maximum (FWHM) of the filter transmission curve; pixel scale 12.25 mas/px , Maire et al. 2016) in field stabilized mode using an apodized Lyot coronagraph, having a focal plane mask of 93 mas radius (Carbillet et al. 2011). A total of four polarimetric cycles were

Table 2.1: Stellar and disk parameters of WaOph 6 from the most recent literature.

Stellar parameters	Value	Ref.
Spectral type	K6	a
Age	0.7 Myr	a
Distance d	122.5 ± 5 pc	b
Mass	$0.9 M_{\odot}$	a
Radius	$2.8 R_{\odot}$	a
Temperature	4205 K	a
Visual magnitude (V band)	13.3 ± 0.01 mag	c
Disk properties		
Inclination i	47.3°	d
Position angle (PA)	174.2°	d
Gas mass ¹	$7.7 \times 10^{-2} M_{\odot}$	e
Dust mass ²	$8 \times 10^{-5} M_{\odot}$	a
Dust mass	$1.4 \times 10^{-4} M_{\odot}$	f

¹ Assuming a gas-to-dust ratio of 100:1 and based on SMA SED modelling.

² Obtained with a power-law index for the grain size distribution $q = 2.5$.

Notes. a) Ricci et al. (2010), b) Gaia Collaboration et al. (2020), c) Zacharias et al. (2012), d) Huang et al. (2018a), e) Andrews et al. (2009), f) This work

Table 2.2: Log of observations.

Date	21-06-2018
Filter	H -band ($1.625 \mu\text{m}$)
UT start/end	01:58:36/02:24:30
Exposure time	96 s
Airmass	~ 1.0
Seeing	$\sim 0.5''$
Coherence time (τ_0)	~ 4 ms
Wind speed	~ 3.8 m/s
Total exposure time	~ 1500 s

recorded, with 96 s of integration time per exposure, resulting in a total integration time of about 25 minutes. Each polarimetric cycle consisted of adjusting the half-wave plate (HWP) at four different switch angles: 0° , 45° , 22.5° , and 67.5° . At each HWP position the two orthogonal linear polarization states are measured simultaneously, resulting in eight images per cycle, corresponding to the Stokes components: $(I \pm Q)/2$, $(I \mp Q)/2$, $(I \pm U)/2$, and $(I \mp U)/2$. To obtain the Stokes components Q^+ , Q^- , U^+ and U^- , one orthogonal state is subtracted from the other at each of the HWP angles. Besides the science data, star center frames at the beginning and end of the sequence, as well as flux calibration frames were obtained. For the star center frames, the deformable mirror (DM) waffle mode was used (see Langlois et al. 2013, for more details on this mode). Two flux calibration frames (images of the target star without the coronagraph) were obtained with an exposure time of 2 s and a neutral density (ND1) filter to prevent saturation. We measure a point spread function (PSF) FWHM of ~ 51 mas by fitting a Gaussian function to the flux frames. The weather conditions were stable during the observations with a seeing of $\sim 0.5''$, a coherence time (τ_0) of ~ 4 ms, and wind speed of ~ 3.8 m/s. The Strehl ratio was about 0.7, however, the low scattered light intensity resulted in a rather low signal-to-noise ratio (S/N).

For the data reduction, we used the IRDAP pipeline² version 1.3.2. (van Holstein et al. 2020). First, the pipeline preprocesses the data by performing the usual sky background subtraction, flat fielding, bad-pixel identification and interpolation, and star centering corrections. Subsequently, polarimetric differential imaging (PDI) is performed by applying the double-sum and double-difference method described in de Boer et al. (2020) to obtain a set of Stokes Q and U frames. Finally, the data are corrected for instrumental polarization and crosstalk effects by applying a detailed Mueller matrix model of the instrument (see van Holstein et al. 2020, for more details on the data reduction procedure), yielding the final Q and U images. The final PDI images are corrected for true north following the procedure established by Maire et al. (2016). IRDAP then obtains the linearly polarized intensity (PI) image using the final Q and U images, from

$$PI = \sqrt{Q^2 + U^2}. \quad (2.1)$$

Next, the pipeline computes the azimuthal Stokes parameters following (de Boer et al. 2020):

$$\begin{aligned} Q_\phi &= -Q \cos(2\phi) - U \sin(2\phi), \\ U_\phi &= +Q \sin(2\phi) - U \cos(2\phi), \end{aligned} \quad (2.2)$$

where ϕ is the position angle (PA) measured east of north with respect to the position of the star. In the definition above, a positive signal in the Q_ϕ image corresponds to a signal that is linearly polarized in the azimuthal direction, while a negative signal denotes radially polarized light in Q_ϕ . U_ϕ contains any signal polarized at $\pm 45^\circ$ with respect to the radial direction. This means that for disks with low inclinations (i.e., $i < 45^\circ$), almost all of the scattered light is expected to be included as a positive signal in Q_ϕ , while the U_ϕ image can be considered as an upper limit of the noise level. In the case of WaOph 6, we expect

²<https://irdap.readthedocs.io><https://irdap.readthedocs.io>

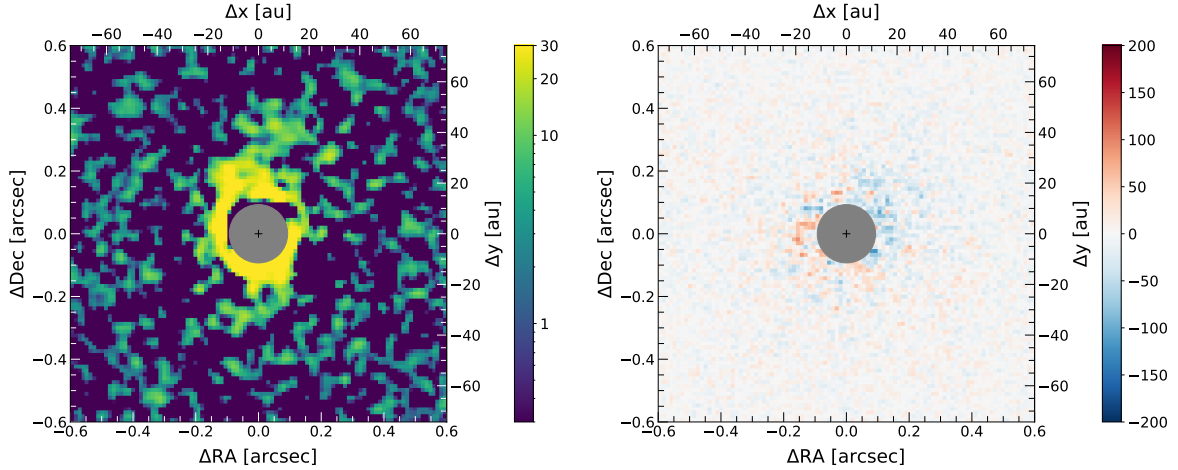


Figure 2.2: *Left:* Close up of the final Q_ϕ SPHERE/IRDIS-DPI image after removing low frequency structures (see text for details) and applying a Gaussian kernel of size $0.1 \times \text{FWHM}$ to smooth the images and enhance the spiral features. *Right:* Close up of the final U_ϕ image showing the positive and negative signal. The 93 mas coronagraph is indicated by the gray circle, and the cross indicates the position of the star. The flux is normalized to the maximum value in the Q_ϕ image.

some physical signal in the U_ϕ image due to the inclination of the disk (see Table 2.1). The resulting Q_ϕ and U_ϕ images are shown in Appendix A.2.

2.4 Disk analysis

2.4.1 The disk in polarized scattered light

In Fig. 2.2 we show the final, processed Q_ϕ and U_ϕ images. Due to the low S/N, we sharpened the images by subtracting a version of them which was convolved by a Gaussian kernel with the size of 10 pixels, which removes low frequency structures, and then we convolved them with a Gaussian kernel of size $0.1 \times \text{FWHM}$ to smooth the images in order to enhance the spiral features. We observe the launch of the spiral arms up to $\sim 0.3''$ (40 au), as seen in the Q_ϕ image (Fig. 2.2, left). As mentioned in Section 2.3, the U_ϕ image (Fig. 2.2, right) in this case contains almost no signal and can be used as an upper limit of the noise level. For a better visualization of the spiral features, we plotted the azimuthal profile by first de-projecting the filtered Q_ϕ image, and taking the average flux within the ring between ~ 27 and 36 au in azimuthal bins of 15° . The distance range is chosen due to the presence of the coronagraph at lower radii, and the S/N decrease at higher radii. In Fig. 2.3, we show the smoothed azimuthal profile. The spiral arms are seen as the two peaks between $20^\circ - 100^\circ$ and $200^\circ - 310^\circ$. To estimate the spiral arm intensity contrast between the spiral and inter-spiral regions, we measured the peak intensities of the spiral arms in radial bins spaced by 2 au. We estimated the inter-spiral region intensity by taking the minimum value in each bin. The contrast is then the ratio between the peak intensities and the inter-spiral intensities. On average, we find the spiral arm contrast to be 1.5.

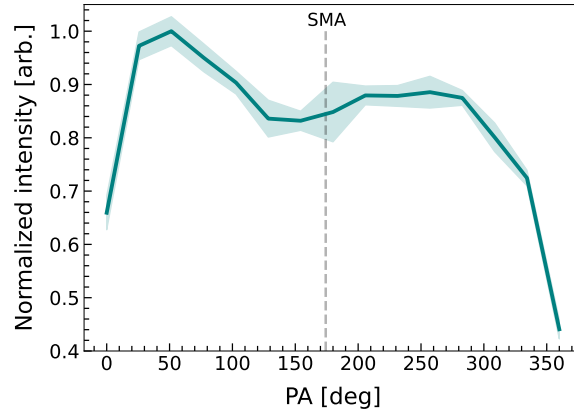


Figure 2.3: Azimuthal profile of the deprojected Q_ϕ image, radially averaged over a ring of 0.22-0.29" ($\sim 27 - 36$ au). The two peaks at around 50° and 210° correspond to the launch locations of the two spiral arms. The uncertainty is taken to be 2σ . The dashed line indicates the location of the disk's semi-major-axis.

2.4.2 Companion candidate analysis

We detect a companion candidate (CC) in our data as shown in the total intensity image in the top panel of Fig. 2.4, where the CC is more visible than in the polarized light frames. The CC is located at a projected distance of ~ 400 au ($\sim 3''$) and has a brightness contrast of 10^{-3} with respect to WaOph 6. We used archival HST data (from 1999-01-23) as an additional epoch to perform an astrometric analysis in order to verify if the CC is bound to the system. The resulting astrometry plot is shown in the bottom panel of Fig. 2.4, where the black curve traces the path a stationary background object would have followed relative to WaOph 6 between the two epochs, and the markers show the position of the CC at both the HST and the SPHERE epochs. Since the CC is located near the final position a background object would be located at, we conclude that the object is not bound to the system, and therefore could not be considered as an external perturber causing the spirals. We note that the CC is not reported in the Gaia EDR3, despite of its presence in the two data sets described above.

2.4.3 Comparison to millimetre observations

WaOph 6 was observed within ALMA/DSHARP (Andrews et al. 2018) in Band 6, at a frequency of 239 GHz (1.3 mm). Observations at these wavelengths sample the millimetre-sized dust grains that are typically located in the disk midplane (see e.g., Villenave et al. 2020). On the other hand, our SPHERE observations trace the light scattered from submicron sized dust grains located at the disk surface which are typically well-coupled to the gas. In this section we do a first comparison of the two data sets.

Radial profiles

In Fig. 2.5 we plot the radial intensity profiles of the SPHERE/IRDIS-DPI H-band image (teal curve), and the ALMA image in Fig. 2.1 (crimson curve). The curves have been normalized to the maximum intensity value on each image for visualization purposes. In order

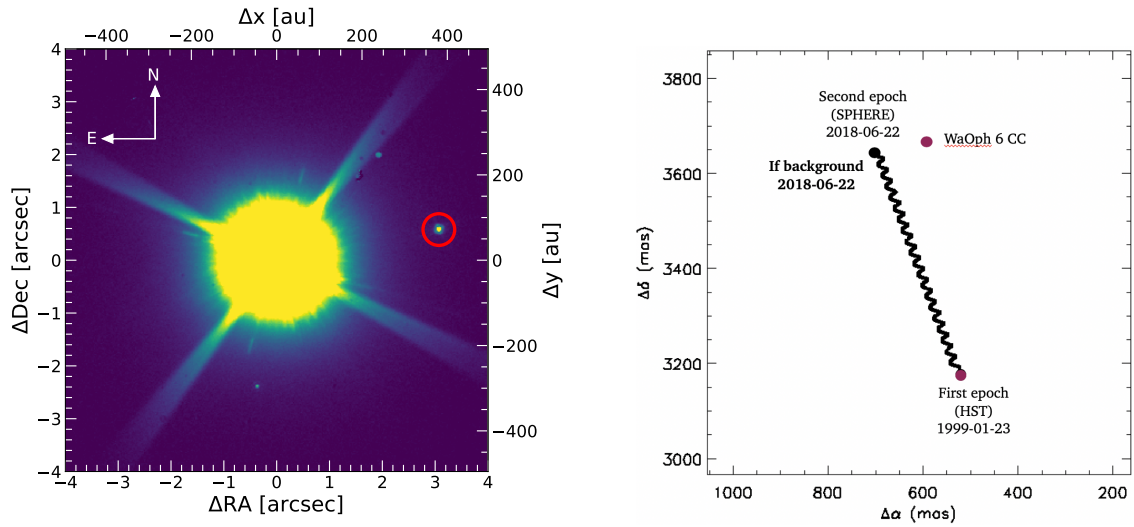


Figure 2.4: *Top:* Total intensity SPHERE/IRDIS-DPI image of WaOph 6. Encircled in red is the CC. *Bottom:* Astrometry plot of the CC of WaOph 6. The markers show the position of the CC, at the initial HST epoch, and further in time at the SPHERE epoch. The black curve traces the path a stationary background object would have followed relative to WaOph 6 between the two epochs.

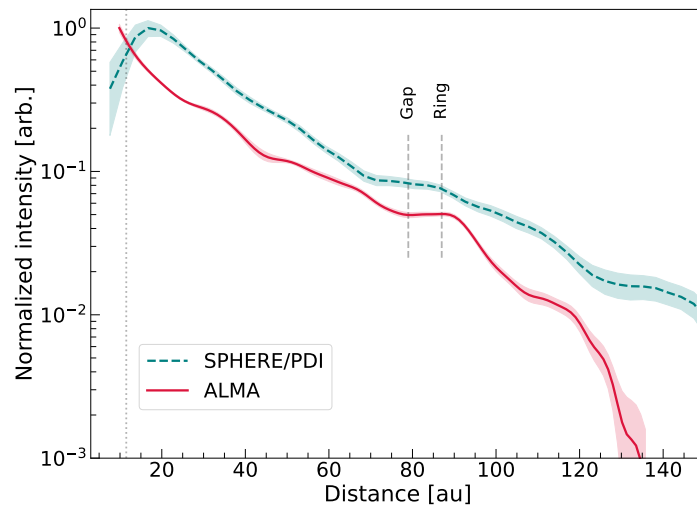


Figure 2.5: Radial intensity profiles of both the SPHERE and ALMA images of WaOph 6. Plotted on a logarithmic scale and normalized to the maximum intensity of each image. The SPHERE profile is taken from the reduced Q_ϕ image with an applied Gaussian kernel of size $0.1 \times \text{FWHM}$ to smooth the curve, and it is shown up to 3σ of the intensity. The dotted line indicates the coronagraph coverage.

Table 2.3: Spiral pitch angles for the protoplanetary disk around WaOph 6.

Source	Spiral arm	Log. μ [°]	Arch. μ [°]
SPHERE	N	$19.79^{+0.12}_{-0.11}$	19.54
	S	$14.04^{+0.07}_{-0.06}$	16.05
ALMA	N1	$13.49^{+0.30}_{-0.19}$	18.97
	S1	$18.26^{+0.04}_{-0.07}$	15.98
	N2	$10.75^{+0.23}_{-0.15}$	17.86
	S2	$9.09^{+0.21}_{-0.10}$	15.26

Note: For the SPHERE data, N corresponds to the northern spiral and S to the southern spiral. In the case of the ALMA data, N1 corresponds to the northern inner spiral, S1 to the southern inner spiral, N2 to the northern outer spiral and S2 to the southern outer spiral. For the Archimedean fit, the pitch angles are estimated at 35 au.

to obtain a smooth profile, we apply a Gaussian kernel of size $0.1 \times \text{FWHM}$ to the reduced Q_ϕ image in Appendix A.2. We obtained the profiles by taking the azimuthal average of the image intensity in rings of radius 3 au. For this we considered the latest literature values for i and PA (listed on Table 2.1), and we use the `aperture_photometry()` function from the `photutils` python package, which allows to perform aperture photometry within elliptical annuli. This permits to get the radial profile without first deprojecting the image.

As expected from the fact that the two images trace different dust sizes, the profiles do not perfectly overlap. A closer look between 70 au and 90 au shows that the substructures created by the gap and the ring described in Section 2.2, are present in both profiles, with a slight shift. The initial drop in the intensity of the SPHERE/IRDIS-DPI profile is due to the use of a coronagraph in these observations. The cut in the ALMA data profile can be attributed to the emission from the large grains being limited to the central ~ 130 au of the disk.

Spiral arms

Next, we performed a spiral search on each data set to compare the location of the spiral arms at both wavelengths. In the case of the SPHERE data, the spiral features are better seen when the image is plotted in polar coordinates, where spiral arms appear as inclined lines. To obtain the polar plot we first deprojected the image and then converted to polar coordinates. We then used the python function `peak_local_max` from the `skimage` package to search for the peak emission points around the location of the spiral arms. To trace the spirals in the ALMA data we used two different images generated using the `tclean` task in CASA 5.4.1 (McMullin et al. 2007). We used `uv-taper = ['0.010arcsec', '0.010arcsec', '10deg']`, and two different robust values (-1.0 and 1.0) to generate an image with higher resolution in the central and in the outer regions, respectively. Then, we searched for peak emission points along the radial direction and took the 3σ emission ones as the spiral arms. We repeated this process in both of the images described above. The resulting spirals are shown

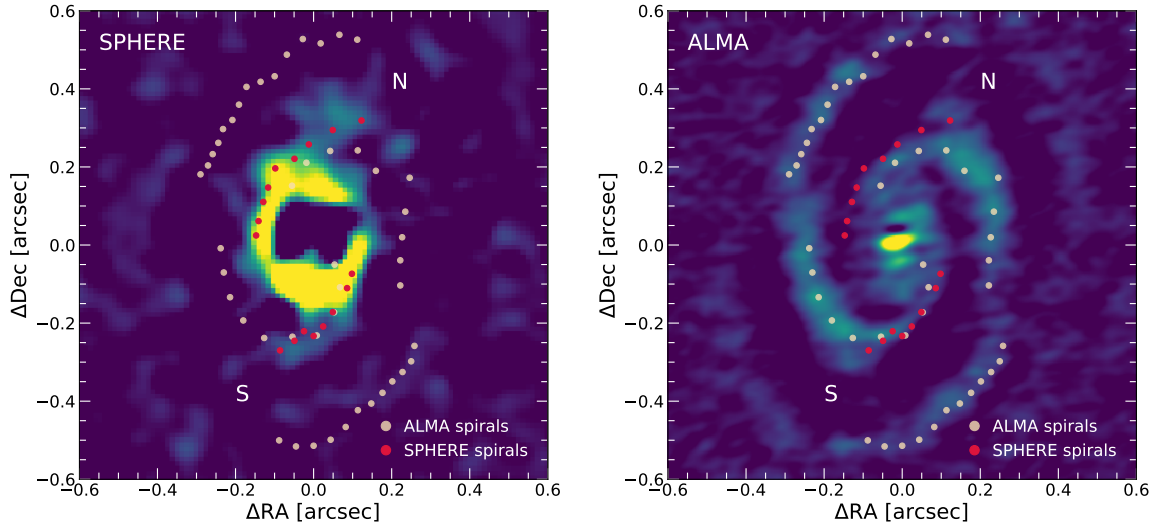


Figure 2.6: *Left:* SPHERE Q_ϕ image as described in Fig. 2.2 but with a Gaussian kernel of size $0.2 \times \text{FWHM}$ with the spiral arms retrieved from both the ALMA and this image overplotted. *Right:* ALMA continuum image generated as described in the Appendix A.3, with the overplotted spiral arms retrieved from both the SPHERE Q_ϕ and this image. The “N” and “S” indicate the northern and southern spirals, respectively.

in Fig. 2.6, where we overplot the retrieved spiral arms on both the SPHERE (left) and the ALMA image (right). To obtain the SPHERE image we followed the same procedure described in Section 2.4.1 with a Gaussian kernel of size $0.2 \times \text{FWHM}$. We did this to match the scaling of the ALMA image for better comparison purposes. To generate the ALMA image, we used the `frank` (Jennings et al. 2020) tool to remove the azimuthally component of the emission of the disk and leave only the non-axisymmetric features, as described in the Appendix A.3. We note that the spiral pattern is much more prominent in the mm continuum than in scattered light. Besides the low S/N of the SPHERE data and the fact that the disk has been reported to be cold, this could also be explained by the anisotropic scattering properties of the dust of different sizes. For a disk that is not edge-on, the larger the particles on the surface layer compared to the wavelength, the more they will scatter light into the disk in forward scattering. Therefore, the amount of light scattered in the line of sight direction would be smaller and would not be detected in scattered light images (e.g., Mulders et al. 2013). Additionally, we notice that there appears to be a break in the spiral arms on the ALMA image at $\sim 0.16''$ (~ 20 au), which cannot be observed in our SPHERE data. In the following we treat this break as a separate set of spirals.

In order to characterise the spirals we considered two models. A logarithmic spiral given by:

$$r = r_0 \cdot \exp(b\theta), \quad (2.3)$$

and an Archimedean spiral, defined as:

$$r = r_0 + b\theta, \quad (2.4)$$

where θ is the polar angle, r_0 is the radius for which $\theta=0$, and b relates to the pitch angle (μ)

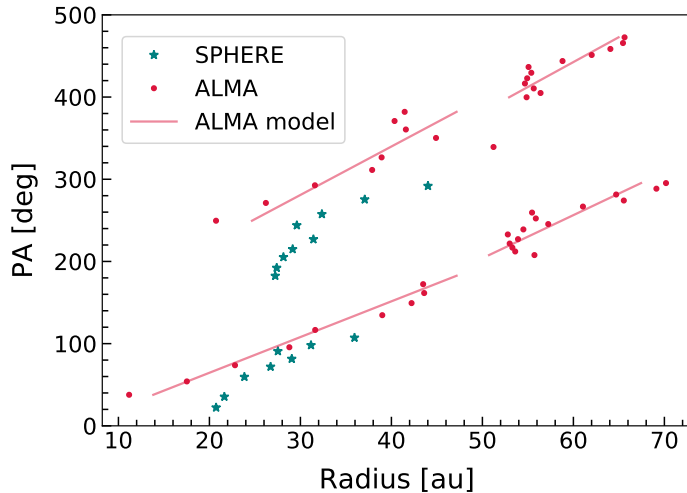


Figure 2.7: Polar plot showing the spiral arms of both the SPHERE (stars) and ALMA (dots) images of WaOph 6. The lines show the Archimedean best fit model for the spirals.

of the spiral. The pitch angle is defined as the angle between the tangents to a spiral arm and a circle drawn from the center of the disk, it describes how tightly the spiral arms are wound. In the logarithmic case, the pitch angle is constant along all radii and it is given by $\mu = \arctan(1/b)$, while for the Archimedean spiral, the pitch angle depends on the radius as $\mu = b/r$. To test the symmetry of the spiral arms, the parameters r_0 and b were fitted separately, while we assumed i and PA to be fixed and equal to the literature values shown in Table 2.1. Therefore, we had four and eight free parameters for the SPHERE and ALMA data, respectively. To fit the data, we used the MCMC code based on emcee (Foreman-Mackey et al. 2013) and described in Kurtovic et al. (2018). A flat prior probability is used for the free parameters. For each fit, we used 250 walkers with two consecutive burning stages of 1000 and 500 steps, and then 1500 steps to sample the parameter space.

The resulting pitch angles for each fit are given in Table 2.3, where for the SPHERE data, N corresponds to the northern spiral and S to the southern spiral; and in the case of the ALMA data, N1 corresponds to the northern inner spiral, S1 to the southern inner spiral, N2 to the northern outer spiral and S2 to the southern outer spiral. For the Archimedean fit, the pitch angles are estimated at 35 au. We find that there are some significant differences between the values of the inner and outer ALMA spirals for the logarithmic model, which leads us to conclude that the two sets might not be part of the same spiral arm. There seems to be additional structure in the region of the discontinuity, however, follow-up deeper observations would be needed to draw any conclusions of the origin of this break. Furthermore, we note that the values of the pitch angle for the corresponding spirals differ from one data set to the other, and that in the case of the Archimedean model, the scattered light pitch angles are slightly higher than those from submillimetre. This can be expected, since we are tracing different regions of the disk (the flared surface vs. the midplane). Moreover, we find that the pitch angles from the Archimedean model decrease with the distance from the star, in agreement with the results of Huang et al. (2018b).

Figure 2.7 shows the spirals retrieved from both data sets in a polar map, along with the best-fit Archimedean model for each arm. We find a discontinuity in the spiral arms for the ALMA data at ~ 50 au. This peculiarity has already been reported by Huang et al. (2018b), who also noted that this discontinuity appears to coincide with a region where there is additional bright emission between the main spiral arms, and comment that it could be explained by either the presence of a ring crossing this region, or “spurs” emerging from the main spirals.

2.4.4 Origin of the spirals

Large perturbations in the disk launch sound waves that result in a spiral shape due to the differential rotation of the disk. Theoretical models have shown that such large perturbations can be driven by the presence of an embedded planetary mass perturber (e.g., Boccaletti et al. 2013), GI (e.g., Goldreich and Tremaine 1979; Tomida et al. 2017), or a combination of both (e.g., Pohl et al. 2015).

Two-arm spirals in disks can be driven by a massive, giant planetary companion ($\gtrsim 5 M_{\text{Jup}}$), that would typically be located at the tip of the primary arm. This scenario suggests, however, that these planets are fainter than predicted by “hot-start” evolutionary models (Dong et al. 2018a), since the number of detections is low.

On the other hand, as pointed out in Section 1.1.1 one criteria to test the GI hypothesis is to use the Toomre parameter Q , which results to be a function of the radius. The Toomre stability criteria states that a disk will be gravitationally stable if $Q \geq 1$ and unstable if $Q < 1$.

In the case of WaOph 6, we estimated the Toomre parameter Q using equation (1.2) and assuming $\Sigma \propto 1/\sqrt{r}$, where r is the distance from the star, throughout the disk (see Appendix A.4 for the detailed calculation) in order to see whether the disk would be stable under these conditions. We obtained that Q varies from 2.2 – 33.2 from the outer part of the disk inward. This indicates that the disk is fairly stable according to the Toomre stability criterion, implying that a large perturbation driving the spiral arms should have come from a source other than GI. Nonetheless, we are aware that this is not an absolute proof of GI not taking place in the disk at some earlier evolutionary state. This analysis only shows that a disk with a surface density $\propto 1/\sqrt{r}$ around a $0.98 M_{\odot}$ star appears to be stable within our assumptions of the disk mass and the gas surface density, which should be taken with caution due to the considerable uncertainties in their calculation. In this context, we decide to test the planetary perturber hypothesis by performing hydrodynamical simulations and radiative transfer to compare with our observations.

2.5 Modelling

In order to test the hypothesis of a forming planet causing the spiral features, we performed 3D gas-only and 2D gas+dust hydrodynamical simulations in which a massive planet at a separations ≥ 90 au generates large-scale spiral arms interior to its orbit. To compare

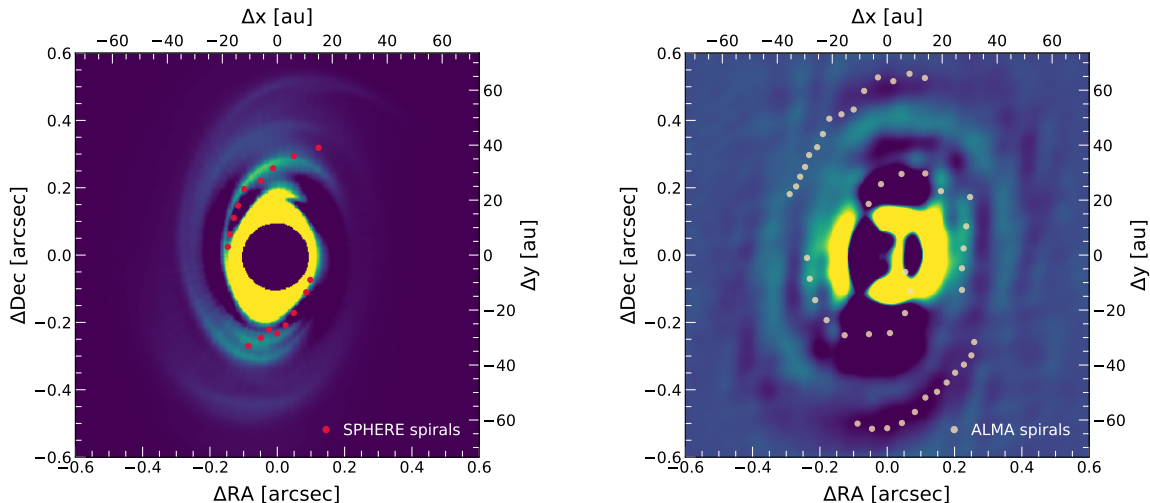


Figure 2.8: Radiative transfer images showing the spirals formed by a $10 M_{\text{Jup}}$ planet at 140 au. *Left:* Synthetic polarized scattered light Q_ϕ image with an analogous Gaussian kernel to the one applied to Fig. 2.6, left. The dark central area shows the coronagraph coverage. *Right:* Synthetic mm continuum image after subtracting the azimuthal average flux on the image plane to enhance the spirals, analogous to the procedure applied to Fig. 2.6, right. The red and white dots denote the location of the observed spirals for each image, respectively.

the results to our observations, we fed the resulting density distributions into a radiative transfer code to generate synthetic images.

2.5.1 Hydrodynamical models

To model the dust on the surface sampled by scattered light, we ran 3D simulations of the gas dynamics using the hydrodynamical code PLUTO (Mignone et al. 2007). The gas distribution was initially set following a vertically isothermal configuration at hydrostatic equilibrium (see, e.g., Fromang et al. 2011). The disk temperature depends on the cylindrical radius R from the center of the domain as $T \propto R^{-1/2}$, whereas the gas pressure scale height is computed as $H = c_s / \Omega_K$, where $c_s \propto T^{1/2}$ is the local sound speed and $\Omega_K \propto R^{-3/2}$ is the Keplerian angular velocity. With the chosen parameters, the disk aspect ratio depends on R as $H/R \propto R^{1/4}$, with $H/R = 0.1$ at $R = 50$ au. The gas volumetric density decreases with R as $\rho \propto R^{-7/4}$, in such a way that the surface density varies as $\Sigma \approx \sqrt{2\pi} H \rho \propto R^{-1/2}$. A locally isothermal equation of state is applied such that the initial temperature distribution is maintained through time.

The hydrodynamical equations were solved in spherical coordinates in a reference frame centered at the star-planet center of mass corotating with the system. The computational domain, given by the region $(r, \theta, \phi) \in [8, 210] \text{ au} \times [\pi/2 - 0.3, \pi/2 + 0.3] \times [0, 2\pi]$, is discretized using a grid of resolution $N_r \times N_\theta \times N_\phi = 256 \times 64 \times 512$ logarithmically spaced in the r -direction and uniformly spaced in the remaining ones. All computed fields are fixed to their initial values at the radial boundaries except for the density and the radial velocity, which are reflected and extrapolated in the ghost zones, respectively. On the vertical boundaries, reflective conditions are applied. The gravitational potential is computed as the

sum of the potentials of the star and the planet. To avoid divergences, the later is modified in the vicinity of the planet location following the prescription by Klahr and Kley (2006), employing a smoothing length equal to half the planet’s Hill radius. For stability purposes, the planet mass is smoothly increased from 0 to its final value in a total time of 100 yr. We also included viscosity with constant $\alpha = 10^{-3}$. The resulting dust mass distribution was computed assuming a perfect coupling between the dust particles and the gas flow, with a uniform dust-to-gas mass ratio of 10^{-2} .

To model the dust evolution in the midplane sampled mainly by the millimetre observations, we ran two-dimensional hydrodynamical simulations using the multi-fluid version of the code FARGO3D³ (Benítez-Llambay and Masset 2016; Benítez-Llambay et al. 2019). It solves the Navier-Stokes equations of the gas and multiple dust species, each one modelled as a pressureless fluid that represents a specific grain size. We traced eight different dust species in our simulations. The initial gas temperature, gas surface density structure, equation of state and gas viscosity prescription of the 2D model are equivalent to our 3D simulations model, described above. The initial dust surface density in our simulation has the same structure as the gas surface density, while set by an initial dust-to-gas mass ratio of 10^{-2} everywhere in the disk. We traced the dynamical evolution of eight dust fluids, that are logarithmically spaced in size, and followed a dust size distribution $n(s) \propto s^{-2.5}$ with minimum and maximum dust sizes of $10 \mu\text{m}$ and $100 \mu\text{m}$. We set the dust intrinsic density to 2.0 g cm^{-3} . The dynamics of the dust fluids is dictated by its local Stokes number (dimensionless stopping time), defined as $\text{St} = \pi a_i \rho_{\text{int}} / 2 \Sigma_{\text{g}}$, where a_i is the grain size of the size-bin, ρ_{int} the intrinsic grain density and Σ_{g} the gas surface density. Dust diffusion was included in the simulation following the same prescriptions implemented in Weber et al. (2019), which are based on the results of Youdin and Lithwick (2007). Dust feedback onto the gas, dust growth, and dust fragmentation were not included in our simulations. The two-dimensional grid is linear in azimuth and logarithmic in radius, using 512 cells in ϕ covering 2π , and 256 cells in r covering from $\sim 8.4 \text{ au}$ to $\sim 420 \text{ au}$. A planet was slowly introduced over $8 \times 10^4 \text{ yr}$ fixed at the given radius, driving spiral density waves in the disk. The planet’s potential was smoothed by a length factor of 60% the disk scale height. For a more detailed description of the FARGO3D multi-fluid simulations see also Weber et al. (2019). Our test runs show that only dust fairly well coupled to the gas follows the spiral density waves (as shown by e.g., Veronesi et al. 2019; Sturm et al. 2020), with Stokes numbers below $\sim 10^{-2}$. Dust particles with larger Stokes number decouple from the gas and form axisymmetric rings. Fixing the disk gas surface density given the mass constraint from the observations, and the dust intrinsic density to a standard value, limiting the maximum dust size to $100 \mu\text{m}$ in our models is required to maintain the Stokes number of the dust observed at millimetre wavelengths below $\sim 10^{-2}$, therefore, the simulated dust particles trace the spiral arm structure. A summary of the parameters used in our simulations can be found in Table 2.4.

³<http://fargo.in2p3.fr><http://fargo.in2p3.fr>

Table 2.4: Summary of simulations parameters.

Parameter	2D gas+dust	3D gas
Aspect Ratio at 100 au	0.12	0.12
Flaring Index	0.25	0.25
Surface Density Slope	0.5	0.5
Alpha Viscosity	10^{-3}	10^{-3}
Stellar Mass	$0.98 M_{\odot}$	$0.98 M_{\odot}$
Planet-to-Star Mass Ratio	10^{-2}	10^{-2}
Planet Orbital Radius	140 au	140 au
# of Cells in r	256	256
# of Cells in ϕ	512	512
# of Cells in θ	-	64
Grid Inner Radius	8.4 au	8 au
Grid Outer Radius	420 au	210 au
Total Evolution Time	4×10^5 yr	4×10^5 yr
Dust-to-Gas Mass Ratio	10^{-2}	-
Maximum Dust Size	100 μm	-
Minimum Dust Size	10 μm	-
Dust Size Slope	2.5	-
Dust Intrinsic Density	2.0 g cm^{-3}	-

We sample the parameter space of a planet with masses between $2 - 15 M_{\text{Jup}}$ and separations between $90 - 160$ au (see Appendix A.5, Fig. A.2 for some of the resulting density maps). The lower limit in the mass range is chosen based on the results of Juhász et al. (2015), who concluded that observable spiral arms are formed for planets with $M > 1 M_{\text{Jup}}$. Tighter constraints on the lower limit of the planet mass can be obtained from spiral arm formation theory. For a planet with a mass larger than three thermal masses ($M_{\text{th}} \equiv c_s^3 / \Omega G = M_{\star} (h/r)_p^3$), two spiral arms will form interior to its orbit (Bae and Zhu 2018). Since we wanted to model $m = 2$ spirals, we chose to place the planets outside of the spiral arm (which extends up to 90 au in the millimetre continuum) based on the results of Dong et al. (2015). Assuming that the planet is outside ~ 90 au and the disk aspect ratio of our model, we obtained that two spirals are formed for planet masses larger than $\sim 4.8 M_{\text{Jup}}$. Another criteria for the planet mass comes from the separation between the primary and secondary spiral arms (ϕ_{sep}). Fung and Dong (2015) obtained that this quantity scales with the planet mass, following $\phi_{\text{sep}} = 102^\circ (q/0.001)^{0.2}$, where in this case q is the planet-to-star mass ratio. If we consider that the spiral arms have a separation range between 135° and 180° , we obtain that the planet mass should be between 4 and $17 M_{\text{Jup}}$. After a few test runs in our simulations, we realized that in order to observe the disk truncate at 90 au (consistent with the disk outer edge in the millimetre continuum), when increasing the separation, we should also increase the planet mass. Snapshots of the gas and total dust surface densities of our 3D and 2D hydro simulations for planets of 5, 10 and $15 M_{\text{Jup}}$ at separations of 130,

140 and 160 au, respectively, are shown in the Appendix A.5.

2.5.2 Radiative transfer

In order to compare the results generated by the procedure described in the last section with our observations, we generated images in both polarized NIR and millimetre continuum using the radiative transfer code RADMC-3D (Dullemond et al. 2012). We obtained synthetic scattered light images using the dust mass distribution computed in the described 3D PLUTO simulations. Based on Ricci et al. (2010), we assumed a dust size distribution $n(s) \propto s^{-2.5}$ and model scattering by submicron particles with sizes ranging between 0.01 and 0.5 μm . To compute the dust mass in this range, we used the total dust mass estimated in this work (see Table 2.1) assuming maximum grain sizes in the mm, to obtain $M_{\text{dust}, < 0.5 \mu\text{m}} = 10^{-9} M_{\odot}$. Opacities are computed assuming a dust composition of 60% astronomical silicates and 40% amorphous carbon grains, taking the optical constants respectively from Draine and Lee (1984) and Li and Greenberg (1997), and combining them following the Bruggeman mixing rule. Scattering matrices were computed assuming spherical dust grains using the BHMIE code (Bohren and Huffman 1983) for Mie scattering. For the scattered light computations, we approximated the grain size distribution using 5 size bins. To smooth out oscillations in the polarization degree occurring when considering spheres of a single size (see, e.g., Keppler et al. 2018), we used a Gaussian size distribution within each bin with a FWHM of 20% of the corresponding grain size. The star was modelled as a point source located at the domain center emitting thermal radiation with characteristics summarized in Table 2.1. We used RADMC-3D to model anisotropic scattering with full treatment of polarization, using a total of 10^8 photon packages. The obtained Stokes Q and U frames were then convolved by a Gaussian PSF with a FWHM of 51 mas to reproduce the resolution of the VLT/SPHERE observations (see Section 2.3), after which we used equation (2.2) to obtain the resulting Q_{ϕ} images.

To compare with the ALMA data, we computed radiative transfer predictions of the dust continuum, in this case, using the output of the dust and gas 2D simulation. We used the dust density field from the simulation as input for RADMC-3D. We expanded the two-dimensional surface density vertically, assuming a Gaussian shape, where the volumetric mass density for each dust bin follows:

$$\rho_i(r) = \frac{\Sigma_i(r)}{\sqrt{2\pi}H_i(r)} \times \exp\left(-\frac{z^2}{2H_i^2}\right), \quad (2.5)$$

where H_i indicates the pressure scale height of the dust bin. The vertical settling of the disk follows a standard diffusion model (Dubrulle et al. 1995):

$$H_i = \sqrt{\frac{\tilde{\alpha}}{\tilde{\alpha} + St_i}} H_g, \quad (2.6)$$

where H_g is the gas pressure scale height, St is the dust Stokes number, and $\tilde{\alpha} = \alpha / Sc_z$ with α the α -viscosity value of the gas. Sc_z is the Schmidt-number, set to 1 Sc_z relates the dust

diffusion coefficient with the gas viscosity $D_z = \nu / Sc_z$ (see also Weber et al. 2019). We used `optool`⁴ to compute the dust absorption and scattering opacities of a mixture using standard Mie theory and Bruggeman rules. We assumed that the composition of the dust grains is a mixture of silicates (internal density of 3.2 g/cm^3), amorphous carbon (internal density of 2.3 g/cm^3), and vacuum. Assuming that the solids in the mixture are 60% silicates and 40% carbon, a volume fraction of 25% of vacuum in the mixture is required so its internal density is $\sim 2 \text{ g/cm}^3$. The dust size distribution is equal to the values used for the simulation, set by the power law $n(s) \propto s^{-2.5}$, with maximum and minimum dust sizes of $100 \mu\text{m}$ and $10 \mu\text{m}$, respectively. The total dust mass in our models is $\sim 10^{-4} M_\odot$. We computed the dust temperature using the Monte Carlo method of Bjorkman and Wood (2001), and the continuum emission image via ray-tracing, taking into account absorption and scattering, assuming Henyey–Greenstein anisotropic scattering. We computed simulated ALMA observations from the radiative transfer synthetic continuum image using CASA (version 5.6) `simobserve` and `tclean` tasks. Following the observations setup from the DSHARP survey (Andrews et al. 2018), we simulated an 8 h integration in configuration C43-8 combined with a 15 min integration in C43-5. Finally, we cleaned the image using `briggs` weighting 1.0. We obtained a beam size of $55 \times 53 \text{ mas}$ and PA of $\sim -55^\circ$, directly comparable to the ALMA observation.

2.5.3 Results and comparison to observations

All tested planets drive $m = 2$ spiral arms whose symmetry increases for larger planetary mass and have a low contrast in the dust surface density (as seen in the density plots shown in Fig. A.2). Given the asymmetry in the $5 M_{\text{Jup}}$ case, we conclude that in case the spirals are caused by a planet, its mass should be at least of approximately $10 M_{\text{Jup}}$. In Fig. 2.8 we show resulting radiative transfer images for a $10 M_{\text{Jup}}$ planet at a separation of 140 au, with spiral arms observable both in the scattered light and millimetre continuum observations. For a better comparison to the simulations, we apply a Gaussian kernel to the image on the left panel, similar to the one used for the SPHERE image in Fig. 2.6, left; and we subtract the azimuthal average flux on the image plane to enhance the spirals on the synthetic millimetre continuum image on the right, analogous to the procedure applied to Fig. 2.6, right. Additionally, we overplot the location of the observed spiral arms. The obtained images resemble the ones detected both in the scattered light and millimetre continuum observations, except for the fact that we are only able to fit either the inner or the outer spirals from the millimetre observations, but not both at the same time (see Fig. A.3, lower panel). This is likely due to missing physics in our simulations, as these models of spirals launched by a single planet are unable to reproduce the break in the spirals observed by ALMA, as well as the gap and the ring features (at 79 and 88 au, respectively) in the observations. We must also note that in order to see spiral arms induced by a planet in millimetre continuum, the dust must be fragmentation limited (e.g., Birnstiel et al. 2010) leading to a small dust maximum size, and therefore, to Stokes numbers small enough to follow the spirals. In protoplanetary

⁴<https://github.com/cdominik/optool>

disks, the maximum grain size is mainly set by radial drift or fragmentation of particles after collisions. The latter depends on the disk viscosity and the threshold considered for the fragmentation velocity of the grains. Assuming low fragmentation velocities for ice grains (e.g., < 1 m/s, as suggested by recent laboratory experiments such as Musiolik and Wurm 2019; Steinpilz et al. 2019), and $\alpha = 10^{-3}$ (as taken in the simulations), the maximum grain size in the entire disk is dominated by fragmentation, limiting the maximum size of $100 \mu\text{m}$ (Pinilla et al. 2021). Kataoka et al. (2016) have found that dust with similar characteristics is traced by millimetre continuum observations of the similarly young disk HL Tau. These characteristics are not required to see spirals generated by GI, where the dust trapping in spirals is efficient for larger dust Stokes numbers (Rice et al. 2004). We also note that none of the parameter sets that we sample are able to reproduce the contrast nor the apparent break in the spiral arms shown in the ALMA data, which might be explained by additional physical processes occurring in the disk. However, more complex simulations including other effects (e.g., dust growth, fragmentation, dust feedback, gas temperature evolution) are beyond the scope of this work. Additionally, we note that a planet of $10 M_{\text{Jup}}$ in such a young disk could have either formed via gravitational collapse when the disk was probably more massive and, therefore, gravitationally unstable (Boss 1997), or formed as a stellar companion from cloud fragmentation due to the planet/star mass ratio ($\sim 1\%$, Reggiani et al. 2016). We would like to mention that this is a first attempt to find a plausible planetary model to explain the observed spiral pattern in the protoplanetary disk around WaOph 6 and that further, deeper observations would be needed to confirm or discard this scenario.

Since we employ an isothermal equation of state, the spirals produced in our simulations are induced solely by Lindblad resonances and not by buoyancy modes, which may be triggered when using finite cooling times. It is argued in Bae et al. (2021) that such modes cannot be observed in millimetre continuum observations, but could potentially be seen in scattered light. The pitch angles for buoyancy resonances shown in that work for up to $2 M_{\text{Jup}}$ planets are generally below those seen in our SPHERE observations (see Table 2.3), which suggests that the observed spirals are likely not triggered by such modes. Future resolved CO line emission observations analysing the disk kinematic structure could help discard or verify this hypothesis (Bae et al. 2021).

2.6 Discussion

2.6.1 Observations in NIR and mm

Our SPHERE/IRDIS-DPI observations show the launch of a $m = 2$ spiral pattern in the disk around WaOph 6. This is a surprising finding, since so far, no spiral arms had been observed in scattered light in disks around K and/or M stars with ages < 1 Myr. Moreover, spiral arms have not been observed at these wavelengths in single T Tauri stars of any age (Garufi et al. 2018). Disks with spiral arms detected in scattered light are thought to be older (with the caveat that stellar ages are highly uncertain), and with stellar hosts of spectral types from G to A (e.g., MWC 758, Dong et al. (2018b), HD 142527, Claudi et al. (2019), HD 100546,

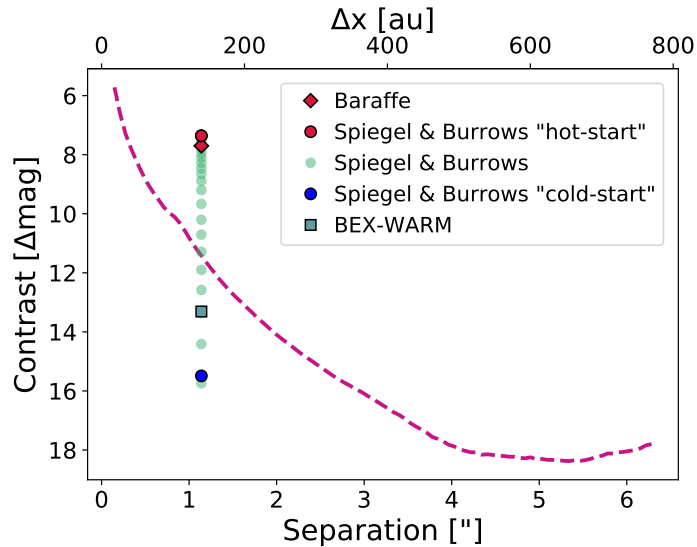


Figure 2.9: Planet detection limits as a function of the separation from the star for the SPHERE H -band. The purple curve is the 3σ contrast obtained from the total intensity SPHERE image of WaOph 6. The markers show the magnitude contrast of the proposed $10 M_{\text{Jup}}$ planet at 140 au estimated from different evolutionary models. The red markers show the resulting contrast for the “hot-start” scenario from the Baraffe et al. (2003) (red diamond) and Spiegel and Burrows (2012) (red dot) models, while the blue dot shows the contrast for a “cold-start” from the Spiegel and Burrows (2012) models. The green square shows the contrast from the BEX-WARM models (see text). And the green dots show the contrast for different initial entropy values from the Spiegel and Burrows (2012) models.

Pérez et al. (2020), AB Aur, Boccaletti et al. (2020), HD 100453, Benisty et al. (2017)). In the millimetre continuum, most of these disks show asymmetric morphologies, along with large cavities (e.g., Tang et al. 2017; Cazzoletti et al. 2018; Pineda et al. 2019). Further observations in both scattered light and millimetre continuum of K and M type stars with disks would be needed to determine whether spiral arms are a common feature in such young disks, as well as the possible implications that this might have in dust and gas evolutionary models. We also note that comparing observations at different wavelengths can contribute greatly to the understanding of the physical processes driving the different morphologies seen in protoplanetary disks.

From our hydrodynamical simulations, we observe that in order to obtain a spiral pattern that can be observed in the millimetre continuum data, the dust particles must have a limited maximum size. This has previously been observed in dust evolution simulations by Gerbig et al. (2019), and can be linked to the young age of the disk.

2.6.2 Upper limits on the brightness of point sources

We used the total intensity image derived from our SPHERE/IRDIS-DPI observations to obtain information on the detection limits for WaOph 6. We built the contrast curve in Fig. 2.9 by considering the contrast between WaOph 6 (the central brightest pixel) and a representative planetary signal in the total intensity image. We took the planetary signal to be three times the noise (root mean square) in 2 pixel wide annuli centered on the star,

at different separations up to $\sim 6''$ (~ 740 au). Additionally, we estimated the foreground extinction in the H-band toward WaOph 6. For this we first estimated the reddening by using the intrinsic $J - H$ magnitude of a K6V star from Pecaut and Mamajek (2013), then using the values in Table 3 of Rieke and Lebofsky (1985), we obtained a visual extinction of $A_V = 5.08$ mag, and an H-band extinction of $A_H = 0.88$ mag.

To estimate the apparent magnitude of our proposed planet, we used two independent evolutionary model predictions. On one hand we considered the evolutionary models by Baraffe et al. (2003) for a $10 M_{\text{Jup}}$ planet at 1 Myr. On the other hand, we used the evolutionary models proposed by Spiegel and Burrows (2012) for both a “hot” and “cold-start” scenarios, and we extrapolated the H-band absolute magnitude (M_H) for our $10 M_{\text{Jup}}$ planet at 0.7 Myr. Considering extinction toward WaOph 6, we obtain $m_H = 15.26$ mag, $m_H = 14.91$ mag, and $m_H = 23.07$ mag, respectively for each model. Finally, with the H-band magnitude for WaOph 6, $m_H = 7.57$ mag, we obtained the following contrasts: $\Delta\text{mag} = 7.70$, $\Delta\text{mag} = 7.36$, and $\Delta\text{mag} = 15.49$ mag, respectively. Furthermore, we obtained the contrasts for our proposed planet in the “warm-start” scenario from the initial entropy values reported by Spiegel and Burrows (2012). And as an additional comparison, we used the Bern EXoplanet cooling curves (BEX, Mordasini et al. 2017) coupled with the COND atmospheric models (Allard et al. 2001) reproducing the cooling under “warm-start” initial conditions (Marleau et al. 2019), and thus denominated BEX-WARM model (see Asensio-Torres et al. 2021, and references therein for more details). As seen in Fig. 2.9, the detectability of our proposed planet strongly depends on the adopted formation model. In case of the “hot-start” scenario, the planet should have been observed, while for a large part of the “warm-start” and for the “cold-start” scenarios, the planet contrast is below our detection limits. Based on the planet mass and location, a “warm” to “cold” start model would be more plausible to explain its existence.

Additional detection limits for WaOph 6 in the L' -band ($\lambda_0 = 3.8 \mu\text{m}$) have been recently reported by Jorquera et al. (2020). They do not detect any companion candidates to the star, but report detection probability maps obtained using the (Baraffe et al. 2003) models. From these they preliminary rule out the presence of companions with masses $> 5 M_{\text{Jup}}$ at separations > 100 au. However, they advise that these estimates might be optimistic, since they do not consider extinction effects, either toward WaOph 6, nor due to the disk dust. An additional caveat comes from the models, as they become very uncertain in accurately predicting the properties of very young planets. It is also important to note that our hydrodynamical simulations do not include additional physical processes that could be ongoing in the disk, coming from the fact that spiral arm formation by a planetary mass object is still not well understood. This could lead to an overestimation of the planet mass, which along with evolutionary models uncertainties, could explain our differing results.

2.7 Summary

We have presented for the first time scattered light SPHERE/IRDIS-DPI observations of the disk around WaOph 6 in the H-band. We analysed the disk morphology, and used archival

ALMA data to compare with ours. We tested the planetary mass perturber hypothesis as the underlying cause for the spiral structure by performing hydrodynamical simulations and using radiative transfer. Our results are summarized below:

1. We observe the launch of a set of $m = 2$ spiral arms up to $\sim 0.3''$ (40 au) in our Q_ϕ SPHERE/IRDIS-DPI images as seen in Fig. 2.2, left. These spirals were first detected using millimetre continuum observations from the ALMA/DSHARP survey. To our knowledge, WaOph 6 is the youngest disk to show spiral features in scattered light (Garufi et al. 2018). We note that this might be of interest for dust and gas evolutionary models.
2. We observe a companion candidate at about $3''$ from the star in our data, as shown in the top panel of Fig. 2.4. After the astrometric analysis described in Section 2.4.2, we were able to determine that the CC is not bound to WaOph 6. With this we also discard the CC being a possible cause of the spiral structure.
3. Comparing our SPHERE observations with archival ALMA/DSHARP data, we find that both the gap and the ring features at 79 and 88 au, respectively, seem to be present in both data sets. We traced the spiral features in both observations as seen in Fig. 2.6. For the ALMA data, we notice a break in the spiral arms of the ALMA image at $\sim 0.16''$ (~ 20 au), which is not observed in our SPHERE data. We treated this break as a separate set of spirals, however, its origin remains unknown. When plotting the spirals in polar coordinates (Fig. 2.7) we find a discontinuity in the spiral arms for the ALMA data at ~ 50 au, already reported by Huang et al. (2018b).
4. To test the planetary mass perturber hypothesis we performed hydrodynamical simulations combined with radiative transfer to compare with the observations. We tested the parameter space of a planet with masses between $2 - 15 M_{\text{Jup}}$ and separations between $90 - 160$ au (i.e., outside of the spiral structure). All tested planets drive $m = 2$ spiral arms. However, none of the parameter sets that we sample are able to reproduce the contrast nor the apparent break in the spiral arms shown in the ALMA data, which may be due to additional physical processes occurring in the disk. Furthermore, the tested planets do not reproduce the gap nor the ring features at 79 and 88 au, respectively, these features need further investigation outside the scope of this work. Given the symmetry of the observed spirals, we find that, if these are caused by a planet, its mass is likely of at least $10 M_{\text{Jup}}$. This is a first attempt to explain the spiral structure seen in both data sets, and more data are needed to better constrain the underlying cause of the spiral features.
5. To determine the sensitivity of our data to possible companions embedded in the disk, we generated the contrast curve in Fig. 2.9 from the total intensity image. With this we obtain contrast limits for a planetary/substellar companion forming inside the disk in polarized light. We estimate the contrast of our proposed planet using different evolutionary models, where the possibility of detection strongly depends on the formation

scenario. A “warm” to “cold” starts would explain the non-detection of the planet in our SPHERE data.

The findings in this Chapter, highlight the still unknown complexity of WaOph 6. The striking presence of a spiral pattern in scattered light even in limited S/N data are worth further, deeper observations of this source. Which will additionally serve to confirm or discard a planetary perturber as a possible cause behind the spiral features.

Chapter 3

High-contrast imaging study on the candidate companions around AH Lep

The contents of this brief chapter are adapted from Brown Sevilla et al. (2019), published in the *Research Note of the American Astronomical Society (RNAAS)*. I was under the supervision of Thomas Henning, Wolfgang Brandner and Markus Feldt, and worked in close collaboration with Faustine Cantalloube.

3.1 Motivation

This Chapter presents the procedure to identify and characterise companion candidates around stars with high-contrast imaging applied to the star AH Lep. It also describes the process needed to determine whether a companion is bound to its host star or if it is a background object.

Section 3.2 introduces the star and previous observations. The observing details and data reduction are described in Section 3.3. A brief analysis of the companion candidates is presented in Section 3.4. The astrometric analysis is detailed in Section 3.5. And the results are summarised in Section 3.6.

3.2 AH Lep

AH Lep ($R.A._{J2000} = 053409.16$, $Dec._{J2000} = -151703.18$) is a young, nearby, solar-type star (G2V). Gaia DR2 and BANYAN Sigma provide a 99.9% probability of the star belonging to the Columba moving group (Bell et al. 2015), yielding an estimated age of 42_{-4}^{+6} Myr (Beuzit et al. 2019). It has a parallax of $p = 17.26$ mas, corresponding to a distance of $d = 57.9$ pc (Gaia Collaboration 2018). The star has been reported to have variable photospheric and X-ray emission (e.g., Burleigh et al. 1998; Cutispoto et al. 2003).

AH Lep was first observed in high-contrast imaging in the H-band with the Subaru telescope as part of the SEEDS survey by Brandt et al. (2014). They used Angular Differential Imaging (ADI, Marois et al. 2006) to search for candidate companions (CCs) around the star and they did not report any CCs within $7.5''$ (~ 400 au). We now present observations of AH Lep with the VLT/SPHERE instrument. As mentioned in Chapter 1, thanks to its advanced

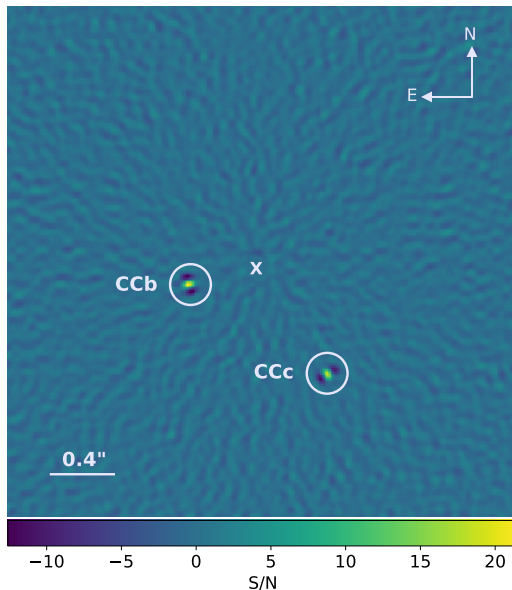


Figure 3.1: SPHERE/IRDIS ANDROMEDA image of AH Lep obtained in $H2$. The white cross indicates the position of the star behind the coronagraph. The two companion candidates CCb and CCc, are shown inside the white circles.

AO system and small inner working angle (IWA), SPHERE delivers much higher resolution and is able to look much closer to the star.

3.3 Observations and data reduction

AH Lep was observed with VLT/SPHERE (Spectro-Polarimetric High-contrast Exoplanet REsearch, Beuzit et al. 2019) installed at ESO Paranal Observatory, Chile, within the SpHERE INfrared survey for Exoplanets (SHINE, Chauvin et al. 2017b). Observations took place on the night of January 28th, 2018, using the IRDIFS mode, which simultaneously allows dual-band imaging with the IRDIS camera (Dohlen et al. 2008; Vigan et al. 2010) in $H2/H3$ filters ($1.59 \mu\text{m}$ and $1.66 \mu\text{m}$, respectively), and Integral Field Spectroscopy (IFS, Claudi et al. 2008) in the YJ bands ($0.95 \mu\text{m} - 1.32 \mu\text{m}$, with a resolution of $R \sim 50$). The data were taken in pupil tracking mode. For the data reduction, we made use of the SPHERE Data Center pipeline (Delorme et al. 2017), using the SPHERE Data Reduction Handling (DRH) software (version 15.0; Pavlov et al. 2008). The basic reduction consists in: subtracting sky background, flat fielding, identifying and interpolating bad-pixels, and performing star center corrections. In addition, for the IFS data, calibration of the wavelengths and of the cross-talk between spectral channels were performed.

To detect and characterise CCs, we used the ANgular Differential OptiMal Exoplanet Detection Algorithm (ANDROMEDA, Cantalloube et al. 2015), which utilizes an inverse problem approach to search for CCs (see Section 1.4.2 for details).

Two candidates were found, namely CCb and CCc, at an angular separation of $421.0 \pm 3.4 \text{ mas}$ and $769.8 \pm 3.5 \text{ mas}$, which correspond to a projected separation of $24.3 \pm 0.1 \text{ au}$ and $44.5 \pm 0.2 \text{ au}$, respectively (see Fig. 3.1). Their derived $H2$ magnitudes are 12.2 mag and

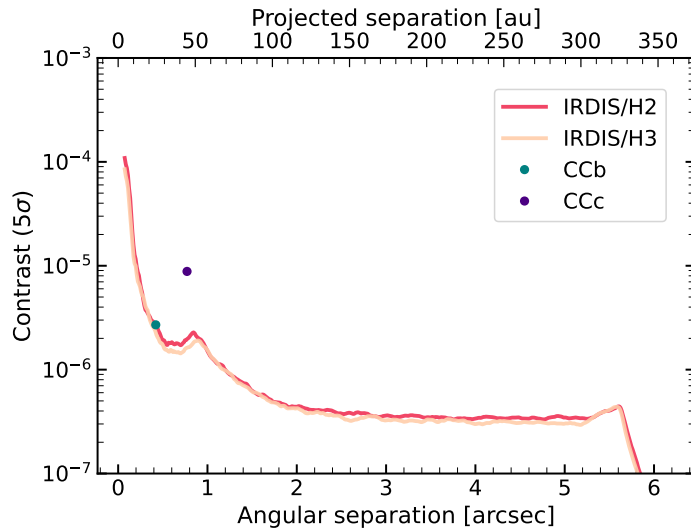


Figure 3.2: 5σ detection limits. Contrast with respect to the star as a function of separation to for the SPHERE/IRDIS $H2H3$ data of AH Lep. The two companion candidates are colour-coded in green and purple, respectively.

12.6 mag fainter than AH Lep, corresponding to a contrast of $12.70 \times 10^{-6} \pm 1.54 \times 10^{-6}$ and $8.62 \times 10^{-6} \pm 1.14 \times 10^{-6}$, respectively.

3.4 Analysis of the companion candidates

Using ANDROMEDA, we obtain the contrast curves for the SPHERE/IRDIS $H2H3$ data as shown in Fig. 3.2, where the two CCs are colour-coded in green and purple, respectively. The derived detection limits imply that the IRDIS data is sensitive to companions brighter than 10^{-5} at ~ 12 au.

In addition, as a first attempt to determine the nature of the CCs, we plotted them in a colour-magnitude diagram (see Fig. 3.3) along with known brown dwarfs and planetary-mass companions. The two CCs fall between the T- and L-dwarf regions of the diagram. Furthermore, we extracted their individual contrast from the IFS data. The results are shown in Fig. 3.4, we found no significant evidence of methane (CH_4) absorption, suggesting that they do not belong to the T-dwarf class. This absence may be due to several reasons, e.g. clouds in their atmospheres. A more detailed analysis of the spectra of the point sources might help to clarify their nature, however, this lies beyond the scope of this study and will be left for future work.

3.5 Astrometric analysis

In order to test if these two companions are bound, we performed an astrometric analysis combining the SPHERE data with archival H -band data from the Gemini Planet Imager (GPI, Macintosh 2014) at the Gemini South telescope on Cerro Pachon, Chile, obtained on

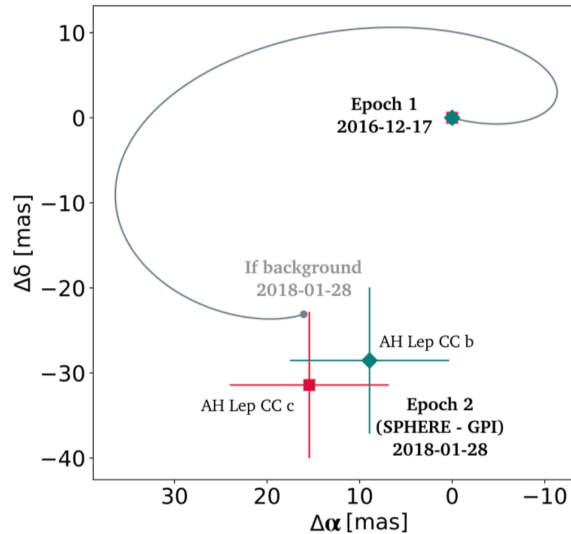


Figure 3.5: Relative astrometry of the CCs of AH Lep. The markers show the measurements of the relative positions of the CCs, at both the initial epoch, and further in time at the SPHERE-GPI epoch. The gray line traces the path a stationary background object would have followed relative to AH Lep between the two epochs.

December 17th, 2016. The GPI data were reduced with the dedicated public pipeline (Perrin et al. 2014; Perrin et al. 2016), and afterwards we applied ANDROMEDA to search for companions. Two CCs were found in this data set, and their astrophysical parameters are consistent with the ones found in the SPHERE data. Our results of the astrometric analysis are shown in Fig. 3.5, where we plot the relative astrometry between the SPHERE and GPI epochs. We also indicate the combined uncertainties of SPHERE+GPI data, which are dominated by the systematic uncertainty between the SPHERE and GPI astrometry, and not by the measurement procedure. We found that the CCs are most likely background sources as they appear to follow the stationary background track. The astrometric analysis was calibrated following the procedures in Maire et al. (2016) for the SPHERE data, and following Konopacky et al. (2014) for the GPI data. Within error bars, the two CCs appear to be co-moving, however, follow-up observations would be needed to confirm or disprove this scenario.

3.6 Summary

In this brief chapter we demonstrate how high-contrast imaging observations are used in order to detect and characterise companion candidates. With this example, we also show the astrometric analysis needed to confirm or disprove whether the companions are bound to the system. In the case of AH Lep, we find that the two companion candidates are not bound to the star. The astrometry analysis suggests that they might be co-moving, but this needs to be confirmed by further observations. Regarding the nature of these objects, we find no significant presence of methane, which suggests they could belong to the L-dwarf class, however, once more further and more detailed observations would be required to confirm this.

Chapter 4

Revisiting the atmosphere of 51 Eridani b with VLT/SPHERE

The contents of this chapter are adapted from Brown-Sevilla et al., [submitted](#) to *Astronomy and Astrophysics (A&A)*, from which I am the first author from a team effort of 29 co-authors. I was under the supervision of Thomas Henning, Markus Feldt, and Wolfgang Brandner, and worked in close collaboration with Anne-Lise Maire, Paul Mollière and Matthias Samland.

4.1 Motivation

The development of adaptive optics (AO) in recent years has allowed ground-based instruments such as the Gemini Planet Imager (GPI; [Macintosh 2014](#)) and the Spectro-Polarimetric High-contrast Exoplanet REsearch instrument (SPHERE; [Beuzit et al. 2019](#)) to detect tens of substellar companions (e.g., [Bowler et al. 2017](#); [Janson et al. 2019](#); [Bohn et al. 2020](#)). Direct imaging allows to perform spectroscopic observations of the companions to probe the properties and composition of their atmospheres. High-contrast imaging is sensitive to the thermal near infrared (NIR) emission of recently formed giant planets and brown dwarfs. The young age of these objects makes them excellent targets for testing planet formation theories (e.g., [Spiegel and Burrows 2012](#); [Mordasini et al. 2009a](#); [Mordasini et al. 2009b](#)), by comparing their luminosity with evolutionary track predictions for models of differing initial entropy, such as hot- or cold-start models (e.g., [Allard et al. 2012](#)). In addition, advancements in the treatment of clouds in atmospheric models, allow to better characterise the detected companions (e.g., [Baudino et al. 2015](#); [Mollière et al. 2020](#); [Carrión-González et al. 2020](#)).

This Chapter presents new NIR spectro-photometric observations of 51 Eri b obtained using VLT/SPHERE as part of the SHINE survey ([Desidera et al. 2021](#); [Langlois et al. 2021](#); [Vigan et al. 2021](#)). These observations were carried out as a follow-up to the ones presented in [Samland et al. \(2017\)](#) and have the highest S/N achieved so far ($S/N \sim 23$ for K1). The radiative transfer code `petitRADTRANS` was used to model the atmospheric spectrum of the planet. An attempt to reproduce the results in SAM17 using the retrieval approach is also presented.

Section [4.2](#) introduces 51 Eri b and previous NIR studies on the planet. Section [4.3](#) describes the spectro-photometric observations. Section [4.4](#) details the data reduction and

spectrum extraction procedures, as well as the derived detection limits in planet contrast and mass. The description of the atmospheric retrieval runs is detailed in Section 4.5. A detailed analysis of selected parameters of the planet and a discussion of the results is presented in Section 4.6, and finally, Section 4.7 displays a summary of the results.

4.2 51 Eri b

51 Eridani b is the first discovered planet by the GPI exoplanet survey (Macintosh et al. 2015). It was first characterised using both J - and H -band spectra from GPI, and L_p -band photometry from Keck/NIRC2. This young giant planet shows strong methane spectral signatures, an unusual feature in most directly imaged exoplanets. The planet orbits 51 Eridani A, a young F0IV star member of the β Pictoris moving group (Zuckerman et al. 2001; Bell et al. 2015). The latest estimate for the isochronal age of the system from *Gaia* EDR3 is ~ 10 Myr (Lee et al. 2022), a much younger age than the commonly adopted ~ 20 Myr. Using photometry from the Transiting Exoplanet Survey Satellite (TESS), Sepulveda et al. (2022) recently determined that 51 Eri is a γ Doradus pulsator with a core rotation period of $0.9^{+0.3}_{-0.1}$ days. The star is part of a hierarchical triple system, along with the M-dwarf binary GJ 3305AB, separated by ~ 2000 au (Feigelson et al. 2006; Kasper et al. 2007). 51 Eri is located at 29.90 ± 0.06 pc, as derived from the precise parallax measurement by the *Gaia* mission (Gaia Collaboration et al. 2021). From $24 \mu\text{m}$ *Spitzer* observations, 51 Eri is known to have an infrared (IR) excess (Rebull et al. 2008), and a debris disk was detected using *Herschel* observations at 70 and 100 μm with a very low IR fractional luminosity of $L_{\text{IR}}/L_* = 2.3 \times 10^{-6}$ and a lower limit on the inner radius of 82 au (Riviere-Marichalar et al. 2014). From WISE observations, Patel et al. (2014) report a warm disk ($T \sim 180$ K) at a radius of 5.5 au assuming blackbody radiation. Therefore, it is likely that the architecture of 51 Eri could resemble that of our Solar System with a two-belt debris disk.

The planet 51 Eri b was confirmed to be bound to the system in a follow-up paper by De Rosa et al. (2015). The authors also carried out a preliminary estimate of the orbital parameters (semi-major axis $a = 14^{+7}_{-3}$ au, orbital period $T = 41^{+35}_{-12}$ yr, inclination $i = 138^{+15}_{-13}$ deg) which suggest that the planet is not coplanar with the binary GJ 3305AB ($i = 92.1 \pm 0.2$, Montet et al. 2015). Recently, Müller and Helled (2021) reported mass and metallicity estimates for 51 Eri b derived from synthetic cooling tracks and the planet's luminosity. Assuming an age range of 17–23 Myr and a hot-start formation scenario, they obtain a mass of $M = 2.3M_{\text{Jup}}$ and a metallicity of $[\text{Fe}/\text{H}] = 0.11$. Another study by Dupuy et al. (2022) presented an upper limit for the mass of the planet of $M < 11M_{\text{Jup}}$ at 2σ using cross-calibration of *Hipparcos* and *Gaia* EDR3 astrometry. They also revise the luminosity of 51 Eri b using a photometric approach and find $\log(L_{\text{bol}}/L_{\odot}) = -5.5 \pm 0.2$ dex. Additionally, they derived a lower limit on the initial specific entropy of the planet which rules out cold-start formation scenarios.

In addition to the discovery paper, there have been two atmospheric analyses to characterise 51 Eri b. By combining SPHERE/IFS YJ and YH , and GPI H spectra, along with photometry from SPHERE (broad-band H , $H23$ and $K12$) and Keck/NIRC2 (L_p), Samland et al.

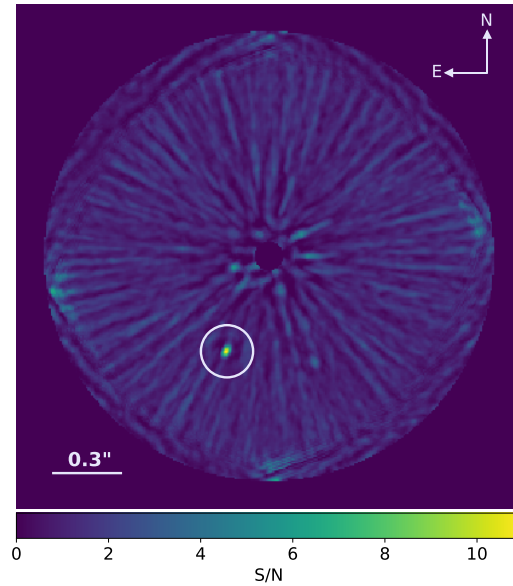


Figure 4.1: Median combined S/N detection map from ANDROMEDA for the SPHERE/IFS data. The circle indicates the position of 51 Eri b. The azimuthal wings around the planet signal is the characteristic planet signature that ANDROMEDA is fitting for in ADI data.

(2017) (hereafter SAM17) found the atmosphere to be cloudy. They report $T_{\text{eff}} = 760 \pm 20$ K, $R = 1.11_{-0.14}^{+0.16} R_{\text{Jup}}$, $\log g = 4.26 \pm 0.25$ dex, $[\text{Fe}/\text{H}] = 1.0 \pm 0.1$ dex, and $f_{\text{sed}} = 1.26_{-0.29}^{+0.36}$ for their best-fit model. On the other hand, Rajan et al. (2017) used GPI spectra in K1K2 and photometry (L_p) along with new Keck/NIRC2 J and H spectra and M_S photometry from the discovery paper and determined the atmosphere to be partially cloudy. Their best-fit model yielded $T_{\text{eff}} = 605\text{-}737$ K, $[\text{Fe}/\text{H}] = 1.0$ and $\log g = 3.5\text{-}4.0$ dex. The three studies made use of self-consistent models and differ mainly in the degree of cloudiness of the atmosphere.

4.3 Observations

New data of 51 Eri was obtained with the VLT/SPHERE high-contrast instrument (Beuzit et al. 2019) within the SHINE (SpHere INfrared survey for Exoplanets, Chauvin et al. 2017b) Guaranteed Time Observations (GTO) program on the night of September 28, 2017. These observations were carried out in the IRDIS_EXT mode, which combines IRDIS in dual-band imaging mode (DBI; Vigan et al. 2010) in the K1K2 ($K1 = 2.110 \mu\text{m}$ and $K2 = 2.251 \mu\text{m}$) filters with IFS (Claudi et al. 2008) in the YH spectral bands (between 0.95 and $1.65 \mu\text{m}$, with spectral resolution $R \sim 33$). An apodized pupil Lyot coronagraph with a focal mask diameter of 185 milli-arcsec, was used for the observations (Carbillet et al. 2011). In order to reduce residual speckle noise, the observations were carried out close to meridian passage using the pupil stabilized mode, which allows the use of ADI post-processing (Marois et al. 2006).

To calibrate the flux and center of the images, unsaturated non-coronagraphic images (hereafter referred to as the point spread function or PSF), as well as coronagraphic images with the deformable mirror (DM) waffle mode (see Langlois et al. 2013, for more details on

Table 4.1: Log of observations.

UT date	28-09-2017
Observing mode	IRDIS_EXT
IRDIS filter	K12
IFS band	YH
IRDIS DIT	24 s
IRDIS NDIT	32
IFS DIT	32 s
IFS NDIT	7×22
Field rotation	44.1 deg
Strehl ratio	0.85 – 0.91
Airmass (start/end)	1.10 – 1.09
Seeing	0.4 – 0.7"
Coherence time (τ_0)	5 – 12 ms

Notes. DIT stands for detector integration time. The Strehl ratio is measured at $1.6 \mu\text{m}$. The seeing and coherence time are measured at $0.5 \mu\text{m}$.

this mode) are generally acquired at the beginning and at the end of the observing sequence. The waffle mode generates four artificial replicas of the star in a “cross” pattern, commonly known as satellite spots. These spots are used to measure the star’s position at the center of the pattern. In order to minimize the uncertainties in the frame centering and the astrometric error, and monitor the photometric stability throughout the sequence, the science frames were also obtained using this mode. Finally, night-time sky images were acquired to estimate the background level in the science frames. The pixel scale and the True North (or north angle offset) were obtained using astrometric calibrators, as described in Maire et al. (2016). The usual calibration images (i.e. flat-field, bias, and spectral calibration) were obtained by the internal calibration hardware of the instrument. The observations were conducted in overall favorable conditions (see Table 4.1), except for the presence of clouds near the end of the observing sequence.

4.4 Data reduction and spectrum extraction

The data were reduced with the SPHERE Data Center pipeline (Delorme et al. 2017), using the SPHERE Data Reduction Handling (DRH) software (version 15.0; Pavlov et al. 2008). This basic reduction consists in performing the usual sky background subtraction, flat fielding, bad-pixel identification and interpolation, star centering corrections and, for IFS, the calibration of the wavelengths and of the cross-talk between spectral channels. We then removed poor-quality frames where a significant drop in stellar flux is detected from the satellite spots photometry, because of interfering cirrus clouds near the end of the observing sequence, only the first 140 of the total of 154 IFS frames were used for the post-processing analysis. We also discarded the second PSF for the flux normalization and only used the first PSF frames. The conditions were very stable from the start of observations for the first

PSF frames until the onset of cirrus clouds. Additionally, we tested different SPHERE data reduction recipes and pipelines, see Appendix B.1 for a detailed discussion on how they compare.

For the data analysis, we used the ANgular Differential OptiMal Exoplanet Detection Algorithm (ANDROMEDA; Cantalloube et al. 2015), which utilizes an inverse problem approach based on a maximum likelihood estimator (Mugnier et al. 2009) to search for companion candidates. Other than 51 Eri b, we detect no additional point sources in our data. The main outputs from ANDROMEDA are the estimated flux map, the S/N map, and the map of the standard deviation of the estimated flux. Figure 4.1 shows the resulting S/N detection map from ANDROMEDA for our IFS data.

Additionally, we performed the reduction with TRAP, a temporal, non-local systematics modelling algorithm to look for point sources at small separations (see Samland et al. 2021). Regarding the S/N ratio, with ANDROMEDA we get $S/N = 23.31$ for K1, and $S/N = 2.82$ for K2, while with TRAP we get $S/N = 18.03$ for K1, and $S/N = 3.52$ for K2. In both cases, there is an improvement in the S/N ratio from SAM17 (7.46 and 1.26 for K1 and K2, respectively using ANDROMEDA). On the other hand, the contrast limits are improved with the TRAP reduction as discussed below in Section 4.4.2. Due to the higher S/N ratio achieved in K1, and to be consistent throughout the paper, we decided to use the results of ANDROMEDA for the following steps.

4.4.1 Spectrum extraction

To construct the spectrum of 51 Eri b, we multiplied the planet contrast at each wavelength from ANDROMEDA by a template spectrum of the host star. This template spectrum was obtained as follows: we used a model stellar spectrum from the BT-NextGen library (Allard et al. 2012) with $T_{\text{eff}} = 7200$ K, $\log g = 4.0$ dex, $[\text{Fe}/\text{H}] = 0.0$ dex, and no alpha enhancement (overabundance of He with respect to metallicity, $[\alpha/\text{Fe}]$), since these parameters are the closest to the ones determined from high-resolution spectra for 51 Eri ($T_{\text{eff}} = 7256$ K, $\log g = 4.13$ dex, and $[\text{Fe}/\text{H}] = 0.0$ dex; Prugniel et al. 2007). Then we fit this model spectrum to the spectral energy distribution (SED) of the star using the χ^2 minimization in the Virtual Observatory SED Analyser (Bayo et al. 2008) to obtain the flux scaling factor to account for the distance of 51 Eri. The SED was built with photometry from Tycho B_T , V_T (Hoeg et al. 1997), WISE W3 (Cutri et al. 2013), Johnson U , V , B (Mermilliod 2006), and IRAS 12 μm (*Infrared Astronomical Satellite (IRAS) Catalogs and Atlases. Volume 7: The Small Scale Structure Catalog*. 1988). Finally, we scaled the model spectrum to the resolution of our IFS data using the python function SpectRes¹.

A similar procedure along with the respective transmission curves for the filters was used to obtain updated IRDIS photometry for K1 and K2. Since the planet is not detected significantly in the K2 filter, we applied forced photometry with ANDROMEDA. This consists in performing a photometric measurement in the K2 images at the position of the planet in the K1 frames. Our results are shown in Table 4.2.

¹<https://spectres.readthedocs.io/en/latest/>

Table 4.2: Photometry retrieved from the IRDIS data.

Filter	λ (μm)	$\Delta\lambda$ (μm)	Flux ($\text{Wm}^{-2}\mu\text{m}^{-1}$)	Contrast	Abs. magnitude
K1	2.110	0.102	$4.418 \times 10^{-17} \pm 1.894 \times 10^{-18}$	$6.304 \times 10^{-6} \pm 2.703 \times 10^{-7}$	15.11 ± 0.04
K2	2.251	0.109	$5.149 \times 10^{-18} \pm 1.822 \times 10^{-18}$	$1.002 \times 10^{-6} \pm 3.546 \times 10^{-7}$	17.11 ± 0.38

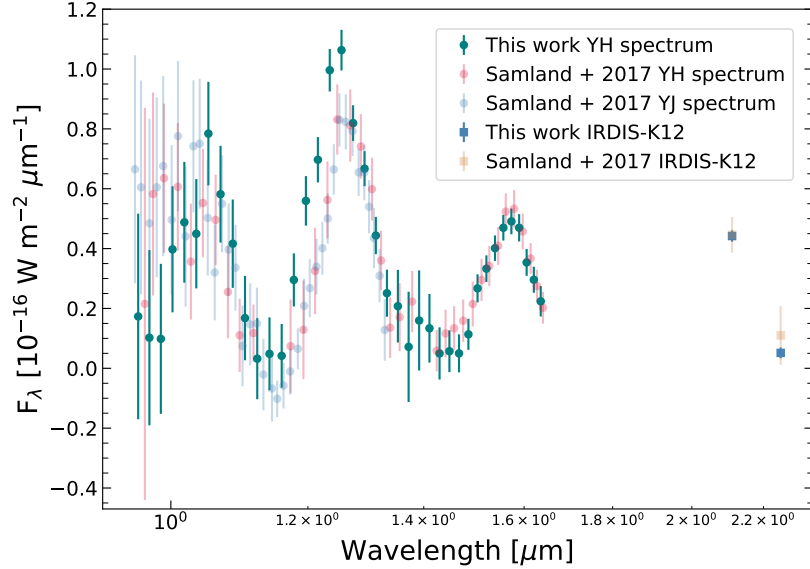
**Figure 4.2:** The newly obtained 51 Eri b *YH* spectrum and *K1K2* photometry. Overplotted for comparison the *YH* spectrum and *K1K2* photometry from Samland et al. (2017).

Figure 4.2 shows the spectrum of 51 Eri b using our IFS data along with the *K1K2* photometric points, overplotted for comparison is the IFS/*YH* spectrum and the *K1K2* photometry presented in SAM17. To further highlight the differences between the *YH* spectra, in Fig. 4.3 we present the relative error as a function of wavelength. For both figures, we removed the spectral channels that were not used in SAM17 (1.14 and 1.41 μm), to allow for a better comparison. Overall, our data exhibits a lower relative error, except for the telluric H_2O absorption bands regions around 1.1 and 1.35 – 1.4 μm (see Appendix B.2), which results in a higher S/N ratio than the data in SAM17.

4.4.2 Detection limits

We used both ANDROMEDA and TRAP to derive 5σ contrast curves for our IRDIS and IFS data. For the IRDIS/*K1-K2* bands, the analysis setup was SDI+ANDROMEDA assuming no planet flux in *K2*. For the IFS-*YH*, we also used SDI+ANDROMEDA assuming a T5 spectral template for putative planets. To convert contrast to mass limits we used the evolutionary tracks of Baraffe et al. (2003) along with the atmosphere model of Baraffe et al. (2015). For the star we used the 2MASS *JHK* magnitudes (Cutri et al. 2003), the L_P magnitude from Macintosh et al. (2015), the newly calculated distance from Gaia Collaboration et al. (2021), and the latest age estimate from Lee et al. (2022). The resulting detection limits are shown in Figure 4.4, we show the curves from ANDROMEDA and in dashed lines the curves obtained

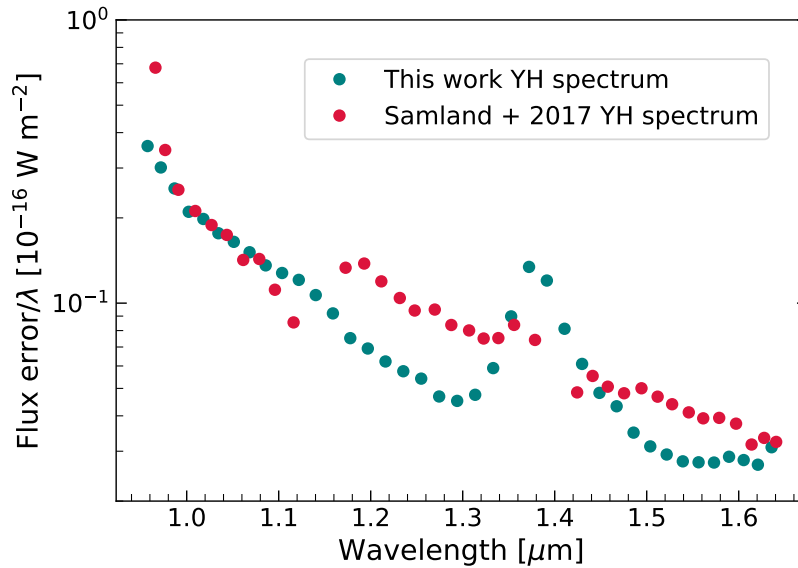


Figure 4.3: Flux uncertainty over wavelength as a function of wavelength for the *YH* spectra of 51 Eri b from this work compared to the one presented in Samland et al. (2017).

with TRAP for the IFS data. The mass limit for the IFS data is cut to the lowest mass computed by the model grid for both pipelines. The *K1* mass curve reaches smaller values than the *K2* mass curve because the *K2* filter matches a methane absorption band that strongly dims the flux of cold giant planets. Our detection limits are corrected for the coronagraphic transmission (Boccaletti et al. 2018) and for small sample statistics (Mawet et al. 2014). From ANDROMEDA we get that the IFS data is sensitive to planets more massive than $3 M_{\text{Jup}}$ at 3 au, and $1 M_{\text{Jup}}$ beyond 4.5 au. While with TRAP we see an additional improvement in the sensitivity of planets down to $2 M_{\text{Jup}}$ at 3 au. We thus achieve a sensitivity about $2 M_{\text{Jup}}$ better than previous studies (e.g., SAM17).

4.5 Retrieval analysis

We used the 1D radiative transfer code `petitRADTRANS`² (*pRT*; Mollière et al. 2019) in its scattering implementation (Mollière et al. 2020) in combination with `PyMultiNest`³ (Buchner 2014) to derive the posterior distributions of the thermal structure, chemical composition, and cloud properties of 51 Eri b. The code takes as an input the spectra of the planet along with prior distributions for the metallicity, *C/O* ratio, $\log g$, radius, a list of molecules to be included, quench pressure, and cloud parameters such as f_{sed} , K_{zz} and $\log \tau_{\text{cloud}}$.

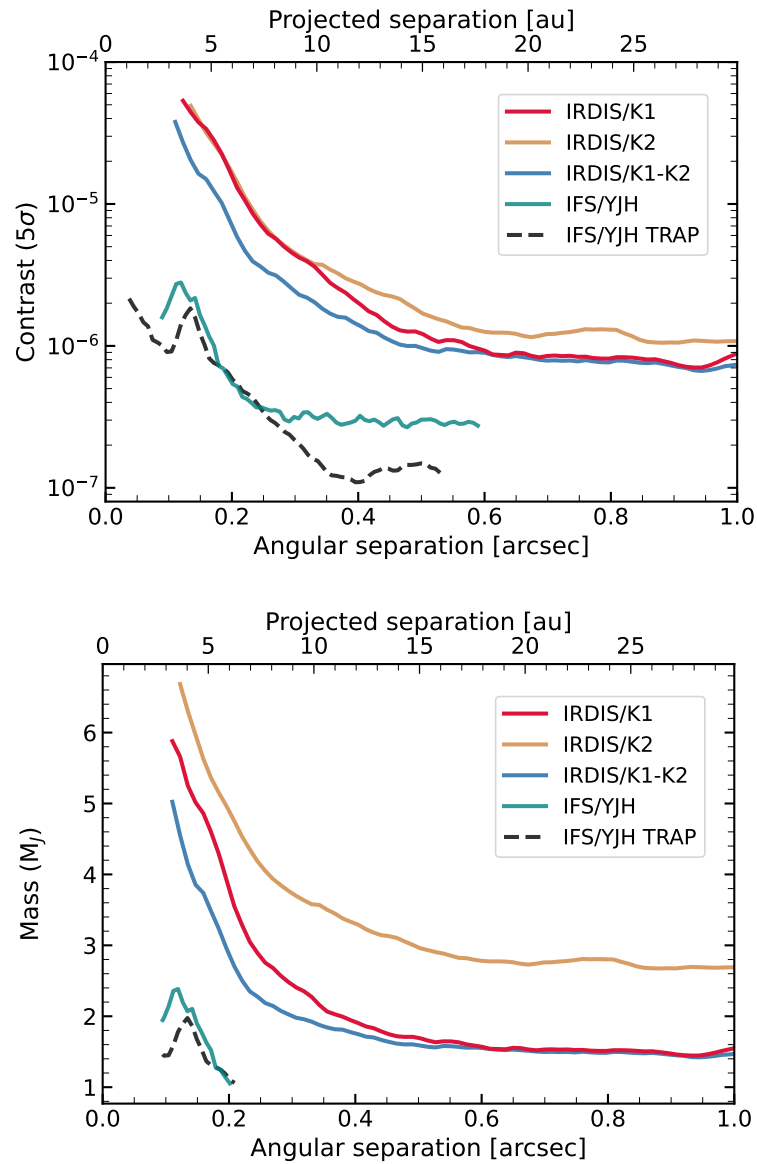


Figure 4.4: 5σ detection limits. Planet contrast (*top*) with respect to the star as a function of separation to the star, and planet mass detection limits (*bottom*) as a function of the separation from the star for the SPHERE/IRDIS_EXT data of 51 Eri b.

Table 4.3: Prior values used for petitRADTRANS retrievals.

Model	Nominal	Both	Enforced clouds
[Fe/H]		-1.5-1.5	
C/O		0.1-1.6	
log g		2.0-5.5	
log τ_{cloud}	-7.0-3.0		-1.0-3.0
f_{sed}		0.0-10.0	
log K_{zz}		5.0-13.0	
Radius (R_{Jup})		0.9-2.0	

4.5.1 Modelling setup

petitRADTRANS setup

The set-up of a pRT retrieval run requires many input parameters determining certain relationships and choices. We describe our set-up in the following:

Retrieved parameters

The following parameters are of prime interest in the retrieval. We assign a flat prior to each - see Table 4.3.

Fe/H The metallicity of the planetary atmosphere.

C/O The carbon-to-oxygen ratio prevalent in the planetary atmosphere.

log g Logarithm of the surface gravity in units of centimeters per second-squared.

f_{sed} The ratio of the mass averaged settling velocity of the cloud particles and the atmospheric mixing speed. Measures the efficiency of sedimentation in the atmosphere.

log K_{zz} Vertical eddy diffusion coefficient of the atmosphere.

Radius Of the planet’s photosphere ($\tau = 2/3$), in units of Jupiter radii.

log p_{quench} Logarithm of pressure at which carbon chemistry is quenched.

σ_{norm} The geometric standard deviation in log-normal size distributions of condensates following Ackerman and Marley (2001).

Additional parameters

An important additional parameter is the effective temperature of the planet, T_{eff} . This is not an explicit input (and thus retrievable) parameter of pRT , but instead has to be calculated by generating a second spectrum for a given set of parameters that covers a wide spectral range in order to estimate the bolometric flux of the planet. Due to the required large wavelength coverage this can be quite time-consuming and is usually only carried out on a subset of the equal weighted posterior distribution.

In addition to these parameters, there are a number of internal “nuisance” parameters that also get prior ranges assigned. These are a set of connecting temperatures (t_1, t_2, t_3), an internal temperature t_{int} , and the two parameters $\log \delta$ and α for the optical depth model $\tau = \delta P^\alpha$. These parameters are later used to determine the atmospheric pressure-temperature (P - T) profile. This P - T model is described in Mollière et al. (2020).

Clouds

From our first retrieval runs on the new data, we observed that the best-fit solutions tended to be non-cloudy ones. According to previously reported results, the photosphere of 51 Eri b is thought to be at least partially cloudy (e.g., Samland et al. 2017; Rajan et al. 2017). We

²<https://petitradtrans.readthedocs.io/>

³<https://johannesbuchner.github.io/PyMultiNest/>

decided to implement the parameter $\log \tau_{\text{cloud}}$ to enforce clouds in the retrieval, which represents the logarithm of the cloud optical depth at the location where the clear atmosphere would become optically thick ($\tau = 1$). These are wavelength averaged optical depths, estimated over the wavelength range of the retrievals. By changing the range of the prior of $\log \tau_{\text{cloud}}$ we were able to enforce clouds in the photospheric region. In order to verify whether a cloud cover is actually present, we split our models into “nominal” and “enforced clouds” ones. Essentially, they are the same model, only differing in the prior range of $\log \tau_{\text{cloud}}$, $[-1, 3]$ for the “nominal”, and $[-7, 3]$ for “enforced clouds” (c.f. Section 4.3).

For the cloud species, we use Na_2S and KCl , which according to Morley et al. (2012) are the most important species at the previously estimated effective temperature of 51 Eri b (700-750 K).

Molecular species

The species contributing to the line opacities in our model are CO , H_2O , CH_4 , NH_3 , CO_2 , H_2S , Na , K , PH_3 , VO , TiO , and FeH . In addition, we include H_2 and He as species contributing to both Rayleigh scattering, and collision induced absorption. The species are retrieved under equilibrium chemistry assumptions and including quenching pressure.

MultiNest setup

To fit model spectra to the data by sampling the posterior probability, we used the nested sampling library PyMultiNest (Buchner 2014), which is in turn based on MultiNest (Feroz and Hobson 2008; Feroz et al. 2009; Feroz et al. 2019). Nested sampling (Skilling 2004; Skilling 2006) is a powerful method, which in contrast to MCMC methods is better at exploring the parameter space and less prone to fall into a local minimum.

Our derived model parameters are chosen to be the median of the marginalized, equal weighted posterior distribution, and the uncertainties quoted refer to the 16th and 84th percentile of said posteriors. Note that the parameters used to generate actual best-fit spectra are generally different from the medians mentioned above and corresponding to the highest log-likelihood. We use Importance Nested Sampling with flat priors (see Section 4.5.1), 4000 initial live points to sufficiently cover the parameter space, and to ensure a high sample acceptance fraction, we use MultiNest’s constant efficiency mode and a sampling efficiency of 0.05.

4.5.2 Input data

Data Set

Our YH -spectrum, like all SPHERE/IFS spectra comprises 39 channels, all of which were fed into the retrieval process. In addition, we use the IRDIS $H2/H3$ photometric filters and broad-band H from SAM17, and $K1/K2$ from this work. Also included are the L_P and M_S Keck/NIRC2 data points from Rajan et al. (2017).

As described in SAM17 and originally in Greco and Brandt (2016), the spectral covariance of the residual speckle noise should be taken into account when computing the likelihood of a model matching data from an IFS-type instrument. We computed the correlation

matrix Ψ for our spectrum in the same way as SAM17. Consequently, in the log-likelihood computation in the retrieval code we used

$$-2 \log \mathcal{L} = (S - F)^T C^{-1} (S - F), \quad (4.1)$$

instead of the simple

$$-2 \log \mathcal{L} = \sum_i ((S_i - F_i) / \sigma_i)^2. \quad (4.2)$$

In both equations, S represents the observed spectrum, and F the model spectrum. See Appendix B.3 for more information.

Can atmospheric retrievals reproduce the previously published results?

In order to determine how far the use of a retrieval method alone impacts the outcome in terms of the derived atmospheric parameters with respect to SAM17's grid of self-consistent models, we ran an additional set of retrievals (nominal and enforcing clouds) on the original data used by SAM17. Note that SAM17 used an SDI+ANDROMEDA data reduction resulting in the reference channels of their spectra not being usable in the model comparison. In addition, they masked out a number of channels due to low signal-to-noise ratios. We took these considerations into account in our reproduction attempts.

4.5.3 Results and comparison with previous data

Retrieval results

In Fig. 4.5 we show the best-fit spectra for the “nominal” model with the new data. Here the black line depicts the best fit spectrum, and the gray lines are randomly drawn spectra from the equally weighted posterior probability distribution. The circles represent the IFS spectrum of 51 Eri b, while the squares depict the photometric points. Overall, the best-fit model is able to reproduce our YH spectrum, as well as the $H2H3$, $K1K2$ and broad-band H photometric points within the uncertainties. We note however, that the M_S photometric point is not fitted in either the “nominal” nor the “enforced clouds” retrievals (see also Fig. B.4). Given the large photometric uncertainties in the M_S data, the best-fit photometry model lies within 2σ of the data. As further discussed in Section 4.6, future mid-IR instruments might help to better constrain this photometric band.

Figure 4.6 shows the corresponding corner plot for the “nominal” model with the posterior probability density functions (PDFs) of selected parameters. The best-fit spectra along with the corner plots for the “enforced clouds” retrieval with our new data, as well as the nominal and enforced clouds retrieval attempts to reproduce SAM17's results, are shown in Appendix B.4. The median of the posterior probability distribution, and the uncertainties representing a 1σ uncertainty range for selected parameters of our four sets of retrievals, are shown in Table 4.4. This subset of parameters was chosen due to their physical relevance.

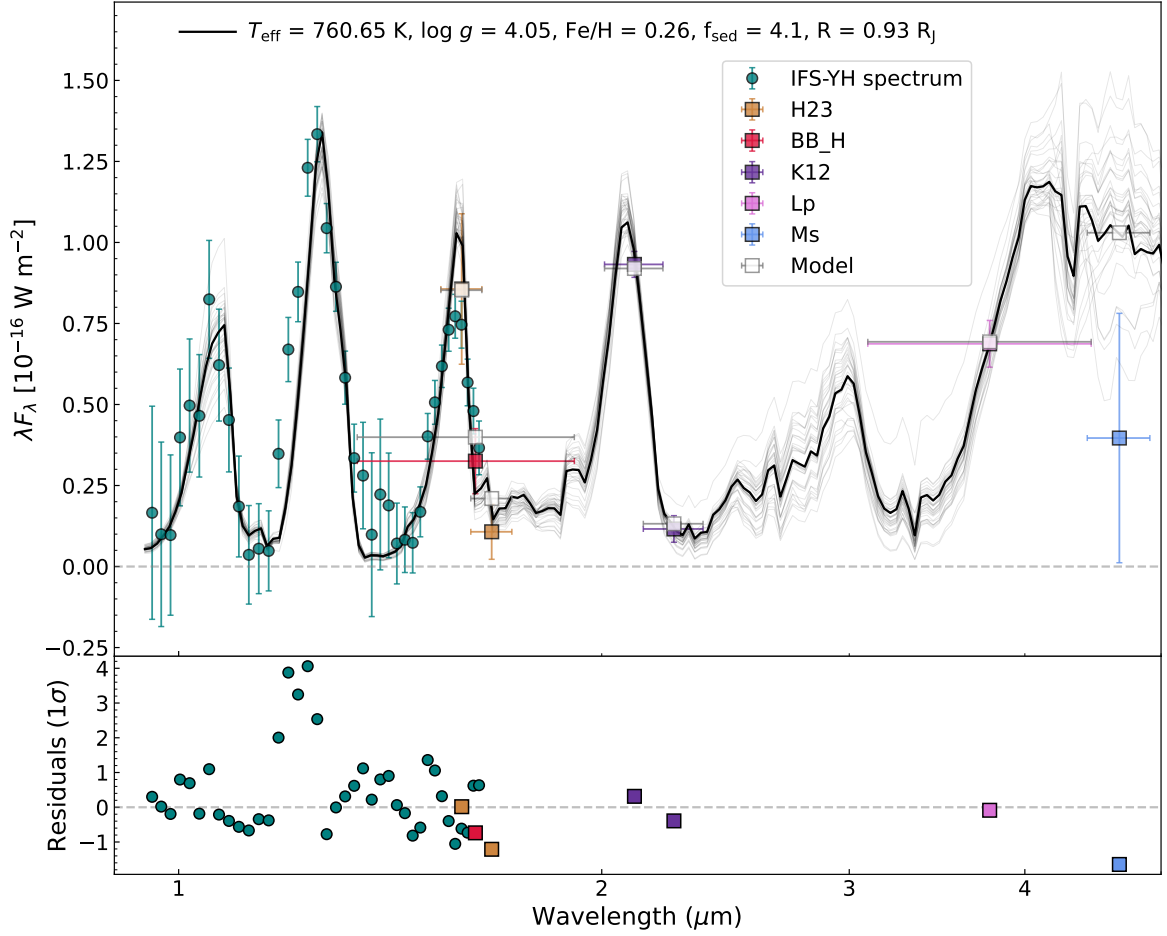


Figure 4.5: petitRADTRANS best-fit spectrum of 51 Eri b for the “nominal” retrieval run (shown in black) on our new SPHERE spectro-photometric data (teal circles and purple squares) along with the photometric points included in SAM17 and Rajan et al. (2017) (shown as squares). The photometric points describe the average flux in the respective filter, the x -error bar represents the filter widths. 34 randomly drawn samples from the posterior probability distribution are shown in gray, to show the spread of model parameter combinations to fit the data. Residuals in multiples of 1σ uncertainties of the data are shown below.

Table 4.4: Median and 1σ uncertainties of the posterior probability distributions from the petitRADTRANS retrievals, using our new data and the data in SAM17.

Run	New nominal	New enforced clouds	Old nominal	Old enforced clouds
[Fe/H]	0.26 ± 0.30	0.29 ± 0.26	-0.09 ± 0.20	0.03 ± 0.25
C/O	0.38 ± 0.09	0.43 ± 0.07	0.80 ± 0.18	0.74 ± 0.16
log g	4.05 ± 0.37	4.46 ± 0.38	4.53 ± 0.38	4.6 ± 0.4
log τ_{clouds}	-5.20 ± 1.44	-0.85 ± 0.16	-4.7 ± 1.7	-0.86 ± 0.17
f_{sed}	4.10 ± 3.62	0.25 ± 0.29	4.8 ± 3.5	0.32 ± 0.42
K_{zz}	8.19 ± 2.06	7.58 ± 0.93	9.4 ± 2.9	7.9 ± 1.5
Radius (R_{Jup})	0.93 ± 0.04	0.99 ± 0.09	1.17 ± 0.10	1.2 ± 0.1
T_{eff} (K)	807 ± 45	744 ± 31	691 ± 22	634 ± 30

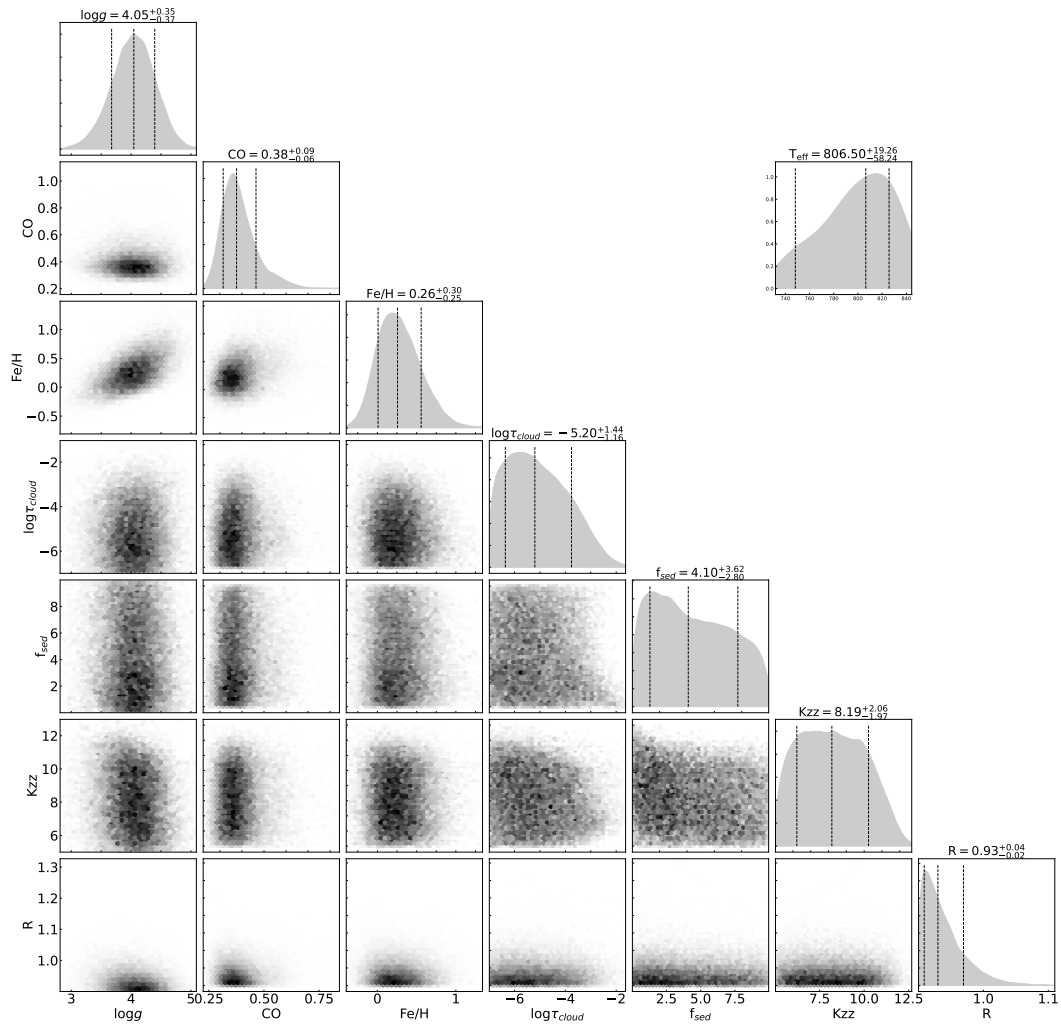


Figure 4.6: Corner plot of the posterior PDFs of the “nominal” retrieval run on the new data set.

Atmospheric retrieval on old data

When comparing our results to the ones derived in SAM17, it is important to understand in how far the difference stems from the use of a retrieval method as opposed to the self-consistent modelling applied in SAM17, and to what extent the different outcomes are a result of the better quality of the 2017 data.

We thus attempted to reproduce SAM17’s previous results using the retrieval approach with pRT . For this we included all the data cited in Samland et al. work, i.e. the YJ and the YH spectra, and the $H2H3$, $K1K2$, L_P , and broad-band H photometric points, all resulting from 2015 and 2016 observations, as well as the GPI spectrum published in the discovery paper (Macintosh et al. 2015). Similarly to the new data, we ran a “nominal” and a “enforced clouds” retrieval using the limits in the $\log\tau$ parameter as described in Section 4.3. When comparing the numbers for the “Old nominal” retrieval in Tab. 4.4 to the ones in SAM17’s Tab. 4.4 (top row, “PTC-C”), we notice that we find a significantly lower metallicity, and very little indication for the presence of clouds. Other parameters differ as well, but are mostly within the 16/84th percentile limits. We discuss this issue, and in particular our attempt to determine whether the object is cloudy or not, in depth in Section 4.6.2.

4.6 Discussion

4.6.1 Parameters of 51 Eri b

In the following we present a discussion of certain parameters of interest of 51 Eri b.

C/O ratio

The atmospheric carbon-to-oxygen ratio has been linked to the formation scenario of exoplanets (Öberg et al. 2011). The different condensation temperatures of water (H_2O), carbon oxide (CO) and carbon dioxide (CO_2) locate their “ice lines” in different parts of the protoplanetary disk, which results in different values of C/O through the disk. A difference in the C/O ratio of a gaseous giant planet compared to its host star’s C/O ratio can provide information about the planet’s formation, depending on whether their C/O ratio is super- or sub-stellar. See, however, Mollière et al. (2022) on how challenging it is to go from C/O to formation, in practice.

We find the C/O ratio of 51 Eri b to be consistent along retrieval runs for the same data set ($C/O \sim 0.4 \pm 0.08$ for the new data and $C/O \sim 0.8 \pm 0.17$ for the data in SAM17), respectively. Compared to the solar C/O ratio assumed by SAM17 (i.e. $C/O = 0.55$), all our retrieved values within error bars differ by ~ 0.1 . However, no definitive conclusions can be drawn since the value for the C/O ratio of the star remains undetermined. The lower flux from the M_S photometric point hints to the presence of carbon monoxide (CO), however, further observations would be needed to use it to constrain the C/O ratio of 51 Eri b.

[Fe/H]

In our retrievals using the data in SAM17 we obtain a metallicity [Fe/H] in the range of -0.09 to 0.30, including uncertainties, which differs from the results of SAM17 who find [Fe/H] = 1.0 ± 0.1 . However, when comparing with retrieval results for two benchmark brown dwarfs, the authors find that they tend to fall in the lower end of the estimated metallicity range for the host star. In our case, we observe a similar behaviour, even for the new data we obtain [Fe/H] ~ 0.26 which is slightly super-stellar (taking the metallicity of 51 Eri to be solar, i.e. [Fe/H] = 0.0). As discussed at length in SAM17, the derived metallicity strongly depends on the *K*-band flux, and indeed our retrieval tends to slightly underfit the *K1*-flux, whereas it was overfitted in SAM17. When artificially enhancing the importance of the *K1*-flux point by lowering its uncertainty by a factor 10, the resulting fit for SAM17's data shows an increased metallicity ([Fe/H] = $0.31^{+0.12}_{-0.13}$), and a higher $\log \tau_{\text{cloud}} = -4.2^{+1.28}_{-1.18}$. These values are closer to SAM17's, but still do not agree. The initial and the remaining difference indicate that parameters derived from retrievals can differ significantly from self-consistent models.

Clouds and $\log \tau_{\text{clouds}}$

Our initial retrievals always resulted in the best-fit models tending towards non-cloudy solutions. Based on previous results, which suggested 51 Eri b's atmosphere to be at least partially cloudy, we included an additional prior to enforce clouds and check the robustness of the retrieval: $\log \tau_{\text{clouds}}$. However, even for the "enforced clouds" retrievals, the value for $\log \tau_{\text{clouds}}$ always tended towards the lower limit of the prior (i.e. towards cloud-free solutions; see Table 4.4). Both f_{sed} and K_{zz} describe the cloud properties (Ackerman and Marley 2001). Our best-fit values for f_{sed} in the "enforced clouds" retrievals are in agreement with previously reported f_{sed} values for brown dwarfs in a similar temperature range as 51 Eri b (e.g., GJ 758 B, GJ 504 b; Vigan et al. 2016; Skemer et al. 2016, respectively). We also note that our values are within the ranges of f_{sed} found by SAM17. A higher f_{sed} corresponds to vertically thinner clouds with larger particle sizes. Our derived values for K_{zz} are within the assumed values in both Macintosh et al. (2015) and SAM17.

In Fig. 4.7 we show the *P-T* profiles resulting from the retrieval runs along with the 1-, 2- and 3 σ confidence intervals for our four different cases. Overplotted are the corresponding self-consistent *P-T* profiles obtained from petitCODE when feeding in the best-fit parameters of the retrievals. We note that the self-consistent *P-T* profiles are less isothermal than the retrieval ones in all cases, following the characteristic atmospheric temperature gradient for models in radiative-convective equilibrium. In this scenario, the only way to reproduce the observed NIR low fluxes is to add clouds, which contradicts our results with the retrieval models. This discrepancy has been observed in other studies (see Section 4.6.2 for an in-depth discussion), and it is yet to be resolved in order to draw conclusions about the cloudiness of exoplanet atmospheres.

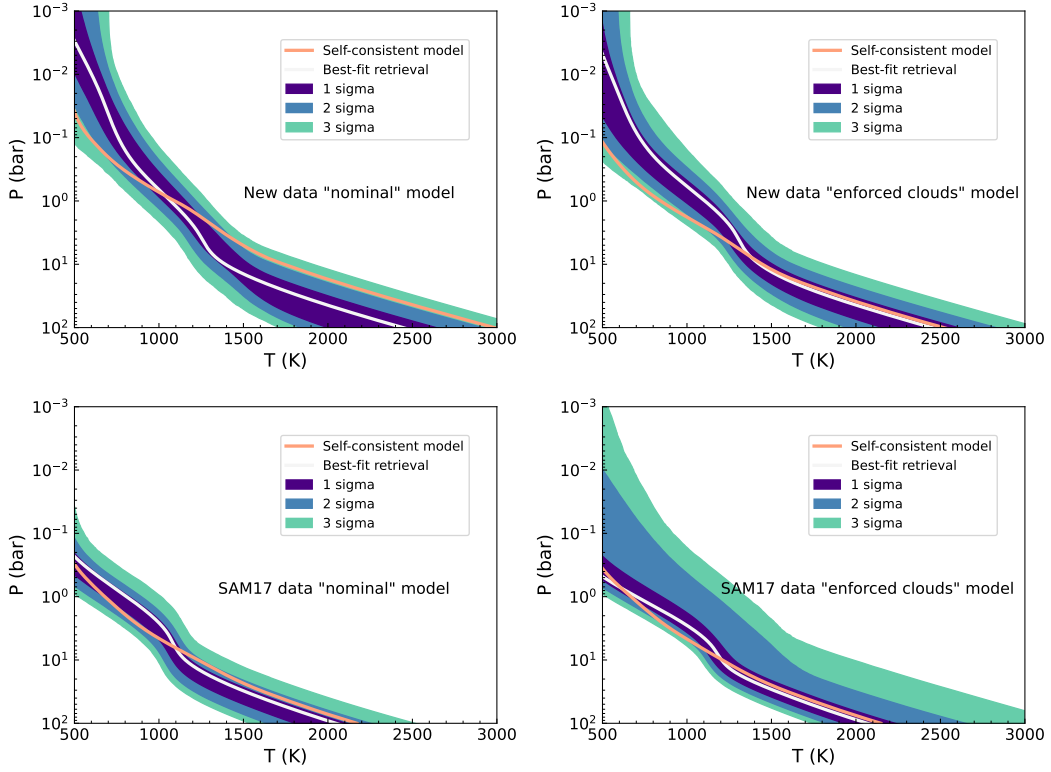


Figure 4.7: Retrieved pressure-temperature profiles in white, with confidence intervals (1-, 2- and 3σ) for our four different retrievals shown in Table 4.4. Overplotted are the resulting self-consistent P - T structures in pink.

Radius and surface gravity

The values we obtain for the radius and surface gravity are in agreement with previous results for the data in SAM17 within uncertainties. As seen in Fig. 4.6 and Fig. B.5, the retrieval finds the best-fitting models towards the lower R_p prior boundary for the new data, while this is not the case for the retrievals using the data in SAM17 (Fig. B.7 and Fig. B.9). We attribute these variations to the different input data. Nevertheless, all values are consistent with the radius of Jupiter within uncertainties, which according to planetary evolution models are slightly smaller than expected for the possible age of the system (i.e. 10 - 20 Myrs; Mordasini et al. 2012).

Mass

To derive an estimate of the mass of 51 Eri b we used the posterior distribution for the surface gravity and radius of our “nominal” model, and the relation $M = g/g_{\text{Jup}} \cdot (R/R_{\text{Jup}})^2$, where $g_{\text{Jup}} = 24.79 \text{ m s}^{-2}$, and $R_{\text{Jup}} = 6.99 \times 10^7 \text{ m}$ are the surface gravity and the volumetric mean radius of Jupiter, respectively. We obtain a mass of $M = 3.9 \pm 0.4 M_{\text{Jup}}$. Additionally, we used the photometric values for the K1K2 bands along with the evolutionary models for extrasolar giant planets from Baraffe et al. (2003). We used both estimates of the age of the system and we obtain a value of $M = 2.4 M_{\text{Jup}}$ at 10 Myr, and $M = 2.6 M_{\text{Jup}}$ at 20 Myr. All mass values of the planet are smaller than the value found by SAM17 ($M = 9.1^{+4.9}_{-3.3} M_{\text{Jup}}$),

however, the formation scenario can strongly impact the mass (and the surface gravity) of the planet, and small masses are possible within the “hot-” and “warm-start” scenarios.

On the other hand, taking the mass estimates from the evolutionary models above and calculating the radius using the relation $R \propto M^{0.01}$ for large planets from Bashi et al. (2017), we obtain: $R = 1.0R_{\text{Jup}}$ for both cases. This radius is in agreement with the one obtained from the retrieval within uncertainties, however, the small discrepancy may be due to the fact that the evolutionary models take into account the internal structure of the planet, while the retrieval estimates the radius only from atmospheric parameters.

4.6.2 Atmospheric retrievals vs self-consistent models

Atmospheric retrievals are now a commonly used tool for fitting the spectra of exoplanets (for a recent review, see Madhusudhan 2019). The general idea of retrievals is that an atmospheric forward model calculates planetary spectra based on a parameterized atmospheric structure, which is then compared to the data. This parametrization is key, because finding the atmospheric temperature, composition, and cloud structure in a physically self-consistent way is a numerically expensive step. Self-consistent models typically assume that the atmosphere is in radiative-convective equilibrium, and couple this assumption to a model solving for the atmosphere’s chemical composition and cloud structure in an iterative fashion (see e.g., Hubeny 2017, for a review). Furthermore, many processes, especially those connected to clouds, are not sufficiently well understood. If the underlying assumptions in the self-consistent model are wrong, this may lead to very wrong conclusions about the atmospheric model’s properties and parameters. However self-consistent models allow us to compare our complete physical understanding against what the data shows. Conversely, retrievals attempt to constrain the atmospheric structure mostly from the data alone (if uninformative priors are chosen), circumventing these issues. This requires data of high enough S/N and spectral coverage, however.

For cloudy directly imaged planets retrievals have proven challenging thus far. This is connected to a degeneracy, or at least a correlation: a cloud generally reddens the spectrum by hiding the deep hot regions of the atmosphere from view. If the cloud was not present, too much flux would escape from the atmosphere, especially in the opacity windows in the Y , J , and H bands. Moreover, an atmospheric model in radiative-convective equilibrium generally results in a large atmospheric temperature gradient, such that the only way to reproduce the red spectral energy distributions (SEDs) of cloudy planets and brown dwarfs is to add clouds. In Tremblin et al. (2015), Tremblin et al. (2016), Tremblin et al. (2017), and Tremblin et al. (2019) atmospheric instabilities that decrease the atmospheric temperature gradient when compared to the equilibrium solution have been suggested to mimic the effect of clouds in the NIR. This can be easily understood: if the deep atmosphere is less hot, no clouds are required to lead to a reduced flux in the YJH -bands. For retrievals with a flexible atmospheric temperature and cloud parameterization this may thus result in atmospheric structures that are cloud-free and too isothermal when compared to classical self-consistent models. Due to the ease with which red exoplanet spectra can be fit with too-isothermal temperature profiles, it is not surprising that a retrieval can fall into this “trap”: different

temperature structure realizations are explored during a retrieval, and if the cloud model is not the “perfect” one, and leads to a slightly worse fit, there is no reason for the retrieval to add a cloud of appreciable opacity to the atmosphere.

This cloud-free retrieval problem appears to be emerging in recent studies (Mollière et al. 2020; Zhang et al. 2021; Kammerer et al. 2021), and we also see it occurring here. Options to enforce a more cloudy solution may include making the atmospheric temperature parameterization less flexible, such that always a strong temperature gradient is present, which then needs to be corrected for by adding a cloud (which was identified as a workaround in Kammerer et al. 2021 when using the atmospheric retrieval code ATM0; Tremblin et al. (2015) and Tremblin et al. (2016)). The danger is that such simple temperature profiles may not be complex enough to capture the atmospheric temperature structure even for a cloud-free planet, leading to potentially biased results for the atmospheric properties. Enforcing a minimum cloudiness in the atmosphere via a cloud optical depth prior, as we attempted to do here, may be another option, but we remind the reader that the retrievals still attempted to be as cloud-free and isothermal as possibly allowed. An ideal solution to this problem is yet to be found.

It is conceivable that these atmospheres are truly mostly cloud-free, and that this is the reason for the retrievals to tend towards these solutions, as also argued for in the Tremblin et al. papers. However, even synthetic cloudy spectra are retrieved to be cloud-free if the cloud model is modified between the synthetic observation and retrieval step (Mollière et al. 2020), such that the absence of clouds in the retrievals cannot be regarded as a proof of the absence of clouds in the atmospheres of real planets. A promising avenue is presented in Burningham et al. (2021). The authors found that adding mid-IR data tracing silicate cloud absorption features at $10\ \mu\text{m}$ will lead to definitely cloudy solutions, as well as temperature structures which are less isothermal compared to the retrievals that neglected the mid-IR data (Burningham et al. 2017). The James Webb Space Telescope’s (JWST) observations of cloudy exoplanets and brown dwarfs with its mid-IR instrument MIRI (Wright et al. 2004), may thus hold great potential to resolve, at least partially, the cloud-temperature gradient degeneracy. A remaining challenge is that the $10\ \mu\text{m}$ region probes lower pressures than the NIR (*YJH* bands), thus probing the silicate feature could merely help to constrain the *P-T* profile in the upper atmosphere. Indeed, Burningham et al. (2021) need to include a second deep cloud to produce the NIR reddening. However, we note that the above could be a general solution for planets but could not be applied to 51 Eri b, since the planet is too cold to have silicate clouds, and too close to the host star to be observed with JWST. A possible solution for cool, closer-in giant planets like 51 Eri b, could be to use the Mid-Infrared ELT Imager and Spectrograph (METIS, Quanz et al. 2015). Finally, we advocate that results from atmospheric retrievals should never be discussed in isolation; we would recommend that a comparison to self-consistent temperature structures, obtained from using the retrieval’s best-fit parameters for the atmospheric composition, gravity, effective temperature, and cloud parameters, is used to infer the degree to which a retrieval is affected by the degeneracy.

4.7 Summary

In this Chapter we presented VLT/SPHERE spectro-photometric observations of 51 Eridani b. The new YH spectrum and $K1K2$ observations show improved S/N compared to previously reported data, allowing us to revise the published flux measurements. We used the radiative transfer code `petitRADTRANS`, which utilizes a retrieval approach to fit the atmospheric parameters. In addition, we attempted to reproduce previous results (obtained with self-consistent models) using this approach and compared the outcomes of retrievals to self-consistent models. Our results can be summarized as follows:

1. We extracted the spectrum of 51 Eri b using the ANDROMEDA algorithm (Fig. 4.2). We obtained new photometric measurements for the $K1K2$ filters ($K1 = 15.11 \pm 0.04$ mag, $K2 = 17.11 \pm 0.38$ mag; Table 4.2).
2. The detection limits derived from our data show an increased sensitivity and rule out the presence of planets more massive than $2 M_{\text{Jup}}$ at 3 au, and $1 M_{\text{Jup}}$ beyond 4.5 au (Fig. 4.4).
3. Our initial retrieval runs tended towards clear atmospheres, to verify the robustness of these results we introduced an additional fit parameter ($\log \tau_{\text{clouds}}$) to enforce clouds. We report the results of four different cases in Table 4.4: a “nominal” and an “enforced clouds” version for our new data + the photometry in SAM17 + Rajan et al., 2017’s M_S ; and for the same data used in SAM17.
4. We are able to obtain a good fit to the observations with pRT (e.g. Fig. 4.5), with the exception of the M_S photometric point, which can be explained by the large uncertainty of the data. Further mid-IR observations in this band could improve the fit and help constrain the C/O ratio of the planet. We observe, that even the “enforced clouds” retrieval runs tend towards non-cloudiness ($\log \tau_{\text{clouds}} = -5.20 \pm 1.44$), which differs from previous results obtained using self-consistent models. This discrepancy may be due to the larger and more flexible parameter space that can be explored with retrievals as opposed to self-consistent models. In particular, the isothermal P - T profiles may imitate the effect of clouds.
5. Overall, our results ($C/O = 0.38 \pm 0.09$, $[Fe/H] = 0.26 \pm 0.30$ dex, $T_{\text{eff}} = 807 \pm 45$ K and $\log g = 4.05 \pm 0.37$) are in agreement with the reported parameters of the planet. One of the major disagreements is the metallicity, which we find to be close to stellar with the new data. Once more, this can be explained by the different methods that atmospheric retrievals and self-consistent models use to fit the data. We estimate the mass of the planet to be between 2 and $4 M_{\text{Jup}}$, which is consistent with both “hot-” and “warm-start” formation scenarios.
6. As an additional test, we used the best-fit parameters from the retrievals to obtain the pressure-temperature structure using a self-consistent model (Fig. 4.7). The results show a larger temperature gradient for the self-consistent models, suggestive of the T -gradient-cloud correlation playing a role.

The results in this Chapter highlight the challenges that are still to overcome when modelling exoplanet atmospheres, as well as the importance of observations at longer wavelengths to determine the presence or absence of clouds. Observations with future instruments that allow the study of additional cloud absorption features such as ELT/METIS, would be required to provide a final conclusion on the cloud-temperature gradient degeneracy.

Chapter 5

Debris disks with SPHERE

The contents of this chapter are based on the first part of Brown-Sevilla et al. [in prep](#). For this work I have been under the supervision of Thomas Henning, Markus Feldt, and Wolfgang Brandner, and I have collaborated with Johan Olofsson, Cecilia Lazzoni, and Anne-Lise Maire.

5.1 Motivation

As mentioned in Sections [1.2](#) and [1.4.4](#), the dust in circumstellar disks is short-lived, therefore, the fact that debris disks can be observed is considered as evidence of planetesimals or planets stirring the disk to replenish the dust that can be detected. For Solar System analogs with two debris belts, the gap between them is assumed to be mainly dust-free. A popular hypothesis to explain their architecture is the existence of one or more planets orbiting within the belts (e.g., Kennedy and Wyatt [2014](#); Matrà et al. [2020](#)), which can be tested in different ways, such as with the use of dynamical models.

This Chapter presents the first part of a study of debris disks observed with SPHERE. This stage is focused on resolved targets that from SED modelling are best reproduced by two different temperatures with luminosity ratios ~ 1 , which are used as indicators of these disks having a double belt structure. The position of the belts is determined from SED modelling and masses of possible planets orbiting in the gaps is estimated from the Hill sphere definition. These values are compared with detection limits derived from the SPHERE data, to determine the observability of these planets for existent observations.

Section [5.2](#) describes the target selection for this study. Section [5.3](#) details the procedure to characterise the gaps in the disks, while Section [5.3.1](#) presents the estimation of the masses and locations of possible planets within the belts. Section [5.4](#) describes the SPHERE observations and data handling. Section [5.5](#) discusses the results of this first part of the study, and the future plans to continue this work are presented in Section [5.5.1](#). Lastly, the key findings are summarised in Section [5.6](#).

5.2 Sample selection

In order to have a comprehensive sample, we looked for extensive catalogs of stars with IR excess. In particular, we focused on the catalogs of Chen et al. ([2014](#)) and Cotten and Song

(2016). Chen et al. 2014 analysed the spectra of 571 stars with ages between 5 Myr and a few Gyr, and spectral types B through K with excesses in the infrared from $5.5 - 35\mu\text{m}$ observed with *Spitzer*, when available they also included $70\mu\text{m}$ observations (for 473 of the stars in their sample). They modelled the Infrared Spectrograph (IRS) and Multiband Imaging Photometer for *Spitzer* (MIPS) $70\mu\text{m}$ excess SEDs using zero, one, and two blackbodies to obtain dust temperatures. On the other hand, Cotten and Song (2016) presented a collection of stars with IR excess from two sources: a literature search for previously claimed IR excess stars, and Tycho-2 cross-correlation with the AllWISE catalog. Their total sample comprises more than 1700 stars with spectral types B through M that they divide into “Prime” (~ 500), for bright, nearby (~ 150 pc), confirmed IR excess stars, and “Reserved” (~ 1200), for distant, faint, and marginal excess candidates.

We crossed-checked the catalogs with the stars that have been observed with SPHERE (Beuzit et al. 2019) both during Guaranteed Time Observations (GTO) and in Open Time (OP), which led to a first sample of 172 stars. To further refine our selection, we modelled the spectral energy distribution (SED) of the stars as described below.

5.2.1 SED Modelling

To construct the SED of the targets we looked for photometric data in the following catalogs: Gaia EDR3 (Gaia Collaboration et al. 2020), Chen et al. 2014, AllWISE (Wright et al. 2010), 2MASS (Skrutskie et al. 2006), Tycho-2 (Høg et al. 2000), and *Herschel*/PACS 70, 100 and $160\mu\text{m}$ (*Herschel* Point Source Catalogue Working Group et al. 2020). Next, to determine whether a star has an IR excess, we used the Virtual Observatory SED Analyser (VOSA) tool (Bayo et al. 2008) which automatically calculates the slope between every IR adjacent points and flags the points for which the slope is smaller than a threshold as having IR excess. Here we noted that only 135 of the 172 stars have sufficient far-IR excess photometry, therefore we proceeded only with these targets.

To determine the stellar model, all the points without IR excess flag are used. We fitted the BT-Settl models (Allard 2014) to the data leaving only the temperature (T_{eff}) as a free parameter and fixing the surface gravity ($\log g$) to 4. To find the best fit solutions, we used PyMultiNest¹ (Buchner 2014). Then we multiplied the resulting stellar models by a flux scaling factor ($\alpha \propto (R_*/d_*)^2$) to account for the distance of the stars in order to match the photometry. Since the photometric profiles have different shapes, we performed “synthetic photometry” using the Filter Profile Service² (Rodrigo and Solano 2020) to compute the predicted photometry for each filter correctly. Then, to fit the IR excess we used one or two Planck functions as needed for the aforementioned points flagged with excess. Finally, we interpolated the stellar model at the corresponding wavelengths such that the total photometry is equal to the stellar model + the Planck function. The luminosities can be computed from the Planck function and the stellar model, and their ratio gives the IR luminosity of the disk.

¹<https://johannesbuchner.github.io/PyMultiNest/>

²<http://svo2.cab.inta-csic.es/theory/fps/>

Table 5.1: Stellar parameters for our targets.

Name	T_{eff} (K)	L_* (L_{\odot})	ref.	d (pc)	M_* (M_{\odot})	Age (Myr)	H (mag)
HD 61005	5600	0.68 ± 0.07	1	36.41 ± 0.02	0.98	50^{+20}_{-10}	6.57 ± 0.04
HD 131835	8100	10.41 ± 2.21	1	130.28 ± 0.72	1.7	16^{+2}_{-6}	7.56 ± 0.03
HD 192425	8540	18 ± 0.56	2	48.51 ± 0.31	2.2	${}^a 413^{+94}_{-56}$	4.80 ± 0.03
HD 95086	7600	6.74 ± 1.46	1	86.25 ± 0.35	1.6	16^{+6}_{-6}	6.86 ± 0.04
HD 10939	9030	25.75 ± 0.78	2	62.09 ± 2.05	2.79	${}^b 346$	5.02 ± 0.02
HD 32297	7700	8.12 ± 1.68	1	132.41 ± 0.84	1.6	${}^c 100^{+300}_{-70}$	7.62 ± 0.05
HD 136246	8510	21.71 ± 2.78	2	115.85 ± 0.46	1.9	17^{+83}_{-11}	7.03 ± 0.06
HD 15115	6900	3.55 ± 0.71	1	48.87 ± 0.27	1.4	45^{+5}_{-10}	*5.86
HD 9672	8900	16.4	4	58.25 ± 0.21	1.9	50^{+20}_{-10}	5.52 ± 0.02
HD 16743	7000	5.50 ± 0.36	1	57.59 ± 0.28	1.5	${}^c 50^{+20}_{-10}$	5.97 ± 0.02

Note: The references in the fourth column are for the effective temperature (T_{eff}) and the luminosity (L_*). 1. Esposito et al. (2020), 2. Morales et al. (2016), 3. Su et al. (2020), 4. Moór et al. (2015). Distances are from Gaia Collaboration et al. (2022). Masses are from Kervella et al. (2021). Ages are from Desidera et al. (2015) and Vigan et al. (2017), except for a (David and Hillenbrand 2015), b (Nielsen et al. 2013), and c (Pearce et al. 2022). The apparent H magnitudes are from 2MASS (Skrutskie et al. 2006), except for HD 15115 (Kalas et al. 2007, marked by *).

To find a bona fide sample of double belt debris disks, we looked at the disk dust temperatures $T_{\text{BB}i}$, and the fractional luminosities f_i , where the sub-index $i = 1,2$ refers to each Planck function. We first selected all the disks for which two Planck functions were needed to model the SED, which reduced our sample to 67 targets. Then we look at the temperature difference ($\Delta T = T_{\text{BB}2} - T_{\text{BB}1}$) as a function of the luminosity ratio (L_2/L_1). A positive ΔT implies that the secondary belt (i.e. not the one accounting for most of the IR excess) is located farther away from the primary belt (given its lower temperature). Since we have only considered photometry up to $160 \mu\text{m}$ in the best case (and the distance from the star scales with the wavelength) these results are not reliable, so we discard these targets as authentic double belt disks. Due to the precision of the available photometric observations, we only keep the targets with a luminosity ~ 1 . This leads to the following criteria to include a target in our sample: systems with $\Delta T < 0$ and $L_1/L_2 \sim 1$. In addition, we discarded the targets that have not been claimed in the literature as resolved. This led to a sample of 10 young (≤ 500 Myr), nearby ($d < 150$ pc) stars with a wide range of spectral types. The SEDs of these targets are shown in Fig. 5.1, where the photometry is shown as red circles, the spectra of the stars is depicted in green, and the contribution of the main and secondary belts in yellow and blue, respectively.

The stellar properties of these systems are listed in Table 5.1. Most of the parameters were taken from the literature as indicated on the table. We adopted Gaia DR3 distances and respective uncertainties (Gaia Collaboration et al. 2016; Gaia Collaboration et al. 2022). We based the determination of the ages on Desidera et al. (2015) as well as the results from Vigan et al. (2017) for certain moving groups. The H -band magnitudes are from 2MASS, unless otherwise indicated.

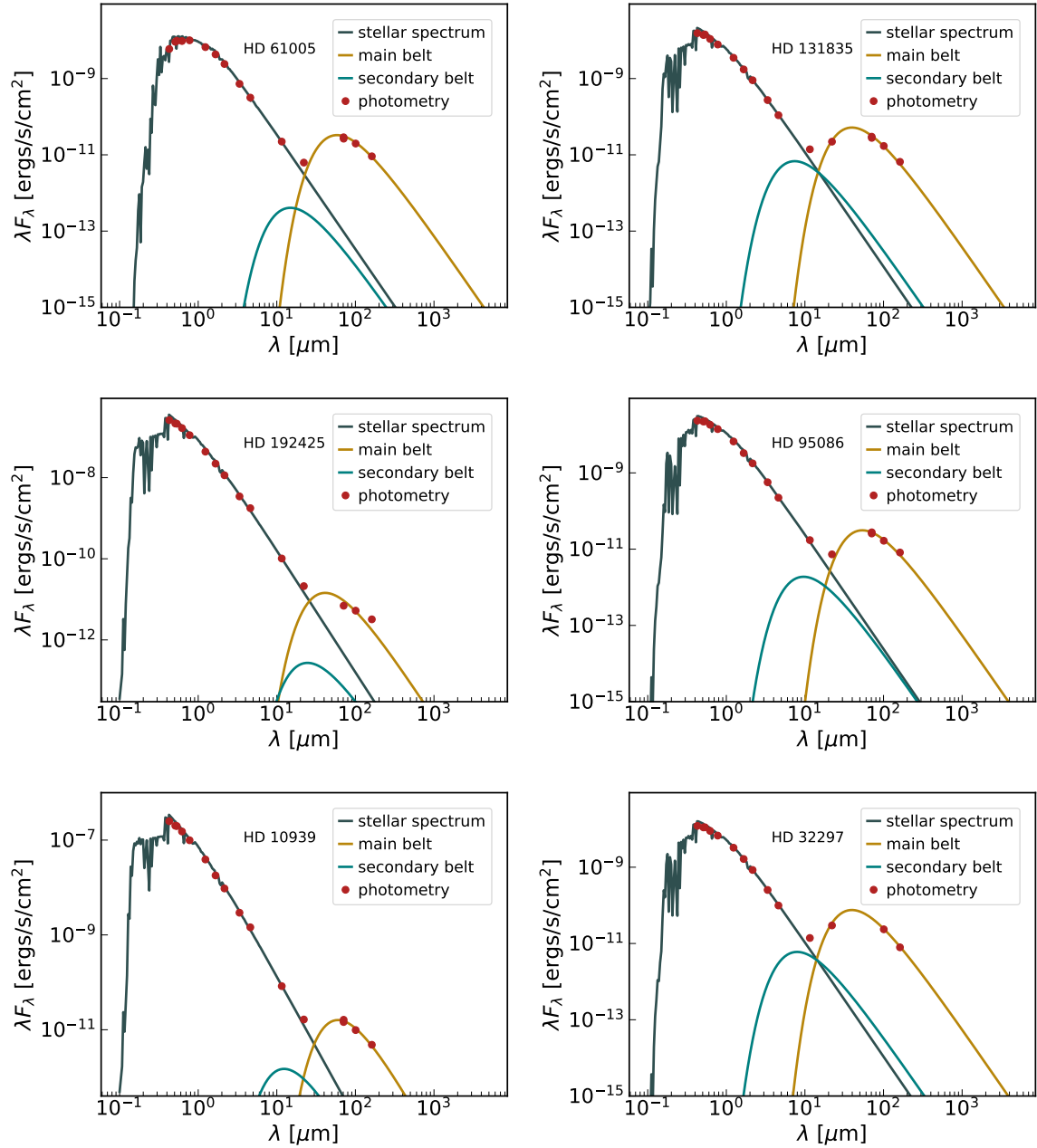


Figure 5.1: Spectral energy distributions (SEDs) for the selected targets in our sample. The photometry from Gaia EDR3, Chen et al. (2014), AllWISE, 2MASS, Tycho-2, and *Herschel* is plotted as red circles. The stellar spectrum is shown in green, while the contributions from the main and secondary belts are shown in yellow and blue, respectively. (*cont.*)

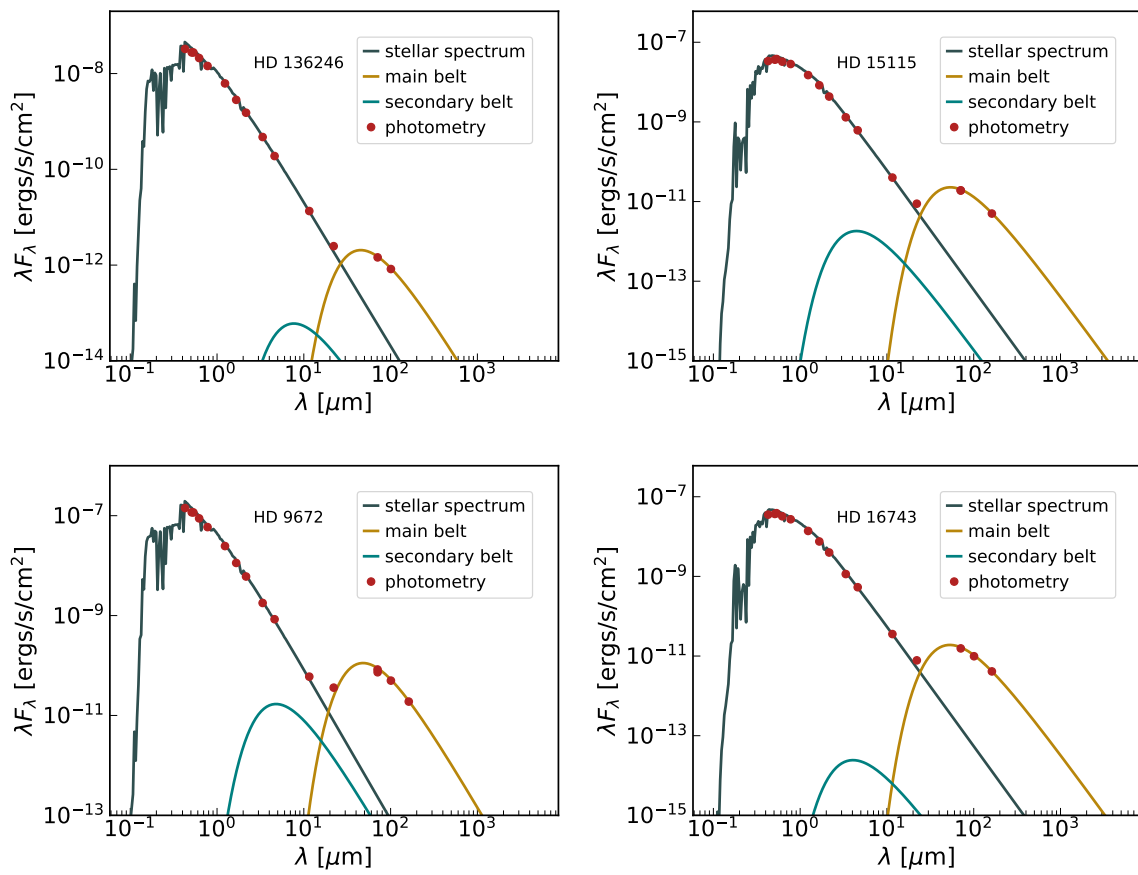


Figure 5.1: (continued)

Table 5.2: Debris disks parameters for the systems in our sample.

Name	$T_{BB,1}$ K	$R_{T,1}$ (au)	$T_{BB,2}$ K	$R_{T,2}$ (au)
HD 61005	246.54	0.90 ± 0.09	62.94	13.96 ± 1.47
HD 131835	495.63	0.88 ± 0.09	92.72	25.17 ± 2.65
HD 192425	149.33	12.76 ± 1.34	89.04	35.89 ± 3.78
HD 95086	382.0	1.19 ± 0.12	68.40	37.21 ± 3.92
HD 10939	296.75	3.86 ± 0.40	61.28	90.63 ± 9.56
HD 32297	461.45	0.89 ± 0.09	92.78	22.20 ± 2.34
HD 136246	478.75	1.36 ± 0.14	81.0	47.63 ± 5.02
HD 15115	822.66	0.18 ± 0.01	68.25	27.13 ± 2.86
HD 9672	767.1	0.46 ± 0.04	76.3	46.65 ± 4.92
HD 16743	903.65	0.19 ± 0.02	69.22	32.82 ± 3.46

T_{BB} is the blackbody temperature from the SED modelling, R_T is the radius of the belt, and the subindices 1,2 represent the main and secondary belt, respectively.

5.3 Characterization of gaps in the disks

In order to determine the radii of the two belts for each target in our sample, we used the radiation equilibrium equation between incoming and outgoing radiation:

$$L_* \Omega (1 - A_b) = L_b, \quad (5.1)$$

where L_* is the luminosity of the star, Ω is the solid angle, A_b is the belt's albedo, and L_b is the luminosity of the belt. After simplifying and solving for the radius of the belt (R_b) we obtain:

$$R_b = \frac{R_*}{2} \left(\frac{T_*}{T_{BB}} \right)^2 (1 - A_b)^{1/2}, \quad (5.2)$$

where R_* is the radius of the star, and T_* and T_{BB} are the effective and blackbody temperatures of the star and belt, respectively. In this case, the albedo takes into account that the dust grains do not behave like perfect blackbodies. Typical values for dust grains albedos are between 0.1 – 0.4 derived from observations (e.g. Kalas et al. 2005; Golimowski et al. 2011; Mulders et al. 2013), we therefore adopted 0.25 ± 0.15 to compute the average radii of the belts and estimate the uncertainties due to the unknown actual grain size. The blackbody temperatures used, as well as the resulting radii are presented in Table 5.2.

5.3.1 Population of planets within the belts

The best tools to constrain the properties of planets that produce a given structure in a disk are numerical simulations. However, they are highly time consuming when dealing with larger samples. For this reason, we chose to use scaling relations between the gaps and the mass of the planets. These relations have been empirically determined and widely used

Table 5.3: Calculated parameters of the possible planets in the disks in our sample.

Name	M_p (M_{Jup})	R_p (au)
HD 61005	2.08 ± 0.94	7.43 ± 0.73
HD 131835	4.33 ± 1.94	13.02 ± 1.32
HD 192425	0.74 ± 0.42	24.32 ± 2.01
HD 95086	4.14 ± 1.86	19.20 ± 1.96
HD 10939	6.78 ± 3.05	47.25 ± 4.78
HD 32297	3.94 ± 1.77	11.55 ± 1.17
HD 136246	5.02 ± 2.25	24.49 ± 2.51
HD 15115	4.22 ± 1.89	13.65 ± 1.43
HD 9672	5.62 ± 2.52	23.55 ± 2.46
HD 16743	4.55 ± 2.03	16.51 ± 1.73

M_p and R_p are the estimated masses and orbital separations of the planets within the gaps.

in previous studies (e.g., Lodato et al. 2019; Asensio-Torres et al. 2021). As a first approximation, we used that the gap width (ΔR), defined as the distance between the minimum emission in the gap and the belt peak, scales with the planet Hill radius:

$$\Delta R = R_{\text{peak}} - R_{\text{gap}} = kR_{\text{Hill}}, \quad (5.3)$$

where the Hill radius, which establishes the region within which the gravity of the planet dominates that of its host star, is given by $R_{\text{Hill}} = a_p(M_p/3M_*)^{1/3}$, with a_p the orbital separation of the planet, M_p and M_* , the masses of the planet and the star, respectively; and k is the number of Hill radii cleared at either sides of the orbit of the planet. In the literature k spans a range from ~ 3 to 20 (e.g., Dong and Fung 2017; Fang and Margot 2013) depending on different assumptions on the disk parameters, such as the viscosity parameter α , the individual gap morphology, or even the number of planets within the gap and their eccentricities. Given the complexity of choosing an appropriate value for k , we decided to adopt $k = 10$ as an initial guess for the part of the study presented here. We are also considering the presence of a single planet orbiting in a circular orbit within the gap for simplicity, although there is the possibility that multiple planets open a common gap (e.g., Zhu et al. 2011) or that a migrating planet opens a wider gap (Friebe et al. 2022). The scenario of multiple planets being present within the gaps will be considered in the further part of this study. The results of our calculations for the masses and locations of the planets are shown in Table 5.3.

Our estimated masses and locations for the planets are shown in Fig. 5.2. To compare our results in the context of the current detected exoplanets, we included all confirmed planets so far detected via transits, radial velocity and imaging. Indeed, the parameter space occupied by our proposed planets lies in the region dominated by the imaging discoveries. In the following section we compared our estimations with the detection limits from SPHERE observations.

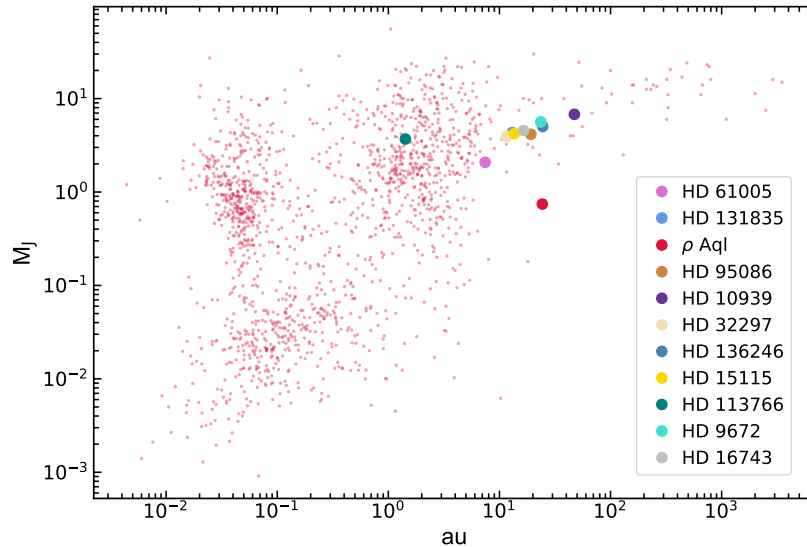


Figure 5.2: Population of potential planets within the gaps of the two belts for the stars in our sample. The mass values are estimated using a proportionality factor of $10R_{\text{Hill}}$ (see Eq. 5.3). The small red circles represent the distributions of confirmed planets via, transits, radial velocity and imaging in the <http://exoplanet.eu/> catalogue.

5.4 SHPERE observations

Most of the stars in our sample were observed in IRDIFS mode with IFS in the YJ mode and IRDIS in dual-band imaging mode (DBI; Vigan et al. 2010) using the $H2H3$ filters, with the exception of the targets HD 61005; which was observed in the IRDIFS_EXT mode, with IFS in the YH and IRDIS in the $K1K2$ filters; and HD 32297, which was observed with IFS in YJ and IRDIS in broad-band H . To scale the flux and center of the images, the usual unsaturated non-coronagraphic images (point spread function or PSF), as well as coronagraphic images with the deformable mirror (DM) waffle mode (Langlois et al. 2013) were acquired at the beginning and at the end of each observing sequence, along with the customary calibration frames for each night. Our sample includes both GTO and OT observations. The log of observations is presented in Table 5.4.

5.4.1 Data reduction

The data were reduced with the SPHERE Data Center pipeline (Delorme et al. 2017), using the SPHERE Data Reduction Handling (DRH) software (version 15.0; Pavlov et al. 2008). The basic reduction consists in performing sky background subtraction, flat fielding, bad-pixel identification and interpolation, star centering corrections and, for IFS, the calibration of the wavelengths and of the cross-talk between spectral channels. In addition, we used dedicated procedures for IFS (Mesa et al. 2015) and the Specal data reduction software (Galicher et al. 2018). For the post-processing, the high-contrast algorithms principal component analysis (PCA), TLOCI (Marois et al. 2014) and Classical ADI (CADI) were used. The observations and data analysis procedures are detailed in Langlois et al. (2021).

Table 5.4: Log of observations of the sample.

Name	Date (UT)	Mode	Filter	t_{exp} (s)	Sky rot. (deg)
HD 61005	2015-03-30	IRDIFS_EXT	K12/YH	64	40.8
HD 131835	2015-05-14	IRDIFS	H23/YJ	64	72.6
HD 192425	2016-06-11	IRDIFS	H23/YJ	64	32.9
HD 95086	2016-04-16	IRDIFS	H23/YJ	64	28.1
HD 10939	2016-09-15	IRDIFS	H23/YJ	64	24.5
HD 32297	2016-12-19	IRDIS/IFS	BB H/YJ	64	25.4
HD 136246	2016-04-03	IRDIFS	H23/YJ	4	26.5
HD 15115	2015-10-26	IRDIFS	H23/YJ	64	29.6
HD 9672	2016-07-24	IRDIFS	H23/YJ	32/64*	23.1
HD 16743	2016-09-21	IRDIFS	H23/YJ	64	35.4

t_{exp} is the exposure time and the sky rotation refers to the parallactic angle of each observation. * for IRDIS and IFS, respectively.

5.4.2 Detection limits

The contrast for each target was obtained following the procedure described in detail in Zurlo et al. (2014) and Mesa et al. (2015). In short, the contrast is defined by the ratio between the flux in coronagraphic and PSF frames, accounting for the integration time and the transmission of the neutral density (ND) filter used in each observation. The resulting 1D contrast limits for our sample are shown in Fig. 5.3 for the IRDIS and IFS observations. The projected separation in au on the top axis was calculated by using the average distance of the targets in our sample ($d \sim 80$ pc). The differences in sensitivity of each observation can be attributed to disk residuals after the post-processing of the data, as well as the weather conditions, sky rotation, variations in the Strehl ratio τ , and magnitudes of the host stars.

To convert the contrast into mass detection limits, we used the AMES-COND evolutionary tracks from Baraffe et al. (2003) along with the atmospheres model of Baraffe et al. (2015). We used the *JHK* 2MASS magnitudes (Cutri et al. 2003) for the stars, and the age estimates in Table 5.1. The mass detection limits for each target are shown in Fig. 5.4 with the possible planets overplotted in green for comparison. In most of the cases, a detection of these planets is still below the current limits. The cases of HD 95086 and HD 16743 are in the marginal zone for detection with their error bars, however, no detection is found in either data set.

5.5 Discussion

The detection limits derived in the previous section are in agreement with the non-detection of Jupiter-mass planets in the gaps between the belts. With the current limits, two systems (HD 95086 and HD 16743) are close to a detection of planets of $\sim 4 M_{\text{Jup}}$. From the stars in our sample, only HD 95086 has been found to host a $4 - 5 M_{\text{Jup}}$ planet at a separation of 52 ± 13 au (Rameau et al. 2013), which has also been imaged with SPHERE (Desgrange et al. 2022). Pearce et al. (2022) have recently found evidence for giant planets ($\gtrsim 1 M_{\text{Jup}}$) interacting

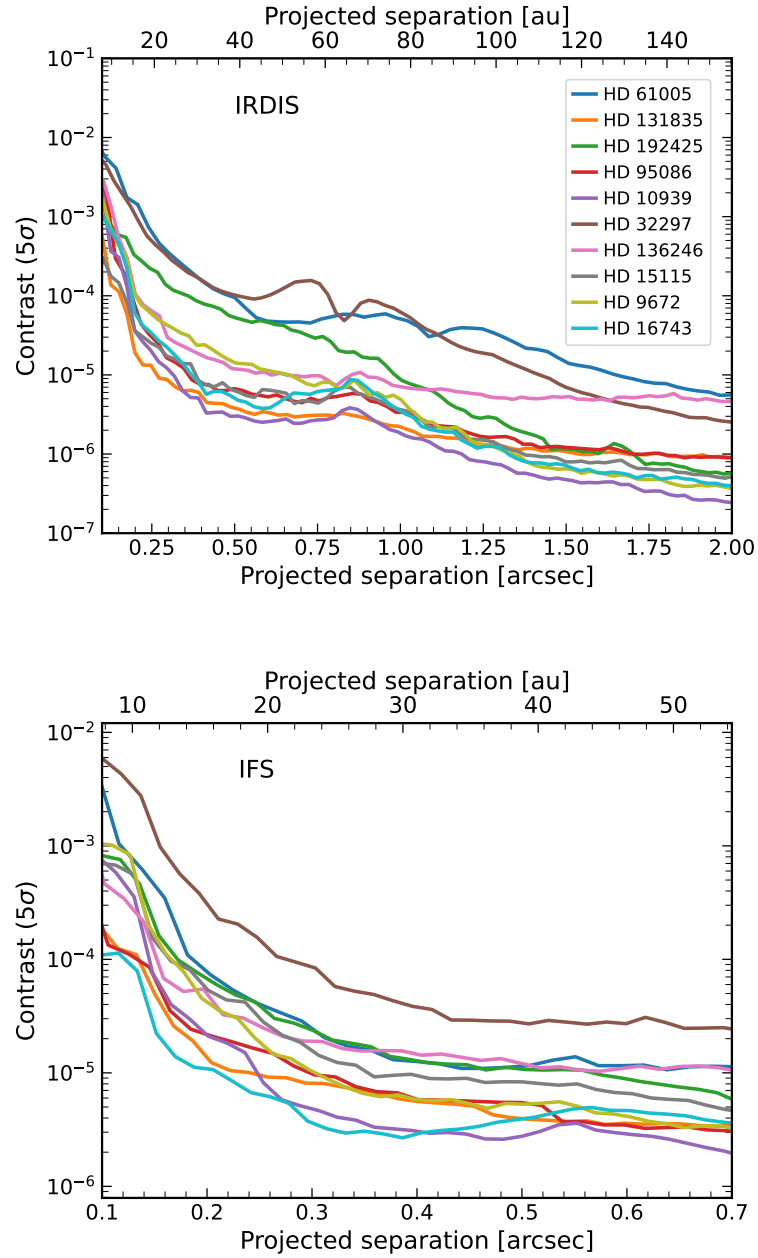


Figure 5.3: 5σ contrast limits from the SPHERE data of our targets. *Top:* for the IRDIS data in $K1$, $BB\ H$, or $H2$ filters, according to the observing mode in Table 5.4. *Bottom:* corresponding contrasts for the IFS data in the inner regions. To convert the semi-major axis to au, we adopted a median distance of the stars within our sample of ~ 80 pc.

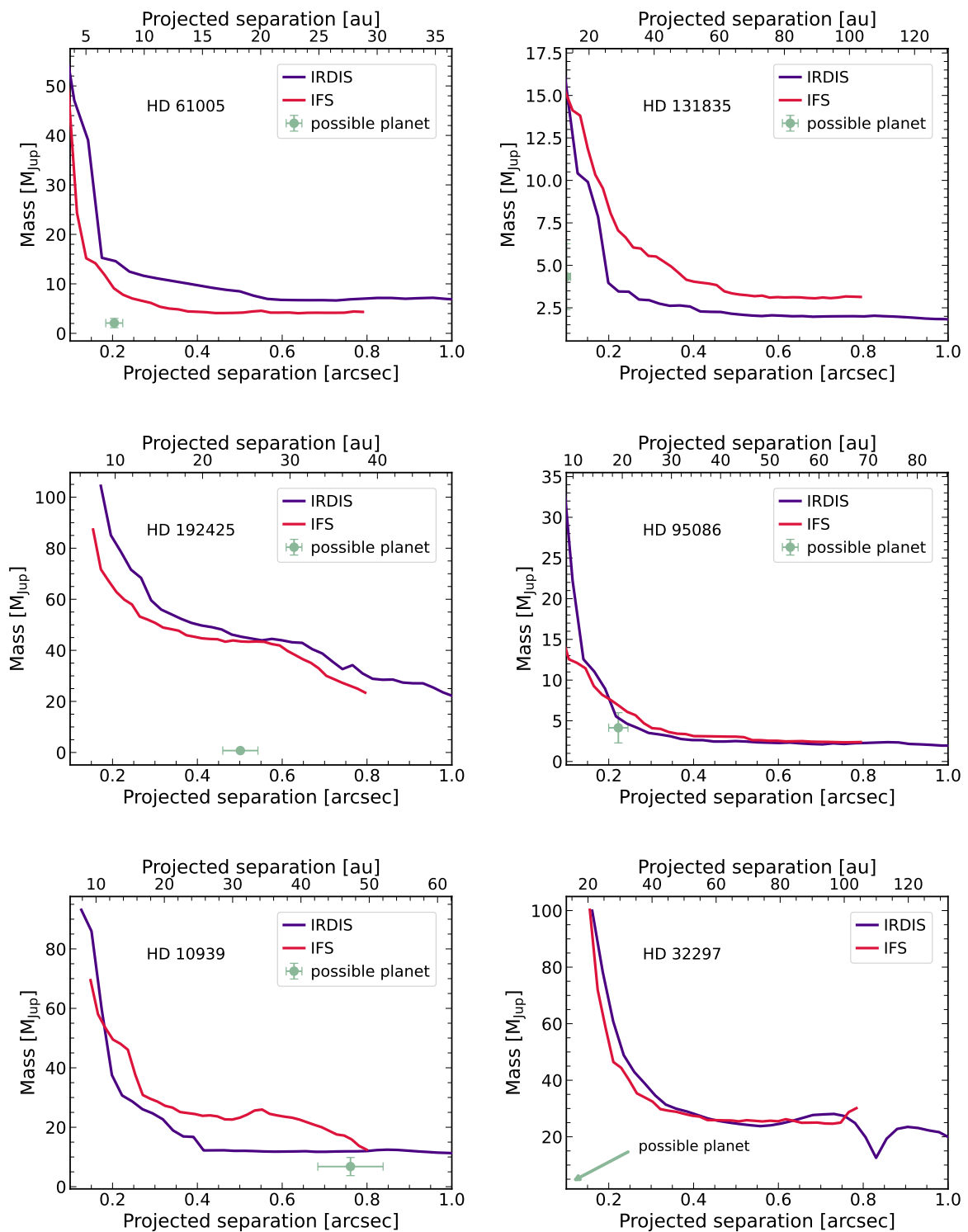


Figure 5.4: Mass detection limits from the SPHERE IRDIS and IFS data of our targets. The possible planets are shown in green circles, and in the case of HD 32297 with an arrow.

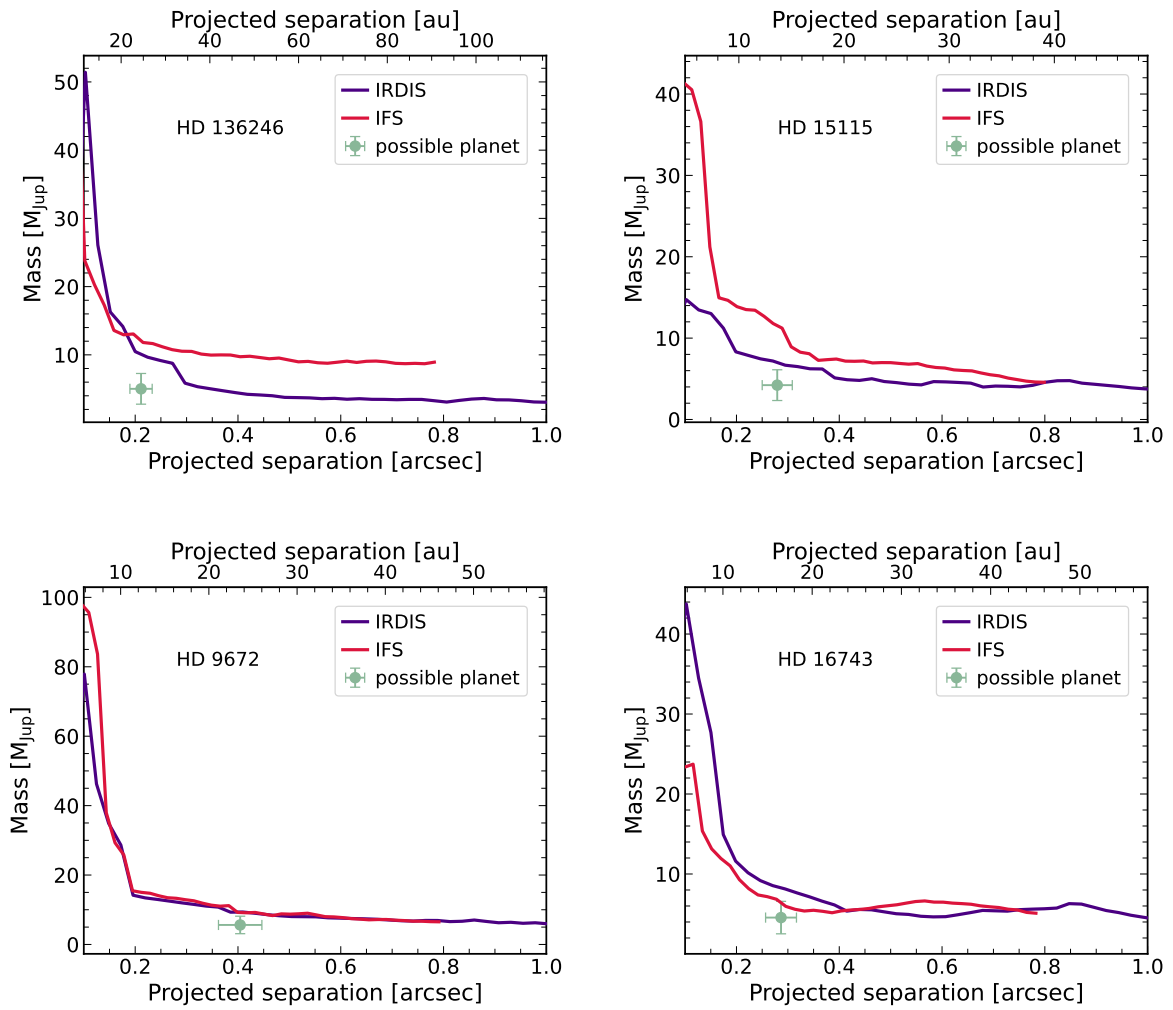


Figure 5.4: (continued)

with HD 9672, however, they do not report a detection. These could be interesting targets to image with the higher sensitivity JWST/NIRCam (e.g., Girard et al. 2022).

It should also be noted that in the process of deriving the parameters for our proposed planets, many assumptions have been made. Starting with the SED modelling which we have performed in a homogeneous fashion without taking into account individual stellar parameters. As previously mentioned, we have also assumed the simplest model of a single planet orbiting within the belts in a circular orbit for each system. Further, we have not taken into account different formation scenarios for these planets. All of these, along with the constraints from the observing conditions and data reduction effects, can contribute to the non-detection results.

However, we note that this has been a first approach to treat a sample of debris disks with a homogeneous indication of double belt architecture from SED modelling, and we will apply the lessons learned to the second part of this study.

5.5.1 Future work

The plans to continue this work include comparing our current estimates for the position of the belts with measurements from resolved observations (when available). We will use this to evaluate the robustness of our SED fits. In the case of large discrepancies, we will include the positions of the belts from the literature in our SED models to determine the effective temperatures from them and redo our calculations for the masses of the planets. Next, we will expand our sample by including two more categories from our original compilation of targets: single belt, and possible double (or multiple) belt disks. For this second part of the study we want to make use of Gaia DR3 and the Hipparcos catalog to measure proper motion anomalies in our targets in order to look for companions. For the stars with multiple belt indication we will repeat the analysis presented here. And compare our results with the detection limits derived from the SPHERE observations, as well as analyse them in the context of the current detected exoplanets.

5.6 Summary

In the first part of this work we focused on the target selection by looking into two large catalogues (Chen et al. 2014; Cotten and Song 2016) and comparing with observations made with SPHERE. We modelled the SED for each star with available IR data and established a criteria to select the targets with a double belt structure from their IR excess. We refined our sample by selecting only the targets that have been resolved in the literature, which will be useful for the next steps of our work. We estimated the radii of the belts and the masses of the possible planets within the gaps. These results were compared with the detection limits from the SPHERE data as well as with the current population of confirmed exoplanets. A second part of this work will include expanding the sample and a more detail investigation of the presence of planets in the disks.

Chapter 6

Conclusions and Outlook

In this thesis, we provided a wide overview on the formation and evolution of planetary systems –from the early stages of formation in protoplanetary disks, through formed planets that can be directly observed, to the late stages of debris disks systems– focusing mainly on the high-contrast imaging technique, combined with the use of other methods such as observations in the mm continuum, hydrodynamical simulations and radiative transfer, as well as atmospheric retrievals and self-consistent models.

High-contrast imaging is a powerful technique to detect and characterise a unique part of the parameter space of exoplanets, allowing to shed light on our understanding of the formation and evolution of giant planets. One of the advantages of detecting the light coming directly from the planets is that it allows to probe deeper into their atmospheres, which can help to better constrain the existing theoretical models to determine the physical parameters of the planets. High-contrast imaging is also an excellent tool to study circumstellar disks which can provide insight into the architectures of planetary systems, and once more, the insights from observations can be applied to the current theoretical models. All of this combined can pave the way to understand the big picture of planet formation and evolution.

In this Chapter, I summarise the main results presented in Chapters 2-5 of this thesis, and describe the plans for short-term research. In the final Section 6.2, I discuss some perspectives for future developments in the field of directly imaged exoplanets.

6.1 Summary

Chapter 2 (published in Brown-Sevilla et al. 2021) presented near-infrared SPHERE polarimetric observations of the protoplanetary disk around WaOph 6. The disk displays a set of two spiral arms that have been imaged in the millimetre continuum with ALMA. We presented for the first time scattered light observations of the disk, where the spiral features can also be distinguished. This is a remarkable finding since up to now, no spiral arms had been observed in disks around young (< 1 Myr) K or M type stars in scattered light.

As pointed out before, multi-wavelength observations help to trace different parts and grain sizes of the disks, as well as give insight into the physical processes driving their morphologies. In this study, we compared the structure of the disk in scattered light and mm continuum, we found that the gap and ring structures previously reported in Huang

et al. (2018b) are also present in our observations, while an unreported break in the spiral arms at $\sim 0.16''$ is present in the ALMA data and not in ours.

As a first attempt to explain the spiral features, we tested the hypothesis of a planetary mass perturber driving the spiral pattern. For this we performed hydrodynamical simulations and radiative transfer testing different planet masses and locations. A planet of at least $10 M_{\text{Jup}}$ outside of the spiral structure ($d \geq 90$ au) is needed to reproduce the symmetric spiral architecture observed in both scattered light and mm continuum. However, none of the parameter combinations is able to reproduce the contrast nor the additional features in the observations, which may be caused by additional physical processes.

Finally, with an analysis of the sensitivity of our data we found that the possibility of detecting the aforementioned planet strongly depends on its formation scenario, explaining the non-detection with a “warm” or “cold-start”.

Chapter 3 (published in Brown Sevilla et al. 2019) is a brief study of the companion candidates around the star AH Lep. Two point sources were identified in SPHERE IRDIS and IFS data, in the $H2H3$ and YJ filters. They are located at a separation from the star of 421.0 ± 3.4 mas and 769.8 ± 3.5 mas, respectively. An astrometric analysis of the two companion candidates revealed that their proper motion is consistent with that of background objects to AH Lep. From the detection limits derived from the observations, we found the IRDIS data to be sensitive to companions brighter than 10^{-5} at ~ 12 au.

Regarding the nature of the point sources, a comparison with known companions places them between the T- and L-dwarf regions in the color-magnitude diagram. However, the spectra extracted from our observations shows no signs of methane absorption, a characteristic feature of T dwarfs, which hints to them belonging to the L spectral type. With this work we demonstrated how the high-contrast imaging technique is used to detect and characterise companion candidates, as well as the necessary process to determine whether they belong to the stellar system or are background objects.

Chapter 4 (Brown-Sevilla et al. submitted) describes the study of the atmosphere of the exoplanet 51 Eridani b. We presented the highest S/N spectro-photometric observations of the planet taken so far with SPHERE. The new data allowed to revise published flux measurements of the planet and obtain updated detection limits. Our data shows increased sensitivity and rules out planets more massive than $2 M_{\text{Jup}}$ at 3 au, and $1 M_{\text{Jup}}$ beyond 4.5 au.

To obtain atmospheric and physical parameters of the planet, we used the retrieval code `petitRADTRANS`, applied to our spectro-photometric data + the photometry in Samland et al. (2017). We obtained a good fit to the observations with the exception of the M_5 photometric point, which might be explained by the large uncertainty of the data. Our findings suggest that the photosphere of the planet is mostly clear, even when enforcing clouds. This can be linked to a correlation between the temperature gradient and clouds, which has been observed in other recent studies (Kammerer et al. 2021).

We compared our results with previously reported ones obtained with SPHERE and GPI NIR data (Samland et al. 2017) using self-consistent models. The outcome from the retrievals

is overall in agreement with previously published results. However, it differs in two main points: the atmospheric fits from self-consistent models are consistent with the photosphere of 51 Eri b being cloudy; and the metallicity $[\text{Fe}/\text{H}]$ in our retrievals is close to solar $[\text{Fe}/\text{H}]$, a much lower value than reported by Samland et al. (2017). The discrepancies might come from the larger and more flexible parameter space that can be explored with retrievals as opposed to self-consistent models.

As a confirmation, we applied the retrieval approach to the previously reported data (SPHERE+GPI) and find similar results to ours. Additionally, we used the best-fit parameters from the retrievals to obtain the pressure-temperature structure using a self-consistent model. The results show a larger temperature gradient for the self-consistent models than for the retrievals, which hints at the temperature gradient-cloud correlation. In this light, we discussed the implications that using either retrieval codes or self-consistent models to interpret exoplanet spectra can have, and advise that these approaches should be discussed in parallel.

The results from this study highlight the challenge that modelling exoplanet atmospheres still represents, as well as the importance of observations at longer wavelengths to determine the presence or absence of clouds.

Chapter 5 (Brown-Sevilla et al. *in prep.*) shows the first part of a study of debris disks observed with SPHERE. We initially focused in the target selection, which we based on the stars with reported IR excesses from two catalogues (Chen et al. 2014; Cotten and Song 2016), cross-checked with the IR excess stars observed with SPHERE. To refine our sample and select systems with a double belt architecture, we modelled the SED of the stars and looked at those which required two temperatures to be fitted. We defined a criteria of a maximum temperature difference and limited luminosity ratio between the belts. Finally, we excluded the targets that have not been listed as resolved in the literature.

With the resulting blackbody temperatures, we estimated the radii of the belts and used the Hill radius definition to obtain the masses of the planets that could be orbiting in the gap between the belts. To determine the detectability of these planets, we extracted the contrast and mass limits from the SPHERE data for each target. We found that with the current sensitivity of the data, the proposed planets are not detectable.

Lastly, we gave a brief description of the plans for the short-term future, which include expanding the current sample to include single belt and possible double (or multiple) belt disks (observed with SPHERE) as well as using Gaia DR3 and the Hipparcos catalog to measure proper motion anomalies and look for companions in the disks. In case of non-detection we will provide contrast and mass limits.

6.2 Outlook

Understanding the connection between exoplanets and circumstellar disks is key for the improvement of planet formation and evolution theories. The results presented in this thesis

demonstrate the current capabilities of the high-contrast imaging technique to study different stages of the evolution of planetary systems and suggest different paths for follow-up studies.

In Chapter 2, we presented scattered light observations of WaOph 6 that for the first time show the spiral structure of the disk at these wavelengths. Deeper NIR observations, for example with JWST/NIRCam (e.g., Girard et al. 2022), could help to better constrain the spiral features and allow for a more detailed comparison with data at different wavelengths. In addition, observations of other very young disks (< 1 Myr) in scattered light would aid to investigate how frequent spiral features are at these ages and possibly shed some light on the origin of these structures.

As pointed out in Chapter 4, many of the physical processes occurring in the atmospheres of planets are not well understood, especially those related to clouds, which may lead to wrong conclusions about the properties and parameters predicted by atmospheric models. The cloud-free retrieval case of 51 Eri b has also been reported for other sources (e.g. HR 8799e and HD 206893 B; Mollière et al. 2020; Kammerer et al. 2021, respectively). Mid-IR observations of these planets, for example with the next generation of imaging instruments that can provide high-resolution spectroscopy such as the JWST/MIRI (Wright et al. 2004) and the upcoming ELT/METIS (Quanz et al. 2015), hold the potential to solve the cloud-temperature gradient degeneracy.

The study of debris disks can also benefit from the aforementioned new-generation instruments, for example by using JWST/NIRCam to look for planetary-mass companions within the belts of the disks as proposed in Chapter 5. Furthermore, multiwavelength observations of circumstellar disks with instruments such as ALMA will aid to reveal the physical processes behind their different architectures. In turn, the constraints derived from observations can be applied to improve the existing models of both gas and dust evolution.

Finally, a combination of detection methods could also be a promising avenue to push the current limitations, for example by looking for proper motion anomalies in the recent Gaia DR3 (Gaia Collaboration et al. 2022) for stars that harbour circumstellar disks to select possible targets for high-contrast imaging observations. In the end, a synergy between different techniques is necessary to provide a broader insight into our understanding of planetary systems.

Appendix A

Complementary material to Chapter 2

A.1 Dust mass estimate

Millimeter continuum observations, obtained assuming optically thin emission (Hildebrand 1983), allow us to use the relation

$$M_{\text{dust}} \simeq \frac{d^2 F_\nu}{\kappa_\nu B_\nu(T(r))}, \quad (\text{A.1})$$

where d is the distance to the star; F_ν is the total flux at a given frequency ν ; κ_ν is the dust opacity at a given frequency, for which we used the common relation applied to disk surveys, $\kappa_\nu = 2.3 \text{ cm}^2 \text{ g}^{-1} \times (\nu/230 \text{ GHz})^{0.4}$ (Andrews et al. 2013); and $B_\nu(T_{\text{dust}})$ is the Planck function for a given dust temperature T_{dust} , that we derived from the relation

$$T_{\text{dust}} = 22 \times (L_*/L_\odot)^{0.16} \text{ K}, \quad (\text{A.2})$$

from van der Plas et al. (2016), which gives $T_{\text{dust}} = 26.05 \text{ K}$. The resulting dust mass from equation (A.1) is reported in Table 2.1, and, assuming a dust/gas mass ratio ($M_{\text{dust}}/M_{\text{gas}}$) of 1:100, within the previously reported values. However, we are aware that the assumptions made to perform this calculation could significantly differ from the actual disk conditions and therefore, this result should be taken with caution.

A.2 Unprocessed reduced Q_ϕ and U_ϕ SPHERE images

Figure A.1 shows the reduced Q_ϕ and U_ϕ images (on the left and right panels, respectively). The raw data was reduced as detailed in Section 2.3. Most of the signal is concentrated in the Q_ϕ image. Due to the low S/N, these images had to be processed for the analysis as described in Section 2.3.1.

A.3 Extracting the non-axisymmetric information from the ALMA data

To recover the millimeter spiral structure, we follow a similar procedure to the one described in the Appendix B of Isella et al. (2019). We start from the calibrated visibilities of the dust continuum emission, available from the DSHARP data release. We run a MCMC (Monte

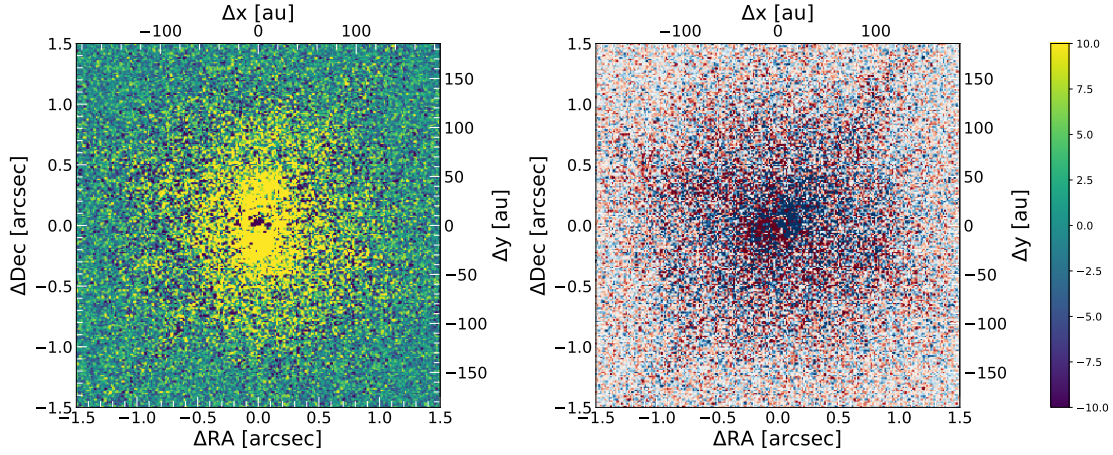


Figure A.1: Reduced Q_ϕ and U_ϕ SPHERE/IRDIS-DPI images. The images are shown up to the distance where the noise dominates. Most of the signal is contained in the Q_ϕ image.

Carlo Markov Chain) with 50 walkers to find the offset (δRA , δDec) that minimizes the imaginary part of the visibilities, this gives us the centroid of the disk. In this MCMC we use a flat prior over both dimensions. After correcting by that center, we use the inclination and position angle measured by Huang et al. (2018a) to deproject the visibilities. Our new deprojected data set is analysed with `frank` (Jennings et al. 2020), and the best visibilities profile found by this package is subtracted from our deprojected data set. The result is a visibility set which only contains the non-axisymmetric information of the disk, shown in the right panel of Figure 2.6.

A.4 Toomre parameter calculation

From equation (1.2), we take

$$\Omega_k = (GM_*/r^3)^{1/2},$$

$$c_s = h\Omega_k,$$

where $h \propto r^{5/4}$, and

$$\Sigma = \Sigma_0 r^{-1/2},$$

where

$$\Sigma_0 = \frac{3M_{\text{disk}}}{4\pi} \frac{1}{r_{\text{max}}^{3/2} - r_{\text{min}}^{3/2}},$$

which finally leads to $Q \propto r^{-5/4}$. We use $r_{\text{min}} = 20$ au due to the inner working angle limit of the observations, and $r_{\text{max}} = 175$ au as the outer radius from the lower limit value

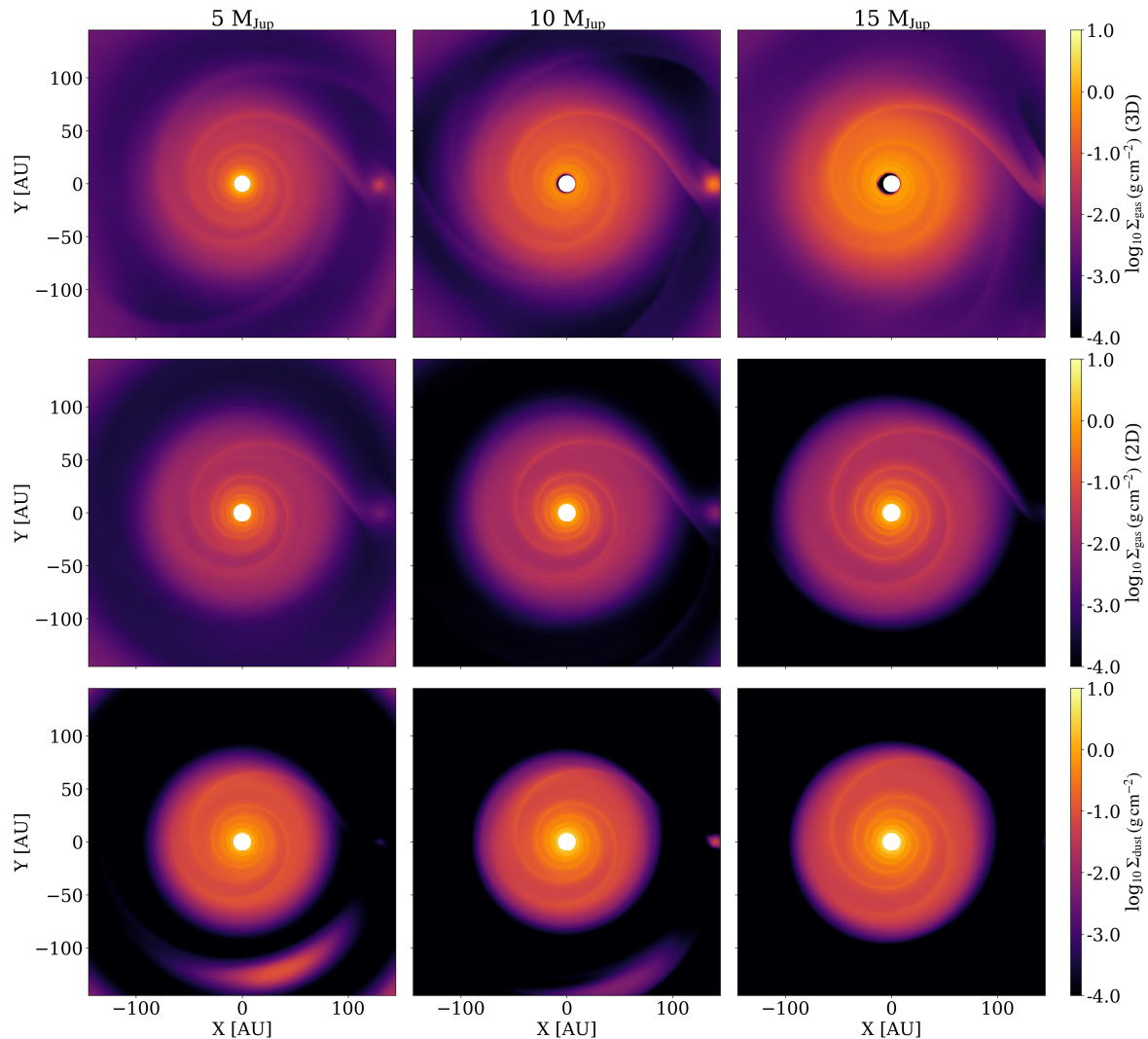


Figure A.2: Density maps from our 3D (top panels) and 2D (middle and bottom panels) hydrodynamical simulations for planets of 5, 10 and 15 M_{Jup} at separations of 130, 140 and 160 au, respectively, shown from left to right. The top and middle panels show the gas surface density maps, while the bottom panels show the dust density maps.

used by Ricci et al. (2010), the only difference when taking the upper limit is that the disk becomes unstable by ~ 330 au.

A.5 Gallery of density distributions from the hydrodynamical simulations and radiative transfer images

Density maps from our 3D gas and 2D gas + dust hydrodynamical simulations for a planet of 5, 10 and 15 M_{Jup} at separations of 130, 140 and 160 au, respectively are shown in Fig. A.2. The resulting radiative transfer images from these simulations are shown in Fig. A.3. For the case of the synthetic ALMA images, our simulations do not fit the inner and outer spirals at the same time (see Section 2.5.3), we show the ones fitting the inner spirals.

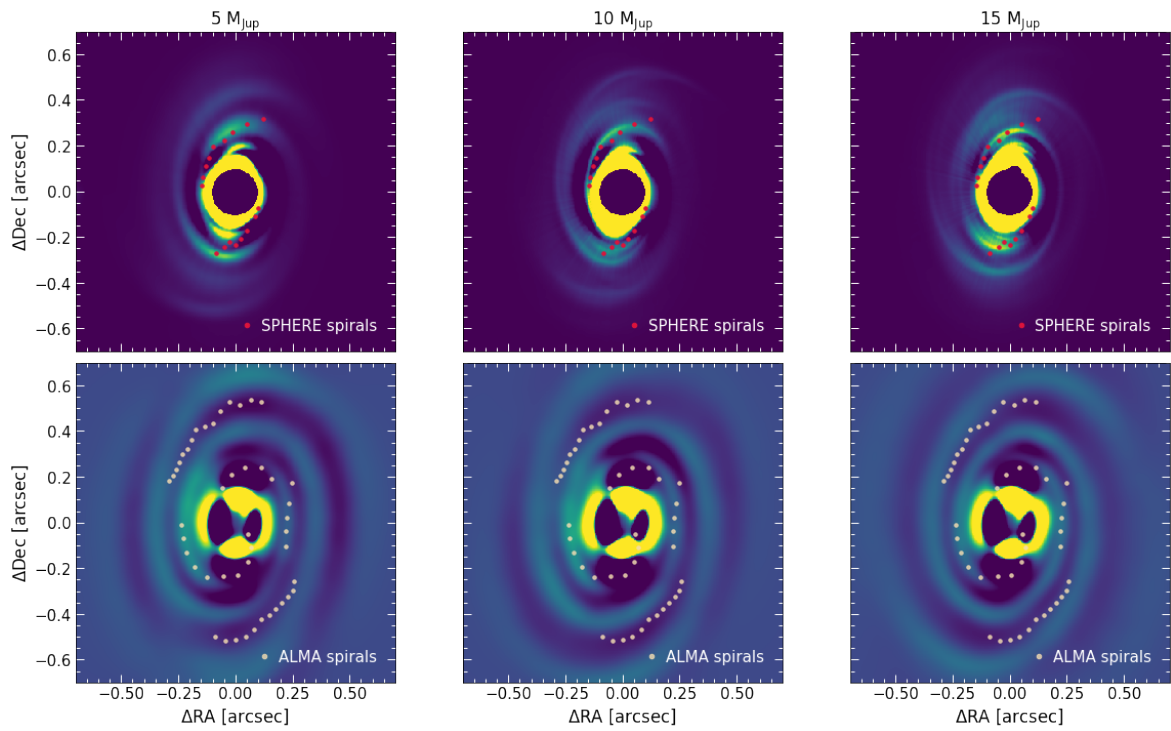


Figure A.3: Resulting radiative transfer images from our 3D (upper panels) and 2D (lower panels) hydrodynamical simulations for the planets described in Fig. A.2. The mass and separation increase from left to right. The images have been processed with the same techniques as the ones in Fig. 2.8 for a better comparison to the observations. For the lower panels, we show the images that fit the inner spirals.

Appendix B

Complementary material to Chapter 4

B.1 Wavelength calibration and spectral differential imaging

SPHERE/IFS data reduction pipelines remove instrumental signatures, calibrate and compute wavelength solutions, extract spectra of individual lenslets from the 2D detector, and re-assemble the data into a 3D data cube with one spectral and two spatial dimensions. The wavelength calibration relies on a range of monochromatic lasers projected on the detector by the calibration unit.

The default of ESO's EsoRex pipeline (Freudling et al. 2013) and the Data Reduction Handling software used by the SPHERE consortium (Pavlov et al. 2008) is to determine the wavelength solution by fitting a 2nd order polynomial to the spectral calibration data. In addition to using spectral lines for the absolute wavelength calibration, the vlt-sphere Python package (Vigan 2020¹) aims at a more refined calibration of the dispersion solution by tracing the radial separation between diagonally opposite satellite spots for each spectral plane in the 3D data cube.

Figure B.1 (top) visualizes the respective dispersion solutions inherent to three different IFS pipelines. Data cubes reduced by EsoRex version 0.42.0 include the median of the shortest wavelengths, and the median dispersion of a linear fit to the wavelength solution as keywords in the FITS header. SPHERE DRH and vlt-sphere (version 1.4.3, with a wavelength calibration issue fixed) provide a separate FITS file with wavelengths corresponding to each spectral plane of the 3D data cube. In the case of SPHERE DRH, this is based on the 2nd order polynomial fit.

As the choice of dispersion solution determines the spectral band-width of individual spectral channels, it also influences the recovered spectral energy distribution of the detected astrophysical sources. This has to be considered, e.g., when applying retrieval techniques to the observational spectra. For Spectral Differential Imaging (SDI) data sets, the dispersion solution serves a second purpose by providing the radial λ/D scaling of the speckles.

We notice that the strongest gradients in the vlt-sphere dispersion solution coincide with edges of telluric H₂O absorption bands (Fig. B.1, bottom). While the star itself could be considered as a flat continuum source between neighbouring spectral channels, the edges of telluric absorption bands result in strong gradients in the number of photons recorded as a function of wavelength. As a consequence, at the blue-ward edge of a telluric absorption

¹<https://github.com/avigan/SPHERE>

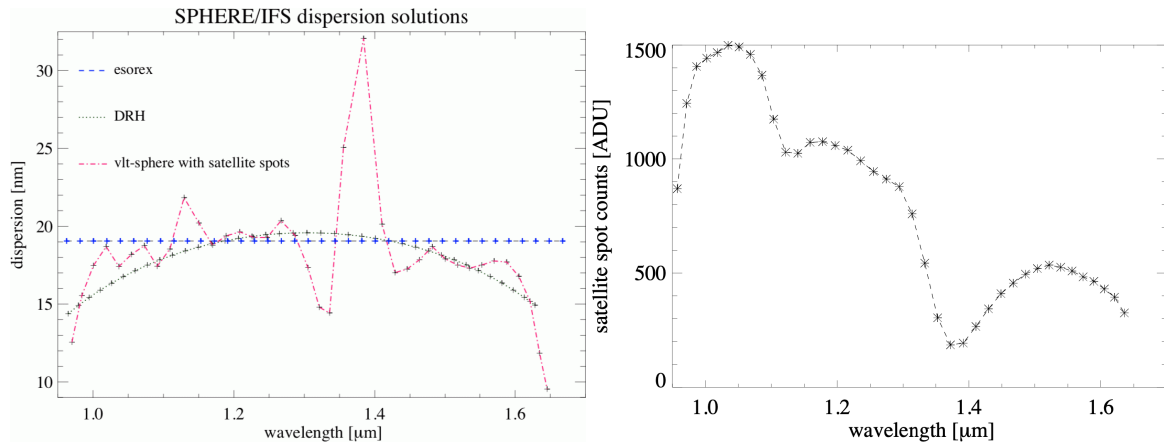


Figure B.1: Top: SPHERE/IFS dispersion solutions of the reduced 3D data cubes resulting from the standard ESO pipeline EsoRex, the Data Reduction and Handling (DRH) of the SPHERE consortium, and the vlt-sphere Python package tracing the separations of satellite spots. Bottom: the satellite spots show strong spectral gradients in the count rates at the edges of telluric absorption bands.

band a channel records more shorter wavelength (“bluer”) than longer wavelength (“redder”) photons. The opposite happens at the red-ward edge of an absorption band. The centroids of satellite spots at the blue edge of an absorption band are thus weighted in favour of short wavelength photons, resulting in a smaller radial separation of opposing spots on the detector. The peak of satellite spots at the red edge of an absorption band are slightly further apart. Thus the vlt-sphere “dispersion solution” is not representative of the intrinsic (smooth) response of the IFS AMICI prism to a “flat spectrum” source, but representative of the response to a source with the spectral characteristics of the satellite spots.

To correct for the above mentioned effect, one could mask the channels around the water absorption bands and use a cubic relation to fit the position of the satellite spots, which would correct the quadratic dispersion computed by fitting the three (four) diode lasers observed in the wavelength calibration for the YJ (YH) IFS modes.

B.2 Telluric monitoring and correction

Continuous satellite spots not only provide means for a continuous spatial registration of the star, but also offer a simultaneous monitoring of the (grey) atmospheric transmission, and of variations in the strength of telluric H₂O absorption bands. Figure B.2 visualizes the variations in atmospheric conditions over the duration of the full sequence of 154 frames of the 2017-09-28 IFS data set. In the top panel we plot the inverse of the normalized IFS satellite spot count rates observed in the 1.4 μm H₂O absorption band. For better comparison with the Paranal atmospheric monitoring data as made available by the ESO archive², we smoothed the SPHERE/IFS data to the same coarse time sampling of ≈120 s. The most noticeable feature is the sharp rise in absorption near the end of the sequence due to an incoming cloud layer. In the middle panel of Fig. B.2 we show the contemporaneous sky

²https://archive.eso.org/wdb/wdb/asm/lhatpro_paranal/form

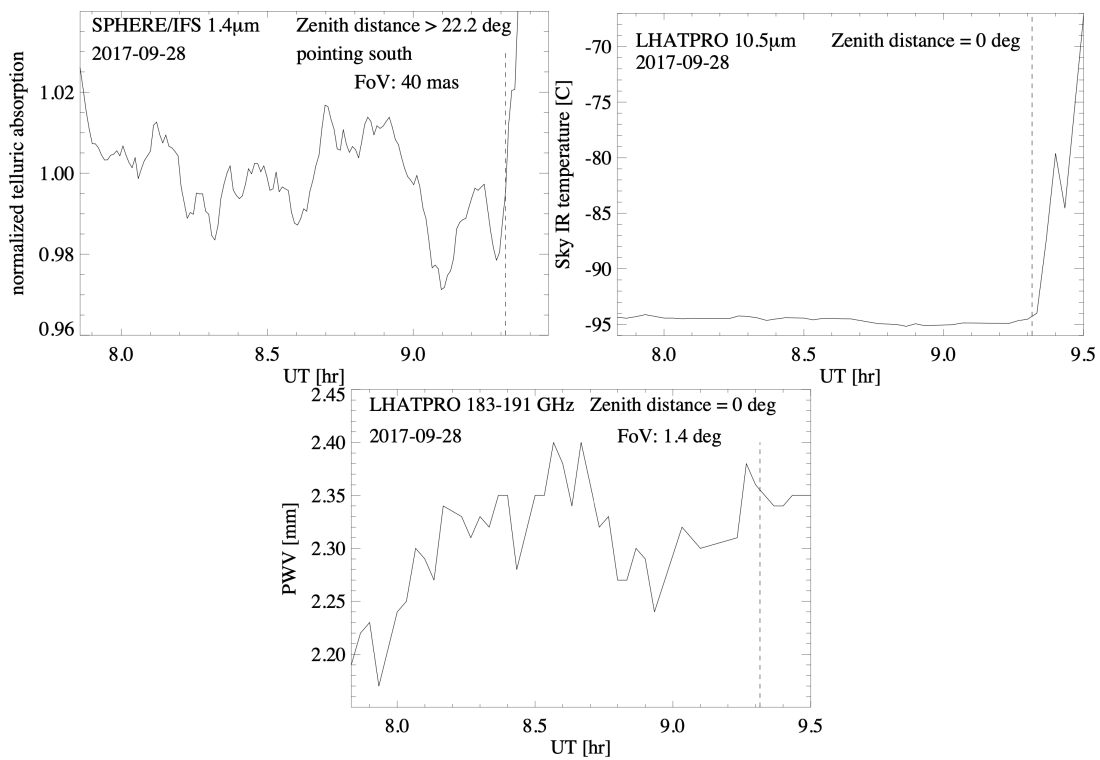


Figure B.2: Top: Telluric absorption as traced by SPHERE/IFS at $\approx 1.4\mu\text{m}$. Middle: Sky infrared temperature as traced by LHATPRO. Bottom: PWV as traced by LHATPRO. The vertical dashed line in all figures marks our cut-off time for the first 140 IFS frames, which form the basis of our spectral analysis, out of a total of 154 IFS data frames.

infrared temperature as measured by the Low Humidity and Temperature Profiling (LHATPRO) instrument (Querel and Kerber 2014). The rise in the telluric absorption seen in the IFS data approximately coincides with the increase in the sky infrared temperature due to clouds. In the bottom panel of Fig. B.2 we show the precipitable water vapour (PWV) measured by LHATPRO. We notice that there is no exact synchronicity between the IFS measurements in the telluric H₂O absorption band and the LHATPRO PWV. Some shape similarity of the PWV variations between UT ≈ 8.1 hr and ≈ 9.1 hr, and the IFS variations between UT ≈ 8.3 hr and ≈ 9.3 hr, which might be explained by telluric water vapour fluctuations first crossing the LHATPRO field of view, and ≈ 12 min later the SPHERE/IFS field of view, is most likely coincidental. A strict correlation between IFS and LHATPRO telluric measurements is not expected, as they monitor different parts of the sky (SPHERE/IFS was tracking 51 Eri, and LHATPRO was staring at zenith), and also cover different fields of view (40 mas for SPHERE/IFS vs. 1.4 deg for LHATPRO).

The data stress the importance of a simultaneous monitoring of the telluric absorption along the line of sight for high precision (better than $\pm 2\%$ for the first 140 frames of the present data set) spectro-photometric observations of exoplanets. This can be accomplished either by employing high spectral resolution, which facilitates the monitoring of individual lines in telluric H₂O absorption bands, or – in the case of low- to medium spectral resolution ($R \lesssim 20\,000$) observations – by simultaneous monitoring of the spectro-photometric signal of the host star (employing, e.g., continuous satellite spots).

B.3 Spectral correlation matrix

The extracted exoplanet spectrum from our SPHERE/IFS data is affected by spectral covariance, which can alter the values of the fitted atmospheric parameters. In order to see by how much our data is affected by this, we followed the methods in Greco and Brandt (2016) to estimate the average spectral correlation ψ_{ij} within an annulus of $1.5\lambda/D$ at the separation of the planet, masking out the planet in a $2\lambda/D$ radius. Where

$$\psi_{ij} \equiv \frac{C_{ij}}{\sqrt{C_{ii}C_{jj}}} = \frac{\langle I_i I_j \rangle}{\sqrt{\langle I_i^2 \rangle \langle I_j^2 \rangle}}, \quad (\text{B.1})$$

here, C is the covariance matrix, and $\langle I_i \rangle$ is the average intensity within the annulus at wavelength λ_i . The covariance matrix is then used to compute the log-likelihood $\ln \mathcal{L}$ according to

$$-2 \ln \mathcal{L} \equiv \chi^2 = (S - F)^T C^{-1} (S - F), \quad (\text{B.2})$$

where S is the observed spectrum, and F is the model spectrum. The correlation matrix for our IFS YH spectrum is shown in Fig. B.3.

We ran a “nominal” retrieval for our 2018 data with 4000 live points using the covariance matrix to compute the log-likelihood. We observe that the values of the fitted parameters remain within error bars to the ones from the retrieval for which we did not use the covariance

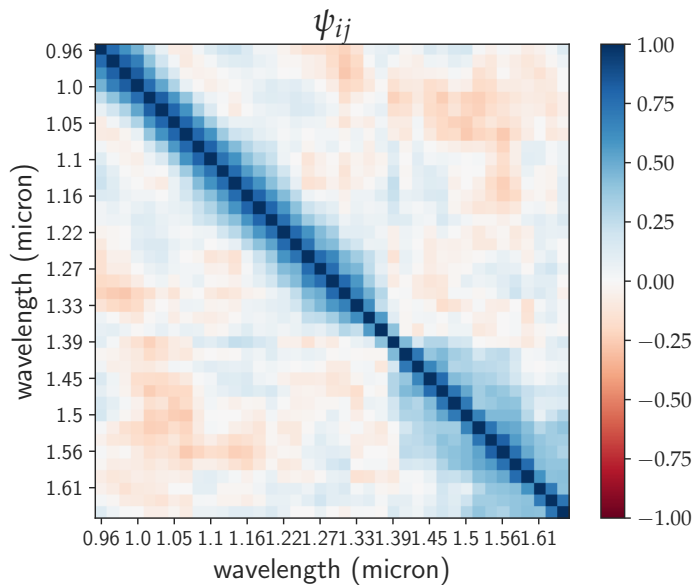


Figure B.3: Spectral correlation matrix between each pair of spectral channels in our SPHERE/IFS data.

Table B.1: Obtained parameter values from SAM17 data

Model	$\log g$	radius	[Fe/H]	CO	f_{sed}	T_{eff}	$\log \tau_{\text{cloud}}$
Nominal	$4.02^{+0.30}_{-0.34}$	$1.00^{+0.08}_{-0.06}$	$-0.20^{+0.20}_{-0.18}$	$0.39^{+0.08}_{-0.07}$	$4.39^{+3.70}_{-3.11}$	716^{+24}_{-36}	$-5.0^{+1.6}_{-1.3}$
Enforced clouds	$4.02^{+0.33}_{-0.34}$	$1.56^{+0.23}_{-0.27}$	$-0.06^{+0.20}_{-0.19}$	$0.42^{+0.05}_{-0.04}$	$0.15^{+0.13}_{-0.08}$	510^{+15}_{-14}	$0.05^{+0.05}_{-0.03}$
Samland17	$4.26^{+0.24}_{-0.25}$	$1.11^{+0.16}_{-0.13}$	$1.03^{+0.10}_{-0.11}$	–	$1.26^{+0.36}_{-0.29}$	760^{+21}_{-22}	–

matrix. However, we decided to include the covariance matrix in all our retrievals.

B.4 Enforced clouds retrieval and attempt to reproduce previous results

Figure B.4 shows the best-fit spectrum along with 34 randomly sampled posterior PDFs for the “enforced clouds” retrieval using our new data + photometric points. The best-fit parameters are quoted in Table 4.4, and the posterior PDFs are shown in Fig. B.5, the values quoted for each parameter correspond to the median of the posterior distribution, the uncertainties show the 16th and 84th percentile, representing a 1σ uncertainty range. In this way the values are not identical to the ones that produce the overall best fit, which are given at the top of Fig. B.4. Being the median, they also do not necessarily correspond to the most probable value that can be seen from the peak of the marginalized posterior distribution shown in Fig. B.5.

Figure B.6 shows the best-fit spectrum along with 100 randomly sampled posterior PDFs for the “nominal” retrieval using SAM17’s data. Figure B.7 shows the corresponding posterior PDFs. The parameters for the best fit spectra are summarized in Table B.1. Values

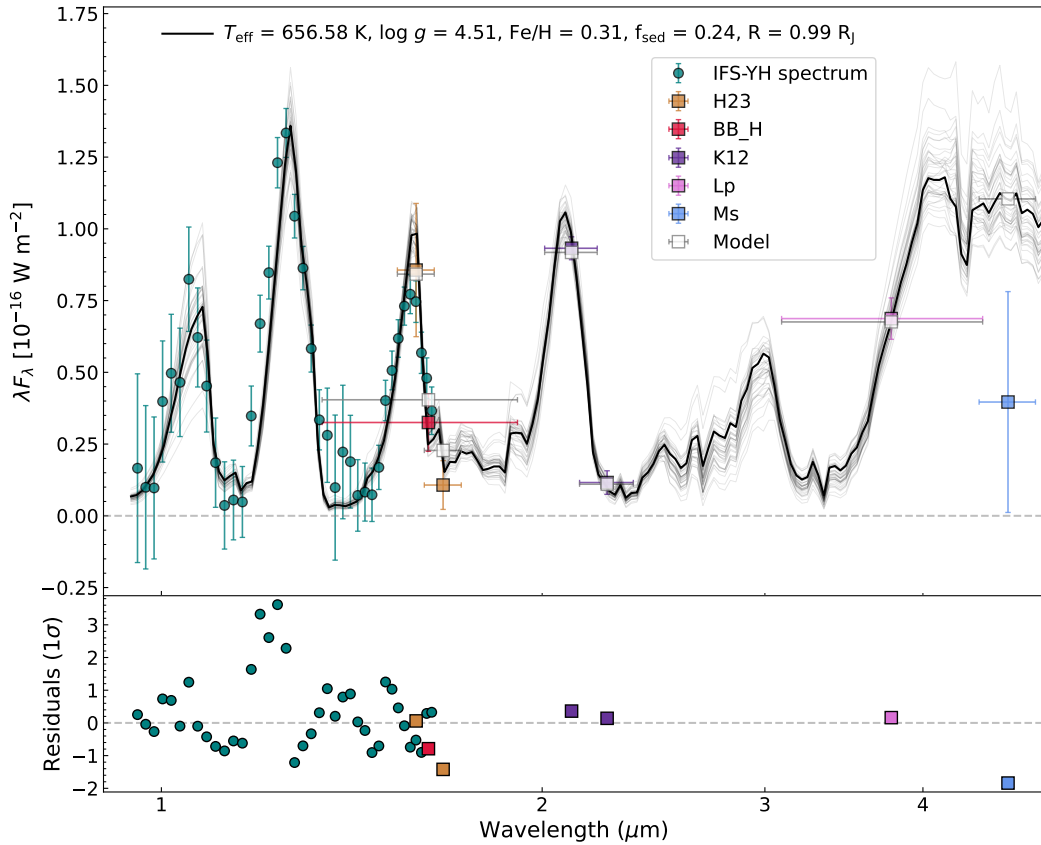


Figure B.4: petitRADTRANS best-fit spectrum of 51 Eri b for the “enforced clouds” retrieval run on our new SPHERE spectro-photometric data (teal circles and purple squares) along with the photometric points included in Samland et al. (2017) (shown as squares). The photometric points describe the average flux in the respective filter, the x -error bar represents the filter widths. 34 randomly drawn samples from the posterior probability distribution are shown in gray, to show the spread of model parameter combinations to fit the data. Residuals in multiples of 1σ uncertainties of the data are shown below.

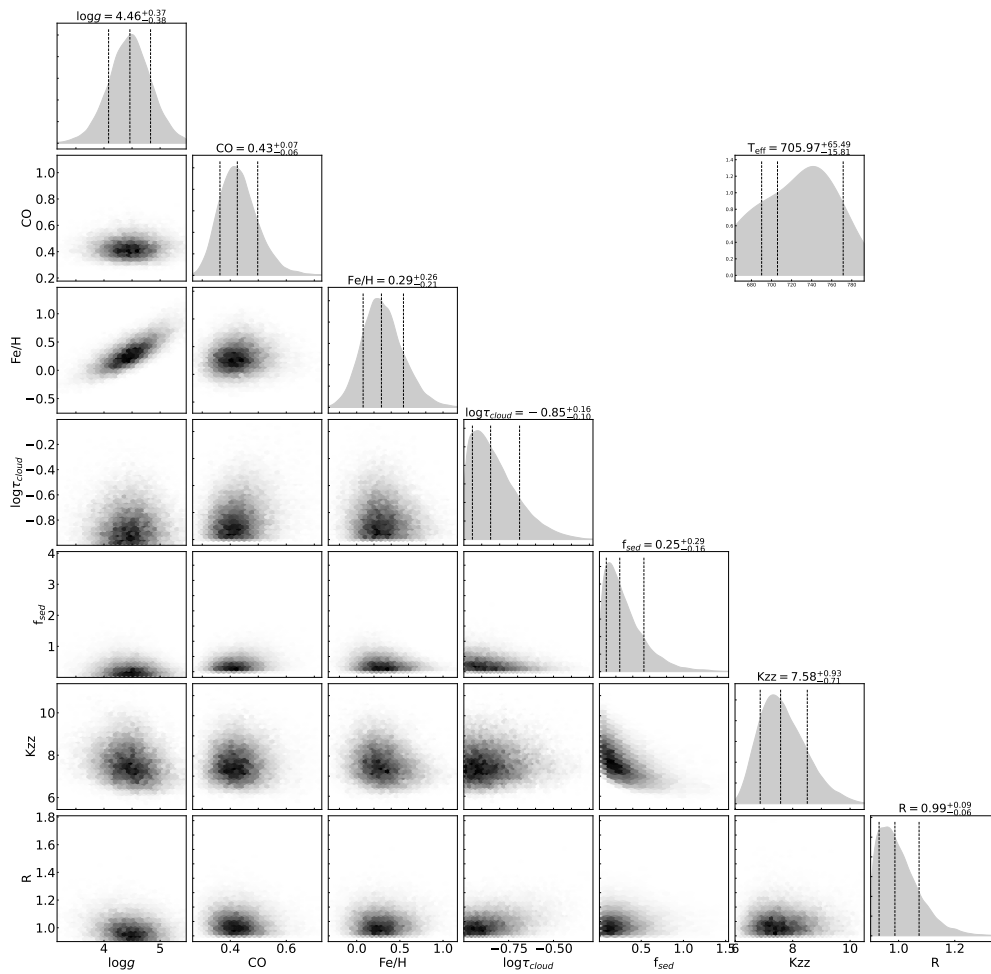


Figure B.5: Corner plot of the posterior PDFs of the “enforced clouds” retrieval run on the new data set.

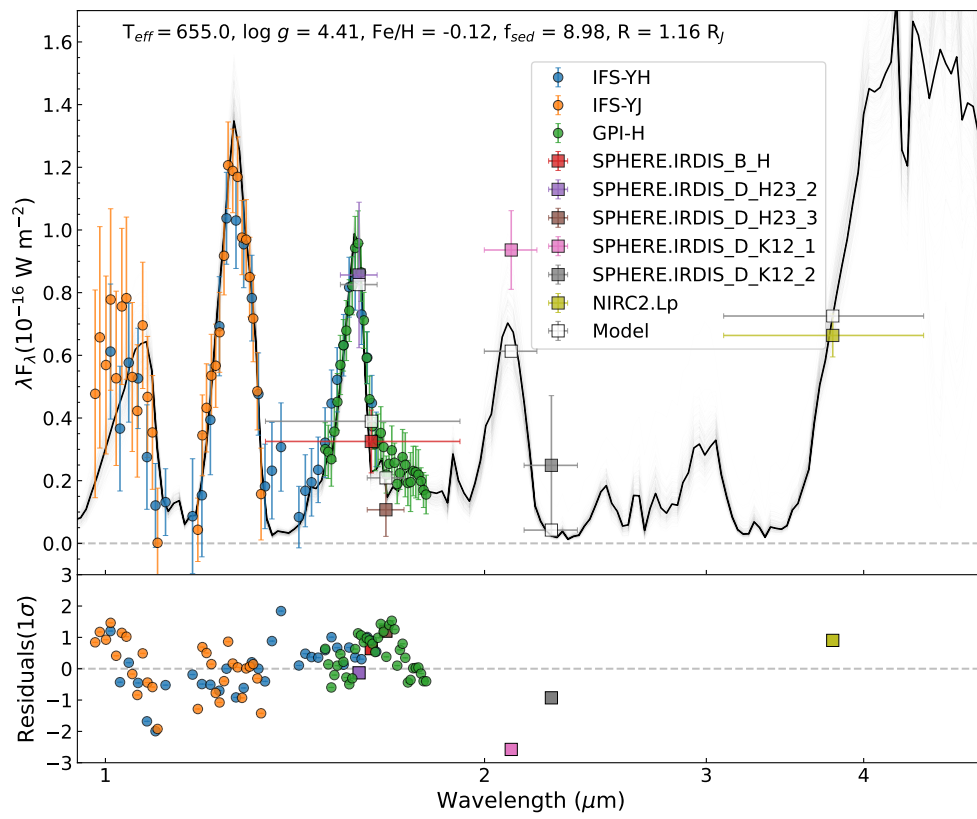


Figure B.6: Best-fit spectrum (top) of the nominal retrieval run on the original data set from Samland et al. (2017). This is to be compared to Figure 11 in Samland et al. (2017).

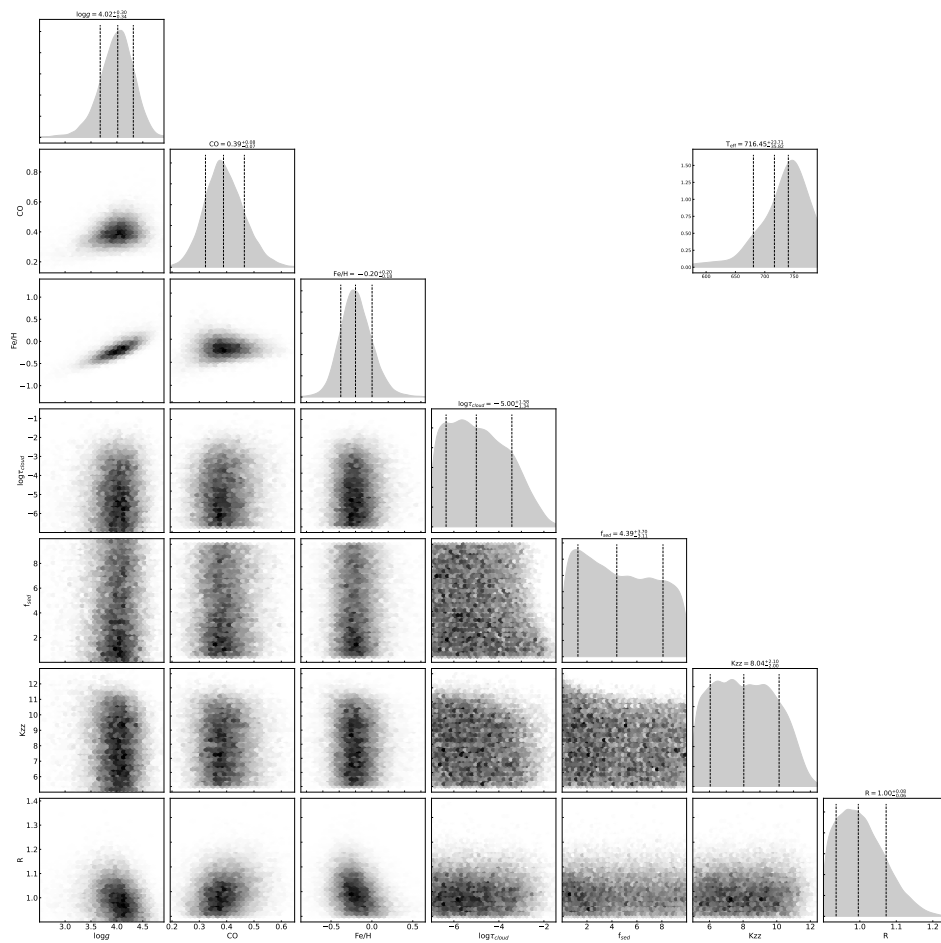


Figure B.7: Corner plot of the posterior PDFs of the retrieval run on the original data set from Samland et al. (2017). This is to be compared to Figure 12 in Samland et al. (2017).

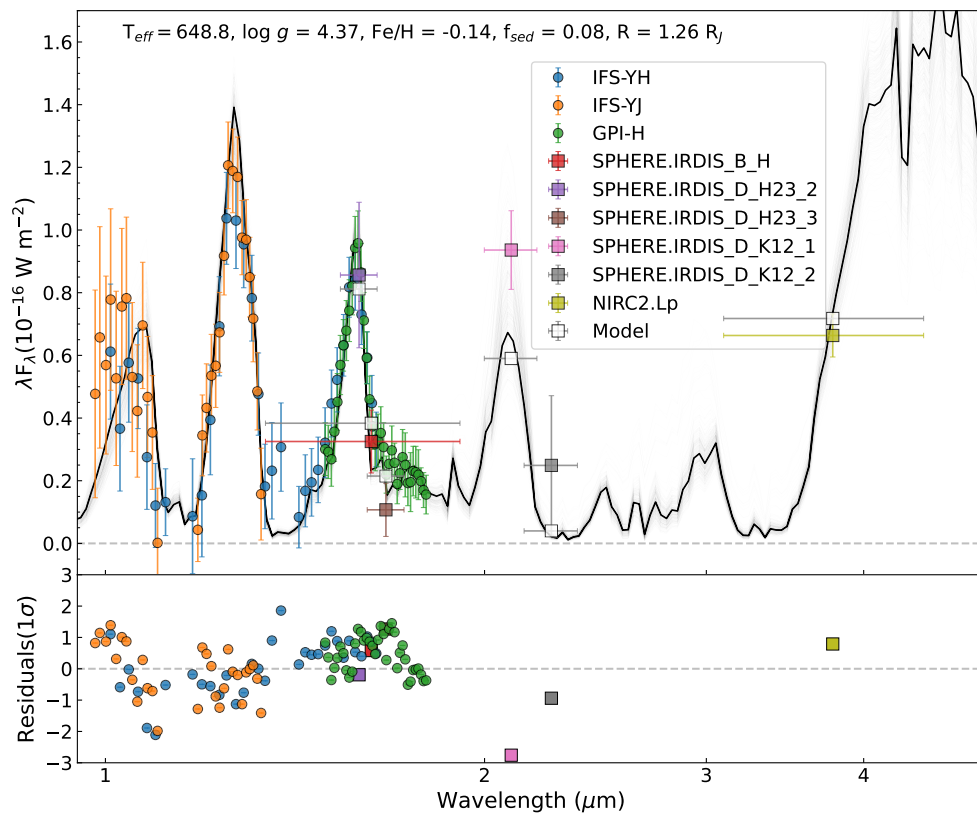


Figure B.8: Best-fit spectrum of the posterior PDFs of the retrieval run on the original data set from Samland et al. (2017) when restricting the range of the τ_{cloud} prior to positive values.

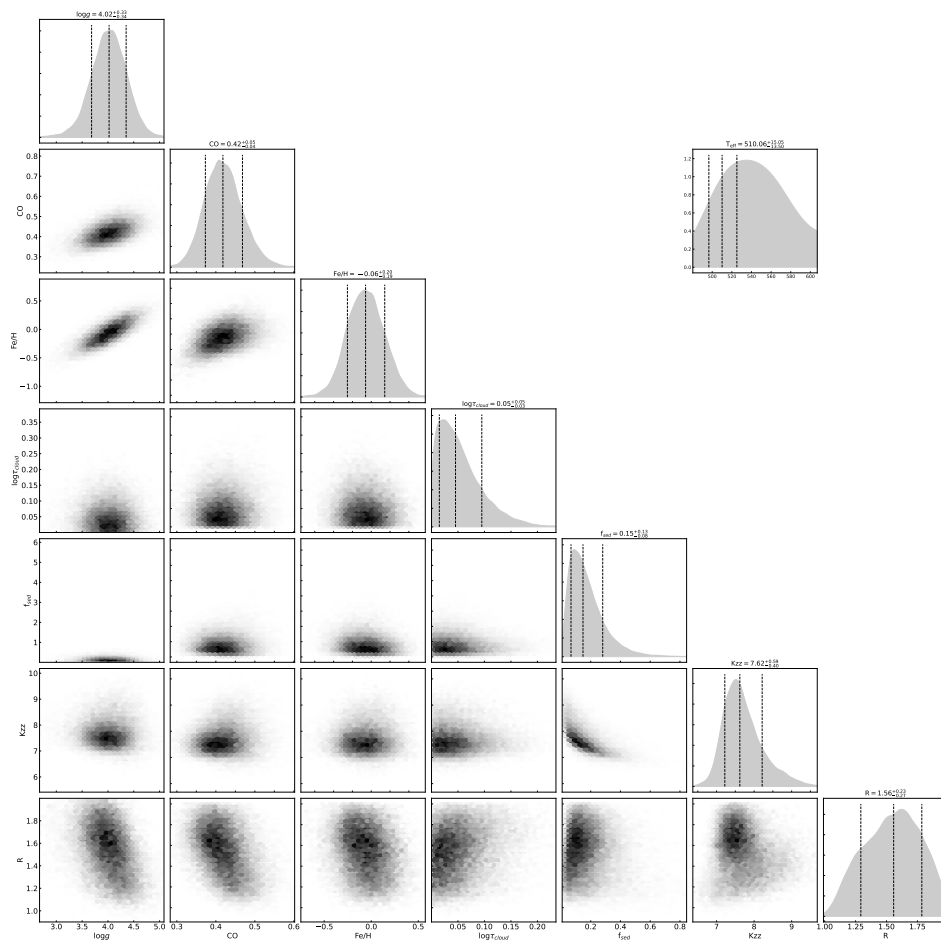


Figure B.9: Corner plot of the posterior PDFs of the retrieval run on the original data set from Samland et al. (2017) when restricting the range of the τ_{cloud} prior to positive values.

and errors quoted in Table B.1 are derived from the equally weighted posterior distribution produced by the Multinest algorithm for each parameter, i.e. marginalized over all parameters except the one in question. The last line gives the parameters derived by Samland et al. (2017) for their best-fitting “PTC-C” model. That latter model implies a cloud fraction of 100%. Figures B.8 and B.9 are analogous to the above but for the “enforced clouds” case.

As can be seen from Table B.1 we reproduce most of the parameters to within the calculated uncertainties, albeit with the major difference that our atmosphere shows no significant trace of clouds, and our metallicity is sub-stellar whereas SAM17 found a strongly super-stellar metallicity. Be reminded that τ_{cloud} denotes the optical depth of the cloud deck at the location where the atmosphere becomes optically thick due to gas opacities alone, i.e. $\tau_{\text{gas}} \approx 1$. This implies, that our nominal solution shows essentially no clouds at all ($\tau_{\text{cloud}} \approx 10^{-5}$ @ $\tau_{\text{gas}} \approx 1$), whereas the enforced clouds solution ($\tau_{\text{cloud}} \approx 1$ @ $\tau_{\text{gas}} \approx 1$) requires a rather unphysical gas giant with a radius of $1.56 R_J$, which for compensation needs to be unusually cool.

List of Publications

The following is a complete list of publications that I have contributed to. The publications marked with * have been used in this thesis.

Publications as leading author

1. ***Samantha B. Brown-Sevilla**, 2022, In prep.
2. ***Samantha B. Brown-Sevilla**, et al., Revisiting the atmosphere of the exoplanet 51 Eridani b with VLT/SPHERE, Submitted to A&A
3. ***Samantha B. Brown-Sevilla**, et al., A multiwavelength analysis of the spiral arms in the protoplanetary disk around WaOph 6, A&A, October 2021, 654, A35
4. **Samantha B. Brown-Sevilla**, et al., A new photometric and dynamical study of the eclipsing binary star HW Virginis, MNRAS, September 2021, 506, 2
5. ***Samantha B. Brown-Sevilla**, et al., High-contrast Imaging Study on the Candidate Companions Around the Star AH Lep, RNAAS, July 2019, Vol. 3, 7

Publications as contributing author

1. Per Calissendorff, et al., including **Samantha B. Brown-Sevilla**, Updated orbital monitoring and dynamical masses for nearby M-dwarf binaries, A&A, October 2022, 666, A16
2. Celia Desgrange, et al., including **Samantha B. Brown-Sevilla**, In-depth direct imaging and spectroscopic characterization of the young Solar System analog HD 95086, A&A, August 2022, 664, 139
3. Beth A. Biller, et al., including **Samantha B. Brown-Sevilla**, Dynamical masses for two M1 + mid-M dwarf binaries monitored during the SPHERE-SHINE survey, A&A, February 2022, 658, 145
4. Anthony Boccaletti, et al., including **Samantha B. Brown-Sevilla**, Investigating point sources in MWC 758 with SPHERE, A&A, August 2021, 652, L8
5. Arthur Vigan, et al., including **Samantha B. Brown-Sevilla**, The SPHERE infrared survey for exoplanets (SHINE). III. The demographics of young giant exoplanets below 300 au with SPHERE, A&A, July 2021, 651, A72

6. Miriam Keppler, et al., including **Samantha B. Brown-Sevilla**, Gap, shadows, spirals, and streamers: SPHERE observations of binary-disk interactions in GG Tauri A, *A&A*, July 2020, 639, A62
7. Aidan Gibbs, et al., including **Samantha B. Brown-Sevilla**, EDEN: Sensitivity Analysis and Transiting Planet Detection Limits for Nearby Late Red Dwarfs, *The Astronomical Journal*, April 2020, 159, 18
8. Dino Mesa, et al., including **Samantha B. Brown-Sevilla**, VLT/SPHERE exploration of the young multiplanetary system PDS70, *A&A*, December 2019, 632, A25
9. Davide Ricci, et al., including **Samantha B. Brown-Sevilla**, Multi-filter Transit Observations of HAT-P-3b and TrES-3b with Multiple Northern Hemisphere Telescopes, *PASP*, June 2017, 129, 976
10. Davide Ricci, et al., including **Samantha B. Brown-Sevilla**, Multifilter Transit Observations of WASP-39b and WASP-43b with Three San Pedro Mártir Telescopes, *PASP*, February 2015, 127, 948

Bibliography

- Ackerman, Andrew S. and Mark S. Marley (Aug. 2001). "Precipitating Condensation Clouds in Substellar Atmospheres". In: *The Astrophysical Journal* 556.2, pp. 872–884. DOI: [10.1086/321540](https://doi.org/10.1086/321540). URL: <https://doi.org/10.1086/321540>.
- Alarcón, Felipe et al. (Dec. 2020). "Chemical Evolution in a Protoplanetary Disk within Planet Carved Gaps and Dust Rings". In: *ApJ* 905.1, 68, p. 68. DOI: [10.3847/1538-4357/abc1d6](https://doi.org/10.3847/1538-4357/abc1d6). arXiv: [2010.08000](https://arxiv.org/abs/2010.08000) [astro-ph.EP].
- Allard, F. (Jan. 2014). "The BT-Settl Model Atmospheres for Stars, Brown Dwarfs and Planets". In: *Exploring the Formation and Evolution of Planetary Systems*. Ed. by Mark Booth, Brenda C. Matthews, and James R. Graham. Vol. 299, pp. 271–272. DOI: [10.1017/S1743921313008545](https://doi.org/10.1017/S1743921313008545).
- Allard, F., D. Homeier, and B. Freytag (June 2012). "Models of very-low-mass stars, brown dwarfs and exoplanets". In: *Philosophical Transactions of the Royal Society of London Series A* 370.1968, pp. 2765–2777. DOI: [10.1098/rsta.2011.0269](https://doi.org/10.1098/rsta.2011.0269). arXiv: [1112.3591](https://arxiv.org/abs/1112.3591) [astro-ph.SR].
- Allard, France et al. (July 2001). "The Limiting Effects of Dust in Brown Dwarf Model Atmospheres". In: *ApJ* 556.1, pp. 357–372. DOI: [10.1086/321547](https://doi.org/10.1086/321547). arXiv: [astro-ph/0104256](https://arxiv.org/abs/astro-ph/0104256) [astro-ph].
- Andrews, Sean M. (Aug. 2020). "Observations of Protoplanetary Disk Structures". In: *Annu. Rev. Astron. Astrophys* 58, pp. 483–528. DOI: [10.1146/annurev-astro-031220-010302](https://doi.org/10.1146/annurev-astro-031220-010302). arXiv: [2001.05007](https://arxiv.org/abs/2001.05007) [astro-ph.EP].
- Andrews, Sean M. and Jonathan P. Williams (Dec. 2007). "A Submillimeter View of Circumstellar Dust Disks in ρ Ophiuchi". In: *ApJ* 671.2, pp. 1800–1812. DOI: [10.1086/522885](https://doi.org/10.1086/522885). arXiv: [0708.4185](https://arxiv.org/abs/0708.4185) [astro-ph].
- Andrews, Sean M. et al. (Aug. 2009). "Protoplanetary Disk Structures in Ophiuchus". In: *ApJ* 700.2, pp. 1502–1523. DOI: [10.1088/0004-637X/700/2/1502](https://doi.org/10.1088/0004-637X/700/2/1502). arXiv: [0906.0730](https://arxiv.org/abs/0906.0730) [astro-ph.EP].
- Andrews, Sean M. et al. (July 2013). "The Mass Dependence between Protoplanetary Disks and their Stellar Hosts". In: *ApJ* 771.2, 129, p. 129. DOI: [10.1088/0004-637X/771/2/129](https://doi.org/10.1088/0004-637X/771/2/129). arXiv: [1305.5262](https://arxiv.org/abs/1305.5262) [astro-ph.SR].
- Andrews, Sean M. et al. (Dec. 2018). "The Disk Substructures at High Angular Resolution Project (DSHARP). I. Motivation, Sample, Calibration, and Overview". In: *ApJ Letters* 869.2, L41, p. L41. DOI: [10.3847/2041-8213/aaf741](https://doi.org/10.3847/2041-8213/aaf741). arXiv: [1812.04040](https://arxiv.org/abs/1812.04040) [astro-ph.SR].
- Asensio-Torres, R. et al. (Aug. 2021). "Perturbers: SPHERE detection limits to planetary-mass companions in protoplanetary disks". In: *A&A* 652, A101, A101. DOI: [10.1051/0004-6361/202140325](https://doi.org/10.1051/0004-6361/202140325). arXiv: [2103.05377](https://arxiv.org/abs/2103.05377) [astro-ph.EP].

- Avenhaus, Henning et al. (Aug. 2018). "Disks around T Tauri Stars with SPHERE (DARTTS-S). I. SPHERE/IRDIS Polarimetric Imaging of Eight Prominent T Tauri Disks". In: *ApJ* 863.1, 44, p. 44. DOI: [10.3847/1538-4357/aab846](https://doi.org/10.3847/1538-4357/aab846). arXiv: [1803.10882](https://arxiv.org/abs/1803.10882) [astro-ph.SR].
- Bae, Jaehan, Richard Teague, and Zhaohuan Zhu (May 2021). "Observational Signature of Tightly Wound Spirals Driven by Buoyancy Resonances in Protoplanetary Disks". In: *ApJ* 912.1, 56, p. 56. DOI: [10.3847/1538-4357/abe45e](https://doi.org/10.3847/1538-4357/abe45e). arXiv: [2102.03899](https://arxiv.org/abs/2102.03899) [astro-ph.EP].
- Bae, Jaehan and Zhaohuan Zhu (June 2018). "Planet-driven Spiral Arms in Protoplanetary Disks. I. Formation Mechanism". In: *ApJ* 859.2, 118, p. 118. DOI: [10.3847/1538-4357/aabf8c](https://doi.org/10.3847/1538-4357/aabf8c). arXiv: [1711.08161](https://arxiv.org/abs/1711.08161) [astro-ph.EP].
- Bai, Xue-Ning and James M. Stone (May 2013). "Wind-driven Accretion in Protoplanetary Disks. I. Suppression of the Magnetorotational Instability and Launching of the Magnetocentrifugal Wind". In: *ApJ* 769.1, 76, p. 76. DOI: [10.1088/0004-637X/769/1/76](https://doi.org/10.1088/0004-637X/769/1/76). arXiv: [1301.0318](https://arxiv.org/abs/1301.0318) [astro-ph.EP].
- Balbus, Steven A. and John F. Hawley (July 1991). "A Powerful Local Shear Instability in Weakly Magnetized Disks. I. Linear Analysis". In: *ApJ* 376, p. 214. DOI: [10.1086/170270](https://doi.org/10.1086/170270).
- Baraffe, Isabelle et al. (June 2003). "Evolutionary models for low mass stars and brown dwarfs at young ages". In: *Brown Dwarfs*. Ed. by Eduardo Martín. Vol. 211, p. 41.
- Baraffe, Isabelle et al. (May 2015). "New evolutionary models for pre-main sequence and main sequence low-mass stars down to the hydrogen-burning limit". In: *A&A* 577, A42, A42. DOI: [10.1051/0004-6361/201425481](https://doi.org/10.1051/0004-6361/201425481). arXiv: [1503.04107](https://arxiv.org/abs/1503.04107) [astro-ph.SR].
- Baruteau, Clément et al. (July 2021). "Observational signatures of eccentric Jupiters inside gas cavities in protoplanetary discs". In: *MNRAS* 505.1, pp. 359–376. DOI: [10.1093/mnras/stab1045](https://doi.org/10.1093/mnras/stab1045). arXiv: [2104.03769](https://arxiv.org/abs/2104.03769) [astro-ph.EP].
- Bashi, Dolev et al. (Aug. 2017). "Two empirical regimes of the planetary mass-radius relation". In: *A&A* 604, A83, A83. DOI: [10.1051/0004-6361/201629922](https://doi.org/10.1051/0004-6361/201629922). arXiv: [1701.07654](https://arxiv.org/abs/1701.07654) [astro-ph.EP].
- Baudino, J. L. et al. (Oct. 2015). "Interpreting the photometry and spectroscopy of directly imaged planets: a new atmospheric model applied to β Pictoris b and SPHERE observations". In: *A&A* 582, A83, A83. DOI: [10.1051/0004-6361/201526332](https://doi.org/10.1051/0004-6361/201526332). arXiv: [1504.04876](https://arxiv.org/abs/1504.04876) [astro-ph.EP].
- Bayo, A. et al. (Dec. 2008). "VOSA: virtual observatory SED analyzer. An application to the Collinder 69 open cluster". In: *A&A* 492.1, pp. 277–287. DOI: [10.1051/0004-6361:200810395](https://doi.org/10.1051/0004-6361:200810395). arXiv: [0808.0270](https://arxiv.org/abs/0808.0270) [astro-ph].
- Bell, Cameron P. M., Eric E. Mamajek, and Tim Naylor (Nov. 2015). "A self-consistent, absolute isochronal age scale for young moving groups in the solar neighbourhood". In: *MNRAS* 454.1, pp. 593–614. DOI: [10.1093/mnras/stv1981](https://doi.org/10.1093/mnras/stv1981). arXiv: [1508.05955](https://arxiv.org/abs/1508.05955) [astro-ph.SR].
- Benisty, M. et al. (Jan. 2017). "Shadows and spirals in the protoplanetary disk HD 100453". In: *A&A* 597, A42, A42. DOI: [10.1051/0004-6361/201629798](https://doi.org/10.1051/0004-6361/201629798). arXiv: [1610.10089](https://arxiv.org/abs/1610.10089) [astro-ph.EP].

- Benítez-Llambay, Pablo, Leonardo Krapp, and Martin E. Pessah (Apr. 2019). “Asymptotically Stable Numerical Method for Multispecies Momentum Transfer: Gas and Multi-fluid Dust Test Suite and Implementation in FARGO3D”. In: *ApJ Supplement* 241.2, 25, p. 25. DOI: [10.3847/1538-4365/ab0a0e](https://doi.org/10.3847/1538-4365/ab0a0e). arXiv: [1811.07925](https://arxiv.org/abs/1811.07925) [astro-ph.EP].
- Benítez-Llambay, Pablo and Frédéric S. Masset (Mar. 2016). “FARGO3D: A New GPU-oriented MHD Code”. In: *ApJ Supplement* 223.1, 11, p. 11. DOI: [10.3847/0067-0049/223/1/11](https://doi.org/10.3847/0067-0049/223/1/11). arXiv: [1602.02359](https://arxiv.org/abs/1602.02359) [astro-ph.IM].
- Beuzit, J. L. et al. (Nov. 2019). “SPHERE: the exoplanet imager for the Very Large Telescope”. In: *A&A* 631, A155, A155. DOI: [10.1051/0004-6361/201935251](https://doi.org/10.1051/0004-6361/201935251). arXiv: [1902.04080](https://arxiv.org/abs/1902.04080) [astro-ph.IM].
- Birnstiel, T. et al. (June 2010). “Testing the theory of grain growth and fragmentation by millimeter observations of protoplanetary disks”. In: *A&A* 516, L14, p. L14. DOI: [10.1051/0004-6361/201014893](https://doi.org/10.1051/0004-6361/201014893). arXiv: [1006.0940](https://arxiv.org/abs/1006.0940) [astro-ph.SR].
- Bjorkman, J. E. and Kenneth Wood (June 2001). “Radiative Equilibrium and Temperature Correction in Monte Carlo Radiation Transfer”. In: *ApJ* 554.1, pp. 615–623. DOI: [10.1086/321336](https://doi.org/10.1086/321336). arXiv: [astro-ph/0103249](https://arxiv.org/abs/astro-ph/0103249) [astro-ph].
- Boccaletti, A. et al. (Dec. 2013). “Multiple spiral patterns in the transitional disk of HD 100546”. In: *A&A* 560, A20, A20. DOI: [10.1051/0004-6361/201322365](https://doi.org/10.1051/0004-6361/201322365). arXiv: [1310.7092](https://arxiv.org/abs/1310.7092) [astro-ph.EP].
- Boccaletti, A. et al. (June 2018). “Observations of fast-moving features in the debris disk of AU Mic on a three-year timescale: Confirmation and new discoveries”. In: *A&A* 614, A52, A52. DOI: [10.1051/0004-6361/201732462](https://doi.org/10.1051/0004-6361/201732462). arXiv: [1803.05354](https://arxiv.org/abs/1803.05354) [astro-ph.EP].
- Boccaletti, A. et al. (May 2020). “Possible evidence of ongoing planet formation in AB Aurigae. A showcase of the SPHERE/ALMA synergy”. In: *A&A* 637, L5, p. L5. DOI: [10.1051/0004-6361/202038008](https://doi.org/10.1051/0004-6361/202038008). arXiv: [2005.09064](https://arxiv.org/abs/2005.09064) [astro-ph.EP].
- Bodenheimer, P. and J. B. Pollack (Sept. 1986). “Calculations of the accretion and evolution of giant planets: The effects of solid cores”. In: 67.3, pp. 391–408. DOI: [10.1016/0019-1035\(86\)90122-3](https://doi.org/10.1016/0019-1035(86)90122-3).
- Astronomy at High Angular Resolution* (Jan. 2016). Vol. 439. Astrophysics and Space Science Library. DOI: [10.1007/978-3-319-39739-9](https://doi.org/10.1007/978-3-319-39739-9).
- Bohn, A. J. et al. (Feb. 2020). “The Young Suns Exoplanet Survey: Detection of a wide-orbit planetary-mass companion to a solar-type Sco-Cen member”. In: *MNRAS* 492.1, pp. 431–443. DOI: [10.1093/mnras/stz3462](https://doi.org/10.1093/mnras/stz3462). arXiv: [1912.04284](https://arxiv.org/abs/1912.04284) [astro-ph.EP].
- Bohren, Craig F. and Donald R. Huffman (1983). *Absorption and scattering of light by small particles*.
- Bonnefoy, M. et al. (Mar. 2016). “First light of the VLT planet finder SPHERE. IV. Physical and chemical properties of the planets around HR8799”. In: *A&A* 587, A58, A58. DOI: [10.1051/0004-6361/201526906](https://doi.org/10.1051/0004-6361/201526906). arXiv: [1511.04082](https://arxiv.org/abs/1511.04082) [astro-ph.EP].
- Borucki, William J. (Mar. 2016). “KEPLER Mission: development and overview”. In: *Reports on Progress in Physics* 79.3, 036901, p. 036901. DOI: [10.1088/0034-4885/79/3/036901](https://doi.org/10.1088/0034-4885/79/3/036901).
- Boss, A. P. (Jan. 1997). “Giant planet formation by gravitational instability.” In: *Science* 276, pp. 1836–1839. DOI: [10.1126/science.276.5320.1836](https://doi.org/10.1126/science.276.5320.1836).

- Bowler, Brendan P. et al. (Jan. 2017). "Planets around Low-mass Stars (PALMS). VI. Discovery of a Remarkably Red Planetary-mass Companion to the AB Dor Moving Group Candidate 2MASS J22362452+4751425*". In: *Astronomical Journal* 153.1, 18, p. 18. DOI: [10.3847/1538-3881/153/1/18](https://doi.org/10.3847/1538-3881/153/1/18). arXiv: [1611.00364](https://arxiv.org/abs/1611.00364) [astro-ph.EP].
- Brandt, Timothy D. et al. (May 2014). "The Moving Group Targets of the SEEDS High-contrast Imaging Survey of Exoplanets and Disks: Results and Observations from the First Three Years". In: *ApJ* 786.1, 1, p. 1. DOI: [10.1088/0004-637X/786/1/1](https://doi.org/10.1088/0004-637X/786/1/1). arXiv: [1305.7264](https://arxiv.org/abs/1305.7264) [astro-ph.EP].
- Bressan, Alessandro et al. (Nov. 2012). "PARSEC: stellar tracks and isochrones with the PADova and TRIeste Stellar Evolution Code". In: *MNRAS* 427.1, pp. 127–145. DOI: [10.1111/j.1365-2966.2012.21948.x](https://doi.org/10.1111/j.1365-2966.2012.21948.x). arXiv: [1208.4498](https://arxiv.org/abs/1208.4498) [astro-ph.SR].
- Brown-Sevilla, S. B. et al. (Oct. 2021). "A multiwavelength analysis of the spiral arms in the protoplanetary disk around WaOph 6". In: *A&A* 654, A35, A35. DOI: [10.1051/0004-6361/202140783](https://doi.org/10.1051/0004-6361/202140783). arXiv: [2107.13560](https://arxiv.org/abs/2107.13560) [astro-ph.EP].
- Brown Sevilla, Samantha B. et al. (July 2019). "High-contrast Imaging Study on the Candidate Companions Around the Star AH Lep". In: *Research Notes of the American Astronomical Society* 3.7, 100, p. 100. DOI: [10.3847/2515-5172/ab336d](https://doi.org/10.3847/2515-5172/ab336d).
- Buchner, Johannes (July 2014). "A statistical test for Nested Sampling algorithms". In: *arXiv e-prints*, arXiv:1407.5459, arXiv:1407.5459. arXiv: [1407.5459](https://arxiv.org/abs/1407.5459) [stat.CO].
- Burleigh, M. R., M. A. Barstow, and J. B. Holberg (Oct. 1998). "A search for hidden white dwarfs in the ROSATEUV survey - II. Discovery of a distant DA+F6/7V binary system in a direction of low-density neutral hydrogen". In: *MNRAS* 300.2, pp. 511–527. DOI: [10.1046/j.1365-8711.1998.01914.x](https://doi.org/10.1046/j.1365-8711.1998.01914.x). arXiv: [astro-ph/9806269](https://arxiv.org/abs/astro-ph/9806269) [astro-ph].
- Burningham, Ben et al. (Sept. 2017). "Retrieval of atmospheric properties of cloudy L dwarfs". In: *MNRAS* 470.1, pp. 1177–1197. DOI: [10.1093/mnras/stx1246](https://doi.org/10.1093/mnras/stx1246). arXiv: [1701.01257](https://arxiv.org/abs/1701.01257) [astro-ph.SR].
- Burningham, Ben et al. (Sept. 2021). "Cloud busting: enstatite and quartz clouds in the atmosphere of 2M2224-0158". In: *MNRAS* 506.2, pp. 1944–1961. DOI: [10.1093/mnras/stab1361](https://doi.org/10.1093/mnras/stab1361). arXiv: [2105.04268](https://arxiv.org/abs/2105.04268) [astro-ph.SR].
- Calcino, Josh et al. (Aug. 2020). "Are the spiral arms in the MWC 758 protoplanetary disc driven by a companion inside the cavity?" In: *MNRAS* 498.1, pp. 639–650. DOI: [10.1093/mnras/staa2468](https://doi.org/10.1093/mnras/staa2468). arXiv: [2007.06155](https://arxiv.org/abs/2007.06155) [astro-ph.EP].
- Cameron, A. G. W. (Feb. 1978). "Physics of the Primitive Solar Accretion Disk". In: *Moon and Planets* 18.1, pp. 5–40. DOI: [10.1007/BF00896696](https://doi.org/10.1007/BF00896696).
- Campbell, Bruce, G. A. H. Walker, and S. Yang (Aug. 1988). "A Search for Substellar Companions to Solar-type Stars". In: *ApJ* 331, p. 902. DOI: [10.1086/166608](https://doi.org/10.1086/166608).
- Cantalloube, F. et al. (Oct. 2015). "Direct exoplanet detection and characterization using the ANDROMEDA method: Performance on VLT/NaCo data". In: *A&A* 582, A89, A89. DOI: [10.1051/0004-6361/201425571](https://doi.org/10.1051/0004-6361/201425571). arXiv: [1508.06406](https://arxiv.org/abs/1508.06406) [astro-ph.IM].
- Carillet, Marcel et al. (May 2011). "Apodized Lyot coronagraph for SPHERE/VLT. I. Detailed numerical study". In: *Experimental Astronomy* 30.1, pp. 39–58. DOI: [10.1007/s10686-011-9219-4](https://doi.org/10.1007/s10686-011-9219-4).

- Carrión-González, Ó. et al. (Aug. 2020). “Directly imaged exoplanets in reflected starlight: the importance of knowing the planet radius”. In: *A&A* 640, A136, A136. DOI: [10.1051/0004-6361/202038101](https://doi.org/10.1051/0004-6361/202038101). arXiv: [2006.08784](https://arxiv.org/abs/2006.08784) [astro-ph.EP].
- Cazzoletti, P. et al. (Nov. 2018). “Evidence for a massive dust-trapping vortex connected to spirals. Multi-wavelength analysis of the HD 135344B protoplanetary disk”. In: *A&A* 619, A161, A161. DOI: [10.1051/0004-6361/201834006](https://doi.org/10.1051/0004-6361/201834006). arXiv: [1809.04160](https://arxiv.org/abs/1809.04160) [astro-ph.EP].
- Chachan, Yayaati, Eve J. Lee, and Heather A. Knutson (Sept. 2021). “Radial Gradients in Dust-to-gas Ratio Lead to Preferred Region for Giant Planet Formation”. In: *ApJ* 919.1, 63, p. 63. DOI: [10.3847/1538-4357/ac0bb6](https://doi.org/10.3847/1538-4357/ac0bb6). arXiv: [2101.10333](https://arxiv.org/abs/2101.10333) [astro-ph.EP].
- Chauvin, G. et al. (Oct. 2004). “A giant planet candidate near a young brown dwarf. Direct VLT/NACO observations using IR wavefront sensing”. In: *A&A* 425, pp. L29–L32. DOI: [10.1051/0004-6361:200400056](https://doi.org/10.1051/0004-6361:200400056). arXiv: [astro-ph/0409323](https://arxiv.org/abs/astro-ph/0409323) [astro-ph].
- Chauvin, G. et al. (Sept. 2017a). “Discovery of a warm, dusty giant planet around HIP 65426”. In: *A&A* 605, L9, p. L9. DOI: [10.1051/0004-6361/201731152](https://doi.org/10.1051/0004-6361/201731152). arXiv: [1707.01413](https://arxiv.org/abs/1707.01413) [astro-ph.EP].
- Chauvin, G. et al. (Dec. 2017b). “SHINE, The SpHere INfrared survey for Exoplanets”. In: *SF2A-2017: Proceedings of the Annual meeting of the French Society of Astronomy and Astrophysics*. Ed. by C. Reylé et al., p. Di.
- Chen, Christine H. et al. (Apr. 2014). “The Spitzer Infrared Spectrograph Debris Disk Catalog. I. Continuum Analysis of Unresolved Targets”. In: *ApJ Supplement* 211.2, 25, p. 25. DOI: [10.1088/0067-0049/211/2/25](https://doi.org/10.1088/0067-0049/211/2/25).
- Chevance, Mélanie et al. (Mar. 2022). “The Life and Times of Giant Molecular Clouds”. In: *arXiv e-prints*, arXiv:2203.09570, arXiv:2203.09570. arXiv: [2203.09570](https://arxiv.org/abs/2203.09570) [astro-ph.GA].
- Chiang, E. I. and P. Goldreich (Nov. 1997). “Spectral Energy Distributions of T Tauri Stars with Passive Circumstellar Disks”. In: *ApJ* 490.1, pp. 368–376. DOI: [10.1086/304869](https://doi.org/10.1086/304869). arXiv: [astro-ph/9706042](https://arxiv.org/abs/astro-ph/9706042) [astro-ph].
- Choi, Jieun et al. (June 2016). “Mesa Isochrones and Stellar Tracks (MIST). I. Solar-scaled Models”. In: *ApJ* 823.2, 102, p. 102. DOI: [10.3847/0004-637X/823/2/102](https://doi.org/10.3847/0004-637X/823/2/102). arXiv: [1604.08592](https://arxiv.org/abs/1604.08592) [astro-ph.SR].
- Cieza, Lucas A. et al. (Dec. 2020). “The Ophiuchus DIsc Survey Employing ALMA (ODISEA)-III: the evolution of substructures in massive discs at 3-5 au resolution”. In: *MNRAS*. DOI: [10.1093/mnras/staa3787](https://doi.org/10.1093/mnras/staa3787). arXiv: [2012.00189](https://arxiv.org/abs/2012.00189) [astro-ph.EP].
- Claudi, R. et al. (Feb. 2019). “SPHERE dynamical and spectroscopic characterization of HD 142527B”. In: *A&A* 622, A96, A96. DOI: [10.1051/0004-6361/201833990](https://doi.org/10.1051/0004-6361/201833990). arXiv: [1812.07814](https://arxiv.org/abs/1812.07814) [astro-ph.SR].
- Claudi, R. U. et al. (July 2008). “SPHERE IFS: the spectro differential imager of the VLT for exoplanets search”. In: *Ground-based and Airborne Instrumentation for Astronomy II*. Ed. by Ian S. McLean and Mark M. Casali. Vol. 7014. Society of Photo-Optical Instrumentation Engineers (SPIE) Conference Series, 70143E, 70143E. DOI: [10.1117/12.788366](https://doi.org/10.1117/12.788366).
- Cotten, Tara H. and Inseok Song (Jan. 2016). “Comprehensive Census and Complete Characterization of Nearby Debris Disk Stars”. In: *Young Stars & Planets Near the Sun*. Ed.

- by J. H. Kastner, B. Stelzer, and S. A. Metchev. Vol. 314, pp. 179–182. DOI: [10.1017/S1743921315006389](https://doi.org/10.1017/S1743921315006389). arXiv: [1510.01142](https://arxiv.org/abs/1510.01142) [astro-ph.SR].
- Cuello, Nicolás et al. (Mar. 2019). “Flybys in protoplanetary discs: I. Gas and dust dynamics”. In: *MNRAS* 483.3, pp. 4114–4139. DOI: [10.1093/mnras/sty3325](https://doi.org/10.1093/mnras/sty3325). arXiv: [1812.00961](https://arxiv.org/abs/1812.00961) [astro-ph.EP].
- Currie, Thayne and Aurora Sicilia-Aguilar (May 2011). “The Transitional Protoplanetary Disk Frequency as a Function of Age: Disk Evolution In the Coronet Cluster, Taurus, and Other 1-8 Myr Old Regions”. In: *ApJ* 732.1, 24, p. 24. DOI: [10.1088/0004-637X/732/1/24](https://doi.org/10.1088/0004-637X/732/1/24). arXiv: [1102.4364](https://arxiv.org/abs/1102.4364) [astro-ph.SR].
- Cushing, Michael C. et al. (Dec. 2011). “The Discovery of Y Dwarfs using Data from the Wide-field Infrared Survey Explorer (WISE)”. In: *ApJ* 743.1, 50, p. 50. DOI: [10.1088/0004-637X/743/1/50](https://doi.org/10.1088/0004-637X/743/1/50). arXiv: [1108.4678](https://arxiv.org/abs/1108.4678) [astro-ph.SR].
- Cutispoto, G. et al. (Oct. 2003). “Fast-rotating Nearby Solar-type Stars”. In: *The Future of Cool-Star Astrophysics: 12th Cambridge Workshop on Cool Stars, Stellar Systems, and the Sun*. Ed. by A. Brown, G. M. Harper, and T. R. Ayres. Vol. 12. Cambridge Workshop on Cool Stars, Stellar Systems, and the Sun, pp. 881–886.
- Cutri, R. M. et al. (2003). *2MASS All Sky Catalog of point sources*.
- Cutri, R. M. et al. (Nov. 2013). *Explanatory Supplement to the AllWISE Data Release Products*. Explanatory Supplement to the AllWISE Data Release Products.
- David, Trevor J. and Lynne A. Hillenbrand (May 2015). “The Ages of Early-type Stars: Strömgren Photometric Methods Calibrated, Validated, Tested, and Applied to Hosts and Prospective Hosts of Directly Imaged Exoplanets”. In: *ApJ* 804.2, 146, p. 146. DOI: [10.1088/0004-637X/804/2/146](https://doi.org/10.1088/0004-637X/804/2/146). arXiv: [1501.03154](https://arxiv.org/abs/1501.03154) [astro-ph.SR].
- de Boer, J. et al. (Jan. 2020). “Polarimetric imaging mode of VLT/SPHERE/IRDIS. I. Description, data reduction, and observing strategy”. In: *A&A* 633, A63, A63. DOI: [10.1051/0004-6361/201834989](https://doi.org/10.1051/0004-6361/201834989). arXiv: [1909.13107](https://arxiv.org/abs/1909.13107) [astro-ph.IM].
- De Rosa, Robert J. et al. (Nov. 2015). “Astrometric Confirmation and Preliminary Orbital Parameters of the Young Exoplanet 51 Eridani b with the Gemini Planet Imager”. In: *ApJ Letters* 814.1, L3, p. L3. DOI: [10.1088/2041-8205/814/1/L3](https://doi.org/10.1088/2041-8205/814/1/L3). arXiv: [1509.07514](https://arxiv.org/abs/1509.07514) [astro-ph.EP].
- Delorme, P. et al. (Dec. 2017). “The SPHERE Data Center: a reference for high contrast imaging processing”. In: *SF2A-2017: Proceedings of the Annual meeting of the French Society of Astronomy and Astrophysics*. Ed. by C. Reylé et al., p. Di. arXiv: [1712.06948](https://arxiv.org/abs/1712.06948) [astro-ph.IM].
- Desgrange, C. et al. (Aug. 2022). “In-depth direct imaging and spectroscopic characterization of the young Solar System analog HD 95086”. In: *A&A* 664, A139, A139. DOI: [10.1051/0004-6361/202243097](https://doi.org/10.1051/0004-6361/202243097). arXiv: [2206.00425](https://arxiv.org/abs/2206.00425) [astro-ph.EP].
- Desidera, S. et al. (Jan. 2015). “The VLT/NaCo large program to probe the occurrence of exoplanets and brown dwarfs in wide orbits. I. Sample definition and characterization”. In: *A&A* 573, A126, A126. DOI: [10.1051/0004-6361/201323168](https://doi.org/10.1051/0004-6361/201323168). arXiv: [1405.1559](https://arxiv.org/abs/1405.1559) [astro-ph.EP].

- Desidera, S. et al. (July 2021). "The SPHERE infrared survey for exoplanets (SHINE). I. Sample definition and target characterization". In: *A&A* 651, A70, A70. DOI: [10.1051/0004-6361/202038806](https://doi.org/10.1051/0004-6361/202038806). arXiv: [2103.04366](https://arxiv.org/abs/2103.04366) [astro-ph.EP].
- Dobbs, C. L. et al. (Jan. 2014). "Formation of Molecular Clouds and Global Conditions for Star Formation". In: *Protostars and Planets VI*. Ed. by Henrik Beuther et al., p. 3. DOI: [10.2458/azu_uapress_9780816531240-ch001](https://doi.org/10.2458/azu_uapress_9780816531240-ch001). arXiv: [1312.3223](https://arxiv.org/abs/1312.3223) [astro-ph.GA].
- Dohlen, Kjetil et al. (July 2008). "The infra-red dual imaging and spectrograph for SPHERE: design and performance". In: *Ground-based and Airborne Instrumentation for Astronomy II*. Ed. by Ian S. McLean and Mark M. Casali. Vol. 7014. Society of Photo-Optical Instrumentation Engineers (SPIE) Conference Series, 70143L, p. 70143L. DOI: [10.1117/12.789786](https://doi.org/10.1117/12.789786).
- Dohnanyi, J. S. (May 1969). "Collisional Model of Asteroids and Their Debris". In: 74, pp. 2531–2554. DOI: [10.1029/JB074i010p02531](https://doi.org/10.1029/JB074i010p02531).
- Dong, Ruobing and Jeffrey Fung (Feb. 2017). "What is the Mass of a Gap-opening Planet?" In: *ApJ* 835.2, 146, p. 146. DOI: [10.3847/1538-4357/835/2/146](https://doi.org/10.3847/1538-4357/835/2/146). arXiv: [1612.04821](https://arxiv.org/abs/1612.04821) [astro-ph.EP].
- Dong, Ruobing, Joan R. Najita, and Sean Brittain (Aug. 2018a). "Spiral Arms in Disks: Planets or Gravitational Instability?" In: *ApJ* 862.2, 103, p. 103. DOI: [10.3847/1538-4357/aaccfc](https://doi.org/10.3847/1538-4357/aaccfc). arXiv: [1806.05183](https://arxiv.org/abs/1806.05183) [astro-ph.SR].
- Dong, Ruobing et al. (Aug. 2015). "Observational Signatures of Planets in Protoplanetary Disks: Spiral Arms Observed in Scattered Light Imaging Can be Induced by Planets". In: *ApJ Letters* 809.1, L5, p. L5. DOI: [10.1088/2041-8205/809/1/L5](https://doi.org/10.1088/2041-8205/809/1/L5). arXiv: [1507.03596](https://arxiv.org/abs/1507.03596) [astro-ph.EP].
- Dong, Ruobing et al. (June 2018b). "The Eccentric Cavity, Triple Rings, Two-armed Spirals, and Double Clumps of the MWC 758 Disk". In: *ApJ* 860.2, 124, p. 124. DOI: [10.3847/1538-4357/aac6cb](https://doi.org/10.3847/1538-4357/aac6cb). arXiv: [1805.12141](https://arxiv.org/abs/1805.12141) [astro-ph.SR].
- Draine, B. T. and H. M. Lee (Oct. 1984). "Optical Properties of Interstellar Graphite and Silicate Grains". In: *ApJ* 285, p. 89. DOI: [10.1086/162480](https://doi.org/10.1086/162480).
- Drazkowska, Joanna et al. (Mar. 2022). "Planet Formation Theory in the Era of ALMA and Kepler: from Pebbles to Exoplanets". In: *arXiv e-prints*, arXiv:2203.09759, arXiv:2203.09759. arXiv: [2203.09759](https://arxiv.org/abs/2203.09759) [astro-ph.EP].
- Dubrulle, B., G. Morfill, and M. Sterzik (1995). "The Dust Subdisk in the Protoplanetary Nebula". In: *Icarus* 114.2, pp. 237–246. ISSN: 0019-1035. DOI: <https://doi.org/10.1006/icar.1995.1058>. URL: <http://www.sciencedirect.com/science/article/pii/S0019103585710585>.
- Dullemond, C. P. et al. (Feb. 2012). *RADMC-3D: A multi-purpose radiative transfer tool*. ascl: [1202.015](https://arxiv.org/abs/1202.015).
- Dupuy, Trent J., G. Mirek Brandt, and Timothy D. Brandt (Jan. 2022). "Limits on the mass and initial entropy of 51 Eri b from Gaia EDR3 astrometry". In: *MNRAS* 509.3, pp. 4411–4419. DOI: [10.1093/mnras/stab3148](https://doi.org/10.1093/mnras/stab3148). arXiv: [2110.13173](https://arxiv.org/abs/2110.13173) [astro-ph.EP].
- Durisen, R. H. et al. (Jan. 2007). "Gravitational Instabilities in Gaseous Protoplanetary Disks and Implications for Giant Planet Formation". In: *Protostars and Planets V*. Ed. by Bo Reipurth, David Jewitt, and Klaus Keil, p. 607. arXiv: [astro-ph/0603179](https://arxiv.org/abs/astro-ph/0603179) [astro-ph].

- Eiroa, C. et al. (July 2013). “DUst around NEarby Stars. The survey observational results”. In: *A&A* 555, A11, A11. DOI: [10.1051/0004-6361/201321050](https://doi.org/10.1051/0004-6361/201321050). arXiv: [1305.0155](https://arxiv.org/abs/1305.0155) [astro-ph.SR].
- Eisner, J. A. et al. (Apr. 2005). “Observations of T Tauri Disks at Sub-AU Radii: Implications for Magnetospheric Accretion and Planet Formation”. In: *ApJ* 623.2, pp. 952–966. DOI: [10.1086/428828](https://doi.org/10.1086/428828). arXiv: [astro-ph/0501308](https://arxiv.org/abs/astro-ph/0501308) [astro-ph].
- Espaillet, C. et al. (Jan. 2014). “An Observational Perspective of Transitional Disks”. In: *Protostars and Planets VI*. Ed. by Henrik Beuther et al., p. 497. DOI: [10.2458/azu_uapress_9780816531240-ch022](https://doi.org/10.2458/azu_uapress_9780816531240-ch022). arXiv: [1402.7103](https://arxiv.org/abs/1402.7103) [astro-ph.SR].
- Esposito, Thomas M. et al. (July 2020). “Debris Disk Results from the Gemini Planet Imager Exoplanet Survey’s Polarimetric Imaging Campaign”. In: *Astronomical Journal* 160.1, 24, p. 24. DOI: [10.3847/1538-3881/ab9199](https://doi.org/10.3847/1538-3881/ab9199). arXiv: [2004.13722](https://arxiv.org/abs/2004.13722) [astro-ph.EP].
- Evans Neal J., II et al. (Apr. 2009). “The Spitzer c2d Legacy Results: Star-Formation Rates and Efficiencies; Evolution and Lifetimes”. In: *ApJ Supplement* 181.2, pp. 321–350. DOI: [10.1088/0067-0049/181/2/321](https://doi.org/10.1088/0067-0049/181/2/321). arXiv: [0811.1059](https://arxiv.org/abs/0811.1059) [astro-ph].
- Fang, Julia and J. Margot (Jan. 2013). “Architecture of Planetary Systems Based on Kepler Data: Number of Planets, Coplanarity, and Packing”. In: *American Astronomical Society Meeting Abstracts #221*. Vol. 221. American Astronomical Society Meeting Abstracts, 407.01, p. 407.01.
- Feigelson, E. D. et al. (Mar. 2006). “51 Eridani and GJ 3305: A 10-15 Myr old Binary Star System at 30 Parsecs”. In: *Astronomical Journal* 131.3, pp. 1730–1739. DOI: [10.1086/499923](https://doi.org/10.1086/499923). arXiv: [astro-ph/0511618](https://arxiv.org/abs/astro-ph/0511618) [astro-ph].
- Feroz, F. and M. P. Hobson (Feb. 2008). “Multimodal nested sampling: an efficient and robust alternative to Markov Chain Monte Carlo methods for astronomical data analyses”. In: *MNRAS* 384.2, pp. 449–463. DOI: [10.1111/j.1365-2966.2007.12353.x](https://doi.org/10.1111/j.1365-2966.2007.12353.x). arXiv: [0704.3704](https://arxiv.org/abs/0704.3704) [astro-ph].
- Feroz, F., M. P. Hobson, and M. Bridges (Oct. 2009). “MULTINEST: an efficient and robust Bayesian inference tool for cosmology and particle physics”. In: *MNRAS* 398.4, pp. 1601–1614. DOI: [10.1111/j.1365-2966.2009.14548.x](https://doi.org/10.1111/j.1365-2966.2009.14548.x). arXiv: [0809.3437](https://arxiv.org/abs/0809.3437) [astro-ph].
- Feroz, Farhan et al. (Nov. 2019). “Importance Nested Sampling and the MultiNest Algorithm”. In: *The Open Journal of Astrophysics* 2.1, 10, p. 10. DOI: [10.21105/astro.1306.2144](https://doi.org/10.21105/astro.1306.2144). arXiv: [1306.2144](https://arxiv.org/abs/1306.2144) [astro-ph.IM].
- Foreman-Mackey, Daniel et al. (Mar. 2013). “emcee: The MCMC Hammer”. In: *PASP* 125.925, p. 306. DOI: [10.1086/670067](https://doi.org/10.1086/670067). arXiv: [1202.3665](https://arxiv.org/abs/1202.3665) [astro-ph.IM].
- Freudling, W. et al. (Nov. 2013). “Automated data reduction workflows for astronomy. The ESO Reflex environment”. In: *A&A* 559, A96, A96. DOI: [10.1051/0004-6361/201322494](https://doi.org/10.1051/0004-6361/201322494). arXiv: [1311.5411](https://arxiv.org/abs/1311.5411) [astro-ph.IM].
- Friebe, Marc F., Tim D. Pearce, and Torsten Löhne (May 2022). “Gap carving by a migrating planet embedded in a massive debris disc”. In: *MNRAS* 512.3, pp. 4441–4454. DOI: [10.1093/mnras/stac664](https://doi.org/10.1093/mnras/stac664). arXiv: [2203.03611](https://arxiv.org/abs/2203.03611) [astro-ph.EP].

- Fromang, S., W. Lyra, and F. Masset (Oct. 2011). “Meridional circulation in turbulent protoplanetary disks”. In: *A&A* 534, A107, A107. DOI: [10.1051/0004-6361/201016068](https://doi.org/10.1051/0004-6361/201016068). arXiv: [1102.0671](https://arxiv.org/abs/1102.0671) [astro-ph.EP].
- Fung, Jeffrey and Ruobing Dong (Dec. 2015). “Inferring Planet Mass from Spiral Structures in Protoplanetary Disks”. In: *ApJ Letters* 815.2, L21, p. L21. DOI: [10.1088/2041-8205/815/2/L21](https://doi.org/10.1088/2041-8205/815/2/L21). arXiv: [1511.01178](https://arxiv.org/abs/1511.01178) [astro-ph.EP].
- Gaia Collaboration (Apr. 2018). “VizieR Online Data Catalog: Gaia DR2 (Gaia Collaboration, 2018)”. In: *VizieR Online Data Catalog*, I/345, pp. I/345.
- Gaia Collaboration et al. (Nov. 2016). “The Gaia mission”. In: *A&A* 595, A1, A1. DOI: [10.1051/0004-6361/201629272](https://doi.org/10.1051/0004-6361/201629272). arXiv: [1609.04153](https://arxiv.org/abs/1609.04153) [astro-ph.IM].
- Gaia Collaboration et al. (Dec. 2020). “Gaia Early Data Release 3: The Gaia Catalogue of Nearby Stars”. In: *arXiv e-prints*, arXiv:2012.02061, arXiv:2012.02061. arXiv: [2012.02061](https://arxiv.org/abs/2012.02061) [astro-ph.SR].
- Gaia Collaboration et al. (May 2021). “Gaia Early Data Release 3. Summary of the contents and survey properties”. In: *A&A* 649, A1, A1. DOI: [10.1051/0004-6361/202039657](https://doi.org/10.1051/0004-6361/202039657). arXiv: [2012.01533](https://arxiv.org/abs/2012.01533) [astro-ph.GA].
- Gaia Collaboration et al. (July 2022). “Gaia Data Release 3: Summary of the content and survey properties”. In: *arXiv e-prints*, arXiv:2208.00211, arXiv:2208.00211. arXiv: [2208.00211](https://arxiv.org/abs/2208.00211) [astro-ph.GA].
- Galicher, R. et al. (July 2018). “Astrometric and photometric accuracies in high contrast imaging: The SPHERE speckle calibration tool (SpeCal)”. In: *A&A* 615, A92, A92. DOI: [10.1051/0004-6361/201832973](https://doi.org/10.1051/0004-6361/201832973). arXiv: [1805.04854](https://arxiv.org/abs/1805.04854) [astro-ph.IM].
- Garufi, A. et al. (Dec. 2018). “Evolution of protoplanetary disks from their taxonomy in scattered light: spirals, rings, cavities, and shadows”. In: *A&A* 620, A94, A94. DOI: [10.1051/0004-6361/201833872](https://doi.org/10.1051/0004-6361/201833872). arXiv: [1810.04564](https://arxiv.org/abs/1810.04564) [astro-ph.SR].
- Gerbig, Konstantin, Christian T. Lenz, and Hubert Klahr (Sept. 2019). “Linking planetesimal and dust content in protoplanetary disks via a local toy model”. In: *A&A* 629, A116, A116. DOI: [10.1051/0004-6361/201935278](https://doi.org/10.1051/0004-6361/201935278). arXiv: [1908.02608](https://arxiv.org/abs/1908.02608) [astro-ph.EP].
- Giles, H. A. C. et al. (July 2018). “Transiting planet candidate from K2 with the longest period”. In: *A&A* 615, L13, p. L13. DOI: [10.1051/0004-6361/201833569](https://doi.org/10.1051/0004-6361/201833569). arXiv: [1806.08757](https://arxiv.org/abs/1806.08757) [astro-ph.EP].
- Girard, Julien H. et al. (Aug. 2022). “JWST/NIRCam coronagraphy: commissioning and first on-sky results”. In: *Space Telescopes and Instrumentation 2022: Optical, Infrared, and Millimeter Wave*. Ed. by Laura E. Coyle, Shuji Matsuura, and Marshall D. Perrin. Vol. 12180. Society of Photo-Optical Instrumentation Engineers (SPIE) Conference Series, 121803Q, 121803Q. DOI: [10.1117/12.2629636](https://doi.org/10.1117/12.2629636). arXiv: [2208.00998](https://arxiv.org/abs/2208.00998) [astro-ph.IM].
- Goldreich, P. and S. Tremaine (Nov. 1979). “The excitation of density waves at the Lindblad and corotation resonances by an external potential.” In: *ApJ* 233, pp. 857–871. DOI: [10.1086/157448](https://doi.org/10.1086/157448).
- Golimowski, D. A. et al. (July 2011). “Hubble and Spitzer Space Telescope Observations of the Debris Disk around the nearby K Dwarf HD 92945”. In: *Astronomical Journal* 142.1, 30, p. 30. DOI: [10.1088/0004-6256/142/1/30](https://doi.org/10.1088/0004-6256/142/1/30). arXiv: [1105.0888](https://arxiv.org/abs/1105.0888) [astro-ph.SR].

- Gomez Gonzalez, Carlos Alberto et al. (July 2017). "VIP: Vortex Image Processing Package for High-contrast Direct Imaging". In: *Astronomical Journal* 154.1, 7, p. 7. DOI: [10.3847/1538-3881/aa73d7](https://doi.org/10.3847/1538-3881/aa73d7). arXiv: [1705.06184](https://arxiv.org/abs/1705.06184) [astro-ph.IM].
- Greco, Johnny P. and Timothy D. Brandt (Dec. 2016). "The Measurement, Treatment, and Impact of Spectral Covariance and Bayesian Priors in Integral-field Spectroscopy of Exoplanets". In: *ApJ* 833.2, 134, p. 134. DOI: [10.3847/1538-4357/833/2/134](https://doi.org/10.3847/1538-4357/833/2/134). arXiv: [1602.00691](https://arxiv.org/abs/1602.00691) [astro-ph.EP].
- Hauschildt, Peter H. et al. (Nov. 1999). "The NEXTGEN Model Atmosphere Grid. II. Spherically Symmetric Model Atmospheres for Giant Stars with Effective Temperatures between 3000 and 6800 K". In: *ApJ* 525.2, pp. 871–880. DOI: [10.1086/307954](https://doi.org/10.1086/307954). arXiv: [astro-ph/9907194](https://arxiv.org/abs/astro-ph/9907194) [astro-ph].
- Henize, K. G. (Apr. 1976). "Observations of southern emission-line stars." In: *ApJ Supplement* 30, pp. 491–550. DOI: [10.1086/190369](https://doi.org/10.1086/190369).
- Herschel Point Source Catalogue Working Group et al. (July 2020). "VizieR Online Data Catalog: Herschel/PACS Point Source Catalogs (Herschel team, 2017)". In: *VizieR Online Data Catalog*, VIII/106, pp. VIII/106.
- Hildebrand, R. H. (Sept. 1983). "The determination of cloud masses and dust characteristics from submillimetre thermal emission". In: *Quarterly Journal of the RAS* 24, pp. 267–282.
- Hoeg, E. et al. (July 1997). "The TYCHO Catalogue". In: *A&A* 323, pp. L57–L60.
- Høg, E. et al. (Mar. 2000). "The Tycho-2 catalogue of the 2.5 million brightest stars". In: *A&A* 355, pp. L27–L30.
- Huang, Jane et al. (Dec. 2018a). "The Disk Substructures at High Angular Resolution Project (DSHARP). II. Characteristics of Annular Substructures". In: *ApJ Letters* 869.2, L42, p. L42. DOI: [10.3847/2041-8213/aaf740](https://doi.org/10.3847/2041-8213/aaf740). arXiv: [1812.04041](https://arxiv.org/abs/1812.04041) [astro-ph.EP].
- Huang, Jane et al. (Dec. 2018b). "The Disk Substructures at High Angular Resolution Project (DSHARP). III. Spiral Structures in the Millimeter Continuum of the Elias 27, IM Lup, and WaOph 6 Disks". In: *ApJ Letters* 869.2, L43, p. L43. DOI: [10.3847/2041-8213/aaf7a0](https://doi.org/10.3847/2041-8213/aaf7a0). arXiv: [1812.04193](https://arxiv.org/abs/1812.04193) [astro-ph.SR].
- Hubeny, Ivan (July 2017). "Model atmospheres of sub-stellar mass objects". In: *MNRAS* 469.1, pp. 841–869. DOI: [10.1093/mnras/stx758](https://doi.org/10.1093/mnras/stx758). arXiv: [1703.09283](https://arxiv.org/abs/1703.09283) [astro-ph.SR].
- Infrared Astronomical Satellite (IRAS) Catalogs and Atlases. Volume 7: The Small Scale Structure Catalog.* (Jan. 1988). Vol. 7.
- Isella, Andrea, John M. Carpenter, and Anneila I. Sargent (Aug. 2009). "Structure and Evolution of Pre-main-sequence Circumstellar Disks". In: *ApJ* 701.1, pp. 260–282. DOI: [10.1088/0004-637X/701/1/260](https://doi.org/10.1088/0004-637X/701/1/260). arXiv: [0906.2227](https://arxiv.org/abs/0906.2227) [astro-ph.SR].
- Isella, Andrea et al. (July 2019). "Detection of Continuum Submillimeter Emission Associated with Candidate Protoplanets". In: *ApJ Letters* 879.2, L25, p. L25. DOI: [10.3847/2041-8213/ab2a12](https://doi.org/10.3847/2041-8213/ab2a12). arXiv: [1906.06308](https://arxiv.org/abs/1906.06308) [astro-ph.EP].
- Janson, M. et al. (Feb. 2010). "Spatially Resolved Spectroscopy of the Exoplanet HR 8799 c". In: *ApJ Letters* 710.1, pp. L35–L38. DOI: [10.1088/2041-8205/710/1/L35](https://doi.org/10.1088/2041-8205/710/1/L35). arXiv: [1001.2017](https://arxiv.org/abs/1001.2017) [astro-ph.EP].

- Janson, Markus et al. (June 2019). “The B-Star Exoplanet Abundance Study: a co-moving 16–25 M_{Jup} companion to the young binary system HIP 79098”. In: *A&A* 626, A99, A99. DOI: [10.1051/0004-6361/201935687](https://doi.org/10.1051/0004-6361/201935687). arXiv: [1906.02787](https://arxiv.org/abs/1906.02787) [astro-ph.EP].
- Jennings, Jeff et al. (May 2020). “frankenstein: protoplanetary disc brightness profile reconstruction at sub-beam resolution with a rapid Gaussian process”. In: *MNRAS* 495.3, pp. 3209–3232. DOI: [10.1093/mnras/staa1365](https://doi.org/10.1093/mnras/staa1365). arXiv: [2005.07709](https://arxiv.org/abs/2005.07709) [astro-ph.EP].
- Jorquera, Sebastián et al. (Dec. 2020). “A search for companions via direct imaging in the DSHARP planet-forming disks”. In: *arXiv e-prints*, arXiv:2012.10464, arXiv:2012.10464. arXiv: [2012.10464](https://arxiv.org/abs/2012.10464) [astro-ph.EP].
- Juhász, A. et al. (Aug. 2015). “Spiral arms in scattered light images of protoplanetary discs: are they the signposts of planets?” In: *MNRAS* 451.2, pp. 1147–1157. DOI: [10.1093/mnras/stv1045](https://doi.org/10.1093/mnras/stv1045). arXiv: [1412.3412](https://arxiv.org/abs/1412.3412) [astro-ph.EP].
- Kalas, Paul, Michael P. Fitzgerald, and James R. Graham (May 2007). “Discovery of Extreme Asymmetry in the Debris Disk Surrounding HD 15115”. In: *ApJ Letters* 661.1, pp. L85–L88. DOI: [10.1086/518652](https://doi.org/10.1086/518652). arXiv: [0704.0645](https://arxiv.org/abs/0704.0645) [astro-ph].
- Kalas, Paul, James R. Graham, and Mark Clampin (June 2005). “A planetary system as the origin of structure in Fomalhaut’s dust belt”. In: *Nature* 435.7045, pp. 1067–1070. DOI: [10.1038/nature03601](https://doi.org/10.1038/nature03601). arXiv: [astro-ph/0506574](https://arxiv.org/abs/astro-ph/0506574) [astro-ph].
- Kammerer, J. et al. (Aug. 2021). “GRAVITY K-band spectroscopy of HD 206893 B. Brown dwarf or exoplanet”. In: *A&A* 652, A57, A57. DOI: [10.1051/0004-6361/202140749](https://doi.org/10.1051/0004-6361/202140749). arXiv: [2106.08249](https://arxiv.org/abs/2106.08249) [astro-ph.EP].
- Kasper, M. et al. (Sept. 2007). “A novel L-band imaging search for giant planets in the Tucana and β Pictoris moving groups”. In: *A&A* 472.1, pp. 321–327. DOI: [10.1051/0004-6361:20077646](https://doi.org/10.1051/0004-6361:20077646). arXiv: [0706.0095](https://arxiv.org/abs/0706.0095) [astro-ph].
- Kataoka, Akimasa et al. (Mar. 2016). “Grain Size Constraints on HL Tau with Polarization Signature”. In: *ApJ* 820.1, 54, p. 54. DOI: [10.3847/0004-637X/820/1/54](https://doi.org/10.3847/0004-637X/820/1/54). arXiv: [1507.08902](https://arxiv.org/abs/1507.08902) [astro-ph.EP].
- Kennedy, G. M. and M. C. Wyatt (Nov. 2014). “Do two-temperature debris discs have multiple belts?” In: *MNRAS* 444.4, pp. 3164–3182. DOI: [10.1093/mnras/stu1665](https://doi.org/10.1093/mnras/stu1665). arXiv: [1408.4116](https://arxiv.org/abs/1408.4116) [astro-ph.EP].
- Kenyon, Scott J. and Benjamin C. Bromley (Mar. 2002). “Collisional Cascades in Planetesimal Disks. I. Stellar Flybys”. In: *Astronomical Journal* 123.3, pp. 1757–1775. DOI: [10.1086/338850](https://doi.org/10.1086/338850). arXiv: [astro-ph/0111384](https://arxiv.org/abs/astro-ph/0111384) [astro-ph].
- (Jan. 2004). “Collisional Cascades in Planetesimal Disks. II. Embedded Planets”. In: *Astronomical Journal* 127.1, pp. 513–530. DOI: [10.1086/379854](https://doi.org/10.1086/379854). arXiv: [astro-ph/0309540](https://arxiv.org/abs/astro-ph/0309540) [astro-ph].
- Keppler, M. et al. (Sept. 2018). “Discovery of a planetary-mass companion within the gap of the transition disk around PDS 70”. In: *A&A* 617, A44, A44. DOI: [10.1051/0004-6361/201832957](https://doi.org/10.1051/0004-6361/201832957). arXiv: [1806.11568](https://arxiv.org/abs/1806.11568) [astro-ph.EP].
- Keppler, M. et al. (July 2020). “Gap, shadows, spirals, and streamers: SPHERE observations of binary-disk interactions in GG Tauri A”. In: *A&A* 639, A62, A62. DOI: [10.1051/0004-6361/202038032](https://doi.org/10.1051/0004-6361/202038032). arXiv: [2005.09037](https://arxiv.org/abs/2005.09037) [astro-ph.SR].

- Kervella, P., F. Arenou, and F. Thevenin (Sept. 2021). “VizieR Online Data Catalog: Stellar and substellar companions from Gaia EDR3 (Kervella+, 2022)”. In: *VizieR Online Data Catalog*, J/A+A/657/A7, J/A+A/657/A7.
- Kinoshita, Shinichi. W., Fumitaka Nakamura, and Benjamin Wu (Nov. 2021). “Star Formation Triggered by Shocks”. In: *ApJ* 921.2, 150, p. 150. DOI: [10.3847/1538-4357/ac1d4b](https://doi.org/10.3847/1538-4357/ac1d4b).
- Kirkpatrick, J. Davy (Sept. 2005). “New Spectral Types L and T”. In: *Annu. Rev. Astron. Astrophys* 43.1, pp. 195–245. DOI: [10.1146/annurev.astro.42.053102.134017](https://doi.org/10.1146/annurev.astro.42.053102.134017).
- Klahr, H. and W. Kley (Jan. 2006). “3D-radiation hydro simulations of disk-planet interactions. I. Numerical algorithm and test cases”. In: *A&A* 445.2, pp. 747–758. DOI: [10.1051/0004-6361:20053238](https://doi.org/10.1051/0004-6361:20053238). arXiv: [astro-ph/0510391](https://arxiv.org/abs/astro-ph/0510391) [astro-ph].
- Kley, Wilhelm (Jan. 2019). “Planet Formation and Disk-Planet Interactions”. In: *Saas-Fee Advanced Course* 45, p. 151. DOI: [10.1007/978-3-662-58687-7_2](https://doi.org/10.1007/978-3-662-58687-7_2).
- Konopacky, Quinn M. et al. (July 2014). “Gemini planet imager observational calibrations V: astrometry and distortion”. In: *Ground-based and Airborne Instrumentation for Astronomy V*. Ed. by Suzanne K. Ramsay, Ian S. McLean, and Hideki Takami. Vol. 9147. Society of Photo-Optical Instrumentation Engineers (SPIE) Conference Series, 914784, p. 914784. DOI: [10.1117/12.2056646](https://doi.org/10.1117/12.2056646). arXiv: [1407.2305](https://arxiv.org/abs/1407.2305) [astro-ph.IM].
- Kral, Q. (Dec. 2016). “Review of gas and dust in debris discs”. In: *SF2A-2016: Proceedings of the Annual meeting of the French Society of Astronomy and Astrophysics*. Ed. by C. Reylé et al., pp. 463–472. arXiv: [1611.06751](https://arxiv.org/abs/1611.06751) [astro-ph.EP].
- Kreidberg, Laura et al. (Jan. 2014). “Clouds in the atmosphere of the super-Earth exoplanet GJ1214b”. In: *Nature* 505.7481, pp. 69–72. DOI: [10.1038/nature12888](https://doi.org/10.1038/nature12888). arXiv: [1401.0022](https://arxiv.org/abs/1401.0022) [astro-ph.EP].
- Krivov, Alexander V. (May 2010). “Debris disks: seeing dust, thinking of planetesimals and planets”. In: *Research in Astronomy and Astrophysics* 10.5, pp. 383–414. DOI: [10.1088/1674-4527/10/5/001](https://doi.org/10.1088/1674-4527/10/5/001). arXiv: [1003.5229](https://arxiv.org/abs/1003.5229) [astro-ph.EP].
- Kuhn, J. R., D. Potter, and B. Parise (June 2001). “Imaging Polarimetric Observations of a New Circumstellar Disk System”. In: *ApJ Letters* 553.2, pp. L189–L191. DOI: [10.1086/320686](https://doi.org/10.1086/320686). arXiv: [astro-ph/0105239](https://arxiv.org/abs/astro-ph/0105239) [astro-ph].
- Kurtovic, Nicolás T. et al. (Dec. 2018). “The Disk Substructures at High Angular Resolution Project (DSHARP). IV. Characterizing Substructures and Interactions in Disks around Multiple Star Systems”. In: *ApJ Letters* 869.2, L44, p. L44. DOI: [10.3847/2041-8213/aaf746](https://doi.org/10.3847/2041-8213/aaf746). arXiv: [1812.04536](https://arxiv.org/abs/1812.04536) [astro-ph.SR].
- Lafrenière, David et al. (May 2007). “A New Algorithm for Point-Spread Function Subtraction in High-Contrast Imaging: A Demonstration with Angular Differential Imaging”. In: *ApJ* 660.1, pp. 770–780. DOI: [10.1086/513180](https://doi.org/10.1086/513180). arXiv: [astro-ph/0702697](https://arxiv.org/abs/astro-ph/0702697) [astro-ph].
- Lafrenière, David et al. (Apr. 2009). “HST/NICMOS Detection of HR 8799 b in 1998”. In: *ApJ Letters* 694.2, pp. L148–L152. DOI: [10.1088/0004-637X/694/2/L148](https://doi.org/10.1088/0004-637X/694/2/L148). arXiv: [0902.3247](https://arxiv.org/abs/0902.3247) [astro-ph.EP].
- Lagrange, A. M. et al. (July 2010). “A Giant Planet Imaged in the Disk of the Young Star β Pictoris”. In: *Science* 329.5987, p. 57. DOI: [10.1126/science.1187187](https://doi.org/10.1126/science.1187187). arXiv: [1006.3314](https://arxiv.org/abs/1006.3314) [astro-ph.EP].

- Langlois, M. et al. (July 2010). "High contrast imaging with IRDIS near infrared polarimeter". In: *Ground-based and Airborne Instrumentation for Astronomy III*. Ed. by Ian S. McLean, Suzanne K. Ramsay, and Hideki Takami. Vol. 7735. Society of Photo-Optical Instrumentation Engineers (SPIE) Conference Series, 77352U, 77352U. DOI: [10.1117/12.857221](https://doi.org/10.1117/12.857221).
- Langlois, M. et al. (2014). "High contrast polarimetry in the infrared with SPHERE on the VLT". In: vol. 9147. Society of Photo-Optical Instrumentation Engineers (SPIE) Conference Series, 91471R, 91471R. DOI: [10.1117/12.2055549](https://doi.org/10.1117/12.2055549).
- Langlois, M. et al. (July 2021). "The SPHERE infrared survey for exoplanets (SHINE). II. Observations, data reduction and analysis, detection performances, and initial results". In: *A&A* 651, A71, A71. DOI: [10.1051/0004-6361/202039753](https://doi.org/10.1051/0004-6361/202039753). arXiv: [2103.03976](https://arxiv.org/abs/2103.03976) [astro-ph.EP].
- Langlois, Maud et al. (Dec. 2013). "Infrared Differential Imager and Spectrograph for SPHERE: Performance Status with Extreme Adaptive Optics before shipment to ESO/VLT". In: *Proceedings of the Third AO4ELT Conference*. Ed. by Simone Esposito and Luca Fini, 63, p. 63. DOI: [10.12839/AO4ELT3.13317](https://doi.org/10.12839/AO4ELT3.13317).
- Latham, David W. et al. (May 1989). "The unseen companion of HD114762: a probable brown dwarf". In: *Nature* 339.6219, pp. 38–40. DOI: [10.1038/339038a0](https://doi.org/10.1038/339038a0).
- Lavie, Baptiste et al. (Sept. 2017). "HELIOS-RETRIEVAL: An Open-source, Nested Sampling Atmospheric Retrieval Code; Application to the HR 8799 Exoplanets and Inferred Constraints for Planet Formation". In: *Astronomical Journal* 154.3, 91, p. 91. DOI: [10.3847/1538-3881/aa7ed8](https://doi.org/10.3847/1538-3881/aa7ed8). arXiv: [1610.03216](https://arxiv.org/abs/1610.03216) [astro-ph.EP].
- Lee, Jinhee, Inseok Song, and Simon J. Murphy (Feb. 2022). "Low-mass members of nearby young stellar moving groups from Gaia EDR3". In: *arXiv e-prints*, arXiv:2202.02699, arXiv:2202.02699. arXiv: [2202.02699](https://arxiv.org/abs/2202.02699) [astro-ph.SR].
- Lee, Wing-Kit and Pin-Gao Gu (Nov. 2015). "The Effect of Vertical Temperature Gradient on the Propagation of Three-dimensional Waves in a Protoplanetary Disk". In: *ApJ* 814.1, 72, p. 72. DOI: [10.1088/0004-637X/814/1/72](https://doi.org/10.1088/0004-637X/814/1/72). arXiv: [1508.06833](https://arxiv.org/abs/1508.06833) [astro-ph.SR].
- Lenzen, Rainer et al. (Mar. 2003). "NAOS-CONICA first on sky results in a variety of observing modes". In: *Instrument Design and Performance for Optical/Infrared Ground-based Telescopes*. Ed. by Masanori Iye and Alan F. M. Moorwood. Vol. 4841. Society of Photo-Optical Instrumentation Engineers (SPIE) Conference Series, pp. 944–952. DOI: [10.1117/12.460044](https://doi.org/10.1117/12.460044).
- Li, A. and J. M. Greenberg (July 1997). "A unified model of interstellar dust." In: *A&A* 323, pp. 566–584.
- Li, Min and Lin Xiao (Mar. 2016). "Lifetimes and Accretion Rates of Protoplanetary Disks". In: *ApJ* 820.1, 36, p. 36. DOI: [10.3847/0004-637X/820/1/36](https://doi.org/10.3847/0004-637X/820/1/36).
- Liu, Beibei and Jianghui Ji (Oct. 2020). "A tale of planet formation: from dust to planets". In: *Research in Astronomy and Astrophysics* 20.10, 164, p. 164. DOI: [10.1088/1674-4527/20/10/164](https://doi.org/10.1088/1674-4527/20/10/164). arXiv: [2009.02321](https://arxiv.org/abs/2009.02321) [astro-ph.EP].
- Lodato, Giuseppe et al. (June 2019). "The newborn planet population emerging from ring-like structures in discs". In: *MNRAS* 486.1, pp. 453–461. DOI: [10.1093/mnras/stz913](https://doi.org/10.1093/mnras/stz913). arXiv: [1903.05117](https://arxiv.org/abs/1903.05117) [astro-ph.SR].

- Long, Feng et al. (Dec. 2018). "Gaps and Rings in an ALMA Survey of Disks in the Taurus Star-forming Region". In: *ApJ* 869.1, 17, p. 17. DOI: [10.3847/1538-4357/aae8e1](https://doi.org/10.3847/1538-4357/aae8e1). arXiv: [1810.06044](https://arxiv.org/abs/1810.06044) [astro-ph.SR].
- Long, Feng et al. (May 2022). "Gas Disk Sizes from CO Line Observations: A Test of Angular Momentum Evolution". In: *ApJ* 931.1, 6, p. 6. DOI: [10.3847/1538-4357/ac634e](https://doi.org/10.3847/1538-4357/ac634e). arXiv: [2203.16735](https://arxiv.org/abs/2203.16735) [astro-ph.EP].
- Lu, Cicero et al. (June 2022). "Trends in Silicates in the β Pictoris Disk". In: *American Astronomical Society Meeting Abstracts*. Vol. 54. American Astronomical Society Meeting Abstracts, 319.07, p. 319.07.
- Lyra, Wladimir and Orkan M. Umurhan (July 2019). "The Initial Conditions for Planet Formation: Turbulence Driven by Hydrodynamical Instabilities in Disks around Young Stars". In: *PASP* 131.1001, p. 072001. DOI: [10.1088/1538-3873/aaf5ff](https://doi.org/10.1088/1538-3873/aaf5ff). arXiv: [1808.08681](https://arxiv.org/abs/1808.08681) [astro-ph.EP].
- Macintosh, B. et al. (Oct. 2015). "Discovery and spectroscopy of the young jovian planet 51 Eri b with the Gemini Planet Imager". In: *Science* 350.6256, pp. 64–67. DOI: [10.1126/science.aac5891](https://doi.org/10.1126/science.aac5891). arXiv: [1508.03084](https://arxiv.org/abs/1508.03084) [astro-ph.EP].
- Macintosh, Bruce (June 2014). "The Gemini Planet Imager". In: *American Astronomical Society Meeting Abstracts #224*. Vol. 224. American Astronomical Society Meeting Abstracts, 301.02, p. 301.02.
- Madhusudhan, Nikku (Aug. 2019). "Exoplanetary Atmospheres: Key Insights, Challenges, and Prospects". In: *Annu. Rev. Astron. Astrophys* 57, pp. 617–663. DOI: [10.1146/annurev-astro-081817-051846](https://doi.org/10.1146/annurev-astro-081817-051846). arXiv: [1904.03190](https://arxiv.org/abs/1904.03190) [astro-ph.EP].
- Maire, Anne-Lise et al. (Aug. 2016). "SPHERE IRDIS and IFS astrometric strategy and calibration". In: *Ground-based and Airborne Instrumentation for Astronomy VI*. Vol. 9908. Society of Photo-Optical Instrumentation Engineers (SPIE) Conference Series, 990834, p. 990834. DOI: [10.1117/12.2233013](https://doi.org/10.1117/12.2233013). arXiv: [1609.06681](https://arxiv.org/abs/1609.06681) [astro-ph.IM].
- Mandell, Avi (2011). "Protoplanetary Disk, Instability". In: *Encyclopedia of Astrobiology*. Ed. by Muriel Gargaud et al. Berlin, Heidelberg: Springer Berlin Heidelberg, pp. 1376–1377. ISBN: 978-3-642-11274-4. DOI: [10.1007/978-3-642-11274-4_443](https://doi.org/10.1007/978-3-642-11274-4_443). URL: https://doi.org/10.1007/978-3-642-11274-4_443.
- Marino, S. et al. (Oct. 2018). "A gap in the planetesimal disc around HD 107146 and asymmetric warm dust emission revealed by ALMA". In: *MNRAS* 479.4, pp. 5423–5439. DOI: [10.1093/mnras/sty1790](https://doi.org/10.1093/mnras/sty1790). arXiv: [1805.01915](https://arxiv.org/abs/1805.01915) [astro-ph.EP].
- Marleau, Gabriel-Dominique et al. (Aug. 2019). "Warm-start planets from core accretion, and H α from accreting planets: Thermal and radiative properties of the accretion shock". In: *AAS/Division for Extreme Solar Systems Abstracts*. Vol. 51. AAS/Division for Extreme Solar Systems Abstracts, 317.21, p. 317.21.
- Marois, Christian et al. (Apr. 2006). "Angular Differential Imaging: A Powerful High-Contrast Imaging Technique". In: *ApJ* 641.1, pp. 556–564. DOI: [10.1086/500401](https://doi.org/10.1086/500401). arXiv: [astro-ph/0512335](https://arxiv.org/abs/astro-ph/0512335) [astro-ph].

- Marois, Christian et al. (Jan. 2014). "TLOCI: A Fully Loaded Speckle Killing Machine". In: *Exploring the Formation and Evolution of Planetary Systems*. Ed. by Mark Booth, Brenda C. Matthews, and James R. Graham. Vol. 299, pp. 48–49. DOI: [10.1017/S1743921313007813](https://doi.org/10.1017/S1743921313007813).
- Martinez, P. et al. (June 2013). "Speckle temporal stability in XAO coronagraphic images. II. Refine model for quasi-static speckle temporal evolution for VLT/SPHERE". In: *A&A* 554, A41, A41. DOI: [10.1051/0004-6361/201220820](https://doi.org/10.1051/0004-6361/201220820). arXiv: [1302.7211](https://arxiv.org/abs/1302.7211) [astro-ph.IM].
- Matrà, Luca et al. (Aug. 2020). "Dust Populations in the Iconic Vega Planetary System Resolved by ALMA". In: *ApJ* 898.2, 146, p. 146. DOI: [10.3847/1538-4357/aba0a4](https://doi.org/10.3847/1538-4357/aba0a4). arXiv: [2006.16257](https://arxiv.org/abs/2006.16257) [astro-ph.EP].
- Matthews, B. C. et al. (Jan. 2014). "Observations, Modeling, and Theory of Debris Disks". In: *Protostars and Planets VI*. Ed. by Henrik Beuther et al., p. 521. DOI: [10.2458/azu_upress_9780816531240-ch023](https://doi.org/10.2458/azu_upress_9780816531240-ch023). arXiv: [1401.0743](https://arxiv.org/abs/1401.0743) [astro-ph.SR].
- Mawet, D. et al. (Sept. 2014). "Fundamental Limitations of High Contrast Imaging Set by Small Sample Statistics". In: *ApJ* 792.2, 97, p. 97. DOI: [10.1088/0004-637X/792/2/97](https://doi.org/10.1088/0004-637X/792/2/97). arXiv: [1407.2247](https://arxiv.org/abs/1407.2247) [astro-ph.IM].
- Mawet, Dimitri et al. (Jan. 2017). "Characterization of the Inner Disk around HD 141569 A from Keck/NIRC2 L-Band Vortex Coronagraphy". In: *Astronomical Journal* 153.1, 44, p. 44. DOI: [10.3847/1538-3881/153/1/44](https://doi.org/10.3847/1538-3881/153/1/44). arXiv: [1612.03091](https://arxiv.org/abs/1612.03091) [astro-ph.SR].
- Mayor, Michel and Didier Queloz (Nov. 1995). "A Jupiter-mass companion to a solar-type star". In: *Nature* 378.6555, pp. 355–359. DOI: [10.1038/378355a0](https://doi.org/10.1038/378355a0).
- McMullin, J. P. et al. (Oct. 2007). "CASA Architecture and Applications". In: *Astronomical Data Analysis Software and Systems XVI*. Ed. by R. A. Shaw, F. Hill, and D. J. Bell. Vol. 376. Astronomical Society of the Pacific Conference Series, p. 127.
- Ménard, F. et al. (July 2020). "Ongoing flyby in the young multiple system UX Tauri". In: *A&A* 639, L1, p. L1. DOI: [10.1051/0004-6361/202038356](https://doi.org/10.1051/0004-6361/202038356). arXiv: [2006.02439](https://arxiv.org/abs/2006.02439) [astro-ph.SR].
- Mermilliod, J. C. (May 2006). "VizieR Online Data Catalog: Homogeneous Means in the UBV System (Mermilliod 1991)". In: *VizieR Online Data Catalog*, II/168, pp. II/168.
- Mesa, D. et al. (Apr. 2015). "Performance of the VLT Planet Finder SPHERE. II. Data analysis and results for IFS in laboratory". In: *A&A* 576, A121, A121. DOI: [10.1051/0004-6361/201423910](https://doi.org/10.1051/0004-6361/201423910). arXiv: [1503.02486](https://arxiv.org/abs/1503.02486) [astro-ph.IM].
- Mignone, A. et al. (Aug. 2007). "PLUTO: a Numerical Code for Computational Astrophysics". In: *JENAM-2007, "Our Non-Stable Universe"*, pp. 96–96.
- Miguel, Y., O. M. Guilera, and A. Brunini (Apr. 2011). "The role of the initial surface density profiles of the disc on giant planet formation: comparing with observations". In: *MNRAS* 412.4, pp. 2113–2124. DOI: [10.1111/j.1365-2966.2010.17887.x](https://doi.org/10.1111/j.1365-2966.2010.17887.x). arXiv: [1010.5061](https://arxiv.org/abs/1010.5061) [astro-ph.EP].
- Milli, J. et al. (Sept. 2012). "Impact of angular differential imaging on circumstellar disk images". In: *A&A* 545, A111, A111. DOI: [10.1051/0004-6361/201219687](https://doi.org/10.1051/0004-6361/201219687). arXiv: [1207.5909](https://arxiv.org/abs/1207.5909) [astro-ph.EP].
- Milli, Julien et al. (Jan. 2016). "Adaptive Optics in High-Contrast Imaging". In: *Astronomy at High Angular Resolution*. Ed. by Henri M. J. Boffin et al. Vol. 439. Astrophysics and

- Space Science Library, p. 17. DOI: [10.1007/978-3-319-39739-9_2](https://doi.org/10.1007/978-3-319-39739-9_2). arXiv: [1701.00836](https://arxiv.org/abs/1701.00836) [astro-ph.IM].
- Mollière, P. et al. (July 2019). “petitRADTRANS. A Python radiative transfer package for exoplanet characterization and retrieval”. In: *A&A* 627, A67, A67. DOI: [10.1051/0004-6361/201935470](https://doi.org/10.1051/0004-6361/201935470). arXiv: [1904.11504](https://arxiv.org/abs/1904.11504) [astro-ph.EP].
- Mollière, P. et al. (Aug. 2020). “Retrieving scattering clouds and disequilibrium chemistry in the atmosphere of HR 8799e”. In: *A&A* 640, A131, A131. DOI: [10.1051/0004-6361/202038325](https://doi.org/10.1051/0004-6361/202038325). arXiv: [2006.09394](https://arxiv.org/abs/2006.09394) [astro-ph.EP].
- Mollière, Paul et al. (July 2022). “Interpreting the Atmospheric Composition of Exoplanets: Sensitivity to Planet Formation Assumptions”. In: *ApJ* 934.1, 74, p. 74. DOI: [10.3847/1538-4357/ac6a56](https://doi.org/10.3847/1538-4357/ac6a56). arXiv: [2204.13714](https://arxiv.org/abs/2204.13714) [astro-ph.EP].
- Montet, Benjamin T. et al. (Nov. 2015). “Dynamical Masses of Young M Dwarfs: Masses and Orbital Parameters of GJ 3305 AB, the Wide Binary Companion to the Imaged Exoplanet Host 51 Eri”. In: *ApJ Letters* 813.1, L11, p. L11. DOI: [10.1088/2041-8205/813/1/L11](https://doi.org/10.1088/2041-8205/813/1/L11). arXiv: [1508.05945](https://arxiv.org/abs/1508.05945) [astro-ph.SR].
- Moór, A. et al. (Feb. 2015). “Stirring in massive, young debris discs from spatially resolved Herschel images”. In: *MNRAS* 447.1, pp. 577–597. DOI: [10.1093/mnras/stu2442](https://doi.org/10.1093/mnras/stu2442). arXiv: [1411.5829](https://arxiv.org/abs/1411.5829) [astro-ph.SR].
- Morales, F. Y. et al. (Nov. 2016). “Herschel-resolved Outer Belts of Two-belt Debris Disks—Evidence of Icy Grains”. In: *ApJ* 831.1, 97, p. 97. DOI: [10.3847/0004-637X/831/1/97](https://doi.org/10.3847/0004-637X/831/1/97).
- Mordasini, C., Y. Alibert, and W. Benz (July 2009a). “Extrasolar planet population synthesis. I. Method, formation tracks, and mass-distance distribution”. In: *A&A* 501.3, pp. 1139–1160. DOI: [10.1051/0004-6361/200810301](https://doi.org/10.1051/0004-6361/200810301). arXiv: [0904.2524](https://arxiv.org/abs/0904.2524) [astro-ph.EP].
- Mordasini, C., G. D. Marleau, and P. Mollière (Dec. 2017). “Characterization of exoplanets from their formation. III. The statistics of planetary luminosities”. In: *A&A* 608, A72, A72. DOI: [10.1051/0004-6361/201630077](https://doi.org/10.1051/0004-6361/201630077). arXiv: [1708.00868](https://arxiv.org/abs/1708.00868) [astro-ph.EP].
- Mordasini, C. et al. (July 2009b). “Extrasolar planet population synthesis. II. Statistical comparison with observations”. In: *A&A* 501.3, pp. 1161–1184. DOI: [10.1051/0004-6361/200810697](https://doi.org/10.1051/0004-6361/200810697). arXiv: [0904.2542](https://arxiv.org/abs/0904.2542) [astro-ph.EP].
- Mordasini, C. et al. (Nov. 2012). “Characterization of exoplanets from their formation. I. Models of combined planet formation and evolution”. In: *A&A* 547, A111, A111. DOI: [10.1051/0004-6361/201118457](https://doi.org/10.1051/0004-6361/201118457). arXiv: [1206.6103](https://arxiv.org/abs/1206.6103) [astro-ph.EP].
- Morley, Caroline V. et al. (Sept. 2012). “Neglected Clouds in T and Y Dwarf Atmospheres”. In: *ApJ* 756.2, 172, p. 172. DOI: [10.1088/0004-637X/756/2/172](https://doi.org/10.1088/0004-637X/756/2/172). arXiv: [1206.4313](https://arxiv.org/abs/1206.4313) [astro-ph.SR].
- Morley, Caroline V. et al. (Dec. 2015). “Thermal Emission and Reflected Light Spectra of Super Earths with Flat Transmission Spectra”. In: *ApJ* 815.2, 110, p. 110. DOI: [10.1088/0004-637X/815/2/110](https://doi.org/10.1088/0004-637X/815/2/110). arXiv: [1511.01492](https://arxiv.org/abs/1511.01492) [astro-ph.EP].
- Mugnier, Laurent M. et al. (May 2009). “Optimal method for exoplanet detection by angular differential imaging”. In: *Journal of the Optical Society of America A* 26.6, p. 1326. DOI: [10.1364/JOSAA.26.001326](https://doi.org/10.1364/JOSAA.26.001326).

- Mulders, G. D. et al. (Jan. 2013). “Why circumstellar disks are so faint in scattered light: the case of HD 100546”. In: *A&A* 549, A112, A112. DOI: [10.1051/0004-6361/201219522](https://doi.org/10.1051/0004-6361/201219522). arXiv: [1210.4132](https://arxiv.org/abs/1210.4132) [astro-ph.SR].
- Müller, Simon and Ravit Helled (Aug. 2021). “Synthetic Evolution Tracks of Giant Planets”. In: *arXiv e-prints*, arXiv:2108.00949, arXiv:2108.00949. arXiv: [2108.00949](https://arxiv.org/abs/2108.00949) [astro-ph.EP].
- Musioli, Grzegorz and Gerhard Wurm (Mar. 2019). “Contacts of Water Ice in Protoplanetary Disks—Laboratory Experiments”. In: *ApJ* 873.1, 58, p. 58. DOI: [10.3847/1538-4357/ab0428](https://doi.org/10.3847/1538-4357/ab0428). arXiv: [1902.08503](https://arxiv.org/abs/1902.08503) [astro-ph.EP].
- Mustill, Alexander J. and Mark C. Wyatt (Nov. 2009). “Debris disc stirring by secular perturbations from giant planets”. In: *MNRAS* 399.3, pp. 1403–1414. DOI: [10.1111/j.1365-2966.2009.15360.x](https://doi.org/10.1111/j.1365-2966.2009.15360.x). arXiv: [0907.1389](https://arxiv.org/abs/0907.1389) [astro-ph.EP].
- Muto, T. et al. (Apr. 2012). “Discovery of Small-scale Spiral Structures in the Disk of SAO 206462 (HD 135344B): Implications for the Physical State of the Disk from Spiral Density Wave Theory”. In: *ApJ Letters* 748.2, L22, p. L22. DOI: [10.1088/2041-8205/748/2/L22](https://doi.org/10.1088/2041-8205/748/2/L22). arXiv: [1202.6139](https://arxiv.org/abs/1202.6139) [astro-ph.EP].
- Nielsen, Eric L. et al. (Oct. 2013). “The Gemini NICI Planet-Finding Campaign: The Frequency of Giant Planets around Young B and A Stars”. In: *ApJ* 776.1, 4, p. 4. DOI: [10.1088/0004-637X/776/1/4](https://doi.org/10.1088/0004-637X/776/1/4). arXiv: [1306.1233](https://arxiv.org/abs/1306.1233) [astro-ph.EP].
- Norfolk, Brodie J. et al. (Sept. 2022). “The Origin of the Doppler Flip in HD 100546: A Large-scale Spiral Arm Generated by an Inner Binary Companion”. In: *ApJ Letters* 936.1, L4, p. L4. DOI: [10.3847/2041-8213/ac85ed](https://doi.org/10.3847/2041-8213/ac85ed). arXiv: [2208.02542](https://arxiv.org/abs/2208.02542) [astro-ph.EP].
- Nuñez, P. D. et al. (Dec. 2017). “A near-infrared interferometric survey of debris-disc stars. VI. Extending the exozodiacal light survey with CHARA/JouFLU”. In: *A&A* 608, A113, A113. DOI: [10.1051/0004-6361/201730859](https://doi.org/10.1051/0004-6361/201730859). arXiv: [1709.01655](https://arxiv.org/abs/1709.01655) [astro-ph.SR].
- Öberg, Karin I., Ruth Murray-Clay, and Edwin A. Bergin (Dec. 2011). “The Effects of Snow-lines on C/O in Planetary Atmospheres”. In: *ApJ Letters* 743.1, L16, p. L16. DOI: [10.1088/2041-8205/743/1/L16](https://doi.org/10.1088/2041-8205/743/1/L16). arXiv: [1110.5567](https://arxiv.org/abs/1110.5567) [astro-ph.GA].
- Offner, Stella S. R. and Christopher F. McKee (July 2011). “The Protostellar Luminosity Function”. In: *ApJ* 736.1, 53, p. 53. DOI: [10.1088/0004-637X/736/1/53](https://doi.org/10.1088/0004-637X/736/1/53). arXiv: [1105.0671](https://arxiv.org/abs/1105.0671) [astro-ph.SR].
- Patel, Rahul I., Stanimir A. Metchev, and Aren Heinze (May 2014). “A Sensitive Identification of Warm Debris Disks in the Solar Neighborhood through Precise Calibration of Saturated WISE Photometry”. In: *ApJ Supplement* 212.1, 10, p. 10. DOI: [10.1088/0067-0049/212/1/10](https://doi.org/10.1088/0067-0049/212/1/10). arXiv: [1403.3435](https://arxiv.org/abs/1403.3435) [astro-ph.SR].
- Pavlov, Alexey et al. (July 2008). “SPHERE data reduction and handling system: overview, project status, and development”. In: *Advanced Software and Control for Astronomy II*. Ed. by Alan Bridger and Nicole M. Radziwill. Vol. 7019. Society of Photo-Optical Instrumentation Engineers (SPIE) Conference Series, 701939, p. 701939. DOI: [10.1117/12.789110](https://doi.org/10.1117/12.789110).
- Pearce, Tim D. et al. (Mar. 2022). “Planet populations inferred from debris discs. Insights from 178 debris systems in the ISPY, LEECH, and LStEN planet-hunting surveys”. In: *A&A* 659, A135, A135. DOI: [10.1051/0004-6361/202142720](https://doi.org/10.1051/0004-6361/202142720). arXiv: [2201.08369](https://arxiv.org/abs/2201.08369) [astro-ph.EP].

- Pecaut, Mark J. and Eric E. Mamajek (Sept. 2013). "Intrinsic Colors, Temperatures, and Bolometric Corrections of Pre-main-sequence Stars". In: *ApJ Supplement* 208.1, 9, p. 9. DOI: [10.1088/0067-0049/208/1/9](https://doi.org/10.1088/0067-0049/208/1/9). arXiv: [1307.2657](https://arxiv.org/abs/1307.2657) [astro-ph.SR].
- Pepper, Joshua et al. (Aug. 2007). "The Kilodegree Extremely Little Telescope (KELT): A Small Robotic Telescope for Large-Area Synoptic Surveys". In: *PASP* 119.858, pp. 923–935. DOI: [10.1086/521836](https://doi.org/10.1086/521836). arXiv: [0704.0460](https://arxiv.org/abs/0704.0460) [astro-ph].
- Pérez, Sebastián et al. (Jan. 2020). "Long Baseline Observations of the HD 100546 Protoplanetary Disk with ALMA". In: *ApJ Letters* 889.1, L24, p. L24. DOI: [10.3847/2041-8213/ab6b2b](https://doi.org/10.3847/2041-8213/ab6b2b). arXiv: [1906.06305](https://arxiv.org/abs/1906.06305) [astro-ph.EP].
- Perrin, Marshall D. et al. (July 2014). "Gemini Planet Imager observational calibrations I: Overview of the GPI data reduction pipeline". In: *Ground-based and Airborne Instrumentation for Astronomy V*. Ed. by Suzanne K. Ramsay, Ian S. McLean, and Hideki Takami. Vol. 9147. Society of Photo-Optical Instrumentation Engineers (SPIE) Conference Series, 91473J, 91473J. DOI: [10.1117/12.2055246](https://doi.org/10.1117/12.2055246). arXiv: [1407.2301](https://arxiv.org/abs/1407.2301) [astro-ph.IM].
- Perrin, Marshall D. et al. (Aug. 2016). "Gemini Planet Imager observational calibrations XI: pipeline improvements and enhanced calibrations after two years on sky". In: *Ground-based and Airborne Instrumentation for Astronomy VI*. Ed. by Christopher J. Evans, Luc Simard, and Hideki Takami. Vol. 9908. Society of Photo-Optical Instrumentation Engineers (SPIE) Conference Series, 990837, p. 990837. DOI: [10.1117/12.2233197](https://doi.org/10.1117/12.2233197).
- Pineda, Jaime E. et al. (Jan. 2019). "High-resolution ALMA Observations of HD 100546: Asymmetric Circumstellar Ring and Circumplanetary Disk Upper Limits". In: *ApJ* 871.1, 48, p. 48. DOI: [10.3847/1538-4357/aaf389](https://doi.org/10.3847/1538-4357/aaf389). arXiv: [1811.10365](https://arxiv.org/abs/1811.10365) [astro-ph.SR].
- Pinilla, Paola, Christian T. Lenz, and Sebastian M. Stammler (Jan. 2021). "Growing and trapping pebbles with fragile collisions of particles in protoplanetary disks". In: *A&A* 645, A70, A70. DOI: [10.1051/0004-6361/202038920](https://doi.org/10.1051/0004-6361/202038920). arXiv: [2011.09178](https://arxiv.org/abs/2011.09178) [astro-ph.EP].
- Pohl, A. et al. (Oct. 2015). "Scattered light images of spiral arms in marginally gravitationally unstable discs with an embedded planet". In: *MNRAS* 453.2, pp. 1768–1778. DOI: [10.1093/mnras/stv1746](https://doi.org/10.1093/mnras/stv1746). arXiv: [1508.04443](https://arxiv.org/abs/1508.04443) [astro-ph.EP].
- Pollack, James B. et al. (Nov. 1996). "Formation of the Giant Planets by Concurrent Accretion of Solids and Gas". In: 124.1, pp. 62–85. DOI: [10.1006/icar.1996.0190](https://doi.org/10.1006/icar.1996.0190).
- Pringle, J. E. (Jan. 1981). "Accretion discs in astrophysics". In: *Annu. Rev. Astron. Astrophys* 19, pp. 137–162. DOI: [10.1146/annurev.aa.19.090181.001033](https://doi.org/10.1146/annurev.aa.19.090181.001033).
- Prugniel, Ph. et al. (Mar. 2007). "New release of the ELODIE library: Version 3.1". In: *arXiv e-prints*, astro-ph/0703658, astro-ph/0703658. arXiv: [astro-ph/0703658](https://arxiv.org/abs/astro-ph/0703658) [astro-ph].
- Quanz, Sascha P. et al. (Apr. 2015). "Direct detection of exoplanets in the 3-10 μm range with E-ELT/METIS". In: *International Journal of Astrobiology* 14.2, pp. 279–289. DOI: [10.1017/S1473550414000135](https://doi.org/10.1017/S1473550414000135). arXiv: [1404.0831](https://arxiv.org/abs/1404.0831) [astro-ph.IM].
- Querel, Richard R. and Florian Kerber (Aug. 2014). "All-sky homogeneity of precipitable water vapour over Paranal". In: *Ground-based and Airborne Instrumentation for Astronomy V*. Ed. by Suzanne K. Ramsay, Ian S. McLean, and Hideki Takami. Vol. 9147. Society of Photo-Optical Instrumentation Engineers (SPIE) Conference Series, 914792, p. 914792. DOI: [10.1117/12.2055500](https://doi.org/10.1117/12.2055500). arXiv: [1408.1753](https://arxiv.org/abs/1408.1753) [astro-ph.IM].

- Quirrenbach, A. et al. (July 2014). "CARMENES instrument overview". In: *Ground-based and Airborne Instrumentation for Astronomy V*. Ed. by Suzanne K. Ramsay, Ian S. McLean, and Hideki Takami. Vol. 9147. Society of Photo-Optical Instrumentation Engineers (SPIE) Conference Series, 91471F, 91471F. DOI: [10.1117/12.2056453](https://doi.org/10.1117/12.2056453).
- Racine, René et al. (May 1999). "Speckle Noise and the Detection of Faint Companions". In: *PASP* 111.759, pp. 587–594. DOI: [10.1086/316367](https://doi.org/10.1086/316367).
- Rafikov, Roman R. (June 2007). "Convective Cooling and Fragmentation of Gravitationally Unstable Disks". In: *ApJ* 662.1, pp. 642–650. DOI: [10.1086/517599](https://doi.org/10.1086/517599). arXiv: [astro-ph/0609549](https://arxiv.org/abs/astro-ph/0609549) [[astro-ph](https://arxiv.org/abs/astro-ph)].
- Rajan, Abhijith et al. (July 2017). "Characterizing 51 Eri b from 1 to 5 μm : A Partly Cloudy Exoplanet". In: *Astronomical Journal* 154.1, 10, p. 10. DOI: [10.3847/1538-3881/aa74db](https://doi.org/10.3847/1538-3881/aa74db). arXiv: [1705.03887](https://arxiv.org/abs/1705.03887) [[astro-ph](https://arxiv.org/abs/astro-ph).EP].
- Rameau, J. et al. (Aug. 2013). "Discovery of a Probable 4-5 Jupiter-mass Exoplanet to HD 95086 by Direct Imaging". In: *ApJ Letters* 772.2, L15, p. L15. DOI: [10.1088/2041-8205/772/2/L15](https://doi.org/10.1088/2041-8205/772/2/L15). arXiv: [1305.7428](https://arxiv.org/abs/1305.7428) [[astro-ph](https://arxiv.org/abs/astro-ph).EP].
- Rebollido, Isabel et al. (Jan. 2022). "The search for gas in debris discs: ALMA detection of CO gas in HD 36546". In: *MNRAS* 509.1, pp. 693–700. DOI: [10.1093/mnras/stab2906](https://doi.org/10.1093/mnras/stab2906). arXiv: [2110.02308](https://arxiv.org/abs/2110.02308) [[astro-ph](https://arxiv.org/abs/astro-ph).EP].
- Reboussin, L. et al. (June 2015). "Sensitive survey for ^{13}CO , CN, H_2CO , and SO in the disks of T Tauri and Herbig Ae stars. II. Stars in ρ Ophiuchi and upper Scorpius". In: *A&A* 578, A31, A31. DOI: [10.1051/0004-6361/201525705](https://doi.org/10.1051/0004-6361/201525705). arXiv: [1504.04542](https://arxiv.org/abs/1504.04542) [[astro-ph](https://arxiv.org/abs/astro-ph).SR].
- Rebull, L. M. et al. (July 2008). "Spitzer MIPS Observations of Stars in the β Pictoris Moving Group". In: *ApJ* 681.2, pp. 1484–1504. DOI: [10.1086/588182](https://doi.org/10.1086/588182). arXiv: [0803.1674](https://arxiv.org/abs/0803.1674) [[astro-ph](https://arxiv.org/abs/astro-ph)].
- Reggiani, M. et al. (Feb. 2016). "The VLT/NaCo large program to probe the occurrence of exoplanets and brown dwarfs at wide orbits. III. The frequency of brown dwarfs and giant planets as companions to solar-type stars". In: *A&A* 586, A147, A147. DOI: [10.1051/0004-6361/201525930](https://doi.org/10.1051/0004-6361/201525930). arXiv: [1510.08453](https://arxiv.org/abs/1510.08453) [[astro-ph](https://arxiv.org/abs/astro-ph).EP].
- Ren, Bin et al. (Aug. 2020). "Dynamical Evidence of a Spiral Arm-driving Planet in the MWC 758 Protoplanetary Disk". In: *ApJ Letters* 898.2, L38, p. L38. DOI: [10.3847/2041-8213/aba43e](https://doi.org/10.3847/2041-8213/aba43e). arXiv: [2007.04980](https://arxiv.org/abs/2007.04980) [[astro-ph](https://arxiv.org/abs/astro-ph).EP].
- Ricci, L. et al. (Oct. 2010). "Dust grain growth in ρ -Ophiuchi protoplanetary disks". In: *A&A* 521, A66, A66. DOI: [10.1051/0004-6361/201015039](https://doi.org/10.1051/0004-6361/201015039). arXiv: [1008.1144](https://arxiv.org/abs/1008.1144) [[astro-ph](https://arxiv.org/abs/astro-ph).SR].
- Rice, W. K. M. et al. (Dec. 2004). "Accelerated planetesimal growth in self-gravitating protoplanetary discs". In: *MNRAS* 355.2, pp. 543–552. DOI: [10.1111/j.1365-2966.2004.08339.x](https://doi.org/10.1111/j.1365-2966.2004.08339.x). arXiv: [astro-ph/0408390](https://arxiv.org/abs/astro-ph/0408390) [[astro-ph](https://arxiv.org/abs/astro-ph)].
- Ricker, George R. et al. (Jan. 2015). "Transiting Exoplanet Survey Satellite (TESS)". In: *Journal of Astronomical Telescopes, Instruments, and Systems* 1, 014003, p. 014003. DOI: [10.1117/1.JATIS.1.1.014003](https://doi.org/10.1117/1.JATIS.1.1.014003).
- Rieke, G. H. and M. J. Lebofsky (Jan. 1985). "The interstellar extinction law from 1 to 13 microns." In: *ApJ* 288, pp. 618–621. DOI: [10.1086/162827](https://doi.org/10.1086/162827).

- Riviere-Marichalar, P. et al. (May 2014). "Gas and dust in the beta Pictoris moving group as seen by the Herschel Space Observatory". In: *A&A* 565, A68, A68. DOI: [10.1051/0004-6361/201322901](https://doi.org/10.1051/0004-6361/201322901). arXiv: [1404.1815](https://arxiv.org/abs/1404.1815) [astro-ph.SR].
- Roddier, F. (Jan. 1981). "The effects of atmospheric turbulence in optical astronomy". In: *Progress in Optics* 19, pp. 281–376. DOI: [10.1016/S0079-6638\(08\)70204-X](https://doi.org/10.1016/S0079-6638(08)70204-X).
- Rodrigo, C. and E. Solano (July 2020). "The SVO Filter Profile Service". In: *XIV.0 Scientific Meeting (virtual) of the Spanish Astronomical Society*, 182, p. 182.
- Rosotti, G. P. et al. (Jan. 2020). "Spiral arms in the protoplanetary disc HD100453 detected with ALMA: evidence for binary-disc interaction and a vertical temperature gradient". In: *MNRAS* 491.1, pp. 1335–1347. DOI: [10.1093/mnras/stz3090](https://doi.org/10.1093/mnras/stz3090). arXiv: [1911.00518](https://arxiv.org/abs/1911.00518) [astro-ph.EP].
- Rousset, Gerard et al. (Feb. 2003). "NAOS, the first AO system of the VLT: on-sky performance". In: *Adaptive Optical System Technologies II*. Ed. by Peter L. Wizinowich and Domenico Bonaccini. Vol. 4839. Society of Photo-Optical Instrumentation Engineers (SPIE) Conference Series, pp. 140–149. DOI: [10.1117/12.459332](https://doi.org/10.1117/12.459332).
- Samland, M. et al. (July 2017). "Spectral and atmospheric characterization of 51 Eridani b using VLT/SPHERE". In: *A&A* 603, A57, A57. DOI: [10.1051/0004-6361/201629767](https://doi.org/10.1051/0004-6361/201629767). arXiv: [1704.02987](https://arxiv.org/abs/1704.02987) [astro-ph.EP].
- Samland, M. et al. (Feb. 2021). "TRAP: a temporal systematics model for improved direct detection of exoplanets at small angular separations". In: *A&A* 646, A24, A24. DOI: [10.1051/0004-6361/201937308](https://doi.org/10.1051/0004-6361/201937308). arXiv: [2011.12311](https://arxiv.org/abs/2011.12311) [astro-ph.EP].
- Sanchis, E. et al. (May 2021). "Measuring the ratio of the gas and dust emission radii of protoplanetary disks in the Lupus star-forming region". In: *A&A* 649, A19, A19. DOI: [10.1051/0004-6361/202039733](https://doi.org/10.1051/0004-6361/202039733). arXiv: [2101.11307](https://arxiv.org/abs/2101.11307) [astro-ph.EP].
- Schmid, H. M. et al. (Nov. 2018). "SPHERE/ZIMPOL high resolution polarimetric imager. I. System overview, PSF parameters, coronagraphy, and polarimetry". In: *A&A* 619, A9, A9. DOI: [10.1051/0004-6361/201833620](https://doi.org/10.1051/0004-6361/201833620). arXiv: [1808.05008](https://arxiv.org/abs/1808.05008) [astro-ph.IM].
- Seidel, J. V. et al. (Sept. 2020). "Hot Exoplanet Atmospheres Resolved with Transit Spectroscopy (HEARTS). V. Detection of sodium on the bloated super-Neptune WASP-166b". In: *A&A* 641, L7, p. L7. DOI: [10.1051/0004-6361/202038497](https://doi.org/10.1051/0004-6361/202038497). arXiv: [2007.01783](https://arxiv.org/abs/2007.01783) [astro-ph.EP].
- Sepulveda, Aldo G. et al. (May 2022). "The Directly-Imaged Exoplanet Host Star 51 Eridani is a Gamma Doradus Pulsator". In: *arXiv e-prints*, arXiv:2205.01103, arXiv:2205.01103. arXiv: [2205.01103](https://arxiv.org/abs/2205.01103) [astro-ph.EP].
- Skemer, Andrew J. et al. (Feb. 2016). "The LEECH Exoplanet Imaging Survey: Characterization of the Coldest Directly Imaged Exoplanet, GJ 504 b, and Evidence for Superstellar Metallicity". In: *ApJ* 817.2, 166, p. 166. DOI: [10.3847/0004-637X/817/2/166](https://doi.org/10.3847/0004-637X/817/2/166). arXiv: [1511.09183](https://arxiv.org/abs/1511.09183) [astro-ph.EP].
- Skilling, John (Nov. 2004). "Nested Sampling". In: *Bayesian Inference and Maximum Entropy Methods in Science and Engineering: 24th International Workshop on Bayesian Inference and Maximum Entropy Methods in Science and Engineering*. Ed. by Rainer Fischer, Roland

- Preuss, and Udo Von Toussaint. Vol. 735. American Institute of Physics Conference Series, pp. 395–405. DOI: [10.1063/1.1835238](https://doi.org/10.1063/1.1835238).
- Skilling, John (Dec. 2006). “Skilling, J.: Nested sampling for general Bayesian computation. *Bayesian Anal.* 1(4), 833–860”. In: *Bayesian Analysis* 1, pp. 833–860. DOI: [10.1214/06-BA127](https://doi.org/10.1214/06-BA127).
- Skrutskie, M. F. et al. (Feb. 2006). “The Two Micron All Sky Survey (2MASS)”. In: *Astronomical Journal* 131.2, pp. 1163–1183. DOI: [10.1086/498708](https://doi.org/10.1086/498708).
- Smith, A. M. S. and WASP Consortium (Mar. 2014). “The SuperWASP exoplanet transit survey”. In: *Contributions of the Astronomical Observatory Skalnaté Pleso* 43.3, pp. 500–512.
- Soummer, Rémi, Laurent Pueyo, and James Larkin (Aug. 2012). “Detection and Characterization of Exoplanets and Disks Using Projections on Karhunen-Loève Eigenimages”. In: *ApJ Letters* 755.2, L28, p. L28. DOI: [10.1088/2041-8205/755/2/L28](https://doi.org/10.1088/2041-8205/755/2/L28). arXiv: [1207.4197](https://arxiv.org/abs/1207.4197) [astro-ph.IM].
- Spiegel, David S. and Adam Burrows (Feb. 2012). “Spectral and Photometric Diagnostics of Giant Planet Formation Scenarios”. In: *ApJ* 745.2, 174, p. 174. DOI: [10.1088/0004-637X/745/2/174](https://doi.org/10.1088/0004-637X/745/2/174). arXiv: [1108.5172](https://arxiv.org/abs/1108.5172) [astro-ph.EP].
- Steinpilz, Tobias, Jens Teiser, and Gerhard Wurm (Mar. 2019). “Sticking Properties of Silicates in Planetesimal Formation Revisited”. In: *ApJ* 874.1, 60, p. 60. DOI: [10.3847/1538-4357/ab07bb](https://doi.org/10.3847/1538-4357/ab07bb). arXiv: [1905.11864](https://arxiv.org/abs/1905.11864) [astro-ph.EP].
- Sturm, J. A., G. P. Rosotti, and C. Dominik (Nov. 2020). “Dust dynamics in planet-driven spirals”. In: *A&A* 643, A92, A92. DOI: [10.1051/0004-6361/202038919](https://doi.org/10.1051/0004-6361/202038919).
- Su, Kate Y. L. et al. (July 2020). “Mid-infrared Studies of HD 113766 and HD 172555: Assessing Variability in the Terrestrial Zone of Young Exoplanetary Systems”. In: *ApJ* 898.1, 21, p. 21. DOI: [10.3847/1538-4357/ab9c9b](https://doi.org/10.3847/1538-4357/ab9c9b). arXiv: [2006.06590](https://arxiv.org/abs/2006.06590) [astro-ph.EP].
- Szalay, J. R. et al. (Oct. 2021). “Collisional Evolution of the Inner Zodiacal Cloud”. In: 2.5, 185, p. 185. DOI: [10.3847/PSJ/abf928](https://doi.org/10.3847/PSJ/abf928). arXiv: [2104.08217](https://arxiv.org/abs/2104.08217) [astro-ph.EP].
- Tang, Ya-Wen et al. (May 2017). “Planet Formation in AB Aurigae: Imaging of the Inner Gaseous Spirals Observed inside the Dust Cavity”. In: *ApJ* 840.1, 32, p. 32. DOI: [10.3847/1538-4357/aa6af7](https://doi.org/10.3847/1538-4357/aa6af7). arXiv: [1704.02699](https://arxiv.org/abs/1704.02699) [astro-ph.GA].
- Tomida, Kengo et al. (Jan. 2017). “Grand-design Spiral Arms in a Young Forming Circumstellar Disk”. In: *ApJ Letters* 835.1, L11, p. L11. DOI: [10.3847/2041-8213/835/1/L11](https://doi.org/10.3847/2041-8213/835/1/L11). arXiv: [1611.09361](https://arxiv.org/abs/1611.09361) [astro-ph.SR].
- Toomre, A. (May 1964). “On the gravitational stability of a disk of stars.” In: *ApJ* 139, pp. 1217–1238. DOI: [10.1086/147861](https://doi.org/10.1086/147861).
- Tremblin, P. et al. (May 2015). “Fingering Convection and Cloudless Models for Cool Brown Dwarf Atmospheres”. In: *ApJ Letters* 804, L17, p. L17. DOI: [10.1088/2041-8205/804/1/L17](https://doi.org/10.1088/2041-8205/804/1/L17). arXiv: [1504.03334](https://arxiv.org/abs/1504.03334) [astro-ph.SR].
- Tremblin, P. et al. (Feb. 2016). “Cloudless Atmospheres for L/T Dwarfs and Extrasolar Giant Planets”. In: *ApJ Letters* 817.2, L19, p. L19. DOI: [10.3847/2041-8205/817/2/L19](https://doi.org/10.3847/2041-8205/817/2/L19). arXiv: [1601.03652](https://arxiv.org/abs/1601.03652) [astro-ph.EP].

- Tremblin, P. et al. (Nov. 2017). “Cloudless Atmospheres for Young Low-gravity Substellar Objects”. In: *ApJ* 850.1, 46, p. 46. DOI: [10.3847/1538-4357/aa9214](https://doi.org/10.3847/1538-4357/aa9214). arXiv: [1710.02640](https://arxiv.org/abs/1710.02640) [astro-ph.SR].
- Tremblin, P. et al. (May 2019). “Thermo-compositional Diabatic Convection in the Atmospheres of Brown Dwarfs and in Earth’s Atmosphere and Oceans”. In: *ApJ* 876.2, 144, p. 144. DOI: [10.3847/1538-4357/ab05db](https://doi.org/10.3847/1538-4357/ab05db). arXiv: [1902.03553](https://arxiv.org/abs/1902.03553) [astro-ph.EP].
- Turner, N. J. et al. (Jan. 2014). “Transport and Accretion in Planet-Forming Disks”. In: *Protostars and Planets VI*. Ed. by Henrik Beuther et al., p. 411. DOI: [10.2458/azu_uapress_9780816531240-ch018](https://doi.org/10.2458/azu_uapress_9780816531240-ch018). arXiv: [1401.7306](https://arxiv.org/abs/1401.7306) [astro-ph.EP].
- van der Plas, G. et al. (Mar. 2016). “Dust Masses of Disks around 8 Brown Dwarfs and Very Low-mass Stars in Upper Sco OB1 and Ophiuchus”. In: *ApJ* 819.2, 102, p. 102. DOI: [10.3847/0004-637X/819/2/102](https://doi.org/10.3847/0004-637X/819/2/102). arXiv: [1602.01724](https://arxiv.org/abs/1602.01724) [astro-ph.SR].
- van Holstein, R. G. et al. (Jan. 2020). “Polarimetric imaging mode of VLT/SPHERE/IRDIS. II. Characterization and correction of instrumental polarization effects”. In: *A&A* 633, A64, A64. DOI: [10.1051/0004-6361/201834996](https://doi.org/10.1051/0004-6361/201834996). arXiv: [1909.13108](https://arxiv.org/abs/1909.13108) [astro-ph.IM].
- Veronesi, B. et al. (Nov. 2019). “Multiwavelength observations of protoplanetary discs as a proxy for the gas disc mass”. In: *MNRAS* 489.3, pp. 3758–3768. DOI: [10.1093/mnras/stz2384](https://doi.org/10.1093/mnras/stz2384). arXiv: [1908.08865](https://arxiv.org/abs/1908.08865) [astro-ph.EP].
- Vigan, A. et al. (Oct. 2008). “Exoplanet characterization with long slit spectroscopy”. In: *A&A* 489.3, pp. 1345–1354. DOI: [10.1051/0004-6361:200810090](https://doi.org/10.1051/0004-6361:200810090). arXiv: [0808.3817](https://arxiv.org/abs/0808.3817) [astro-ph].
- Vigan, A. et al. (Sept. 2010). “Photometric characterization of exoplanets using angular and spectral differential imaging”. In: *MNRAS* 407.1, pp. 71–82. DOI: [10.1111/j.1365-2966.2010.16916.x](https://doi.org/10.1111/j.1365-2966.2010.16916.x). arXiv: [1004.4825](https://arxiv.org/abs/1004.4825) [astro-ph.IM].
- Vigan, A. et al. (Mar. 2016). “First light of the VLT planet finder SPHERE. I. Detection and characterization of the substellar companion GJ 758 B”. In: *A&A* 587, A55, A55. DOI: [10.1051/0004-6361/201526465](https://doi.org/10.1051/0004-6361/201526465). arXiv: [1511.04076](https://arxiv.org/abs/1511.04076) [astro-ph.EP].
- Vigan, A. et al. (July 2017). “The VLT/NaCo large program to probe the occurrence of exoplanets and brown dwarfs at wide orbits. IV. Gravitational instability rarely forms wide, giant planets”. In: *A&A* 603, A3, A3. DOI: [10.1051/0004-6361/201630133](https://doi.org/10.1051/0004-6361/201630133). arXiv: [1703.05322](https://arxiv.org/abs/1703.05322) [astro-ph.EP].
- Vigan, A. et al. (July 2021). “The SPHERE infrared survey for exoplanets (SHINE). III. The demographics of young giant exoplanets below 300 au with SPHERE”. In: *A&A* 651, A72, A72. DOI: [10.1051/0004-6361/202038107](https://doi.org/10.1051/0004-6361/202038107). arXiv: [2007.06573](https://arxiv.org/abs/2007.06573) [astro-ph.EP].
- Vigan, Arthur (Sept. 2020). *vlt-sphere: Automatic VLT/SPHERE data reduction and analysis*. Astrophysics Source Code Library, record ascl:2009.002. DOI: [10.5281/zenodo.6563998](https://doi.org/10.5281/zenodo.6563998). ascl: [2009.002](https://arxiv.org/abs/2009.002).
- Villeneuve, M. et al. (Oct. 2020). “Observations of edge-on protoplanetary disks with ALMA. I. Results from continuum data”. In: *A&A* 642, A164, A164. DOI: [10.1051/0004-6361/202038087](https://doi.org/10.1051/0004-6361/202038087). arXiv: [2008.06518](https://arxiv.org/abs/2008.06518) [astro-ph.SR].

- Wahhaj, Z. et al. (Apr. 2021). "A search for a fifth planet around HR 8799 using the star-hopping RDI technique at VLT/SPHERE". In: *A&A* 648, A26, A26. DOI: [10.1051/0004-6361/202038794](https://doi.org/10.1051/0004-6361/202038794). arXiv: [2101.08268](https://arxiv.org/abs/2101.08268) [astro-ph.EP].
- Walter, F. M. (July 1986). "X-Ray Sources in Regions of Star Formation. I. The Naked T Tauri Stars". In: *ApJ* 306, p. 573. DOI: [10.1086/164367](https://doi.org/10.1086/164367).
- Weber, Philipp et al. (Oct. 2019). "Predicting the Observational Signature of Migrating Neptune-sized Planets in Low-viscosity Disks". In: *ApJ* 884.2, 178, p. 178. DOI: [10.3847/1538-4357/ab412f](https://doi.org/10.3847/1538-4357/ab412f). arXiv: [1909.01661](https://arxiv.org/abs/1909.01661) [astro-ph.EP].
- Whipple, F. L. (Jan. 1972). "On certain aerodynamic processes for asteroids and comets". In: *From Plasma to Planet*. Ed. by Aina Elvius, p. 211.
- Williams, Jonathan P. and Lucas A. Cieza (Sept. 2011). "Protoplanetary Disks and Their Evolution". In: *Annu. Rev. Astron. Astrophys* 49.1, pp. 67–117. DOI: [10.1146/annurev-astro-081710-102548](https://doi.org/10.1146/annurev-astro-081710-102548). arXiv: [1103.0556](https://arxiv.org/abs/1103.0556) [astro-ph.GA].
- Wolszczan, A. and D. A. Frail (Jan. 1992). "A planetary system around the millisecond pulsar PSR1257 + 12". In: *Nature* 355.6356, pp. 145–147. DOI: [10.1038/355145a0](https://doi.org/10.1038/355145a0).
- Wright, Edward L. et al. (Dec. 2010). "The Wide-field Infrared Survey Explorer (WISE): Mission Description and Initial On-orbit Performance". In: *Astronomical Journal* 140.6, pp. 1868–1881. DOI: [10.1088/0004-6256/140/6/1868](https://doi.org/10.1088/0004-6256/140/6/1868). arXiv: [1008.0031](https://arxiv.org/abs/1008.0031) [astro-ph.IM].
- Wright, Gillian S. et al. (Oct. 2004). "The JWST MIRI instrument concept". In: *Optical, Infrared, and Millimeter Space Telescopes*. Ed. by John C. Mather. Vol. 5487. Society of Photo-Optical Instrumentation Engineers (SPIE) Conference Series, pp. 653–663. DOI: [10.1117/12.551717](https://doi.org/10.1117/12.551717).
- Wyatt, M. C. (Apr. 2005). "The insignificance of P-R drag in detectable extrasolar planetesimal belts". In: *A&A* 433.3, pp. 1007–1012. DOI: [10.1051/0004-6361:20042073](https://doi.org/10.1051/0004-6361:20042073). arXiv: [astro-ph/0501038](https://arxiv.org/abs/astro-ph/0501038) [astro-ph].
- Wyatt, M. C. et al. (June 2015). "Five steps in the evolution from protoplanetary to debris disk". In: *Astrophysics and Space Science* 357.2, 103, p. 103. DOI: [10.1007/s10509-015-2315-6](https://doi.org/10.1007/s10509-015-2315-6). arXiv: [1412.5598](https://arxiv.org/abs/1412.5598) [astro-ph.EP].
- Xie, Chen et al. (Aug. 2022). "Reference-star differential imaging on SPHERE/IRDIS". In: *arXiv e-prints*, arXiv:2208.07915, arXiv:2208.07915. arXiv: [2208.07915](https://arxiv.org/abs/2208.07915) [astro-ph.EP].
- Yang, Hongjing et al. (Oct. 2022). "KMT-2021-BLG-0171Lb and KMT-2021-BLG-1689Lb: two microlensing planets in the KMTNet high-cadence fields with followup observations". In: *MNRAS* 516.2, pp. 1894–1909. DOI: [10.1093/mnras/stac2023](https://doi.org/10.1093/mnras/stac2023). arXiv: [2205.12584](https://arxiv.org/abs/2205.12584) [astro-ph.EP].
- Youdin, Andrew N. and Jeremy Goodman (Feb. 2005). "Streaming Instabilities in Protoplanetary Disks". In: *ApJ* 620.1, pp. 459–469. DOI: [10.1086/426895](https://doi.org/10.1086/426895). arXiv: [astro-ph/0409263](https://arxiv.org/abs/astro-ph/0409263) [astro-ph].
- Youdin, Andrew N. and Yoram Lithwick (Dec. 2007). "Particle stirring in turbulent gas disks: Including orbital oscillations". In: 192.2, pp. 588–604. DOI: [10.1016/j.icarus.2007.07.012](https://doi.org/10.1016/j.icarus.2007.07.012). arXiv: [0707.2975](https://arxiv.org/abs/0707.2975) [astro-ph].
- Zacharias, N. et al. (July 2012). "VizieR Online Data Catalog: UCAC4 Catalogue (Zacharias+, 2012)". In: *VizieR Online Data Catalog*, I/322A, I/322A.

- Zhang, Michael et al. (Feb. 2022). "Escaping Helium from TOI 560.01, a Young Mini-Neptune". In: *Astronomical Journal* 163.2, 67, p. 67. DOI: [10.3847/1538-3881/ac3fa7](https://doi.org/10.3847/1538-3881/ac3fa7). arXiv: [2110.13150](https://arxiv.org/abs/2110.13150) [astro-ph.EP].
- Zhang, Yapeng, Ignas A. G. Snellen, and Paul Mollière (Dec. 2021). "The $^{12}\text{CO}/^{13}\text{CO}$ isotopologue ratio of a young, isolated brown dwarf. Possibly distinct formation pathways of super-Jupiters and brown dwarfs". In: *A&A* 656, A76, A76. DOI: [10.1051/0004-6361/202141502](https://doi.org/10.1051/0004-6361/202141502). arXiv: [2109.11569](https://arxiv.org/abs/2109.11569) [astro-ph.EP].
- Zhu, Zhaohuan et al. (Mar. 2011). "Transitional and Pre-transitional Disks: Gap Opening by Multiple Planets?" In: *ApJ* 729.1, 47, p. 47. DOI: [10.1088/0004-637X/729/1/47](https://doi.org/10.1088/0004-637X/729/1/47). arXiv: [1012.4395](https://arxiv.org/abs/1012.4395) [astro-ph.SR].
- Zuckerman, B. et al. (Nov. 2001). "The β Pictoris Moving Group". In: *ApJ Letters* 562.1, pp. L87–L90. DOI: [10.1086/337968](https://doi.org/10.1086/337968).
- Zurlo, A. et al. (Dec. 2014). "Performance of the VLT Planet Finder SPHERE. I. Photometry and astrometry precision with IRDIS and IFS in laboratory". In: *A&A* 572, A85, A85. DOI: [10.1051/0004-6361/201424204](https://doi.org/10.1051/0004-6361/201424204). arXiv: [1410.1754](https://arxiv.org/abs/1410.1754) [astro-ph.EP].

Acknowledgements

These last four years have been a roller coaster of events and emotions, and I would not have been able to be writing these words if it weren't for the support and guidance of different people I met along the way.

First and foremost, I would like to thank my supervisors, Thomas Henning, Markus Feldt, and Wolfgang Brandner. Thomas, thank you for giving me the opportunity of doing a PhD at MPIA, for your understanding in difficult times and for all the research ideas. Markus, thank you for your support and all the "quick and dirty" python scripts. Wolfgang, thank you for your encouragement and your patience every time I went to you with questions.

I am also grateful to all my collaborators. Miriam, Paola, Paul, Anne-Lise, David, Marcelo, Matthias, Faustine, Hubert, and Steve for all your help and patience throughout paper and proposal writing, for your time and all the useful discussions!

I would also like to thank Sabine Reffert, for being part of my Thesis Committee and now one of the referees of this thesis. And thank you Cornelis Dullemond and Björn Malte Schäfer for agreeing to be part of my defense committee.

I am also grateful to Christian Fendt and Huang Witte-Nguy for running the IMPRS program and taking such interest in the students making us feel welcome and cared for. I would also like to thank all the MPIA staff, for their help and kindness every time I had a problem and for making MPIA a very nice place to work.

To my IMPRS generation, for all the pub nights, the dinners and the trips that we could share before the pandemic! I would also like to thank my office-mates, past and current, for the interesting conversations and laughs at the "kinder garden office" and at the Elsässerlab. Thank you Martin for teaching me the right ways of making coffee and ventilating properly, and for inviting me to be part of EDEN! Thank you Timmy for always making me laugh even in stressful times. Thank you also to the members of the outreach team and to the rest of the organisers of Astronomy on Tap, for giving me the chance to share the love of science with others outside of work!

To all the people that throughout the years became good friends: to Khatia, for being my first friend in Heidelberg. To Paz, gracias por tu apoyo en los momentos más difíciles y por ser un ejemplo de que se puede seguir adelante. Isma, gracias por tu buen humor y por enseñarme chileno. Liz, gracias por darme tu apoyo cuando lo necesité y por siempre animarme. Marcelo, gracias por tu amistad y por los memes. Y gracias a ambos por las tardes en el Mensa, los paseos y las sesiones de trabajo! Seba, gracias por las aventuras en Australia y por tus buenos consejos. Rubén, gracias por las caminatas y charlas durante el confinamiento. Nico, gracias por resolver mis dudas de ALMA y por tu paciencia para explicar. Gianca, grazie mille for being my gym buddy, and for all the delicious pasta dinners! Olga, gracias amiga for all the nice moments we shared in the other side of the world! Lucia, thank you for encouraging me to scuba dive and for sharing your wisdom with me! Gus, gracias por tu amabilidad y por recorrer Valencia conmigo! Irina and Greg, thank you for all the nice gatherings and short-trips you organised and for letting me take care of Arya.

Last but not least, I would like to thank my family, en especial a pa y a mami, gracias por todo su cariño y apoyo a lo largo de estos años. Amandinne y Anita, gracias por siempre hacerme reír y por compartir los buenos y malos momentos. Abuelita Tere, gracias por todo tu amor y por haber sido my fan #1, y tío Pancho, gracias por siempre creer en mí y apoyarme. Gracias por todo!

And finally, I want to thank the person that has been by my side during the writing of this thesis and much more, Chris. Thank you for proof-reading parts of this thesis and for your always insightful comments. Thank you for your love and unconditional support along the ups and downs, I wouldn't have made it without you.